UNIVERSIDADE TÉCNICA DE LISBOA
INSTITUTO SUPERIOR TÉCNICO

Study of the Production of the $\rho + \omega$ and ϕ Vector-Mesons in Lead Induced Collisions at 158 GeV/Nucleon

Estudo da Produção dos Mesões-vector $\rho + \omega$ e ϕ em Colisões Induzidas por Chumbo a 158 GeV/Nucleão

Translation of the original thesis written in Portuguese

Catarina Marques Quintans

Dissertation for obtaining the degree as Physics PhD

Supervisor:
Doutora Maria Paula Frazão Bordalo e Sá
President:
Reitor da Universidade Técnica de Lisboa
Juri:
Doutor Louis Kluberg
Doutor Jorge Venceslau Comprido Dias de Deus
Doutora Nicole Willis
Doutora Maria Paula Frazão Bordalo e Sá
Doutor Sérgio Eduardo Campos Costa Ramos

November 2002

Abstract

The heavy ion collisions at ultra-relativistic energies allows for the production of extremely hot and dense systems. For limit conditions of temperature and density, QCD predicts a phase transition from hadronic matter to a deconfined quarks and gluons plasma. One of the expected signatures of the plasma is an enhancement of strange particles production. The increase of the ratio $\phi/(\rho+\omega)$ as a function of the collision centrality is thus considered a good evidence of the phase transition.

In the Experiment NA50 from CERN a lead ion beam of 158 A GeV collides on a lead target. A spectrometer allows for the identification of the correlated muon pairs produced. Dimuons (and dileptons in general) are considered a good probe, since their have almost no interactions after production, thus keeping their initial properties.

The study of the $\rho+\omega$ and ϕ vector-meson production is done in different P_T and E_T regions. The dimuon mass spectra are corrected for acceptance and smearing effects and then fitted by a 5 free parameters function: the 3 resonances normalizations and 2 parameters to describe the continuum.

The present study concludes that the $\phi/(\rho+\omega)$ ratio does not depend on P_T, but it increases with the collision centrality. The analysis of the effective temperatures shows that $T_{\rho+\omega} \approx T_\phi = 220$ MeV, independently of the centrality.

Agradecimentos — Thanks

À minha orientadora, Professora Paula Bordalo, gostaria de agradecer todo o apoio prestado, a atenção e a disponibilidade manifestados. As muitas discussões de física que me proporcionou, o seu sentido crítico e entusiasmo postos nos trabalhos em curso foram determinantes para a execução deste estudo.

Ao Professor Sérgio Ramos gostaria igualmente de manifestar o meu agradecimento pelas muitas discussões e sobre os mais diversos temas de Física, e pelo apoio sempre presente.

Um agradecimento muito especial é devido aos meus colegas de grupo Gonçalo Borges, Helena Santos e Teresa Claudino, pela companhia, o encorajamento e as discussões não apenas sobre Física.

To all my colleagues in the NA50 Collaboration I would like to express my gratitude. Participating in this Collaboration was very gratifying for me, in both scientific and human aspects. I would like to thank in particular the discussions and the help I received in many occasions from Dr. Louis Kluberg, Dr. Bernard Chaurand, Prof. Nicole Willis, Prof. Marie Pierre Comets and Dr. Laurence Villatte.

A todos os colegas do LIP agradeço a ajuda e os bons momentos partilhados. Em particular gostaria de agradecer ao Jorge Gomes e ao João Paulo Martins a disponibilidade sempre demostrada para resolverem os muitos problemas computacionais que foram surgindo ao longo deste trabalho.

Aos meus pais e irmãos, ao Bruno, Sofias, Gil e Jorge, um muito obrigada pela vossa infinita paciência, por estarem presentes nalguns momentos muito difíceis, e também pelos muitos momentos óptimos que temos partilhado ao longo destes anos.

Ao LIP (Laboratório de Instrumentação e Física Experimental de Partículas) agradeço o apoio financeiro e os meios técnicos que me disponibilizaram.

À Fundação para a Ciência e Técnologia agradeço o apoio financeiro, indispensável à realização deste trabalho, que me prestaram, através do programa PRAXIS XXI.

Contents

1 Introduction **1**

1.1 The quark gluon plasma . . . 1

1.1.1 Where to find the plasma and how to recreate it . . . 1

1.1.2 A collision's evolution . . . 2

1.2 Plasma signatures using dileptons . . . 3

1.2.1 Hadronic modifications in the dense medium . . . 4

1.2.2 Additional strangeness production . . . 12

1.2.3 Other plasma signatures . . . 17

1.3 Future searches for the QGP . . . 19

2 Experimental apparatus **23**

2.1 Beam detectors . . . 24

2.1.1 BH detector . . . 24

2.1.2 Interaction detectors . . . 24

2.1.3 Anti-halo detectors . . . 25

2.2 The target region . . . 25

2.3 Detectors for centrality measurements . . . 25

2.3.1 The multiplicity detector . . . 25

2.3.2 The electromagnetic calorimeter . . . 26

2.3.3 The zero degree calorimeter . . . 27

2.4 The muon spectrometer . . . 28

2.4.1 Absorbers . . . 28

2.4.2 Scintillating hodoscopes . . . 29

2.4.3 Multiwire chambers . . . 30

2.4.4 The magnet . . . 30
2.5 The trigger system . . . 31
2.6 The data acquisition system . . . 32
2.7 Reconstruction of tracks . . . 32

3 Data selection **33**
3.1 The statistics of the data . . . 33
3.2 The image cut . . . 34
3.3 The target selection . . . 35
3.4 The diagonal cut . . . 36
3.5 Geometrical cut . . . 38
3.6 The kinematic region studied . . . 41
3.7 Subtraction of the combinatorial background . . . 43

4 Method of analysis **49**
4.1 The physics generations . . . 50
4.1.1 Mass generation . . . 51
4.1.2 Transverse momentum generation . . . 52
4.1.3 Generation on rapidity, $\cos\theta_{CS}$ and azimuthal angle . . . 52
4.2 Adjustment of the Monte-Carlo to the data . . . 53
4.3 The simulated distributions and the geometrical cut . . . 57
4.4 Acceptances and smearing . . . 63

5 Experimental results **67**
5.1 Relative production of the vector-mesons ϕ and $\rho+\omega$ . . . 67
5.1.1 $\frac{\phi}{\rho+\omega}$ as a function of P_T and E_T . . . 68
5.1.2 $\frac{\phi}{\rho+\omega}$ as a function of P_T . . . 72
5.1.3 $\frac{\phi}{\rho+\omega}$ as a function of E_T . . . 75
5.2 Temperatures of $\rho+\omega$ and ϕ . . . 75
5.2.1 The inverse slope from the M_T distribution . . . 77
5.2.2 Temperatures as a function of centrality . . . 79
5.3 $\rho+\omega$ and ϕ multiplicities . . . 84

5.3.1 The minimum bias events distribution 85
5.3.2 Multiplicities measurement 87
5.4 Other data selections and respective analysis 90
5.4.1 Selection NOCIMD 90
5.4.2 Analysis with beam pile-up rejection 98
5.5 Study of the systematic errors 100
5.5.1 Differences between MC and data 104
5.5.2 Systematic error from the background subtraction 105
5.5.3 Final systematic error 107
5.5.4 Temperature calculation including systematic errors 107

6 Results discussion **113**
6.1 Stability of the results 113
6.1.1 Study in 5 E_T regions 113
6.1.2 χ^2 per point study 114
6.1.3 Sensitivity to the deconvolution method 120
6.1.4 Sensitivity to the fit function 122
6.1.5 Sensitivity to the ρ pole 127
6.1.6 The continuum line shape 128
6.1.7 Study of the M_T distributions' scaling 129
6.2 Comparison with other results 131
6.2.1 Comparison with other analyses 132
6.2.2 Comparison with other systems 135
6.3 Conclusions 140

A The Breit-Wigner functions **143**

B Definition of some interesting variables **147**
B.1 Rapidity and pseudo-rapidity 147
B.2 The Collins-Soper frame 148
B.3 Variables for collision centrality 148
B.3.1 Energy density 149

B.3.2 Impact parameter, N_{col} and N_{part} 150
B.3.3 The L variable 153

C Fine tuning of the $P * Dtarget$ cut **155**

List of Figures

1.1 Diagram of temperature *versus* baryonic density. 2

1.2 An heavy ion collision, seen in collision's CM. 3

1.3 Space-time evolution of the quark gluon plasma created in an heavy ion collision according to Bjorken model. 4

1.4 Ratio of dielectrons produced in Ca+Ca collisions and C+C collisions at 1 A GeV/c (experimental results from DLS). 8

1.5 Dielectron spectrum obtained by the CERES experiment in p+Au (a) and S+Au (b) collisions. Represented is also the sum of all the expected physics contributions [1][2]. 9

1.6 Dimuon mass spectrum obtained by the HELIOS-3 experiment in p+W and S+W collisions at 200 A GeV/c. Distributions are normalised to the total number of charged particles [3]. 10

1.7 Phase spaces of HELIOS-3, CERES, NA38 and NA50 [4]. 10

1.8 Dimuon spectrum obtained by the NA38 experiment in p+U (a) and S+U (b) collisions at 200 A GeV/c. Represented is also the sum of the expected physics contributions, including an empirical extrapolation of Drell-Yan to the low mass region. 11

1.9 Multi-strange particle production in Pb+Pb collisions, compared to their production in proton induced collisions, in the experiment NA57 [5]. 16

1.10 Effective temperature T versus the particle's mass, for Pb+Pb collisions at 158 GeV/nucleon. 16

1.11 Ratio J/ψ/DY as a function of the transverse energy, obtained by NA50 in Pb+Pb collisions at 158 A GeV/c. 20

2.1 NA50 experimental apparatus for Pb+Pb collisions. 23

2.2 Schematic view of the NA50 target region, with centrality detectors and hadron absorbers. 26

2.3 NA50 main absorber. 29

2.4 Coincidence $V^i = R1^i \times R2^i$ for the dimuon trigger system [6]. 29

2.5 Frontal view of the magnet (a); magnetic field lines created (b). 31

3.1 Distribution of $\mu^+\mu^-$ events seen by the active target system. Position 4 corresponds to the lead sub-target location. NOCIBI=14 or 24 means that only one of the blades associated with position 4 identified a signal of amplitude higher than its discrimination threshold. 35

3.2 Diagonal cut. a)E_T *vs* E_{ZDC} correlation before the cut and the target selection; b)E_T *vs*E_{ZDC} correlation before the cut and with target selection; c)After axis rotation; d)E_T *vs*E_{ZDC} correlation after the diagonal cut. . . . 36

3.3 Maximum correlation straight line of E_T *vs* E_{ZDC}, and definition of the θ rotation angle. 37

3.4 Gaussian fit to the projection in the transverse axis of the E_T *vs* E_{ZDC} correlation. 38

3.5 Definition of the distance *Dtarget* of an extrapolated track to the beam line. 39

3.6 Momentum distribution of the convergent and divergent muons. Selection of $\mu^+\mu^-$ events with $M \geq 3$ GeV/c^2 and NOCIBI=4 40

3.7 The χ^2 probability of $(P * Dtarget)^2$, for convergent and divergent tracks. Selection of $\mu^+\mu^-$ events with $M \geq 3$ GeV/c^2 and NOCIBI=4 40

3.8 Distribution of the $\mu^+\mu^-$ events reconstructed vertex with $M < 2.5$ GeV/c^2. Superimposed are the distributions before and after the $P * Dtarget$ cut (4% cut). 41

3.9 Dimuon rapidity distribution, including all the statistics of $\mu^+\mu^-$ events with $M < 2.5$ GeV/c^2, with all cuts applied. Superimposed is the accepted rapidity window. 42

3.10 Total events analysed. Dimuons of opposite sign and of same sign(a); estimated background, and signal dimuons obtained after background subtraction(b). 44

3.11 Mass spectrum of opposite sign dimuons, signal events, and the ratio background/signal. Data integrated in the regions $1.4 \leq P_T < 3.5$ GeV/c and $5 \leq E_T < 150$ GeV. 47

4.1 Distributions of simulated (a) and accepted (b) MC events, as functions of the dimuons mass, transverse momentum, rapidity and $\cos\theta_{CS}$. 54

4.2 Distributions of accepted MC events after reconstruction and cuts, as functions of measured mass, transverse momentum and rapidity. 55

4.3 Iterative method for the adjustment of the Monte-Carlo to the data. 56

4.4 Matrices containing the weights for the multidimensional MC correction. Matrix (M,P_T) and matrix (Y), after 2 iterations. 57
4.5 Comparison between the mass distributions of reconstructed Monte-Carlo events and the experimental mass spectra. Ratio MC/Data without correction, and after one or two iterations. 58
4.6 Comparison between the P_T distributions of reconstructed Monte-Carlo events and the experimental P_T spectra. Ratio MC/Data without correction, and after one or two iterations. 59
4.7 Comparison between the rapidity distributions of reconstructed Monte-Carlo events and the experimental rapidity spectra. Ratio MC/Data without correction, and after one or two iterations. 60
4.8 Generated Monte-Carlo distributions as functions of the dimuons mass, transverse momentum and rapidity, before (black) and after (red) applying the weights to adjust MC to data. 61
4.9 Comparison between the σ coefficients tuned on the Monte-Carlo $P * Dtarget$ distributions and those tuned on data, for convergent and divergent tracks. 62
4.10 Acceptance as a function of the dimuons mass, P_T and rapidity. 63
4.11 Inverse smearing matrices, as functions of the dimuons mass, P_T and rapidity (integrations on the same regions as in figure 4.10).) 64
4.12 Differential acceptance convoluted with smearing as a function of the dimuons transverse momentum, per P_T regions, for $5 \leq E_T < 150$ GeV. 65
4.13 Differential acceptance convoluted with smearing as function of the dimuon's transverse momentum, by regions of mass, for $5 \leq E_T < 150$ GeV. 66

5.1 Fit to the dimuons mass spectrum in the region $1.8 \leq P_T < 2.0$ GeV/c and $42 \leq E_T < 150$ GeV. 69
5.2 Ratios $\phi/(\rho + \omega)$ as a function of P_T, per 9 E_T regions. 70
5.3 Ratios $\phi/(\rho + \omega)$ as a function of E_T, per 4 P_T regions. 71
5.4 Fits to the dimuon mass spectra, in 4 P_T regions, integrated in $5 \leq E_T < 150$ GeV. 73
5.5 Fits to the dimuon mass spectra, in 4 P_T regions, integrated in $42 \leq E_T < 150$ GeV. 74
5.6 Ratios $\phi/(\rho+\omega)$ as a function of P_T, in the integrated regions $5 \leq E_T < 150$ GeV and $42 \leq E_T < 150$ GeV. 75
5.7 Fits to the dimuon mass spectra, in 9 E_T regions, and for the integrated region $1.4 \leq P_T < 3.5$ GeV/c. 76

5.8 Fit to the $\rho+\omega$ and ϕ cross-sections, as a function of the dimuons transverse mass. Data integrated in $5 \leq E_T < 150$ GeV. 79

5.9 Fit to the mass spectra, for temperature studies, per E_T bins in the region $1.4 \leq P_T < 1.6$ GeV/c. 80

5.10 Fit to the mass spectra, for temperature studies, per E_T bins in the region $1.6 \leq P_T < 1.8$ GeV/c. 81

5.11 Fit to the mass spectra, for temperature studies, per E_T bins in the region $1.8 \leq P_T < 2.0$ GeV/c. 82

5.12 Fit to the mass spectra, for temperature studies, per E_T bins in the region $2.0 \leq P_T < 3.5$ GeV/c. 83

5.13 Correlation N_{part} versus b for Pb+Pb collisions at 158 GeV/nucleon, using the Glauber model with Woods-Saxon nuclear density profiles (given in [7]). 86

5.14 Correlation E_T *vs* E_{ZDC} for MB events (a); with NOCIBI=4 selection (b); and after diagonal cut (c). 87

5.15 Distribution of MB events as a function of the transverse energy, with NOCIBI=4 selection and after diagonal cut. 88

5.16 Multiplicities of $\rho+\omega$ and ϕ, evaluated in the regions $3 \leq Y < 4$ and $1.4 \leq P_T < 3.5$ GeV/c. 89

5.17 Multiplicities per participant of $\rho+\omega$ and ϕ, as a function of the number of participants. Fit with a straight line $y = P_1 + P_2 x$. 89

5.18 Gaussian fit to the transverse projection of the E_T *vs* E_{ZDC} correlation, for the NOCIMD selection. 92

5.19 χ^2 probability of $(P*Dtarget)^2$, for convergent and divergent tracks. Event selection including $\mu^+\mu^-$ with $M \geq 3$ GeV/c^2 and NOCIMD=4. 92

5.20 Reconstructed vertex distribution, for $\mu^+\mu^-$ events with $M < 2.5$ GeV/c^2, and selected with NOCIMD (a). Superimposed are the distributions before and after $P*Dtarget$ cut at 3%. Reconstructed vertex distribution for the corresponding signal events after cuts. 93

5.21 Signal events distribution as a function of E_T, with NOCIBI selection (in black) and NOCIMD selection (in red). 94

5.22 Ratios $\phi/(\rho+\omega)$ as a function of P_T, for the integrated region $5 \leq E_T < 150$ GeV. Comparison of results using NOCIMD or NOCIBI selection. 95

5.23 Ratios $\phi/(\rho+\omega)$ as a function of E_T, in the integrated region $1.4 \leq P_T <$ 3.5 GeV/c. Comparison of results obtained with NOCIMD and NOCIBI selections. 96

5.24 Fit to the cross-sections of $\rho+\omega$ and ϕ as a function of the transverse mass, to obtain effective temperatures. NOCIMD selection. 98

5.25 $\rho + \omega$ and ϕ effective temperatures, as a function of the transverse energy, obtained with NOCIMD or NOCIBI selections, and only considering statistical errors. 100

5.26 Signal events distribution as a function of E_T, with and without NIBHAB cut; and ratio of the two E_T spectra. 101

5.27 Ratios $\phi/(\rho+\omega)$ as a function of P_T, for the integrated region $5 \leq E_T < 150$ GeV. Comparison of analyses with and without NIBHAD cut. 102

5.28 Ratios $\phi/(\rho+\omega)$ as a function of E_T, with NOCIBI selection. Comparison of analyses with and without NIBHAD cut. 102

5.29 Dependency of the background subtraction R parameter with the impact parameter b, according to a MC simulation for Pb+Pb collisions at 158 GeV/nucleon [8]. 106

5.30 Ratios $\phi/(\rho + \omega)$ using $R = 1$ compared to the ones using R from MC (according to figure 5.29). 108

5.31 Fit to obtain the effective temperatures of $\rho+\omega$ and ϕ, considering statistic and systematic errors. 108

5.32 $\rho + \omega$ and ϕ effective temperatures, considering statistical and systematic errors on the cross-sections, as a function of E_T. 111

6.1 Ratios $\phi/(\rho + \omega)$ as a function of P_T, in 5 E_T regions. 115

6.2 Comparison between the ratios $\phi/(\rho + \omega)$ as a function of E_T, per P_T regions, with 5 or 9 points in E_T. 116

6.3 χ^2 per point distributions of the fits to the mass spectra shown in figure 5.4. The points with $\chi^2 > 5$ are located above the red line. 118

6.4 Fit to the deconvoluted mass spectra, rejecting the points with $chi^2 > 5$. The rejected points, not taken in account by the fit, are shown in red. . . . 119

6.5 Ratios $\phi/(\rho + \omega)$ as a function of P_T, rejecting or not the data points with $\chi^2 > 5$ in the fit to the mass spectra. 120

6.6 Example of the alternative deconvolution procedure. Mass distribution of signal events (a); after smearing correction (b); after smearing and acceptance correction (c). 121

6.7 Comparison of the ratio $\phi/(\rho + \omega)$ obtained by the method of correcting for acceptance and smearing effects separately, and the standard method. . 122

6.8 Fit to the mass spectra integrated in the region $5 \leq E_T < 150$ GeV, with a modified relativistic Breit-Wigner function for the ρ. 125

6.9 Ratios $\phi/(\rho + \omega)$ as a function of P_T, in the region $5 \leq E_T < 150$ GeV, using the relativistic BW ρ line shape, compared with the results using the classical one. 126

6.10 Ratios $\phi/(\rho+\omega)$ as a function of P_T, for $5 \leq E_T < 150$ GeV, fixing $\omega/\rho = 1.6$. Comparison with the standard analysis. 128

6.11 Stability of the ρ pole, when it is let as a free parameter of the mass spectra fits. The red line shows the ρ pole given by the PDG, and the black one the mean value obtained here. 129

6.12 Fit to the mass spectra in 9 E_T regions, using the continuum line shape fitted in the reconstructed MC distributions (in red). 130

6.13 Ratios $\phi/(\rho + \omega)$ obtained using a continuum fitted in the reconstructed and modified MC, or using the standard decreasing exponential. 132

6.14 Effective temperatures fit for ρ+ω and for ϕ, including statistic and systematic errors in the cross-sections, and using as M_T scaling $M_T\ exp(-M_T/T)$. 134

6.15 Comparison between different analyses of the lead data, this analysis and the non-deconvoluted analysis. 135

6.16 Measured hadronic effective temperatures for Pb+Pb collisions at 158 GeV/nucleon, compared to the quarks coalescence model MICOR. 136

6.17 Comparison of the ratio $\phi/\rho+\omega)$ as a function of P_T for Pb+Pb collisions at 158 GeV/nucleon with sulphur and proton induced collisions at 200 GeV/nucleon (taken by NA38). 137

6.18 Comparison of the ratio $\phi/(\rho+\omega)$ as a function of E_T for Pb+Pb collisions at 158 GeV/nucleon with sulphur induced collisions at 200 GeV/c (NA38). 138

6.19 Effective temperatures of ρ+ω and ϕ as a function of E_T obtained in Pb+Pb collisions at 158 GeV/nucleon. Comparison with temperatures obtained in S+U collisions at 200 GeV/nucleon (NA38). 139

A.1 Comparison of different possible parameterisations of ρ^o, being the classical and relativistic with fixed width; and the ones used by HELIOS and the present study, relativistic and with variable width. 146

B.1 The Collins-Soper frame and definition of the θ_{CS} and ϕ_{CS} angles. 148

B.2 Nucleon-nucleon collision scheme. 150

C.1 Distributions of the shifts for convergent muons, Dx and Dy as a function of the momentum of the muons, and corresponding distribution of the $P * Di$ variable, with $i = x$ and y. 156

C.2 χ^2_{pdtgt} probability distributions of convergent (a) and divergent (b) tracks, with a selection of $\mu^+\mu^-$ events with $M < 2.5$ GeV/c^2 and NOCIBI=4 . . . 157

C.3 χ^2_{pdtgt} probability distributions for the first and second muon of signal events, in a set with $M < 2.5$ GeV/c^2, $P_\mu < 12$ GeV/c and with NOCIBI=4 selection. 158

List of Tables

1.1 Mass, total width, lifetime and branching ratio into dimuons of the vector-mesons ρ, ω, ϕ e J/ψ [9]. . . . 4

3.1 Statistics of Pb+Pb 1998 data taking. Sum of dimuons $\mu^+\mu^-$, $\mu^+\mu^+$ and $\mu^-\mu^-$. 34

3.2 Minimisation of the gaussian width σ fitted in the transverse projection of the E_T *vs* E_{ZDC} correlation. . . . 37

3.3 Total statistics of analysed data, per P_T and E_T regions. The ratio bkg/sgn is for the region $0.65 \leq M < 1.2$ GeV/c^2. . . . 46

5.1 Ratio $\phi/(\rho+\omega)$, per transverse momentum and transverse energy regions. In brackets the χ^2 per degree of freedom of the fit to the mass spectrum . . 72

5.2 $\phi/(\rho+\omega)$ in 4 P_T regions, with the mass spectra integrated in 2 E_T regions. 75

5.3 $\phi/(\rho+\omega)$ in 9 E_T regions, for the mass spectra integrated in $1.4 \leq P_T < 3.5$ GeV/c. . . . 77

5.4 Dimuon transverse mass regions for the resonances $\rho+\omega$ and ϕ. . . . 78

5.5 Number of events $\rho+\omega$ e ϕ produced in the acceptance window given in section 3.6, in each P_T region, and normalised to the width of the corresponding region in M_T. Spectra integrated in $5 \leq E_T < 150$ GeV. . . . 78

5.6 Effective temperatures for $\rho+\omega$ and ϕ, per E_T regions. . . . 84

5.7 Pb+Pb 1998 data statistics, with NOCIMD selection. Sum of the dimuons $+-$,$++$ and $--$. . . . 90

5.8 Minimisation of the Gaussian width σ fitted in the transverse projection of the E_T *vs* E_{ZDC} correlation, for the NOCIMD selection. . . . 91

5.9 Signal events statistics with NOCIMD selection and after cuts from table 5.7 are applied. . . . 94

5.10 Ratios $\phi/(\rho+\omega)$ in 4 P_T regions, for data integration in the region $5 \leq E_T < 150$ GeV, and with NOCIMD selection. . . . 95

5.11 Ratios $\phi/(\rho+\omega)$ in 9 E_T regions, for data integrated in $1.4 \leq P_T < 3.5$ GeV/c, and with selection NOCIMD. 96

5.12 Ratios $\phi/(\rho+\omega)$, per P_T and E_T regions. Between brackets the χ^2 per degree of freedom of the fit is shown. 97

5.13 Effective temperatures for $\rho+\omega$ and ϕ, per E_T regions, with NOCIMD selection. Errors quoted are only statistical. 99

5.14 Ratios $\phi/(\rho+\omega)$ in 4 P_T regions, for the mass spectra integrated in $5 \leq E_T < 150$ GeV. NOCIBI selection with NIBHAD cut. 101

5.15 Ratios $\phi/(\rho+\omega)$ in 9 E_T regions, for the mass spectra integrated in $1.4 \leq P_T < 3.5$ GeV/c. Selection NOCIBI with NIBHAD cut. 103

5.16 Ratios $\phi/(\rho+\omega)$ in 4 P_T regions, with a MC adjusted to the data in 3 iterations. 104

5.17 Systematic error from the differences between simulated and experimental distributions. 105

5.18 Number of participants, number of collisions, impact parameter and the correspondence to the R factor, for this analysis' mean E_T values. 107

5.19 Ratios $\phi/(\rho+\omega)$ in 9 E_T regions, with data integrated in $1.4 \leq P_T < 3.5$ GeV/c, using the R factors obtained from MC simulation using VENUS, or using R=1. 109

5.20 Relative difference for the number of resonant events $\rho+\omega$ and ϕ and for the ratio $\phi/(\rho+\omega)$, from the analysis with background subtraction using R from MC relative to the standard analysis. 109

5.21 Relative difference in the $\rho+\omega$ and ϕ number and in the ratio $\phi/(\rho+\omega)$, between the analysis using background subtraction with R from the MC and the standard analysis, per P_T regions. 110

5.22 Final mean systematic errors affecting measurements. 110

5.23 $\rho+\omega$ and ϕ effective temperatures, per E_T regions. Standard analysis, including statistical and systematic errors. 110

6.1 $\phi/(\rho+\omega)$ ratio, in 4 P_T regions and 5 E_T regions. The χ^2 per degree of freedom of the fit to the mass spectra is inside brackets. 114

6.2 Ratios $\phi/(\rho+\omega)$ in 4 P_T regions, for the mass spectra integrated in $5 \leq E_T < 150$ GeV region, rejecting points with $\chi^2 > 5$, identified in the standard fit. Comparison with the standard analysis. 117

6.3 Relative deviations on the resonant event numbers $\rho+\omega$ and ϕ and on the ratio $\phi/(\rho+\omega)$, between the *standard* analysis and the one rejecting points with $\chi^2 > 5$. 117

6.4 Relative differences in the number of $\rho + \omega$s and ϕs and in the ratio, for the standard analysis and for the one in which the data is deconvoluted for acceptance and smearing separately. 122

6.5 Ratios $\phi/(\rho + \omega)$ in 4 P_T regions, for the mass spectra integrated in $5 \leq E_T < 150$ GeV region, with ρ described by a modified relativistic Breit-Wigner function. Comparison with the standard analysis. 124

6.6 Relative differences in the number of resonant events and in the $\phi/(\rho+\omega)$ ratio, with ρ parametrised by a modified relativistic Breit-Wigner function or by a classical Breit-Wigner. 124

6.7 Ratios $\phi/(\rho+\omega)$ in 4 P_T regions, for the mass spectra integrated in all the E_T region, fixing $\omega/\rho = 1.6$, compared to the standard analysis. 127

6.8 Relative differences in the number of $\rho + \omega$ and ϕ resonant events and in the $\phi/(\rho + \omega)$ ratio, between the analysis with fixed $\omega/\rho = 1.6$ and the standard analysis. 127

6.9 Ratios $\phi/(\rho + \omega)$ in 9 transverse energy regions, using a continuum line shape fitted in the MC. Comparison with the results from the standard analysis. 131

6.10 Relative differences in the number of $\rho+\omega$ and ϕ resonant events and in the ratio $\phi/(\rho+\omega)$, between the standard analysis and one using the continuum fitted in the MC. 133

6.11 $\rho+\omega$ and ϕ effective temperatures, obtained with two different methods of analysis, and different scalings in M_T, from the NA50 experiment. 133

Chapter 1

Introduction

"(...)The experiments on CERN's Heavy Ion program presented compelling evidence for the existence of a new state of matter(...). The collisions created temperatures over 100000 times as hot as the centre of the sun, and energy densities twenty times that of ordinary nuclear matter, densities which have never before been reached in laboratory experiments. (...) This state of matter found in heavy ion collisions at the SPS features many of the characteristics of the theoretically predicted quark-gluon plasma, the primordial soup in which quarks and gluons existed before they clumped together as the universe cooled down."
CERN official press release at 10th February 2000

1.1 The quark gluon plasma

According to Quantum Chromodynamics (QCD), the theory that explains the strong force, the colour interaction between quarks is attractive, reason why the energy of the system decreases when pairs $q\bar{q}$ are created. The vacuum, defined as the state of minimum energy, is filled with $q\bar{q}$ pairs, constituting a condensate. Thus, for zero temperature and density the QCD vacuum has a non-trivial structure, with a non-zero quarks condensate — meaning explicitly broken chiral symmetry. When the temperature and/or density increase, a phase transition occurs to a mode with higher chiral symmetry where, in the state of minimum energy, the quarks condensate tends to zero.

When matter undergoes a transition from its usual hadronic state to another state of higher symmetry, the quark gluon plasma, chiral symmetry is restored, and asymptotic colour deconfinement occurs. This colour deconfinement means that quarks and gluons do not feel the strong force between each other, and are no longer confined inside hadrons.

1.1.1 Where to find the plasma and how to recreate it

It is believed that the early Universe was first in a state of quark gluon plasma. The hadronization occurred later, as a consequence of the expansion and cooling it underwent, about 10 microseconds after the Big Bang.

Nowadays the plasma phase can eventually exist inside neutron stars [1] whose core is believed to have a density higher than the critical density of phase transition.

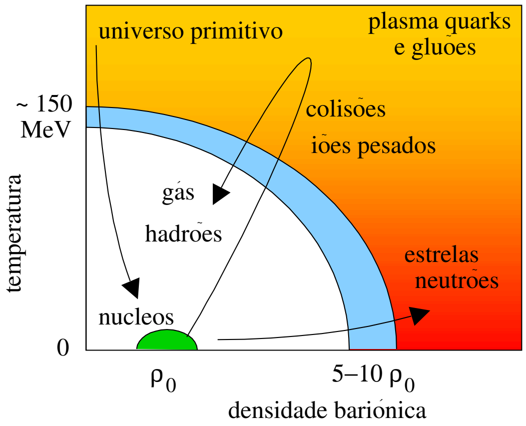

Figure 1.1: Diagram of temperature *versus* baryonic density.

Ultra-relativistic heavy ion collisions make it possible to study the properties of matter in extreme conditions of temperature and/or density. Fixed target experiments have been done since more than twenty years, using highly energetic beams of increasingly heavier ions, trying to reach the critical temperature of phase transition.

1.1.2 A collision's evolution

At high energies, the colliding ultra-relativistic ions look like squeezed in the longitudinal direction, when seen in their centre-of-mass reference frame (figure 1.2).

According to the hydrodynamical Bjorken model [10], the two colliding ions are almost transparent to each other, they cross and while departing they leave in between them a "hot" interaction region (an interacting pion gas or a quark gluon plasma), where the particles density does not depend on the rapidity [2]. Two fragmentation regions are defined, one for the target, the other for the projectile, connected by a region of central rapidity (the transparency region), highly excited and producing most of the secondary particles emitted. These acquire transverse momentum from the multiple collisions in between them.

The collisions in the system redistribute the energy lost by the beam, with thermalization eventually being reached if the interacting system lives for long enough time. It

[1]Neutron stars are originated from other stars that, after spending all their hydrogen and light elements "fuel", undergo a gravitational collapse, exploding as supernovas. The remnant matter, extremely massive, becomes a neutron star, cold but very dense.

[2]The definition of the kinematic variable rapidity is given in Appendix B.

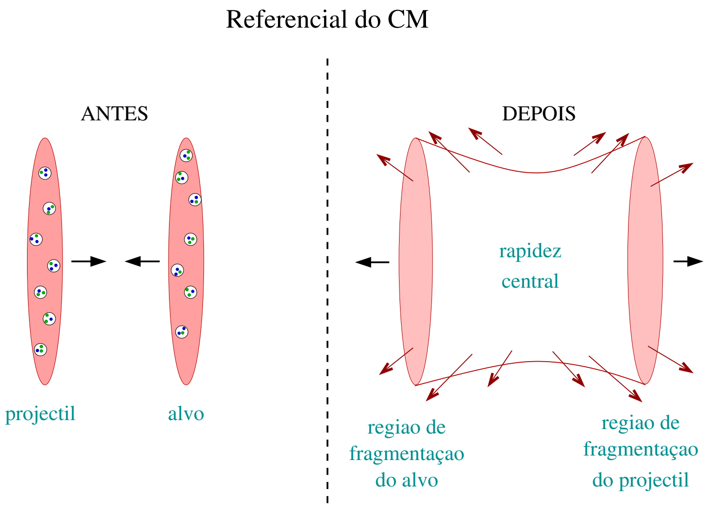

Figure 1.2: An heavy ion collision, seen in collision's CM.

is also due to the collisions that thermodynamic pressure is produced, giving rise to the collective expansion of the hot region. While expanding the system gets cooler, and this expansion proceeds up to the freezing of the interactions, when the freeze-out temperature is reached (figure 1.3).

1.2 Plasma signatures using dileptons

The dileptons emitted by the dense medium are ideal probes for its study, since they do not interact hadronically. The production of thermal dileptons can occur in the quark gluon plasma, through the annihilation processes:

$$q\bar{q} \rightarrow \gamma^* \rightarrow l^+l^- \quad , \tag{1.1}$$

or it can also occur in a pion gas, mainly through the annihilations:

$$\pi^+\pi^- \rightarrow \gamma^* \rightarrow l^+l^- \quad . \tag{1.2}$$

Since thermal radiation is proportional to T^4, the production of thermal dileptons must be more abundant in the early stages of the collision, when the temperature is higher.

The dileptons invariant mass spectrum differs depending on their thermal origin. Dileptons coming from the annihilation of pions have a production threshold at $2m_\pi$, presenting an excess in the ρ mass region. The increase of thermal dileptons next to m_ρ comes from the fact that the reaction (eq:piao) can also proceed through the formation of a ρ vector-meson, $\pi^+\pi^- \rightarrow \rho \rightarrow l^+l^-$, since this light resonance has the quantum numbers of the photon. Thermal dileptons originating from the quark gluon plasma have an exponential distribution without a production threshold (since, for the concerned temperatures, the quarks mass is negligible).

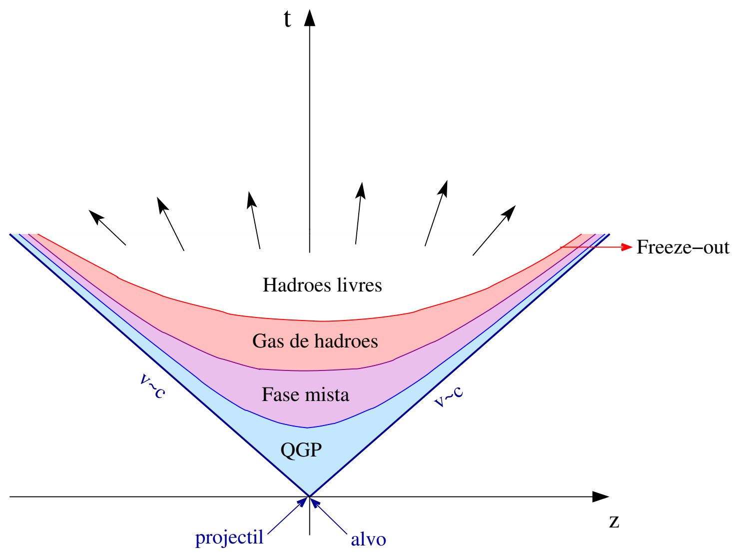

Figure 1.3: Space-time evolution of the quark gluon plasma created in an heavy ion collision according to Bjorken model.

1.2.1 Hadronic modifications in the dense medium

The study of the dilepton invariant mass spectrum allows to understand the properties of the medium, from the vector-meson peaks analysis. Table 1.1 summarises some vector-mesons characteristics.

Vector-meson	M_v (MeV/c^2)	Γ_v^{tot} (MeV/c^2)	τ_v (fm/c)	$BR_v^{\mu\mu}$
ρ	769.3±0.8	150.2±0.8	1.314±0.007	$(4.60\pm0.28)\times10^{-5}$
ω	782.6±0.1	8.44±0.09	23.4±0.2	$<1.8\times10^{-4}$
ϕ	1019.42±0.01	4.46±0.03	44.3±0.3	$(3.7\pm0.5)\times10^{-4}$
J/ψ	3096.87±0.04	0.087±0.005	2268±130	$(5.9\pm0.1)\times10^{-2}$

Table 1.1: Mass, total width, lifetime and branching ratio into dimuons of the vector-mesons ρ, ω, ϕ e J/ψ [9].

The ρ vector-meson has a lifetime of only τ_ρ=1.3 fm/c, contrary to the resonances ω, ϕ and J/ψ, whose lifetimes are relatively long. As a result, its decay into dileptons occurs near the production point, and it is even possible that it decays inside the nucleus.

Fast decays of the ρ are counter-balanced by their additional production from secondary interactions. In this way, a chemical equilibrium of ρs can last for much longer than this particle's lifetime. Since the decay channel into dileptons is open for longer, an increase in the number of produced ρs is expected. In this sense the ρ can be seen as a clock to measure the life time of the interaction region [11]. But this mechanism will only be effective if the resonance's properties remain unchanged in the dense medium created at collision time, and this contradicts some QCD based predictions.

ρ properties, and in general hadron properties, may change significantly in a dense medium, as noted in 1991 by Brown and Rho [12], who predicted an universal scaling of the hadrons mass in a nuclear medium with respect to their masses in vacuum. However, how exactly these properties change is a controversial subject. The scaling factors are expected to differ from particle to particle, but different models and starting assumptions lead to contradicting predictions, including for the same particle.

ρ vector-meson

QCD sum rules [13], that relate the meson masses to the quark condensate in vacuum $\langle q\bar{q}\rangle_o$, or "effective Lagrangian model" based calculations applied to particles collisions [14], are possible ways of treating the in-medium hadronic modifications problem.

The ρ effective mass is expected to decrease with increasing density, due to the chiral symmetry restoration. The quark condensate in vacuum is non-zero, thus giving a mass to the lightest quarks of $\approx$ 1 to 10 MeV (this is the quark's "bare mass"; the mass that we can indirectly measure experimentally is the quark's "constituent mass", of $\approx$ 300 MeV for the lightest quarks). The chiral symmetry is restored by increasing the temperature or density, resulting in a decrease of the quark's mass:

$$m_q^* = m_q(1 - 0.35\frac{\rho_\mathrm{B}}{\rho_o}) \tag{1.3}$$

where ρ_B is the medium baryonic density and ρ_o=0.17 fm^{-3} the nuclear matter density. As a consequence the bound states mass also decreases:

$$m_\rho^* = m_\rho(1 - 0.18\frac{\rho_\mathrm{B}}{\rho_o}) \tag{1.4}$$

m$_\rho^*$ being the in-medium effective mass of the resonance and m$_\rho$ its mass in vacuum. According to these studies [13] [14], for $\rho_\mathrm{B} = \rho_o$ the mass reduction of the ρ is about 18%.

On the other hand, studying this problem from the VDM perspective [3] one may conclude that the chiral symmetry at T$\neq$0 can also mean an increase of the ρ mass, because of the degeneracy of this particle and its chiral partner, the axial-vector meson a_1 (whose mass is m$_{a_1}$ $\approx$ 1230 MeV/c^2 in vacuum). This degeneracy in a dense medium is an important signature for the chiral symmetry restoration.

The width of the ρ vector-meson and, as a general rule, that of any resonance, may increase in a dense medium, since in a many-body system new decay channels appear besides the ones already existing in vacuum. But, on the other hand, some decay channels

[3]The Vector Dominance Models (VDM) are based on the fact that some vector-mesons have the same quantum numbers of the photon ($J^{PC} = 1^{--}$ and charge, baryonic number and strangeness are zero), as for the light resonances ρ, ω and ϕ (states of spin and parity $J^P = 1^-$). These models consider that the photon-hadron interaction is always dominated by vector-meson mediated processes — i.e. the photon goes to a vector-meson that interacts with the target-hadron.

like $\rho \to \pi\pi$ may be partially suppressed in a dense medium, due to the reduced phase space resulting from the mass decrease of the ρ.

The system originated from the heavy ions collision is basically made of pions and kaons. Collisions in between these particles are very likely to occur — at the SPS energies ($\sqrt{s} \approx 17$ GeV for Pb+Pb collisions) there are about 5 mesons per nucleon [15] — and so the system is temporarily kept by these [16]. The pions annihilation in the dense medium is one of the main ρ sources [4]. The ρ decays also predominantly into pions, this being the most important decay channel contributing to its total width. Thus, pion modifications in the dense medium can affect the ρ properties [17][5]. The sum of all ρ scattering processes in the hot pion gas leads to the broadening of the resonance, of about 100 MeV for T=200 MeV, according to Haglin [16]. There are also meson-baryon couplings that, even if there are not much baryons in the medium, affect the ρ properties, with a substantial broadening being expected from this, but without an associated mass shift.

Recent studies show that conclusions taken from QCD sum rules applied to the ρ are model dependent. This limits very much their predictive power, and can even result in contradictory predictions [19] [20][21].

The ρ modifications in a dense medium are nowadays a subject of intense theoretical debate and the existing experimental evidences are not yet conclusive. So, in this work the mass and width of the ρ are taken as given in the [9], and the consequences of these assumptions on the final results are then discussed.

ω vector-meson

The ω vector-meson, with a more or less long lifetime, decays with higher probability outside the interaction region (fast ωs), its decay inside the nucleus being much less likely (slow ωs). The width presented in table 1.1 refers to the first situation. The resonance in a dense medium corresponds to the second one, and can be described by a Breit-Wigner function with mass and width distorted by the nuclear medium. Although the two components of this resonance's decay into dileptons must be always present in a heavy ion collisions produced system, the in-medium component, being more weak, is only experimentally observable in particular kinematic windows with good mass resolution.

The ω momentum distribution is a good observable to study this signal. Calculations based on an intra-nuclear cascade model show that, for low energies mainly, the ω longitudinal momentum P_L is lower for in-medium decays than for decays in the vacuum. Thus the study of in-medium ω decays requires event selections of low P_L dileptons [22].

This structure of two shifted longitudinal momentum distributions can be observed assuming that, according to QCD sum rules, the ω mass in a dense medium is modified

[4]Contrary to the proton-nucleus collisions, where this process is negligible

[5]Although, some authors think that, due to its nature of Goldstone boson, the Brown and Rho scaling does not apply to the pion [18].

similar to the ρ, with a 0.18 scaling coefficient (equation (1.4)), and considering ωs produced at rest inside the nucleus. But if the ω polarizability depends on its momentum (a possibility that is also plausible for the ρ) the QCD sum rules predict a smaller mass shift — and as a consequence, the in-medium and in the vacuum longitudinal momentum peaks approach, such that the observation of this signature is no longer possible.

The partial width of the most important ω decay channel $\omega \rightarrow 3\pi$ is not significantly modified in the dense medium. But it is expected that the total resonance's width increases, due to the opening of a new decay channel $\omega \rightarrow \rho\pi$ as a consequence of the low mass shift of the ρ.

ϕ vector-meson

The lifetime of the ϕ is higher than the one from the ρ or the ω and so the probability for its decay inside the nucleus is much smaller than the one for decays outside the nucleus. Also the scattering cross-sections for the ϕ in the medium are much smaller. Thus the in-medium component for the momentum distribution is much lower than the component for decay in the vacuum.

A scenario where a broadening of the ϕ peak occurs is although possible. ϕ decays mostly into a kaon pair. In the dense medium, one expects both a ϕ mass decrease and a kaon mass decrease, according to the Brown and Rho scaling. If the kaon's mass decreases more than the ϕ's in medium, the phase space for the decay $\phi \rightarrow K^+K^-$ increases, resulting in a resonance's broadening. If on the contrary the ϕ's mass decreases more than the kaon's, the decay channel is suppressed.

The mass of the ϕ in a dense medium decreases according to [13]:

$$m_\phi^* \approx m_\phi(1 - 0.15\ y\ \frac{\rho_{\mathrm{B}}}{\rho_o}) \tag{1.5}$$

where y is the strangeness content of the nucleon[6]. For $y = 0.15$ one obtains a ϕ mass reduction of 2%, having $\rho_{\mathrm{B}} = \rho_o$ [25].

The ϕ can be studied experimentally through its decay into kaons, or through the dilepton channel $\phi \rightarrow l^+l^-$. Due to the high probability of interaction for final state kaons and anti-kaons, only ϕs decaying during or after freeze-out can be detected when using this channel. On the contrary, the dilepton channel is sensitive to ϕs emitted throughout the whole collision history, including to those that decay inside the initially very dense region, before freeze-out.

[6]The strangeness content of the nucleon $y = 2\langle p|s\bar{s}|p\rangle/\langle p|u\bar{u} + d\bar{d}|p\rangle$ measures the contribution of strange sea quarks in the nucleon. This quantity is nowadays being studied. The value $y = 0.15 \pm 0.10$ is obtained from perturbation theory [23], while [24] obtains $y = 0.21 \pm 0.20$.

Experimental results

The comparison with experimental results is crucial to conclude something about in-medium vector-meson modifications. Ultra-relativistic heavy ion experiments have been done at Bevalac/LBL by the DLS Collaboration [26][27] (energies of 1 GeV/nucleon); at SPS/CERN (energies of 40 to 200 GeV/nucleon); and at RHIC ($\sqrt{s}$ = 130 and 200 GeV/nucleon).

Experiments CERES and HELIOS-3 at SPS/CERN observed at the beginning of the nineties, an excess of dileptons in the mass region $M_{l\bar{l}} < m_{\rho,\omega}$ in sulphur induced collisions at 200 GeV/nucleon. Also the experiment DLS observed an excess of dileptons in Ca+Ca collisions at 1 GeV/nucleon compared to what was expected from theory [28].

The experiment DLS at Bevalac studies the dielectrons produced in p+p, p+d, p+Be, Ca+Ca, C+C, He+Ca and d+Ca at 1 A GeV/c. The experiment's acceptance window selects $0.05 \leq M_{ee} < 1.25$ GeV/c^2; $P_T < 0.8$ GeV/c and $0.5 \leq Y^{lab} < 1.9$. Results from this experiment show a dielectron excess in Ca+Ca collisions with respect to C+C collisions, for $M_{ee} \geq 0.5$ GeV/c^2 (figure 1.4). The y-axis on the right-hand side of figure 1.4 refers to a mass spectra fit assuming $d\sigma/dM \propto (A_b A_t)^\alpha$. One can observe that the excess of dielectrons has a A dependence with $\alpha > 1$, contrary to the ones originated from conventional hadronic processes. This excess cannot be explained as an additional contribution to the dielectron continuum from $\pi^+\pi^-$ annihilation, since this process has $\alpha = 1.00 \pm 0.05$ [29]. In fact, at Bevalac energies there are much less produced pions than at SPS (the ratio pion/nucleon is ≈ 0.2 at Bevalac, while it is ≈ 5 at SPS), and so one does not expect a big contribution from pion annihilation at DLS. In-medium ρ vector-meson modifications cannot explain the observed excess neither [15].

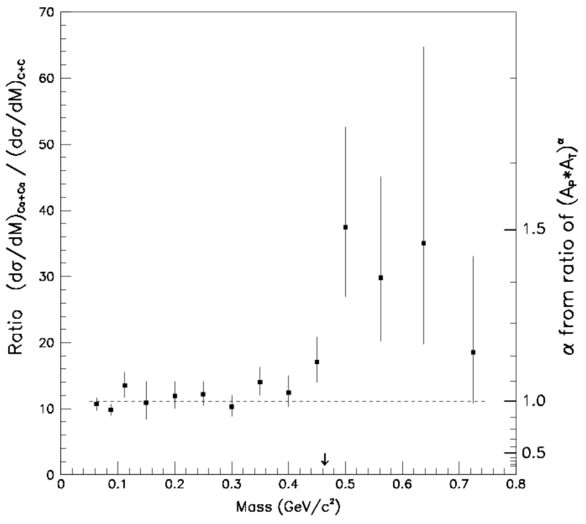

Figure 1.4: Ratio of dielectrons produced in Ca+Ca collisions and C+C collisions at 1 A GeV/c (experimental results from DLS).

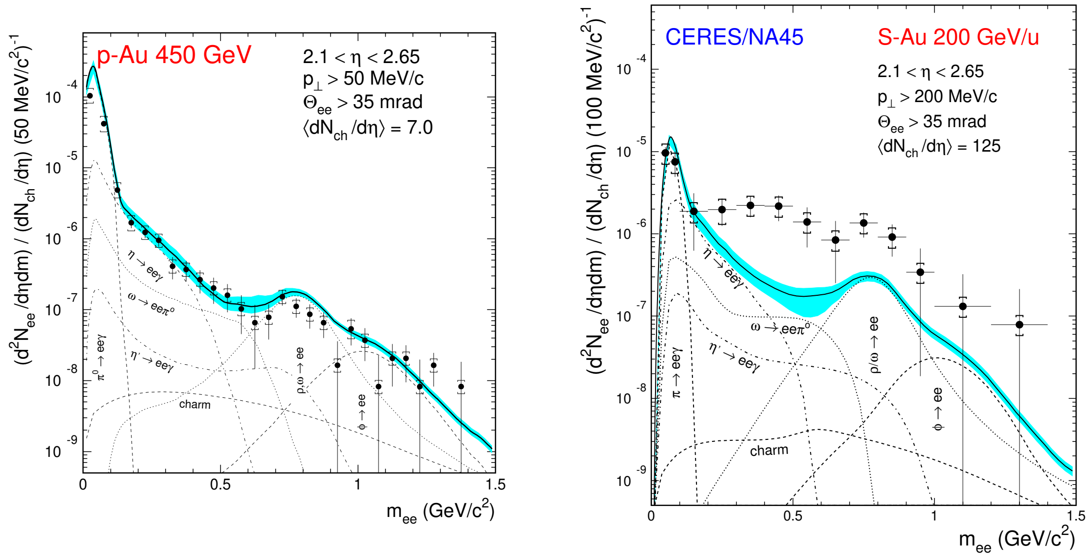

(a) (b)

Figure 1.5: Dielectron spectrum obtained by the CERES experiment in p+Au (a) and S+Au (b) collisions. Represented is also the sum of all the expected physics contributions [1][2].

The CERN experiment CERES (NA45) compares the dielectron mass spectrum from S+Au at 200 GeV/nucleon to the one from p+Au collisions at 450 GeV, observing an important dielectron excess in the low mass region (figure 1.5). The excess factor in the region from 0.2 to 1.5 GeV/c^2 is 5.0 ± 0.7(stat.)$\pm$2.0(syst.) with respect to the expected hadronic contributions [1].

The analysis of the dielectron mass spectra is not easy, since these correspond to a time integration of the system's evolution. If there are any vector-meson modifications in the dense medium, in particular for the ρ, they will show up in the spectra as a sum of ρs emitted in time evolving conditions of temperature and density.

Li *et al* [30] suggest that the excess seen by CERES is due to a strong contribution from pion annihilation to the ρ peak ($\pi^+\pi^- \rightarrow \rho \rightarrow e^+e^-$) in the region $2m_\pi \leq M_{e^+e^-} < m_\rho$, adding to a mass decrease of the ρ with respect to its in-vacuum value, that can go as low as 350 MeV. Thus, CERES results are interpreted as a signature for the chiral symmetry restoration. Although Li *et al* model assumes a hot interaction region that expands and cools in chemical equilibrium, an hypothesis not plausible for many authors, another study from Cassing *et al* [31], based on a covariant transport model out of equilibrium, reaches the same conclusion. More conventional scenarios, as the collisional broadening of the ρ in a dense medium [19], or pion propagation modifications in medium [17], can also explain the CERES excess results.

CERES results in Pb+Au collisions at 158 A GeV/nucleon confirm the excess already seen in sulphur induced collisions. In this case, the excess factor in the mass region from 0.3 to 0.7 GeV/c^2 is 5.8 ± 0.8(stat.) ± 1.5(syst.). The experiment also verified that the excess increases very much with the centrality of the collisions, as predicted by the thermal radiation hypothesis. A dependence with the dielectron transverse momentum is also observed, the excess being higher for low p_T [32].

The CERN experiment HELIOS-3 (NA34-3) identifies dimuons produced in proton and sulphur induced collisions at 200 GeV/nucleon with tungsten targets. This experiment also observes an excess of dimuons in S+W collisions (see figure 1.6). Using for comparison the sum of hadronic contributions as extrapolated from p+W collisions [33], one obtains an excess factor of $1.65 \pm 0.15(stat.)$, for the integrated mass region from 0.2 to 1.5 GeV/c^2. The fact that this value is much lower than the one obtained by CERES can be due to the different rapidity windows of CERES and HELIOS-3 (figure 1.7).

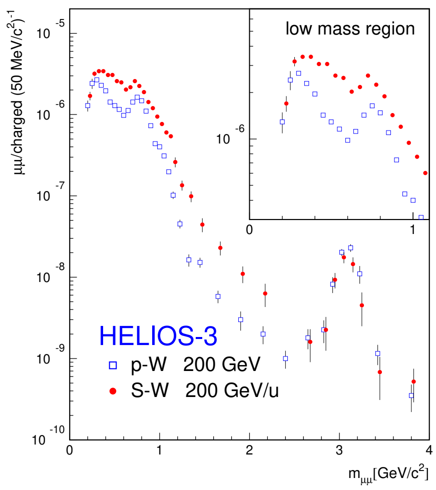

Figure 1.6: Dimuon mass spectrum obtained by the HELIOS-3 experiment in p+W and S+W collisions at 200 A GeV/c. Distributions are normalised to the total number of charged particles [3].

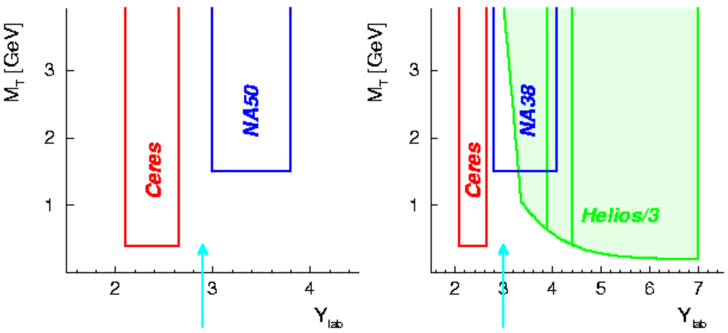

Figure 1.7: Phase spaces of HELIOS-3, CERES, NA38 and NA50 [4].

Cassing *et al* [34] try to explain the HELIOS-3 excess using a covariant transport model. They conclude that the S+W data can only be reproduced assuming also, besides the conventional hadronic contributions (Dalitz decays and direct decays of vector-mesons) and pion annihilation, ρ modifications in the dense medium. Namely, they verify that assuming a ρ mass shift the data can be fitted, while in a scenario of ρ broadening this is not possible.

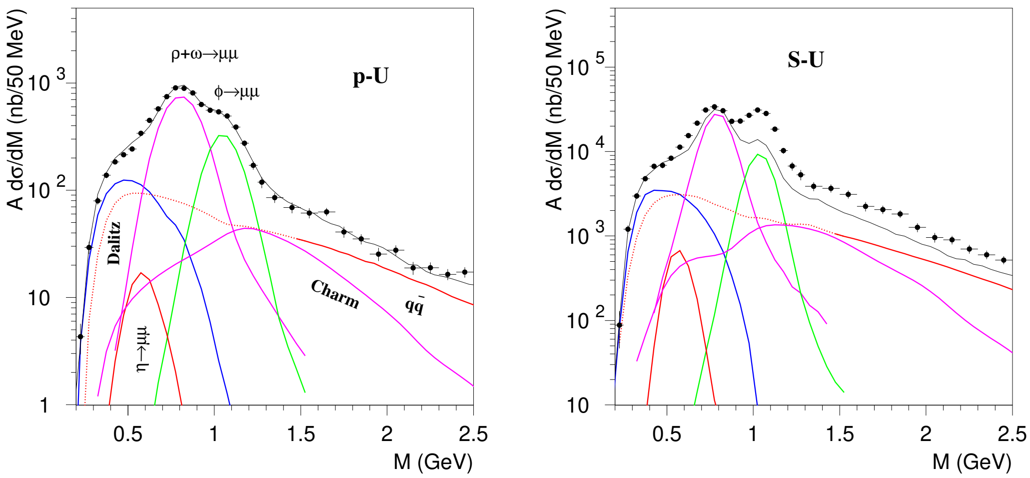

(a) (b)

Figure 1.8: Dimuon spectrum obtained by the NA38 experiment in p+U (a) and S+U (b) collisions at 200 A GeV/c. Represented is also the sum of the expected physics contributions, including an empirical extrapolation of Drell-Yan to the low mass region.

As observed by the DLS experiment, also the NA38 experiment and its successor NA50 from CERN observed a dimuon excess in the region $0.4 \leq M_{\mu\mu} < 0.65$ GeV/c^2 in S+S, S+Cu and S+U collisions at 200 GeV/nucleon, and in Pb+Pb collisions at 158 GeV/nucleon, relative to the sum of hadronic contributions expected. The excess factor is 1.75 ± 0.11 for S+U [35].

Figure 1.8 presents the differential cross-section as a function of the dimuon mass, together with the conventional hadronic contributions expected, namely Dalitz decays and direct decays of ρ, ω e ϕ. Included is also the Drell-Yan contribution for $M < 1.5$ GeV/c^2 extrapolated empirically from higher masses[7]. Considering the kinematic region of the experiment, that mainly accepts dimuons with high transverse momentum, this process contribution seems necessary to be included (contrary to what happens in the CERES case, for example, since there the dielectrons mean P_T is much smaller).

Besides the dimuon excess in the mass region lower than m_ρ, figure 1.8 shows an important increase of the ϕ peak, attributed to an enhancement of the strangeness pro-

[7] Although the Drell-Yan process contribution cannot be calculated from perturbative QCD in the dimuon low mass region, it seems reasonable to assume a non-zero contribution in that region.

duction, that will be discussed later on in this chapter and is the main subject of this study.

The dimuon excess in the mass region $M \geq 1.5$ GeV/c^2 is another sign of non-conventional behaviour obtained by this experiment, even more striking for Pb+Pb collisions. This excess seems compatible both with an increase in open charm production (semi-leptonic decays of $D\bar{D}$ pairs), or with thermal dimuon emission.

1.2.2 Additional strangeness production

One of the predicted signatures of the quark gluon plasma, proposed by J. Rafelski and B. M$\ddot{u}$ller in 1982, is the increased production of strange particles in the heavy ion collisions as compared to proton induced collisions [36]. The production of $s\bar{s}$ pairs in a quark gluon plasma is energetically favoured when compared to their production in an hadron gas. In the hadron gas the $s\bar{s}$ pairs can only be created through energetic collisions between particles without strangeness content. The production reaction with the lowest threshold is $p + n \rightarrow \Lambda + K + n$, requiring a minimum energy of 671 MeV. On the contrary, in the quark gluon plasma the threshold for the production of $s\bar{s}$ pairs is very low, since the s quark bare mass is only 75 to 170 MeV [9] and so to produce a pair it is only necessary a maximum of $2m_s \approx 300$ MeV.

The gluon abundance in the plasma is another factor that favours the strangeness production. The gluon fusion $gg \rightarrow s\bar{s}$ is the process responsible for about 90% of the $s\bar{s}$ pairs produced [37]. Besides, this production is favoured with respect to the production of u and d quark pairs, due to the Pauli's Exclusion Principle. In the heavy ion collisions at SPS energies the produced system is not entirely transparent, being rich in baryons in the fragmentation regions. Thus, the chemical potential for u and d quarks is non-zero, contrary to s quarks — their continued production would result in the system to go out from chemical equilibrium — so it is easier to produce $s\bar{s}$ pairs [38]. This results in the production of hadrons with open strangeness, mostly kaons (about 70% of all strangeness produced) and Λs.

The time needed for the system to reach equilibrium, if this system is a quark gluon plasma, is 20 to 30 times shorter than in the case of an hadron gas [39] (and comparable with the time for two hadrons to cross each other).

Multiple strange baryons

The relative production of baryons and anti-baryons with strangeness content is a good signature for the quark gluon plasma. The direct production of these particles in an hadrons collision requires high energies and times of the order of 100 fm/c, higher than the lifetime of an interacting hadron gas (a few tens of fm/c). Thus, the production of strange hadrons in an hadronic gas is less probable the higher is their content in s

quarks. On the contrary, a quark gluon plasma is rich in s quarks and so, after the phase transition into an hadron gas, one expects to observe the hierarchy:

$$\frac{(\Lambda)_{QGP}}{(\Lambda)_{HG}} < \frac{(\Xi)_{QGP}}{(\Xi)_{HG}} < \frac{(\Omega)_{QGP}}{(\Omega)_{HG}} \tag{1.6}$$

since this particle's strangeness is $\mathrm{S}(\Lambda) = -1$, $\mathrm{S}(\Xi) = -2$ and $\mathrm{S}(\Omega) = -3$.

ϕ production

The *phi* vector-meson, main subject of this study, is a bound state $s\bar{s}$. The study of its relative production with respect to non-strange mesons was pointed out by A. Shor in 1985 as a possible signature for the formation of a quark gluon plasma [40].

The ϕ production in p+p collisions is suppressed, according to the OZI Rule[8], the production of hadronic states $s\bar{s}$ being possible only through 3 gluon processes (i.e. processes of order α_s^3), highly improbable. Besides, the ϕ meson is not fed by other particles' decays, contrary to the open strangeness mesons K and the baryons Λ.

The ϕ vector-meson can transport information from the initial stages of the plasma hadronization process, thanks to its low interaction cross-section with non-strange hadrons [41] ($\sigma_{int} < 10$ mbarn). Once produced the ϕ can leave the hot interaction region without going through multiple scattering. Although, some authors [16] don't agree with this idea, and from kinetic theory calculations they argue that the ϕ mean free path in a hot hadron gas is a function that decreases strongly with temperature. Thus, it is possible that the ϕs produced at the beginning of the hadronization process, with the system still near the critical temperature, suffer multiple scattering and thermalize before leaving the interaction region — loosing the memory of earlier stages.

In the heavy ion experiments triggering on dimuons the ratio $\phi/(\rho + \omega)$ allows to know the strangeness production, since these three resonances decay into dimuons. This ratio is easy to obtain in NA38 and NA50, from the invariant mass spectrum, with the experimental advantage that most of the systematical errors cancel. Thus, the formation of a hot interacting system can be deduced, comparing the relative production of the ϕ meson in heavy ion collisions as compared to its production in proton induced collisions.

Effective temperature of the ϕ

The dense system created in an heavy ion collision can be described hydrodynamically — all the produced particles (matter) flow with the same collective velocity. For

[8]The OZI Rule (from Okubo-Zweig-Iizuka) is a topological rule stating that transitions whose Feynman diagrams have disconnected quark lines are suppressed. In the QCD context, it was understood that these disconnected diagrams are in fact connected by the strong force propagator, the gluon.

each particle, the production cross-section as a function of the transverse momentum or transverse mass ($M_T = \sqrt{P_T^2 + M^2}$, with M being the particle's mass) gives information relative to the thermalization of the system and its collective expansion.

From the transverse mass distributions one can extract the "effective temperature" that characterises each particle — the inverse slope of the distribution. Rigorously, this scaling with M_T is described by a Bessel function $K_1(M_T/T)$:

$$\frac{d\sigma}{dM_T} = M_T^2 K_1(M_T/T) \tag{1.7}$$

The effective temperature T only depends on two parameters: the temperature of thermal freeze-out T_{fo} at which the already hadronized system stops interacting, and the mean velocity $\langle v_T \rangle$ of the collective expansion (the flow) in the transverse plane [42].

In a non-relativistic regime (i.e. if the particle's mass is not negligible, $M \gg P_T$) we have:

$$T = T_{fo} + M \langle v_T \rangle^2 \quad , \tag{1.8}$$

and so it is possible to know separately T_{fo} and $\langle v_T \rangle$, and the effective temperature is observed to vary linearly with the particle's mass.

In the relativistic regime, when the particle's transverse momentum is very high ($P_T \gg M$), the mass can be neglected and the observed effective temperature is the same for all particles. In this case, it is not possible to disentangle T and $\langle v_T \rangle$. The transverse momentum or transverse mass distribution of each particle shows a typical blue-shifted behaviour:

$$T = T_{fo} \sqrt{\frac{1 + \langle v_T \rangle}{1 - \langle v_T \rangle}} \quad . \tag{1.9}$$

This is the case for the pions, for example, that are always relativistic.

Experimental results

Several experiments have been studying since 20 years the strangeness production in heavy ion collisions, at SIS (the Heavy Ion Synchrotron from the German facility GSI), with low energy but high density; at AGS (from BNL), with energies $\sqrt{s} = 2$ to 6 A GeV; and at the SPS (from CERN) experiments NA34/HELIOS-3, NA35/NA49, NA38/NA50 and WA97/NA57, with energies much higher ($\sqrt{s} = 17.2$ and 19.4 A GeV).

While the strangeness production at AGS can be explained as resulting from the superposition of nucleon-nucleon collisions and from hadronic reinteractions, the results from the SPS experiments cannot be explained this way. [43].

The first measurement of a strangeness production excess in heavy ion collisions was obtained by the NA35 experiment, in S+S and S+Ag collisions at 200 GeV/nucleon, with respect to p+p and p+A collisions. This experiment observed an increase in the ratio K/π in ion collisions compared to proton induced ones, by a factor 2.

The experiment NA38 studied the strangeness production from the ratio $\phi/(\rho+\omega)$, having observed an increase in this ratio for collisions induced by sulphur ions at 200 GeV/nucleon, with respect to p+W collisions with the same beam energy [44]. For S+U collisions this increase is by a factor 2 to 3, depending on the centrality. Later, a comparative study with p+U collisions [35] confirmed this increase, that can be seen in figure 1.8. It was also verified that the increase in the ratio $\phi/(\rho+\omega)$ does not depend on the dimuons transverse momentum. These results are shown in detail in Chapter 6, for comparison with the ones obtained by the NA50 experiment in Pb+Pb collisions.

Also the experiment HELIOS-3 observed an increase of the ratio $\phi/(\rho+\omega)$ in central S+W collisions at 200 GeV/nucleon, by approximately a factor 2, with respect to p+W collisions at the same energy [45].

The hierarchy in the production of multiply strange baryons in lead collisions at 158 A GeV, studied by the experiment NA57 (and by its predecessor WA97) is one of the more interesting results obtained at CERN in what concerns the strangeness production, and is shown to be in agreement with the prediction from 1.6 . In figure 1.9 these results are shown [5], as a function of the mean number of participants (evaluated according to the Wounded Nucleon Model — see appendix B).

From NA57, the increased production of the Ω baryons in Pb+Pb collisions with respect to proton induced collisions is by a factor 15. In the centrality region covered by the experiment's acceptance, the hyperon production per participant seems to be constant, i.e. there seems to be a proportionality with the system's volume. The strangeness increased production in Pb+Pb collisions is independent of the centrality, for a number of participants higher than 100.

While for p+p collisions there is no dependence of the T parameter with the particle's mass, for most particles coming from nucleus-nucleus collisions there seems to exist a proportionality of non-relativistic kind, as seen in figure 1.10. Although, some particles do not obey to this behaviour. This is the case for the Ω baryon (baryon with triple strangeness content), with an effective temperature much lower than expected [9]. Also the effective temperature of the ϕ and J/ψ resonances obtained by NA50 is much smaller than expected [46].

Recently, the experiment NA50 showed that ϕ (and maybe ρ and ω) and J/ψ particles have M_T distributions with much higher slope (i.e. with lower T) than expected [47][48]. The T parameter of the ϕ vector-meson is measured both by NA49, from the decay channel $\phi \to K^+K^-$, and by NA50, from the channel $\phi \to \mu^+\mu^-$. The different

[9] A possible explanation is that of an early kinetic decoupling of the Ω (because no resonances can feed their production through scattering with the many pions existing in the medium).

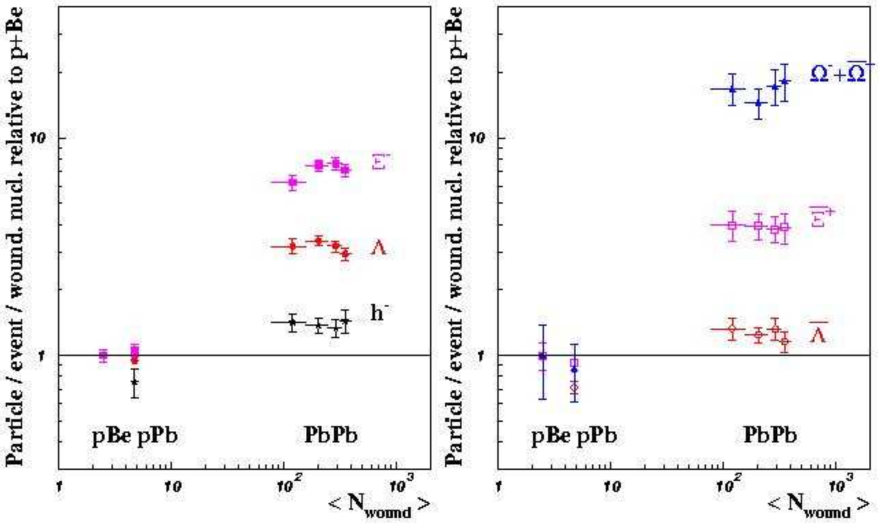

Figure 1.9: Multi-strange particle production in Pb+Pb collisions, compared to their production in proton induced collisions, in the experiment NA57 [5].

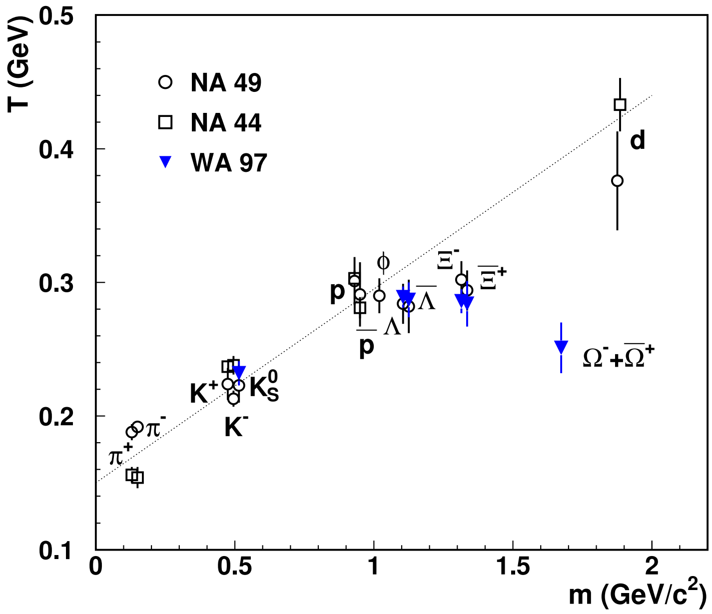

Figure 1.10: Effective temperature T versus the particle's mass, for Pb+Pb collisions at 158 GeV/nucleon.

temperatures obtained, T_ϕ(NA49) = 305 ± 15 MeV [49] and T_ϕ(NA50) = 227 ± 10 MeV [50] have raised big interest [10]. According to several theoretical studies, this discrepancy is due to the hadronic multiple scattering of the kaons in-medium, resulting in a broadening of the ϕ spectrum as a function of the transverse mass — leading to a higher observed temperature [51][52][53]. These results will be discussed in detail in Chapter 6.

1.2.3 Other plasma signatures

Other signals of phase transition from the hadronic matter into a state of deconfined quarks and gluons have been proposed. On one hand, one looks for the information relative to the equation of state describing the hydrodynamical system created in the collision, through the study of global variables; on the other hand, more or less direct signatures of the quark gluon plasma, testifying the early stages of the collision, are searched for.

Global variables

The equation of state of the hot system created in an heavy ion collision can be simulated using rigorous lattice QCD methods[11]. In this way, it is possible to predict critical values for the thermodynamical variables during the phase transition, that can then be compared with the ones obtained experimentally.

The collective transverse expansion (flow) of the interaction region is directly related to the pressure. For ion peripheral collisions, the region of the two nuclei superposition is almond shaped in the transverse plane, and gets more and more spherical with the interaction region expansion. On the other way, the intense multiple scattering makes the system approach fast thermalization and results in the increase of pressure. Due to the existent deformation, pressure gradients develop, resulting in a stronger expansion in the shorter direction (i.e. in the reaction plane) favouring spherical form. This phenomenon is called elliptic flow [54]. The existent data, namely those obtained at the American collider RHIC, agree very well with hydrodynamical calculations assuming the system's thermalization after 0.5 fm/c, for a time when the density is much higher than the critical density [55] ($\epsilon_c \approx 2$ GeV/fm^3).

As explained before, from the hadrons transverse momentum distribution one can conclude about the freeze-out temperature and the transverse velocity of the collective expansion. This information, together with the results from Hanbury-Brown and Twiss (HBT) interferometry allows to disentangle the thermal and collective motion contributions to the observed effective temperature. HBT analyses rely on the fact that in the

[10] These temperatures, as well as the ones from figure 1.10, are obtained fitting the particles' transverse mass distributions not with the Bessel's function approximation (5.4), but with the function $d\sigma/dM_T \propto M_T\, exp(-M_T/T)$. This approximation gives a systematic shift for the low transverse momentum region.

[11] Although rigorous, these methods are still not much realistic.

anti-symmetrization of identical particles' wave functions an interference term arises from their correlation in the energy-momentum space. With a Fourier transformation it is possible to obtain, from this correlation, the space-time distribution of the source-system where the particles originated. The transverse radius R_T of the system measured with HBT interferometry , relates to T_{fo} and $\langle v_T \rangle$ by [56]:

$$R_T = R/\sqrt{1 + \xi \langle v_T \rangle^2 \frac{M_T}{T_{fo}}} \tag{1.10}$$

where $\xi \approx 1$. According to the NA49 data [57] using simultaneously equations (1.9) and (1.10) one obtains, for lead collisions at 158 GeV/nucleon, $T_{fo} \approx 100$ MeV and $\langle v_T \rangle \approx 0.55c$. The NA49 HBT analysis allows also to conclude that the interacting system increases transversely by a factor 2.4 .

Thermal dileptons and direct photons

The photons (real or virtual) emitted by the quark gluon plasma probe the system properties at their emission time, including in the first evolution stage of the hot interaction region.

While virtual photons originate dileptons, and for this reason they are easy to study, real photons are much harder to analyse, due to the huge background from π^o and η^o. The so-called direct photons are obtained after background subtraction. In the resulting spectra one has still to identify the contribution from photons originated in hard scattering between partons from target and projectile nucleons [58]. The observation of thermal dileptons or thermal direct photons is not a signature for the deconfined state of the source system, but only an indicator of its temperature [59].

The WA98 experiment observes an excess in their central lead collisions data at 158 GeV/nucleon [60]. This direct photon excess may be interpreted as originating from a quark gluon plasma with initial temperature of 300 MeV.

Also the NA38 and NA50 experiments observe a dimuon excess in the intermediate mass region between the ϕ and J/ψ peaks [61][62]. In this spectrum region, one has to consider the contributions from the Drell-Yan process and open charm processes (semi-leptonic decays of D $\bar{\text{D}}$ pairs). The observed excess relative to the summed contribution of these two processes is compatible both with thermal dimuons emitted by a quark gluon plasma [63], and with an enhancement on the open-charm contribution due to secondary gluon interactions [64].

Suppression of *charmonia*

The suppression of hadrons $c\bar{c}$, as the vector-mesons J/ψ and ψ' and χ_c,in a deconfined medium was proposed by Matsui and Satz in 1986 as a signature of the quark gluon plasma [65]. In a very dense medium, the c and $\bar{c}$ quarks feel no longer the presence of each other, due to the colour screening (Debye screening) of neighbouring quarks and gluons. While the system expands and cools, the two get farther and farther apart, so that at freeze-out time they are already too far to bind as a J/ψ, ψ' or χ_c, and they form open charm particles instead[12].

Besides this mechanism of J/ψ suppression occurring in heavy ion collisions (the so-called anomalous suppression), there are also hadronic contributions to the suppression, from the J/ψ interaction with both nuclear matter and with particles produced along with the J/ψ in the collision, the comovers (normal suppression mechanisms).

The NA50 experiment observed an anomalous suppression of the J/ψ resonance in central collisions of Pb+Pb at 158 A GeV/c [66][67], one of the strongest evidences of the creation of an extremely hot and dense state of matter at SPS, a state that cannot be explained as conventional nuclear matter. Figure 1.11 shows the ratio J/ψ/DY [13] as a function of the transverse energy. Represented is also the curve corresponding to the normal nuclear absorption [68].

1.3 Future searches for the QGP

With the end of the ions program of the SPS accelerator (expected to occur by the end of 2003) the CERN fixed target experiments that integrated this program have been concluding their data takings through the last years, in a process that resulted in the press release of February 2000, partly reproduced at the beginning of this chapter. Although this program obtained results that seem compatible with the production of a quark gluon plasma in Pb+Pb collisions at 158 GeV/nucleon, the confirmation of these results is of fundamental importance, as well as the investigation of the properties of the created state of matter.

The NA60 experiment is one of the last heavy ion experiments approved to run at the SPS. Having taken data on proton induced collisions in 2002, this experiment, that will use the NA50 spectrometer, together with a pixels vertex detector, to improve the

[12]The Debye screening occurs with all quark flavours, not only for $c\bar{c}$ pairs. Although, because charmonia formation is a rare process, the balance between its suppression due to colour screening and its additional production due to the decrease of the quarks mass in the dense medium, the first process is more important.

[13]The Drell-Yan process is used here to normalise the J/ψs produced, so that most of the systematical errors are cancelled. This process is well studied and understood, and behaves identically for proton or lead induced collisions. Its cross-section is proportional to the number of nucleon-nucleon collisions.

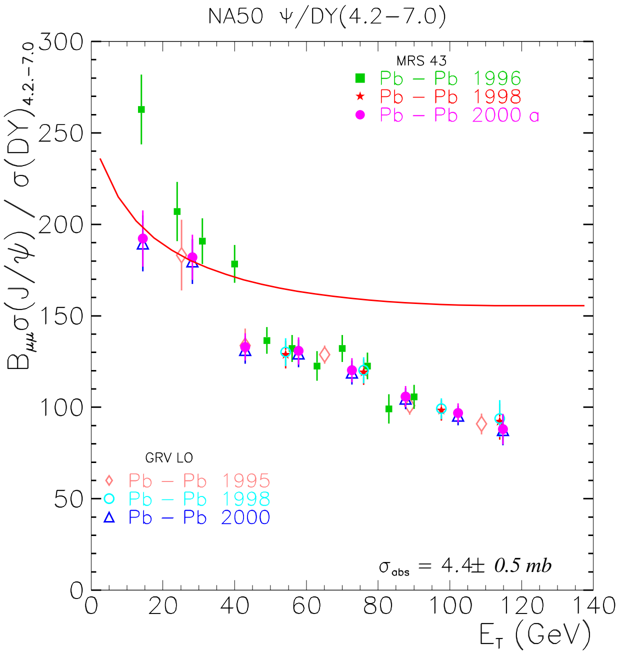

Figure 1.11: Ratio J/ψ/DY as a function of the transverse energy, obtained by NA50 in Pb+Pb collisions at 158 A GeV/c.

mass resolution mainly in the region of the ρ ω and ϕ resonances, and identify the decay vertex of D and $\bar{D}$ mesons. In 2003, NA60 will study In+In collisions at 158 A GeV/c. The excess of events seen by NA50 in the intermediate mass region will be investigated in more detail by this experiment [69].

Future searches for the plasma must investigate extensively the phase diagram shown in figure 1.1, both accessing higher temperatures, and higher densities.

The RHIC collider in the USA is the first from this new era of experiments, with Au+Au collisions at $\sqrt{s_{NN}}$ = 130 and 200 GeV. The temperature reached in the early stages of these collisions is clearly higher than the critical temperature for phase transition, the energy density being about an order of magnitude above ϵ_c. The four RHIC experiments — STAR, PHENIX, BRAHMS and PHOBOS — started their data takings in 2001, the first results being published only very recently. New signatures predicted for the quark gluon plasma became accessible in heavy ion collisions at RHIC, namely those related to jets physics and very high P_T distributions.

The LHC collider at CERN is expected to start taking data in 2008. Two of the approved LHC experiments, ALICE and CMS, will study heavy ion collisions (probably lead ions) accelerated at $\sqrt{s_{NN}} \approx 5$ TeV. At these energies, there will be an enormous multiplicity of produced particles. On the other hand, it will be possible to study bottomnia states, similarly to what NA50 did for charmed bound states J/ψ and ψ'. The particles' maximum transverse momentum produced will be more than an order of magnitude higher than the ones from SPS.

On the other extreme of the phase diagram of temperature versus baryonic density, the future experiments at the SIS synchrotron from GSI are going to reach densities similar to the ones that exist in the core of neutron stars, ten times higher than the nuclear matter density.

The experiment HADES at SIS will take data soon, from Ni+Ni collisions at 1.93 A GeV. In the dileptonic channel, the ϕ mass resolution will be 10 MeV/c^2. Thus, this experiment will be sensible to possible hadronic modifications in the dense medium [25]. The expected SIS upgrade will include the HADES electrons spectrometer and several sub-detectors used for particle identification and centrality measurements. Au+Au collisions at 25 GeV/nucleon will allow to study in-medium modifications of short-lived vector-mesons like the ρ; multiple strange baryon production; and the production of both open charm and charmonia states (the experiment will measure about 3.2 $\times 10^4$ J/ψs per week in Au+Au collisions at 25 GeV/nucleon, to be compared with the 1.3 $\times 10^5$ J/ψs per week obtained by NA50 in Pb+Pb collisions at 158 GeV/nucleon) [70].

Chapter 2

Experimental apparatus

The NA50 experiment is a fixed target experiment using a lead ^{208}Pb ion beam accelerated at an ultra-relativistic energy of 158 GeV/nucleon, obtained from the proton synchrotron SPS at CERN. The accelerator has a 20 s cycle, with a 4.5 s spill [1]. The beam Lorentz factor is $\gamma \approx 10$. The correlated muon pairs detected at small angles in the laboratory reference frame (due to the Lorentz contraction effect) is the signal detected by the experiment, in a small central rapidity window (emission at $\approx 90^o$ in the collision's centre-of-mass reference frame).

The NA50 experimental apparatus consists on a muon spectrometer, complemented by an electromagnetic calorimeter, an hadronic calorimeter, a multiplicity detector, and several detectors for beam control. Figure 2.1 gives a schematic view of the apparatus.

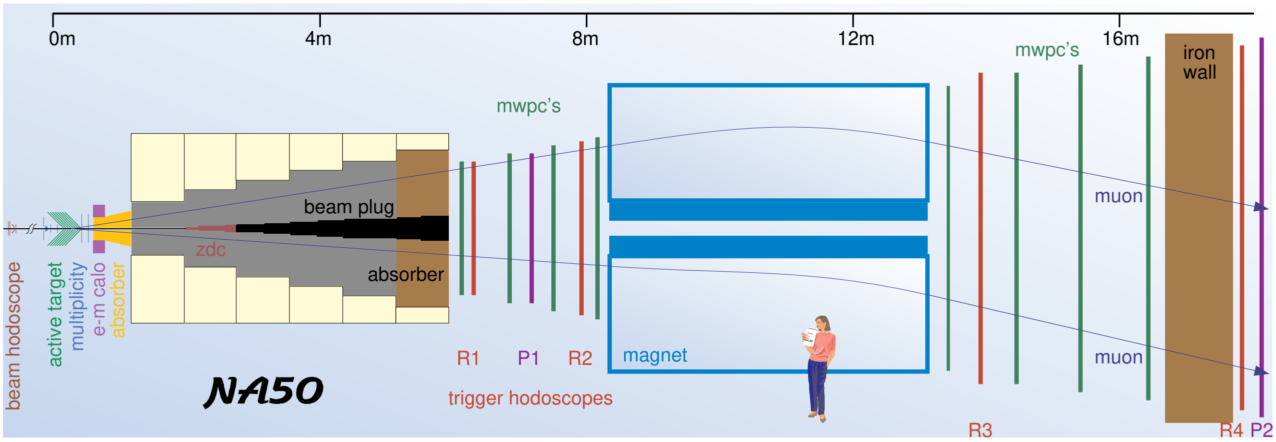

Figure 2.1: NA50 experimental apparatus for Pb+Pb collisions.

[1] The lead ion ^{208}Pb beam is injected from the PS into the SPS. Inside the SPS its equivalent momentum per charged particle increases from 13 GeV/c up to 400 GeV/c. The cycle of the machine includes the acceleration and subsequent slow extraction of the beam to the experiments, every 20 seconds. An ion extraction is called burst, and its duration in time is the spill [71].

2.1 Beam detectors

The beam detectors are located upstream from the target, the most important one being the Beam Hodoscope BH. It is placed 22 m from the target, where the beam transverse dispersion allows for the counting of the incoming ions. These cross the detector quartz blades, resisting the high radiation dose due to the huge beam intensity, of the order of 7×10^7 ions/burst.

2.1.1 BH detector

The Beam Hodoscope is made of two planes of horizontal quartz blades, transversal to the beam direction. From these, only the first one is actually used during the data takings, to minimise the interaction length. The second plane of the BH is used in special runs, for the measurement of the detector's efficiency. The 16 constituent blades of the first plane are 0.7 mm thick, corresponding to 2.2% interaction length (λ_{int} (quartz)=3.2 cm for lead ions [72]). The lead ions crossing the quartz blades produce Čerenkov radiation, captured by the optical fibres connected to the blades up to the photomultipliers (one photomultiplier per blade).

This detector is used for several purposes. It counts the incoming ions on the lead beam, a very important measurement for the luminosity calculation. It allows to identify piled-up beam — a situation occurring every time there are two ions seen by the detector in the same time window of 20 ns. The BH is also used to stabilise the trigger of the experiment [2], giving a time reference for the arrival of the incoming ion, with less than 1 ns jitter [3].

2.1.2 Interaction detectors

The interaction detectors BHI and BHI-New are located next to the beam hodoscope, to identify lead ion interactions on the BH, whose fragments could interact on the target thus originating "parasite" events. There are two BHI detectors and four BHI-New, each one having a scintillator blade plus a lead blade.

The BHI are placed 17 cm downstream from the second BH plane, on both sides of the beam, and have a rectangular geometry. The BHI-New shape is as quarters of ring centred on the beam line, located 1 m after the BHI detectors. These cover complementary rapidity regions, and do not interfere with the beam non-interacting on the BH.

Lead ion interactions on the BH produce mainly pions. These decay into photon pairs when crossing the lead blades, originating a signal in the scintillator that allows

[2] The trigger is the real time decision to acquire an event.
[3] The term jitter refers to small fluctuations on the time measurement.

for the detection of parasite events. This represents a 20% cut, on events that would otherwise not be recognised by the active target system.

2.1.3 Anti-halo detectors

Two anti-halo detectors (BAH and BAH-New) are located 51 cm and 19 cm upstream from the target. Each of them consists on a quartz blade with a central hole 3 mm in diameter, crossed by the collimated ion beam. These detectors identify events whose originating ion was not collimated, or charged fragments from previous parasitic interactions occurred upstream from the target.

2.2 The target region

The data analysed here were obtained with a single lead target 3 mm thick and 1 cm $\times$ 2 cm transversal dimension. The target frame can accommodate up to 7 sub-targets aligned with the beam. In this data taking only position 4 was occupied. Next to each sub-target position there are two quartz blades (on the left and on the right of each sub-target and immediately downstream from it). The blades emit Čerenkov radiation when crossed by charged particles (mostly π e K) originating from in-target interactions. When the beam hits the target δ electrons are produced, creating a noise seen by the quartz blades. A threshold is chosen, above which a signal of Pb+Pb interaction is recognised by the quartz blades.

Two quartz blades are located before the first sub-target position, to detect lead-air interactions upstream from the target. Figure 2.2 shows the target region in detail, together with the centrality detectors.

2.3 Detectors for centrality measurements

Two calorimeters and a multiplicity detector allow to measure the centrality of the Pb+Pb collisions. The electromagnetic calorimeter and the zero degree calorimeter (ZDC) measure the neutral transverse energy of the produced particles and the energy of the spectator nucleons, respectively. The multiplicity detector measures the multiplicity of charged particles produced.

2.3.1 The multiplicity detector

The multiplicity detector is placed downstream from the target and before the pre-

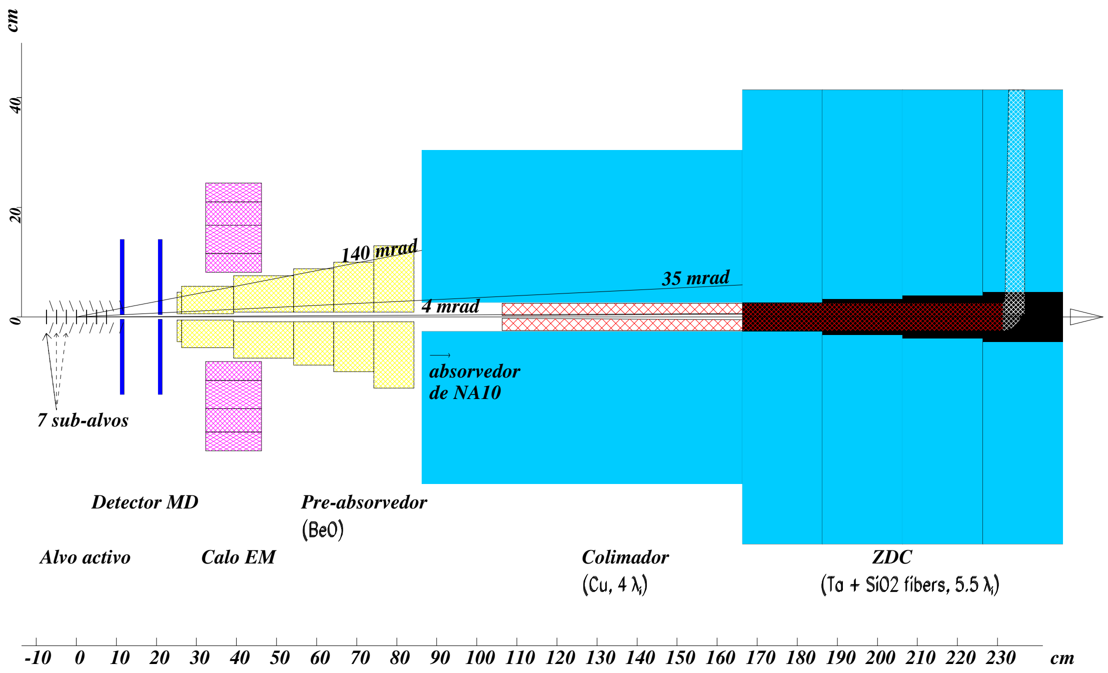

Figure 2.2: Schematic view of the NA50 target region, with centrality detectors and hadron absorbers.

absorber. It is made of two planes (MD1 and MD2) with about 7000 silicon strips each, in a ring shape [73][74]. Since silicon is a radiation hard material the detector can be put right next to the interaction region. The two planes identify the pions produced whenever an interaction takes place, signaling the sub-detector where it occurred. The multiplicity of charged particles produced is measured from the strips occupancy. The superposition of the two planes covers the pseudo-rapidity region $\eta \in [1.9, 4.2]$.

2.3.2 The electromagnetic calorimeter

The electromagnetic calorimeter is located after the multiplicity detector. It is made of lead and scintillating fibers, forming four concentric hexagonal "rings" with six sextants each. This detector measures the energy deposited by the neutral particles emitted in the interval $\eta \in [1.1, 2.3]$, out of the spectrometer acceptance. The inner region of the calorimeter, corresponding to the angular acceptance of the spectrometer, is filled by a pre-absorber made of BeO, a material with lower radiation length, thus originating less muons' multiple scattering.

The many π^os produced in Pb+Pb collisions have a short lifetime, decaying into photon pairs. Electromagnetic cascades are begun in the lead. The scintillating fibres are the active element of the calorimeter, and transport the signal up to the photomultipliers.

The neutral transverse energy produced is calculated from the expression:

$$E_T = C_N \sum_{i=1}^{4} E_i \sin\theta \tag{2.1}$$

where C_N is a normalisation constant depending on the sub-target position where the interaction occurred, and variable i is for the four calorimeter rings. θ angle is the mean angle defined by the i^{th} ring, the beam line and the sub-target position N.

The neutral transverse energy resolution for the NA50 experiment is:

$$\frac{\sigma(E_T)}{E_T} = \frac{0.72}{\sqrt{E_T(GeV)}} \tag{2.2}$$

i.e., about 11% at $E_T \approx 40$ GeV and about 8% at $E_T \approx 90$ GeV.

Contamination due to charged particles crossing the calorimeter is estimated by a Monte-Carlo simulation to be 40% of the total energy deposited. This contribution is subtracted in order to have a measurement of the neutral transverse energy.

2.3.3 The zero degree calorimeter

The zero degree calorimeter is placed inside the absorber, on the beam line. It is made of tantalum conversion plates, with silicon optical fibres inserted [4]. Measures are based on the Čerenkov effect. The detector is preceded by a copper collimator 60 cm long, with a central conical shaped hole whose diameter is only slightly larger than the beam transversal dispersion, in order to prevent the ZDC from counting the energy from particles produced in the collisions.

In the detector's active region the quartz fibres are oriented parallel to the beam, along 65 cm ($\approx 20\ \lambda_I$). They are then curved at 90^o, working as light-guides up to the photomultipliers. The ZDC measures the deposited energy of the particles that do not interact in the target, in the pseudo-rapidity region $\eta \geq 6.3$.

The energy resolution of this detector when using lead beam at 158 GeV/c per nucleon is [76]:

$$\frac{\sigma(E_{ZDC})}{E_{ZDC}} = \frac{3.39}{\sqrt{E_{ZDC}(GeV)}} + 0.062 + \frac{775}{E_{ZDC}(GeV)} \tag{2.3}$$

i.e. 12% for $E_T \approx 40$ GeV ($E_{ZDC} \approx 22$ TeV) and 19% for $E_T \approx 90$ GeV ($E_{ZDC} \approx 8$ TeV).

Besides the measurement of the non-participant particles energy, the ZDC also allows for piled-up beam identification, completely independent from the beam hodoscope BH.

[4]This kind of optical fibres are being increasingly used in experimental high energy physics due to their radiation hardness. Within the angular acceptance of the ZDC, the radiation dose the detector receives along the whole data taking period with Pb beam at 158 A GeV/c is of the order of 4 Mrad [75].

The two detectors together accomplish an efficiency for beam pile-up rejection higher than 99% [77].

2.4 The muon spectrometer

The NA50 muon spectrometer, made of absorbers, multiwire chambers, scintillating hodoscopes and a deflector magnet, was conceived and previously used by the past experiments NA10 [78] and NA38. It selects correlated muons coming from the target, allowing to reconstruct muon tracks and identify the production vertexes.

The spectrometer consists of two telescopes (sets of multiwire chambers and hodoscopes), with a magnet in between, covering the pseudo-rapidity region $2.8 \leq \eta < 4.0$.

2.4.1 Absorbers

Lead ion collisions produce a huge amount of particles, mainly pions and kaons that have a large probability to decay into muons, thus originating a background to the dimuon signal detection. The absorbers minimise this background that otherwise would saturate the multiwire chambers and hodoscopes on the first telescope.

In NA50 there is a beryllium oxide (BeO) preabsorber filling the inner region of the electromagnetic calorimeter and extending as a cone up to the main absorber of the experiment. It is basically a block of material 60 cm long, with a central hole for the non-interacting beam to pass through.

The main absorber of the experiment, shown in figure 2.3, is 4.8 m in length. It is made of uranium and tungsten blocks in the most central part, absorbing the non-interacting beam; and of iron and carbon blocks in the following radial layer, covering an angular acceptance for muons produced in-target from 32 to 116 mrad, absorbing the hadronic particles produced in the collisions. A concrete exterior layer covers the whole absorber.

The absorbers stop the produced hadrons but on the other hand they are a source of multi-scattering for the muons. So, the choice of materials when building an absorber is done maximising the interaction length λ_I ($\lambda_I \propto A^{1/3}$), so that the produced hadrons are absorbed, while minimising the muons multi-scattering (the scattering angle being $\theta_o \propto \sqrt{l/X_o}$), as well as the radiation length X_o ($X_o \propto \frac{A}{Z^2}$), so that the muons' energy loss is the less possible ($-\frac{dE}{dx} \propto \frac{Z}{A}$).

One last absorber, an iron wall 1.2 m thick, is placed before the fourth scintillating hodoscope. From all the in-target produced particles, only the muons achieve to cross this last absorber.

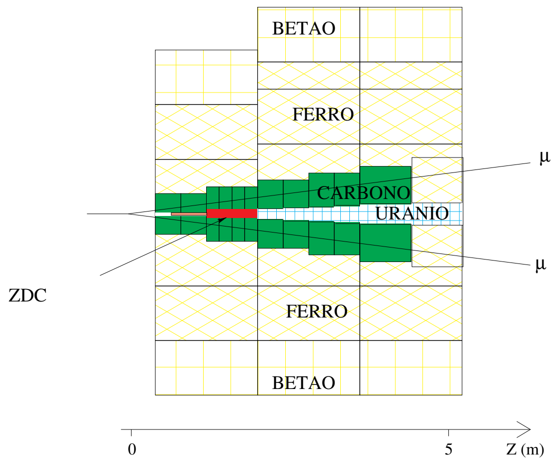

Figure 2.3: NA50 main absorber.

2.4.2 Scintillating hodoscopes

The four scintillating hodoscopes, two per telescope, give the time coincidences that produce the dimuon trigger of the experiment. They have an hexagonal symmetry, each sextant being made of scintillators (30 for R1 and R2, 24 for R3 and 32 for R4), placed parallel to the exterior border of the sextant. Scintillators R1 and R2 are homothetic with respect to the target, so that the coincidence $V^i = R1^i \times R2^i$ (or $\times R2^{i-1}$) between two i scintillators of R1 and R2 is defined when a particle coming from the target region crosses them (figure 2.4).

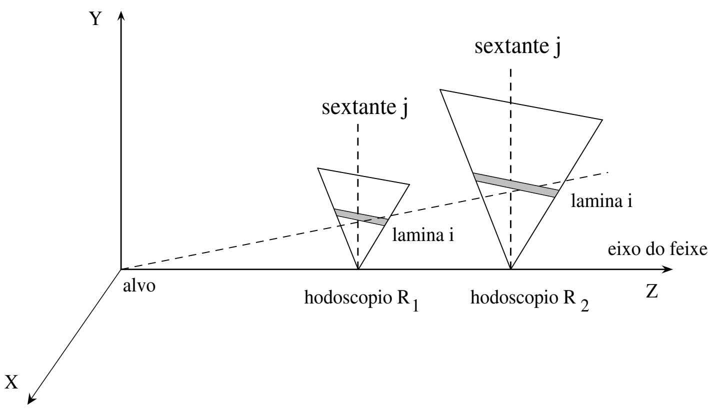

Figure 2.4: Coincidence $V^i = R1^i \times R2^i$ for the dimuon trigger system [6].

The trigger hodoscopes efficiency is controlled by two other hodoscopes, P1 and P2, placed before and after the magnet, during dedicated special runs. These hodoscopes have radial symmetry, with each sextant being divided into eight sectors. Since there is a magnetic toroidal field, the selection of events to measure the trigger efficiency is done from the univoque coincidence of sectors in P1 and P2.

2.4.3 Multiwire chambers

The eight multiwire proportional chambers PC1 to PC8, four per telescope, are used for the tracking of the muons trajectory, from the physical addresses of touched wires. They have hexagonal symmetry, each chamber with three independent wire planes, spaced 2.2 cm apart and rotated by 60^o with respect to each other.

Spacing between wires is 0.3 cm, thus having a spatial resolution of $0.3/\sqrt{12}$ cm. The inside volume of the chambers, in between cathodes and in the wires (anodes) is filled with a gas mixture at atmospheric pressure. When a muon crosses the chamber, electrons are emitted due to the gas ionization, and these are attracted to the wires because of the applied magnetic field.

2.4.4 The magnet

The deflector magnet ACM (from *Air-Core Magnet*) between the two telescopes is an iron and air magnet with hexagonal symmetry, where the iron sectors represent only 30% of the total region (figure 2.5 (a)). With a length of 4.8 m and a maximum radius of 2 m, it defines a polar acceptance for the spectrometer, and an azimuthal acceptance that corresponds to the air sectors in between coils.

The current on the coils is AC with a value of 7000 A, synchronised with the SPS cycle, creating a toroidal magnetic field of $B_o = 0.4$ Tm (figure 2.5 (b)):

$$\vec{B}(r) = \frac{B_o}{r}\,\vec{u}_\phi \tag{2.4}$$

where r is the distance from the beam axis and $\vec{u}_\phi$ the azimuthal unitary vector. When crossing the magnet, the muon's trajectory is deflected, but keeping the same azimuthal plane. The bending angle is inversely proportional to the muon transverse momentum.

The 7000 A current on the coils is the maximum supported by the magnet, such that the mass resolution is optimised for the J/ψ region — the NA38 experiment used a 4000 A current, obtaining a resolution of $\sigma_\psi = 145$ MeV/c^2 for the J/ψ, while when using 7000 A the mass resolution is $\sigma_\psi = 96$ MeV/c^2.

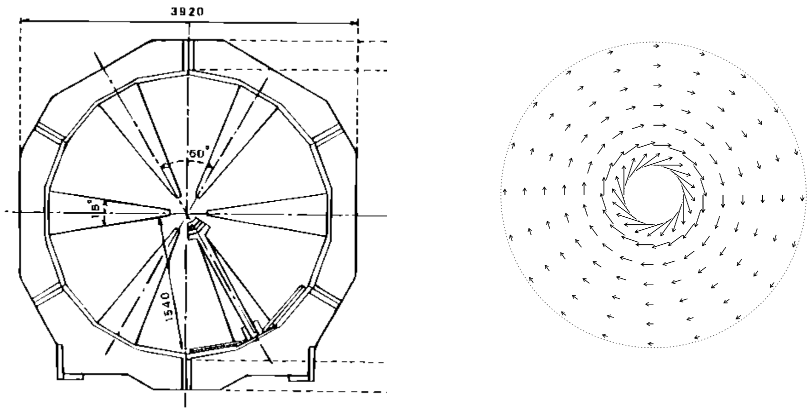

(a) (b)

Figure 2.5: Frontal view of the magnet (a); magnetic field lines created (b).

2.5 The trigger system

The trigger system is implemented in several levels. The first one requires the V coincidence between the homothetic scintilattors of R1 and R2 hodoscopes, in a time window of 18 ns, as shown in figure 2.4 . The 32 possible coincidences $V^i \times 32$ possibilities for a signal in the R4 hodoscope define the so-called "correlation matrices". These matrices' diagonals give the $(V, R4)$ coincidences that relate the muon tracks on the first and second telescopes, according to their transverse momentum. The R3 hodoscope is used to validate these coincidences.

For a toroidal magnetic field, the track bending angle is inversely proportional to its transverse momentum. Thus, the correlation matrix classifies the muons transverse momentum according to four classes. This information is sent to a programmable module, the magic box, relating the two tracks that constitute the dimuon, and giving a first estimate of its mass:

$$M \approx P_{T\ 1} + P_{T\ 2} \quad . \tag{2.5}$$

The magic box produces an output signal every time there are at least two muons in different sextants in a given time window. This signal, once time stabilised, gives the trigger for the other detectors.

Since NA50 is a high flux experiment, a trigger with high timing precision is crucial, so that pile-up is minimised. For this, a dedicated program for the trigger synchronisation was performed.

The trigger stabilisation is given by a mean-timer defining the time window of 18 ns counted from the detection of coincidence between R1 and R2 hodoscope scintillators signals. The jitter introduced when doing the mean time between the scintillators two half-sextants signals is reduced by half using the logic **OR** for the V coincidences in each half-sextant (TSJ or trigger without jitter). The TSJ validation by a signal coming from the BH detector defines an even more precise reference (T0J or trigger zero jitter), with a jitter smaller than 1 ns.

2.6 The data acquisition system

Normal data taking conditions with a lead ion beam of 158 GeV/nucleon mean a nominal data acquisition rate of 1.5 Mby/s. In order to process the data the fastest way possible, minimising the deadtime, each sub-detector acquisition (partition) is processed in parallel.

During the 4.5 s spill each sub-detector information is stored in a temporary memory, through a network of 24 transputers, with maximum storage of 5000 events per burst, corresponding to 17 Mbytes of data [79].

The burst information is then transfered to a memory located in the acquisition unit. During the inter-burst, for each event a microprocessor reads all the partitions, and verifies the presence of information from all detectors, and its coherence. After validation the all the data corresponding to all events from the burst are recorded in magnetic tape. Details of the acquisition system can be found in [80].

2.7 Reconstruction of tracks

The reconstruction of the muon trajectories is done off-line, by the program DIMUREC. For each event, at least two tracks must be reconstructed from the signals from the multiwire chambers. For each track, one must establish the track correspondence before and after the magnet, in an air sector at the magnet mean transverse plane. There is also the additional requirement for the simultaneous information of tracks crossing the trigger hodoscopes, and for the backwards extrapolation of tracks to the target region to allow the reconstruction of an event vertex.

The reconstruction process is started from the second telescope, because it is less illuminated, thus making easier the tracking process from the chamber hits. The detailed description of the reconstruction process is given for example in [81].

Chapter 3

Data selection

The experimental data are registered in magnetic tape, under the form of the addresses of touched wires in the chambers, of signal amplitudes in the calorimeter rings, of the impulse of a particle crossing the hodoscope slices, and of signals of the remaining sub-detectors. The decoding of these data is done off-line, by a program that allows to reconstruct the muon tracks and the production vertex of the events. The compacted information of the kinematic variables of each event is kept in μDSTs (from Data Storage Tapes), for later analysis.

The RELMIC program was used in the analysis here presented, allowing a primary events selection. All tracks passing outside the fiducial region of the detector are rejected, as are also the tracks whose image[1] is outside that region. The joint information from several sub-detectors (BHI-New, BAH and BH) allows to reject events for which the projectile ion is a "parasite" — events whose projectile ion is coming from a previous interaction upstream from the target (thus it is no longer a lead ion), for this using the signal from the anti-halo detectors (BAH and BAH-New).

3.1 The statistics of the data

In this study two distinct data selections are made based on target identification, one given by the active target system, the other by the multiplicity detector (Chapter 6). A third analysis, which starts from the set of events pre-defined by the selection given by the active target, and demands additionally a cut of beam pile-up (NIBHAD cut), is also presented in Chapter 6.

In the first case, it is required that for each event an interaction in-target is seen by both quartz blades associated to the position 4 (the position where the only lead sub-

[1] One calls image to the track that would be obtained if the muon had electric charge opposite to its own.

target used in this data taking was placed). The system allows to identify peripheral interactions, in which only one of the blades, left or right, has seen a signal of amplitude higher than the discrimination threshold (NOCIBI=14 or 24). These constitute 6% of the events signaled by the target identification algorithm. The remaining 94%, identified simultaneously by both blades, are used in this study (NOCIBI=4). Although this choice implies a penalty in the statistics of peripheral interactions, it also implies a cleaner data sample.

Selection	Events
dimuon Triggers	22.0×10^6
After NOHALO cut	20.5×10^6
After NOCIBI cut	13.2×10^6
After pile-up cut	11.5×10^6
After image cut	5.3×10^6
NOCIBI=4 selection	5.0×10^6
After kinematical cuts	4.8×10^6
After diagonal cut	3.5×10^6
After $P * Dtarget$ cut	3.3×10^6

Table 3.1: Statistics of Pb+Pb 1998 data taking. Sum of dimuons $\mu^+\mu^-$, $\mu^+\mu^+$ and $\mu^-\mu^-$.

The table 3.1 shows the statistics used in the analysis with event selection given by the active target (NOCIBI selection), corresponding to runs **7026** to **7613**, of a total of 381 runs, after rejecting anomalous runs. These runs correspond already to a selection of data with the detector in its standard configuration. The kinematical cuts allow to accept only dimuons in the rapidity window $0.05 \leq \mathrm{Y}^{CM} < 1.05$, and in the angular domain $-0.5 \leq \cos\theta_{CS} < 0.5$ (angle θ in the Collins-Soper reference frame, explained in detail in Appendix B). The momentum of the individual muons in each pair must obey $P_\mu < 75$ GeV/c; the events have also to be accepted by the diagonal cut on the E_T *versus* E_{ZDC} correlation plot, and by the target transverse plane cut $P * Dtarget$.

3.2 The image cut

The image cut consists of verifying, for each muon track, if its image track (which corresponds to simulate the muon at the entrance of the magnet with charge opposite to its own) is accepted by the reconstruction criteria. As one can see from table 3.1, this cut eliminates 46% of the events. However, it is essential for the symmetrization of the sets of like sign dimuon events. One verifies that the spectrometer acceptance is not the same for muon pairs $\mu^+\mu^+$ in negative (positive) field and for pairs $\mu^-\mu^-$ in positive field (negative). The image cut allows to symmetrize these acceptances, so that the combinatorial background subtraction, which will be explain later, is correct.

3.3 The target selection

The target selection consists in accepting only the events for which the active target system identifies an interaction in the position where the lead sub-target is located (the NOCIBI=4 position). Since only one of the sub-target holder positions is occupied, in this case with a 3 mm thick lead target, it is demanded that both scintillating blades associated with this position detect an interaction simultaneously. Although there is a previous condition for the event's reconstructed vertex to be located in the target region (NOCIBI selection mentioned on the third line of table 3.1), the NOCIBI=4 cut eliminates events for which the scintillator blades do not give a signal (NOCIBI=8); where interaction is signaled, but not in the position where the lead sub-target is located; or where only one of the blades associated to the target position identifies the interaction (NOCIBI=14, 24). In figure 3.1 one can see the total distribution of $\mu^+\mu^-$ events before this selection.

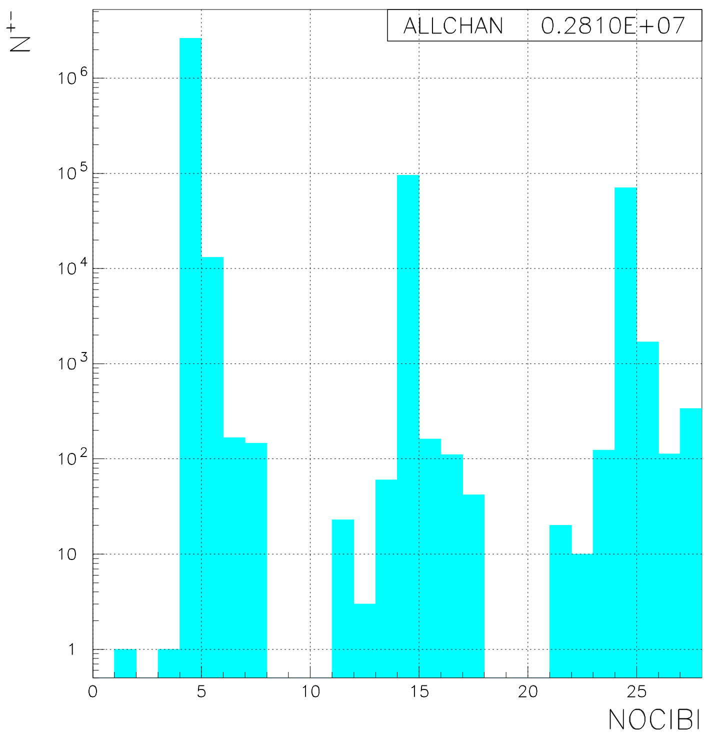

Figure 3.1: Distribution of $\mu^+\mu^-$ events seen by the active target system. Position 4 corresponds to the lead sub-target location. NOCIBI=14 or 24 means that only one of the blades associated with position 4 identified a signal of amplitude higher than its discrimination threshold.

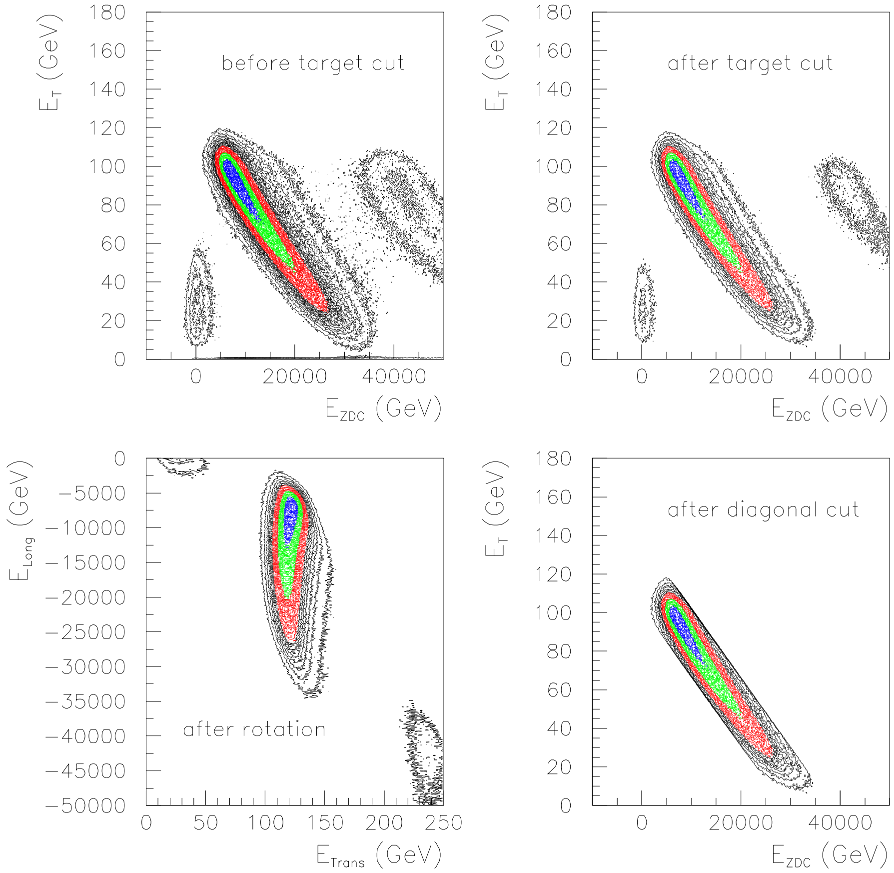

Figure 3.2: Diagonal cut. a)E_T *vs* E_{ZDC} correlation before the cut and the target selection; b)E_T *vs*E_{ZDC} correlation before the cut and with target selection; c)After axis rotation; d)E_T *vs*E_{ZDC} correlation after the diagonal cut.

3.4 The diagonal cut

The diagonal cut is the selection of events within a band corresponding the almost linear correlation between the two NA50 calorimeters, the electromagnetic calorimeter and the zero degree calorimeter (figure 3.2). The width of this band is defined as being two standard deviations for each side of the diagonal straight line of the most likely correlation.

To determine the line of maximum correlation between the two variables (figure 3.3) a rotation is done into a system of orthogonal axis in which one of the axis corresponds to the transverse cut and another to the longitudinal cut of the band.

θ (mrad)	σ	x_o
3.99	9.04	125.58
3.79	8.86	122.98
3.59	**8.85**	**120.31**
3.39	8.97	117.56
3.19	9.35	114.78

Table 3.2: Minimisation of the gaussian width σ fitted in the transverse projection of the E_T *vs* E_{ZDC} correlation.

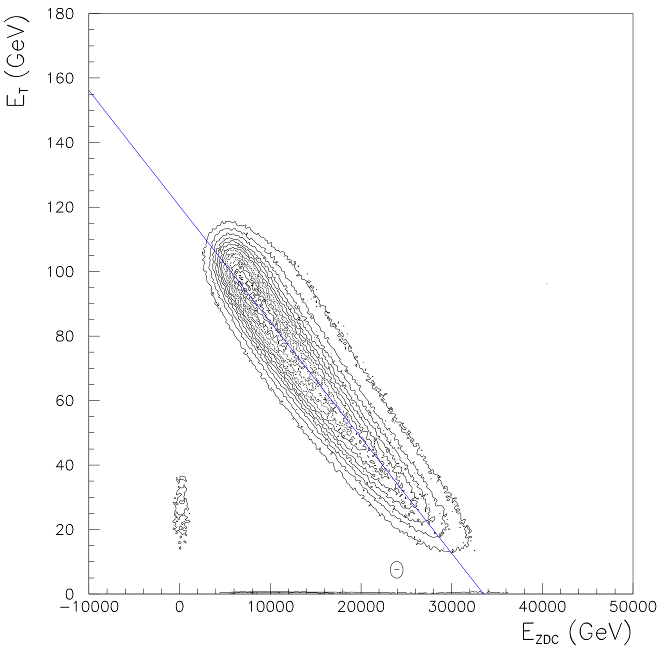

Figure 3.3: Maximum correlation straight line of E_T *vs* E_{ZDC}, and definition of the θ rotation angle.

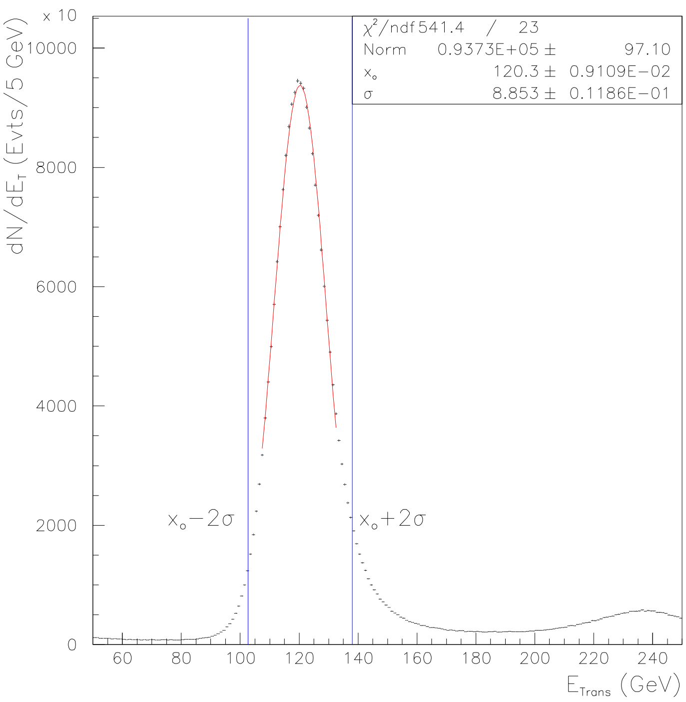

Figure 3.4: Gaussian fit to the projection in the transverse axis of the E_T *vs* E_{ZDC} correlation.

The scattered values around the line of maximum correlation should be Gaussian distributed. The rotation angle is optimised by minimising the Gaussian width of the fit in the projection in the transverse axis. As an example of this process, table 3.2 shows the results of this optimisation. Figure 3.4 shows the cut chosen in the transverse projection of the E_T *vs* E_{ZDC} correlation.

The vertical lines that cut the Gaussian tails at 2σ are then recalculated in the E_T *vs* E_{ZDC} reference frame, in order to find the diagonal bands of the cut. With this method, the relation between the transverse neutral energy released and the beam spectators energy (E_{ZDC}) is in the acceptance window:

$$(102.61 - 3.59 \times 10^{-3} E_{ZDC}) < E_T < (138.02 - 3.59 \times 10^{-3} E_{ZDC}) \quad . \qquad (3.1)$$

3.5 Geometrical cut

The event selection is improved with the $P * Dtarget$ cut. On the target transverse plane the tracks for which the extrapolation is too far from the vertex in the beam line are rejected. The cut takes into account the dependence of the tracks dispersion in the target

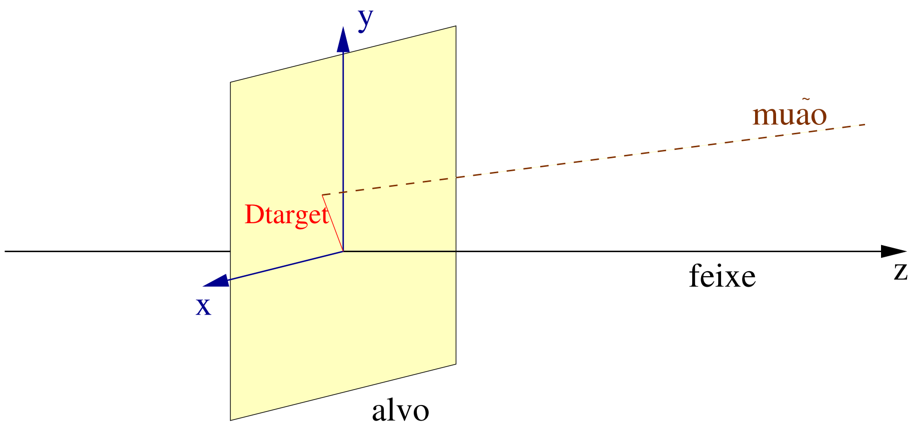

Figure 3.5: Definition of the distance *Dtarget* of an extrapolated track to the beam line.

plane with the tracks momentum, and also the fact that there is a different behaviour for convergent or divergent tracks[2]. As one can see in figure 3.6, their dimuon momentum distributions are slightly different.

Therefore, one defines the distance *Dtarget* to the beam axis (figure 3.5):

$$Dtarget = \sqrt{(Dx)^2 + (Dy)^2} \tag{3.2}$$

The distance *Dtarget* varies inversely with the track momentum, so that the quantity $P * Dtarget$ is approximately momentum independent, and it has a Gaussian distribution. Therefore, $(P * Dtarget)^2$ shows a χ^2 probability function ([82], page 925). The χ^2 probability of the variable $(P * Dtarget)^2$ is a measure of the distance between the track and the vertex on the beam line, in the target plane.

The choice of the cut to be applied to the data is done by studying the χ^2 probability distribution of $(P * Dtarget)^2$ of the convergent and divergent tracks, for a selection of $\mu^+\mu^-$ events as clean as possible. It is intended to avoid contamination from the combinatorial background (muons from pion and kaon decays), since muons from these events do not come from the primary vertex. Therefore, this study selects only the events with $M \geq 3$ GeV/c^2, for which the ratio signal/background is high (sgn/bkg ≈ 19). In Appendix C one can find a detailed description of the method used for the determination of the χ^2 probability of $P * Dtarget$.

As one can see from figure 3.7, for probabilities equal or higher than 4% the probability distribution is horizontal. This means that for these events the $P * Dtarget$ has a Gaussian behaviour.

The $P * Dtarget$ cut is independent of the mass, so that the result of the study of high masses may be applied to the low mass region, namely the same coefficients for the

[2]The convergence or divergence of the tracks refers to the bending at their passage through the magnet. Convergent tracks get closer to the beam line on the second telescope, while divergent tracks get farther away from that axis.

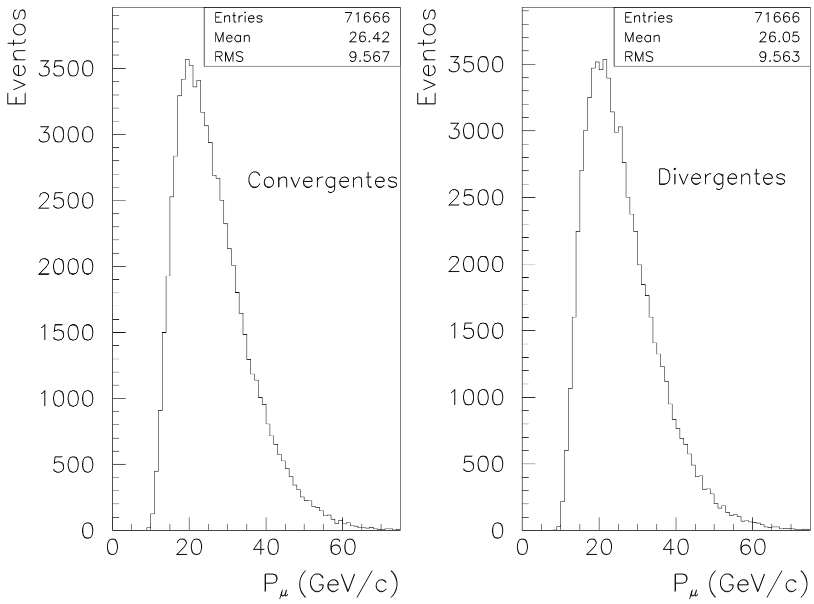

Figure 3.6: Momentum distribution of the convergent and divergent muons. Selection of $\mu^+\mu^-$ events with $M \geq 3$ GeV/c^2 and NOCIBI=4 .

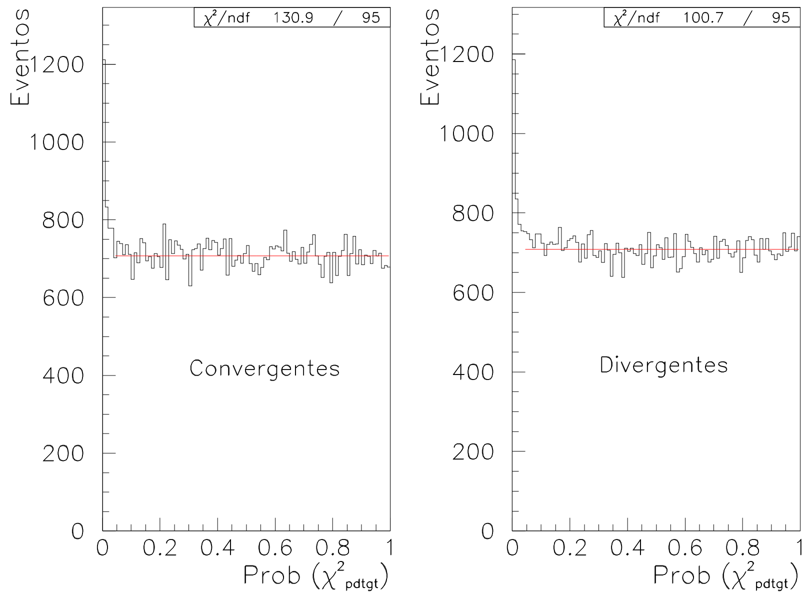

Figure 3.7: The χ^2 probability of $(P * Dtarget)^2$, for convergent and divergent tracks. Selection of $\mu^+\mu^-$ events with $M \geq 3$ GeV/c^2 and NOCIBI=4 .

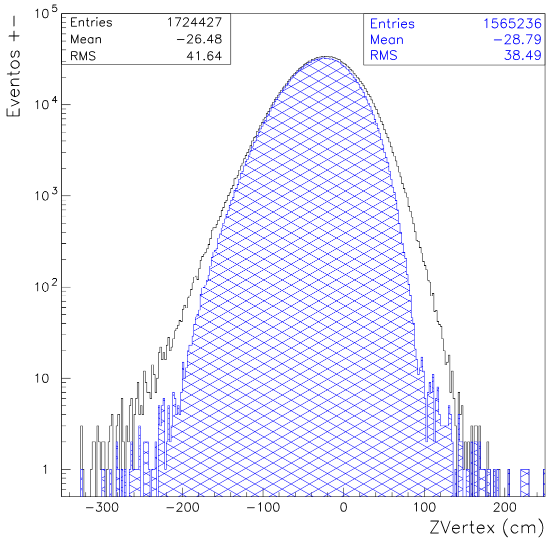

Figure 3.8: Distribution of the $\mu^+\mu^-$ events reconstructed vertex with $M < 2.5$ GeV/c^2. Superimposed are the distributions before and after the $P * Dtarget$ cut (4% cut).

$P * Dtarget$ calculation and the same cut value. However, because for $M < 2.5$ GeV/c^2 the contribution from combinatorial background events is significant, the χ^2 probability tracks distribution is not horizontal, not even for values much higher than the cut one. The effect is more pronounced for muons of low momentum [83]. As is demonstrated in Appendix C (C.3), the distribution corresponding to signal muons (after background subtraction) is approximately horizontal, even if the statistics used in that study is small, which confirms the hypothesis that the probability distribution for low masses will be non-horizontal because of the superposition of two different distributions, one from signal tracks, and the other from background tracks.

Figure 3.8 presents the distribution of the vertex of accepted $\mu^+\mu^-$ events along the zz axis (Zvertex variable), with or without the $P * Dtarget$ cut. Only dimuons with mass $M < 2.5$ GeV/c^2 are selected, and one verifies that the mean value of the distribution is smaller after the cut, being closer to the target position (Z ≈ -45 cm). Before the cut the distribution was more shifted downstream due to the strong contribution from combinatorial background in this sample. The width of the distribution is also smaller after the cut, as expected.

3.6 The kinematic region studied

As was already mentioned, the NA50 spectrometer acceptance window in rapidity is restricted to $3 \leq Y^{lab} < 4$. For the low mass region, the rapidity range chosen in the

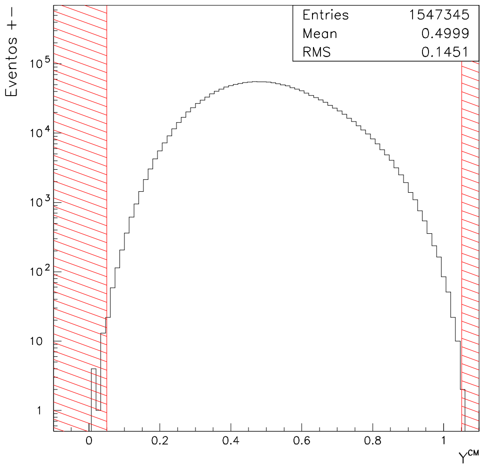

Figure 3.9: Dimuon rapidity distribution, including all the statistics of $\mu^+\mu^-$ events with $M < 2.5$ GeV/c^2, with all cuts applied. Superimposed is the accepted rapidity window.

centre-of-mass frame, is:

$$0.05 \leq Y^{CM} < 1.05 \tag{3.3}$$

in order to avoid empty bins, but maintaining a unit of rapidity in total, approximately centred (figure 3.9).

The distribution of events in the $\cos\theta_{CS}$ variable, with θ_{CS} measured in the Collins-Soper reference frame, has its maximum at 90^o. The acceptance of the experiment in $\cos\theta_{CS}$ corresponds to the region:

$$-0.5 \leq \cos\theta_{CS} < 0.5 \quad , \tag{3.4}$$

used in this analysis; the few events emitted at small angles are rejected.

The mass spectrum studied in this analysis, 0.25$\leq M_{\mu\mu} < 2.5$ GeV/c^2, is divided in 5 regions:

$$\begin{aligned} 0.25 \leq M &< 0.65 \\ 0.65 \leq M &< 0.9 \\ 0.9 \leq M &< 1.2 \\ 1.2 \leq M &< 2.0 \\ 2.0 \leq M &< 2.5 \text{ GeV/c}^2 \quad . \end{aligned}$$

The first region corresponds to the very low masses continuum, dominated by the contribution of Dalitz decays from pseudo-scalars η and η' and from the vector-meson ω; the second and third regions include the ρ and ω resonances and the ϕ resonance, respectively;

and the last two correspond to the intermediate mass regions (IMR), mostly dominated by the semi-leptonic decays of $D\bar{D}$ pairs and the Drell-Yan process.

The dimuons transverse momentum selected in this analysis is $P_T < 3.5$ GeV/c. Having in mind the P_T differential study, 6 regions are defined, approximately equally populated:

$$\begin{aligned}
1.2 &\leq P_T \\
1.2 &\leq P_T < 1.4 \\
1.4 &\leq P_T < 1.6 \\
1.6 &\leq P_T < 1.8 \\
1.8 &\leq P_T < 2.0 \\
2.0 &\leq P_T < 3.5 \text{ GeV/c} \quad .
\end{aligned}$$

The neutral transverse energy released in the collisions is studied in 9 regions also approximately equally populated, defined in the $5 \leq E_T < 150$ GeV window:

$$\begin{aligned}
5 &\leq E_T < 29 \\
29 &\leq E_T < 42 \\
42 &\leq E_T < 53 \\
53 &\leq E_T < 64 \\
64 &\leq E_T < 74 \\
74 &\leq E_T < 83 \\
83 &\leq E_T < 93 \\
93 &\leq E_T < 105 \\
105 &\leq E_T < 150 \text{ GeV} \quad .
\end{aligned}$$

The last of these regions corresponds to the events situated beyond the “knee” of the distribution in transverse energy (the Gaussian fluctuations of the maximum transverse energy released in a Pb+Pb collision). Figure 5.21 shown in Chapter 5 presents the dimuon signal distribution as a function of the transverse energy.

3.7 Subtraction of the combinatorial background

During data acquisition, both the muon pairs with opposite charge and the muon pairs with the same charge are registered by the experiment. These last ones are used to statistically estimate the fortuitous muon pairs of opposite charge that, being originated by uncorrelated decays of pions and kaons, constitute a combinatorial background that must be subtracted.

To obtain the signal of correlated muon pairs of opposite charge, the following expression is used:

$$N^{sgn} \;=\; N^{+-} \;-\; 2\;R\;(\sqrt{N^{++}\;N^{--}}|_{field\;-} \;+\; \sqrt{N^{++}\;N^{--}}|_{field\;+}) \quad , \tag{3.5}$$

where $R = 1$ is used, valid if the multiplicity of particles produced in the collisions is high enough to have statistical significance. This hypothesis is correct in the case of central collisions of lead or sulphur ions with heavy targets, but is not valid for proton induced collisions (in this case $R \approx 1.25$ [81]), or for very peripheral collisions. In Chapter 6 an estimate of the systematic error associated with using $R = 1$ in all Pb+Pb collisions is done.

Figure 3.10 a) shows the mass distribution of opposite charge dimuons, compared with the one for like sign dimuons. The distributions of signal events (sgn) and background events (bkg) are superimposed in figure 3.10b).

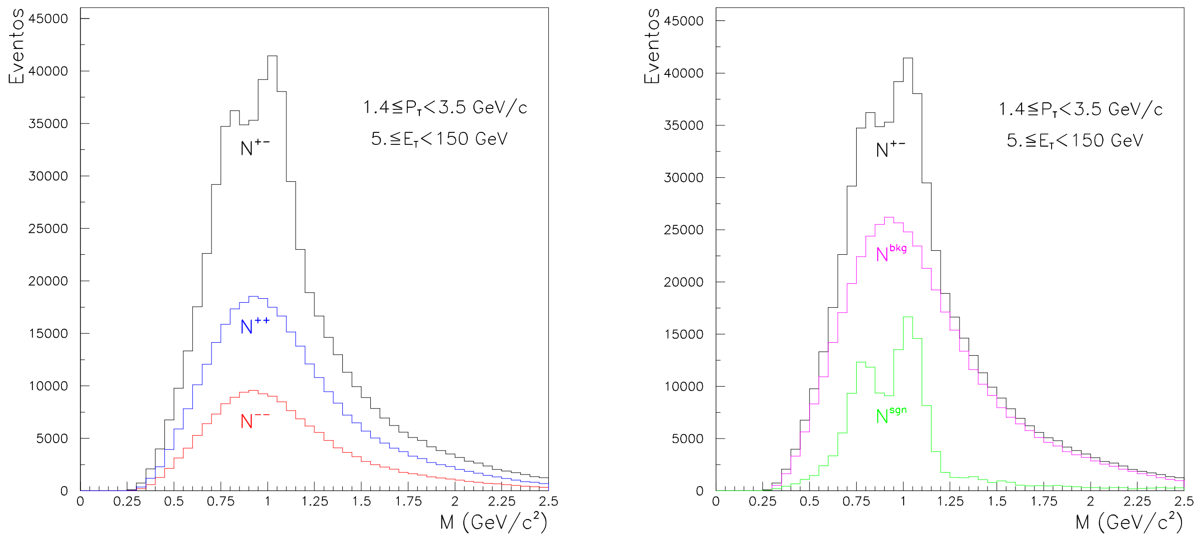

(a) (b)

Figure 3.10: Total events analysed. Dimuons of opposite sign and of same sign(a); estimated background, and signal dimuons obtained after background subtraction(b).

Table 3.3 shows the data statistics used in the analysis, per P_T and E_T regions, before and after combinatorial background subtraction. It shows also the mean value of the ratio background/signal (bkg/sgn) in the mass region of the resonances ($0.65 \leq M <$ 1.2 GeV/c^2), for each region. In this table, column $\forall P_T$ means an integration of the data, before background subtraction, in the region $1.4 \leq P_T < 3.5$ GeV/c; and the column $\forall E_T$ means an integration of the data in the region $5 \leq E_T < 150$ GeV. Figure 3.11 gives an example of the dimuon mass spectrum, integrated in transverse momentum and neutral transverse energy, for all $\mu^+\mu^-$ dimuons, the corresponding signal, and also the ratio background/signal. In this last plot, a fit with an horizontal line in the mass region of the resonances confirms that in that region the number of background events is approximately twice the number of signal events.

Events	Type	$\Delta P_T(1)$	$\Delta P_T(2)$	$\Delta P_T(3)$	$\Delta P_T(4)$	$\Delta P_T(5)$	$\Delta P_T(6)$	$\forall P_T$
$\Delta E_T(1)$	$\mu^+\mu^-$	22616	6241	6697	5205	3175	3595	18672
	sgn	2285	1497	2160	2143	1596	2178	7810
	bkg/sgn	1.49	2.02	1.32	0.90	0.59	0.30	0.82
$\Delta E_T(2)$	$\mu^+\mu^-$	63516	16685	18107	14175	8717	10168	51167
	sgn	5001	2784	4326	4618	3467	5238	17418
	bkg/sgn	4.87	2.90	1.83	1.29	0.85	0.46	1.10
$\Delta E_T(3)$	$\mu^+\mu^-$	82046	21241	22700	17641	11090	12432	63863
	sgn	5514	2942	4659	5011	3866	5691	18888
	bkg/sgn	3.39	3.32	2.32	1.57	1.14	0.61	1.43
$\Delta E_T(4)$	$\mu^+\mu^-$	103330	26585	28083	21530	13477	14827	77917
	sgn	5725	3332	5309	5183	4367	6098	20644
	bkg/sgn	4.20	3.56	2.68	1.75	1.26	0.74	1.61
$\Delta E_T(5)$	$\mu^+\mu^-$	109535	27683	29006	22497	13590	14873	79966
	sgn	5902	2841	4611	5086	3479	5354	18085
	bkg/sgn	3.85	4.55	3.30	2.05	1.78	0.87	1.98
$\Delta E_T(6)$	$\mu^+\mu^-$	108593	27320	28674	21735	13570	14712	78691
	sgn	5433	2580	4214	4347	3640	5286	17106
	bkg/sgn	4.06	4.73	3.36	2.32	1.66	0.89	2.06
$\Delta E_T(7)$	$\mu^+\mu^-$	126883	32348	33647	25516	15358	16675	91196
	sgn	5673	3692	5000	4987	3564	5368	18549
	bkg/sgn	3.45	4.28	3.63	2.58	1.91	1.12	2.37
$\Delta E_T(8)$	$\mu^+\mu^-$	133302	33478	34849	26199	15974	17412	94434
	sgn	6061	2862	4372	4246	3546	5306	16932
	bkg/sgn	5.64	6.22	4.10	2.66	2.03	1.16	2.48
$\Delta E_T(9)$	$\mu^+\mu^-$	34622	8804	9127	6810	4103	4462	24502
	sgn	1584	944	1453	1124	825	1455	4497
	bkg/sgn	1.25	3.27	2.52	2.76	2.57	1.00	2.28
$\forall E_T$	$\mu^+\mu^-$	784443	200385	210890	161308	99054	109156	580408
	sgn	42262	22304	35252	35959	27635	41413	139440
	bkg/sgn	6.72	4.68	3.04	2.10	1.54	0.83	1.84

Table 3.3: Total statistics of analysed data, per P_T and E_T regions. The ratio bkg/sgn is for the region $0.65 \leq M < 1.2$ GeV/c^2.

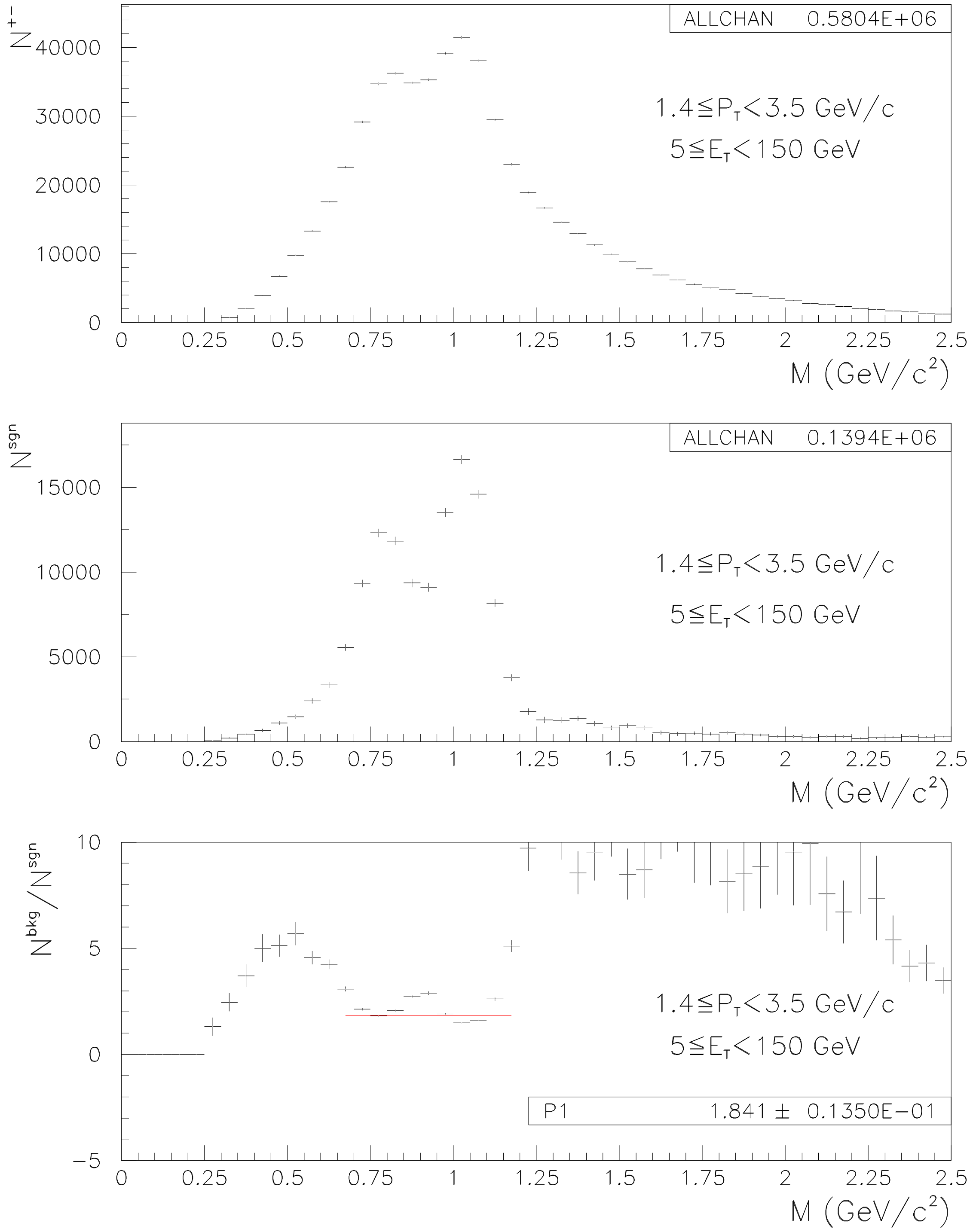

Figure 3.11: Mass spectrum of opposite sign dimuons, signal events, and the ratio background/signal. Data integrated in the regions $1.4 \leq P_T < 3.5$ GeV/c and $5 \leq E_T < 150$ GeV.

Chapter 4

Method of analysis

The purpose of this study is to make a multidimensional analysis of the dimuon spectrum in the low mass region, namely of the vector-mesons $\rho + \omega$ and ϕ, per P_T and E_T regions. However, the kinematic variables that are accessible, both directly and indirectly, are "distorted" by the finite resolution of the measurement devices, and by the limited acceptance of the apparatus. To go from measured variables to physics variables (the ones that in fact describe the kinematics of the dimuon production) one has to make use of a deconvolution method.

A Monte-Carlo generation allows to simulate the emission of dimuons produced in lead lead collisions, and their passage through the experimental apparatus. From the ratio between the spectra in the measured variable and the spectra in the generated variable one can obtain the acceptance and smearing functions.

The distributions of reconstructed events on the measured variables are corrected by the acceptance and smearing functions, in a multidimensional process of deconvolution, which enables to obtain the produced events distributions on the generated variables, according to the expression:

$$\frac{d^2N^{Ger}}{dP_T^g dM^g} = \int\int \frac{d^2N^{Rec}}{dP_T^m dM^m} \frac{S_{P_T}(P_T^m \rightarrow P_T^g) S_M(M^m \rightarrow M^g)}{A(P_T^g, M^g)} dP_T^m dM^m \tag{4.1}$$

where S_{P_T} and S_M represent the smearing inverse matrices as functions of the dimuons transverse momentum and mass, respectively; and $A(P_T^g, M^g)$ is the acceptance of the spectrometer as a function of the generated variables, obtained according to:

$$A(P_T^g, M^g) = \frac{d^2N^{Rec}/dP_T^g dM^g}{d^2N^{Ger}/dP_T^g dM^g} \quad . \tag{4.2}$$

Another equivalent method for the deconvolution of the data is according to the expression:

$$\frac{d^2N^{Ger}}{dP_T^g dM^g} = \int\int \frac{d^2N^{Rec}}{dP_T^m dM^m} A^{*-1}(P_T^m, M^m; P_T^g, M^g) dP_T^m dM^m \tag{4.3}$$

where A^* is an acceptance convoluted with smearing, calculated from the measured and the generated variables:

$$A^*(P_T^m, M^m; P_T^g, M^g) = \frac{d^2N^{Rec}/dP_T^m dM^m}{d^2N^{Ger}/dP_T^g dM^g} \quad . \tag{4.4}$$

In this study, the second method of deconvolution was chosen, because the treatment of the errors is simpler.

4.1 The physics generations

The Monte-Carlo simulation of the physics processes which contribute to the mass range that is being studied (the region $0.35 \leq M < 2.5$ GeV/c^2) is done using the code DIMUJET. This program enables the generation of dimuon signal events according to predefined distributions. The ρ, ω and ϕ resonances were considered; as was the continuum that results from a set of processes, such as Dalitz decays of the pseudo-scalars η and $\eta\prime$ and of the vector-meson ω, the Drell-Yan process and semi-leptonic decays of D$\bar{\text{D}}$ pairs, described by an empirical function. The generations are done on the kinematic variables: mass, transverse momentum, rapidity, $\cos\theta_{CS}$ and the azimuthal angle ϕ_{CS} of the dimuon.

The generated events pass through a detailed simulation of the experimental apparatus, which includes the energy losses and the multiple scattering when passing through matter (mainly in the absorber), the Fermi motion of the nucleons in the nucleus and the efficiencies of the several sub-detectors. The accepted MC events are recorded in the same format as the real data (*raw data*), and are subsequently reconstructed using the same reconstruction code that is used for the experimental data, the DIMUREC code. The reconstructed MC events in terms of the measured variables are submitted to the same cuts as the experimental ones, and using the obtained distributions one calculates the acceptances convoluted with smearing, according to equation 4.4 .

4.1.1 Mass generation

The dimuon mass spectrum is generated as a sum of the resonances ρ, ω and ϕ that decay into dimuons,

$$\rho,\ \omega,\ \phi\ \rightarrow \mu^+\mu^-$$

and of a physics continuum resulting from the joint contribution of Dalitz decays (also called internal conversion processes):

$$\eta,\ \eta'\ \rightarrow\ \gamma\gamma^*\ \rightarrow\ \gamma\mu^+\mu^- \quad ,$$

$$\omega\ \rightarrow\ \pi^o\gamma^*\ \rightarrow\ \pi^o\mu^+\mu^- \quad ,$$

of semi-leptonic decays of $D\bar{D}$ pairs (open charm processes):

$$D^+\ \rightarrow\ \bar{K^o}\mu^+\nu_\mu \quad , \quad D^-\ \rightarrow\ K^o\mu^-\bar{\nu}_\mu \quad , \quad D^o\ \rightarrow\ K^-\mu^+\nu_\mu \quad e \quad \bar{D}^o\ \rightarrow\ K^+\mu^-\bar{\nu}_\mu \quad ;$$

and of the Drell-Yan process (annihilation of one quark from a target-nucleon with a quark from a projectile-nucleon):

$$q\bar{q}\ \rightarrow\ \gamma^*\ \rightarrow\ \mu^+\mu^- \quad .$$

The ρ, ω and ϕ resonances are simulated as classical Breit-Wigner functions, with the mass poles and widths presented in table 1.1, and given by the PDG [9]:

$$BW_r = \frac{\Gamma_r^2/4}{(M-m_r)^2+\Gamma_r^2/4} \tag{4.5}$$

where $r \equiv \rho, \omega, \phi$. As discussed in Appendix A, nowadays it is considered that the vector-meson ρ, of very short lifetime, does not behave as a true resonance, and therefore its description as a classical Breit-Wigner is inadequate. There are several theoretical proposals for alternative ways of describing the ρ, as a modified relativistic Breit-Wigner, with a width depending on the energy (or on the invariant mass). Nevertheless, on this simulation it was decided to describe the ρ as a classical Breit-Wigner in first approximation, because, as will be shown ahead, the generated Breit-Wigners are afterwards "modeled" to the shape of the experimental distributions.

The several contributions to the physics continuum are quite difficult to simulate in a realistic way. While the Dalitz decays are dominant in the mass region $M < 0.65$ GeV/c^2, the $D\bar{D}$ decays, along with the Drell-Yan mechanism, dominate in the region $1.2 \leq M < 2.5$ GeV/c^2. These two latter mechanisms are "hard" processes, and cannot be calculated by perturbative QCD in the low mass region. The extrapolation of their contributions to this region is therefore very delicate. On this study, it was decided to simulate the sum of all the processes that contribute to the continuum by using an effective parametrisation, namely a decreasing exponential. The following process of weighting the simulated spectra to resemble the data allows the exact description of the continuum experimental shape.

Thus, the mass spectrum is simulated in the region $0.35 \leq M < 2.5$ GeV/c^2 according to the function:

$$\frac{d\sigma}{dM} \propto A_\rho BW_\rho + A_\omega BW_\omega + A_\phi BW_\phi + B_1 exp(-B_2\ M) \tag{4.6}$$

with the area of the Breit-Wigner functions normalised to unity and $A_\rho = 1$, $A_\omega = 1.15$, $A_\phi = 0.86$. The choice of these values was made recalling that the NA38 experiment measured a ratio $\phi/(\rho+\omega) \approx 0.4$ for central S+U collisions. The ratio ω/ρ could not be measured by the experiment because, as in NA50, the experimental mass resolution is much worse than the mass difference of the two resonances. Nevertheless, the fit to the experimental data has shown that $\omega/\rho \approx 1$, instead of what one would expect from the PDG information[1]. For the parameters describing the continuum, the values $B_1 = 9$ and $B_2 = 4.5$ [81] were chosen. The mass generation window is from 0.25 to 3.5 GeV/c^2, wider than the region being studied, to account for the smearing effect.

4.1.2 Transverse momentum generation

The generation on the dimuons transverse momentum is done according to a Bessel function:

$$\frac{d\sigma}{dP_T} \propto P_T K_1(-M_T/T) \tag{4.7}$$

where $M_T = \sqrt{M^2 + P_T^2}$ is the dimuon transverse mass, and the parameter T is the inverse slope of the distribution on P_T (or M_T). In this simulation one uses $T = 236$ MeV, a value close to the one found experimentally in S+U collisions [84]. The chosen generation window is $P_T < 5$ GeV/c.

The generated distributions as functions of the dimuons transverse momentum per mass regions are then adjusted, to better describe the experimental distributions.

4.1.3 Generation on rapidity, $\cos\theta_{CS}$ and azimuthal angle

The rapidity distribution is simulated using a Gaussian function, according to:

[1] According to the PDG, if we admit that the production cross sections for ρ and ω are the same, and that the ratio of their branching ratios (BR) into dimuons is identical to the one into dielectrons, one obtains $\omega/\rho = 1.6$. But the BR included in the PDG are obtained essentially in proton induced collisions, and therefore it is possible that this ratio has a different value in heavy ions collisions.

$$\frac{d\sigma}{dY} \propto exp(-\frac{Y^2}{2\sigma_o^2}) \quad . \tag{4.8}$$

This distribution is centred on $Y = 0$, because the colliding system is approximately symmetrical (although not entirely, because one has an ion beam of ^{208}Pb, whereas the target is a mixture of ^{206}Pb and ^{208}Pb). The value $\sigma_o = 1.25$ is used, a value measured experimentally by the NA49 collaboration for the vector-meson ϕ in Pb+Pb collisions at 158 GeV/nucleon [85]. The used generation window is é $-0.25 \leq Y < 1.25$.

The distribution on $\cos\theta_{CS}$ is simulated with the shape:

$$\frac{d\sigma}{d\cos\theta_{CS}} \propto 1 + \cos^2\theta_{CS} \quad . \tag{4.9}$$

This shape is adequate to the angular distribution of the dimuons from the physics continuum, as demonstrated by the NA10 experiment. For the resonances though, a constant distribution is more appropriate. This difference implies the need for a correction to the final cross sections. The chosen generation window is $-0.7 \leq \cos\theta_{CS} < 0.7$, a little wider than the angular acceptance window of NA50 ($-0.5 \leq \cos\theta_{CS} < 0.5$), to avoid distortions from the smearing effect.

The distribution as a function of the azimuthal angle ϕ_{CS} was generated as uniform in the whole window $0 \leq \phi_{CS} < 2\pi$.

4.2 Adjustment of the Monte-Carlo to the data

In figure 4.1 one can see the generated distributions as functions of the mass, the transverse momentum, the rapidity and the $\cos\theta_{CS}$ of the dimuon, according to the generation functions presented before. In the same figure, the accepted dimuons distributions, after passing through the simulation of the spectrometer, are also presented.

In figure 4.2 one can see the integrated distributions in the regions of interest, after the reconstruction of the simulated event tracks by the reconstruction code, and after applying the same cuts as the ones applied to the data.

These distributions of reconstructed MC events are similar to the experimental ones. A multidimensional iterative method is used, so that the MC describes more precisely the experimental data. In this method, by comparing the reconstructed and the generated MC, per mass, P_T or rapidity bins, one obtains the correction matrices. Figure 4.3 shows schematically the iterative process used to approximate the Monte-Carlo to the data.

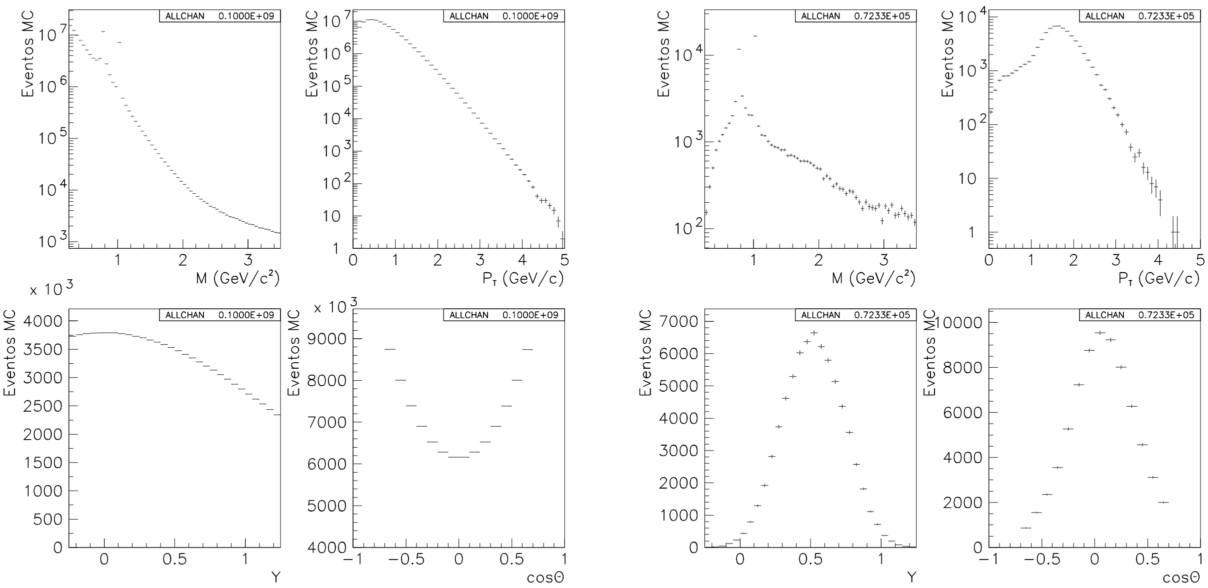

(a) (b)

Figure 4.1: Distributions of simulated (a) and accepted (b) MC events, as functions of the dimuons mass, transverse momentum, rapidity and $\cos\theta_{CS}$.

In figure 4.4 the matrices containing the weights to apply to the generated events so that the reconstructed MC distributions describe better the experimental distributions are shown.

Each cell of those (M,P_T,Y) matrices constitutes a weight to apply, event by event, to the generated MC events. In this way the shape of the distributions of generated Monte-Carlo events is modified. Figures 4.5, 4.6 and 4.7 show the ratios of the reconstructed Monte-Carlo to the experimental distributions, as functions of the dimuons mass, transverse momentum and rapidity. In each figure, three steps of the iterative process are presented: before any correction to the MC; after correction with one iteration; and after correction with two iterations. A fit by an horizontal straight line, in each of the regions of interest, shows that the differences between the MC and the data tend to disappear, and are already very small after two iterations. The χ^2 of the fit also improves with the number of iterations, which constitutes another indicator that the process converges. In this study, it was shown that two iterations are enough for a good correspondence between the MC and the data.

In figure 4.8 one can see the mass, transverse momentum and rapidity generated distributions, before and after the adjustment to the shape of the data.

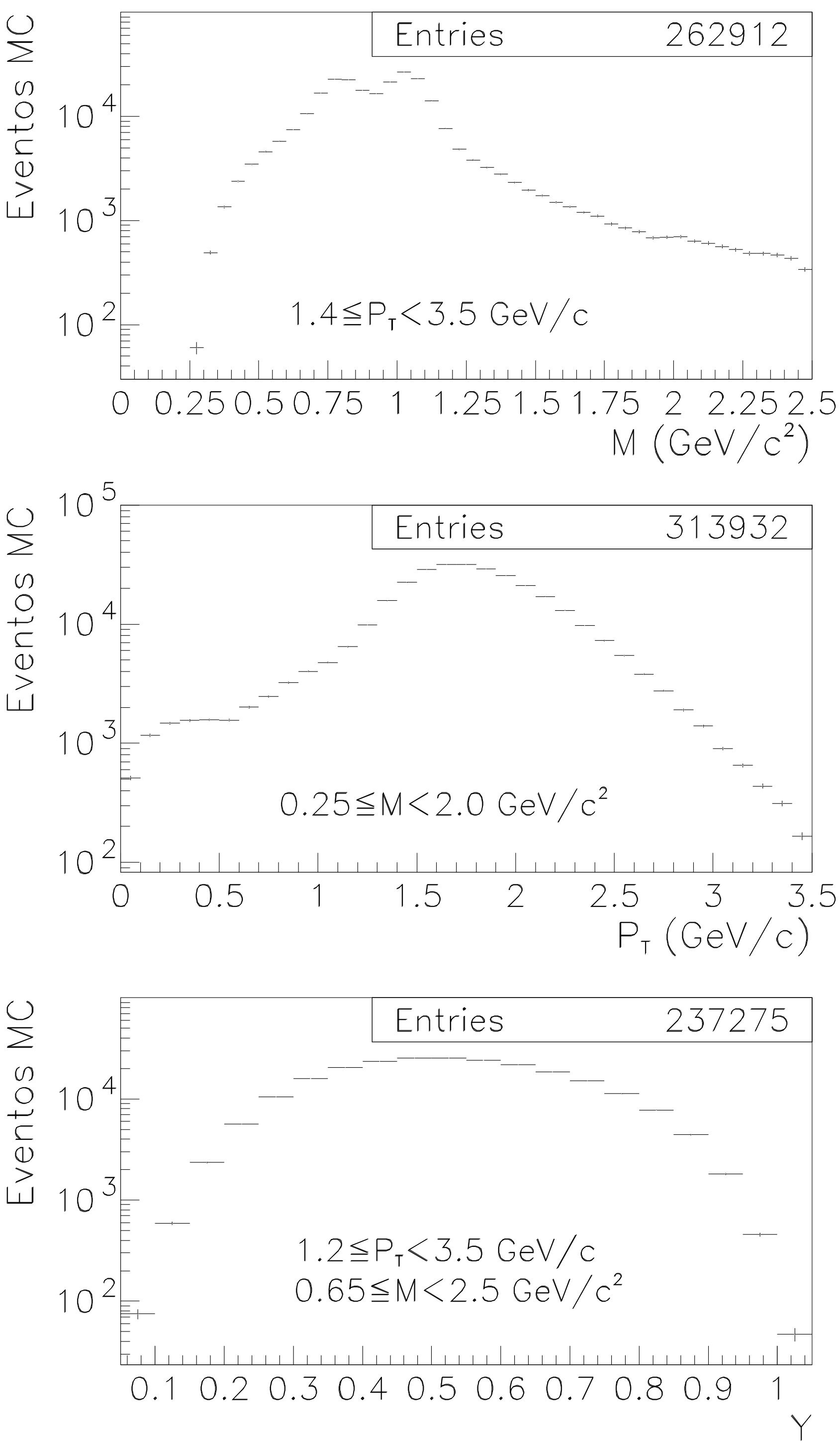

Figure 4.2: Distributions of accepted MC events after reconstruction and cuts, as functions of measured mass, transverse momentum and rapidity.

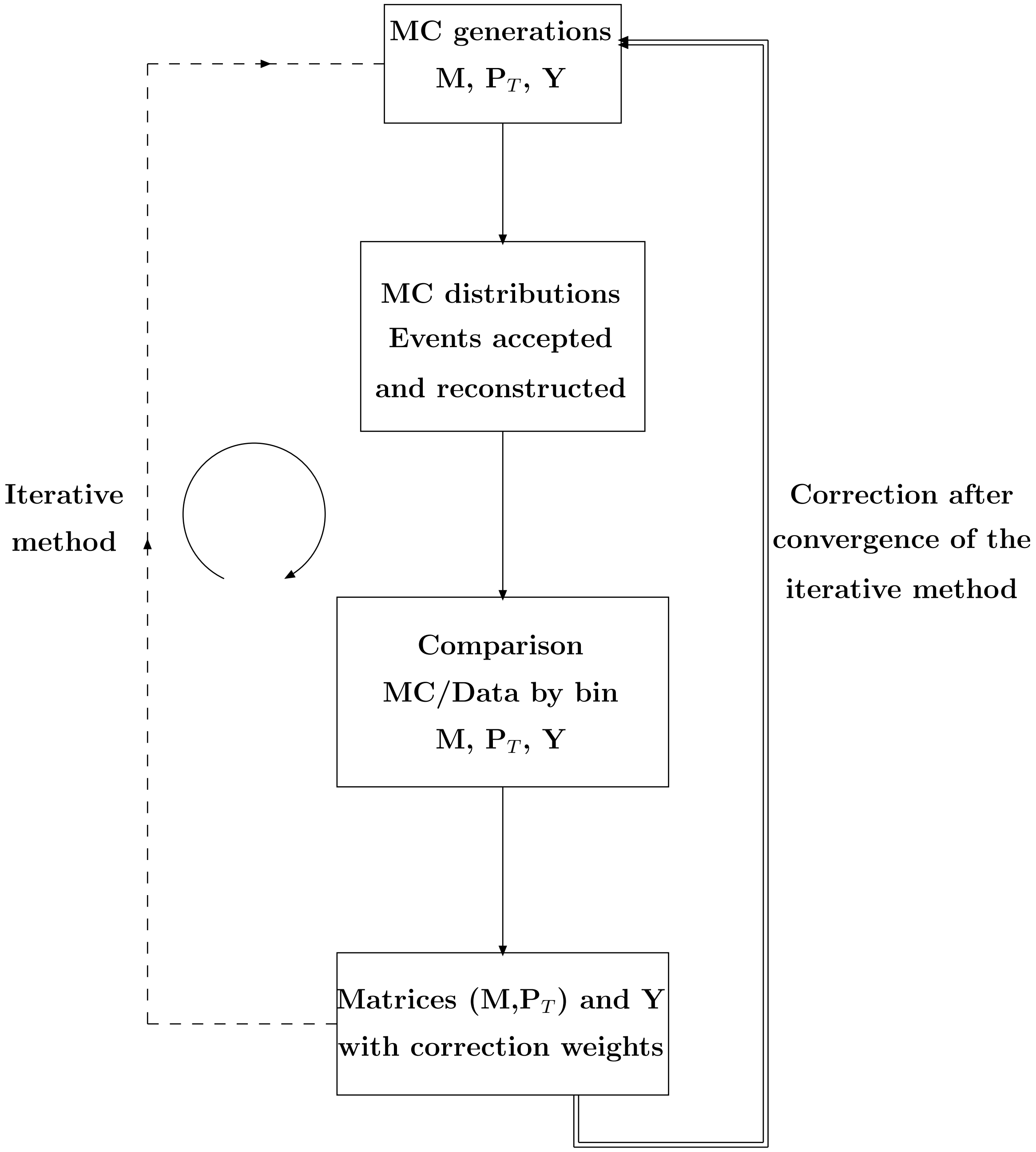

Figure 4.3: Iterative method for the adjustment of the Monte-Carlo to the data.

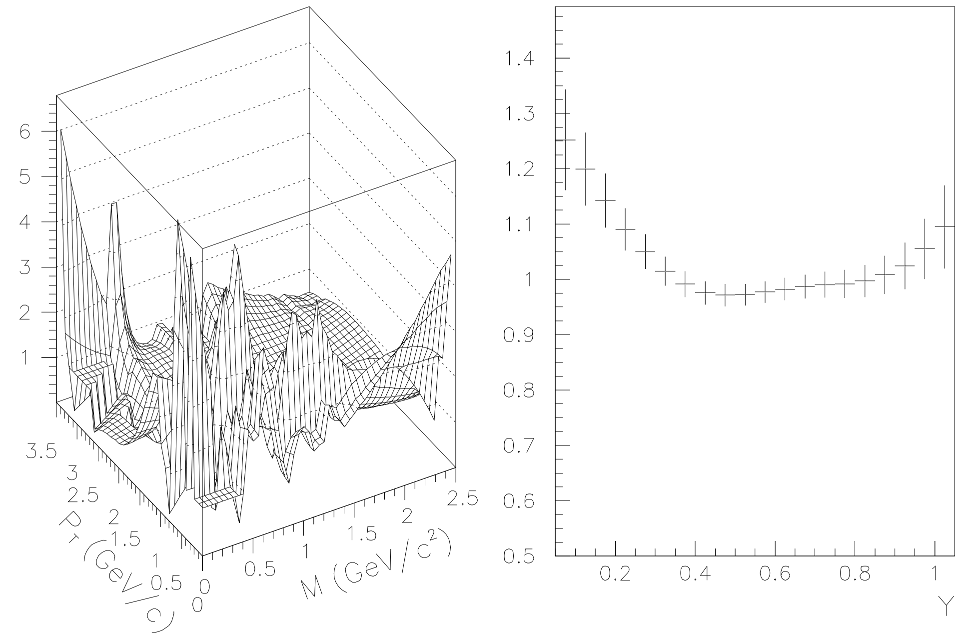

Figure 4.4: Matrices containing the weights for the multidimensional MC correction. Matrix (M,P_T) and matrix (Y), after 2 iterations.

4.3 The simulated distributions and the geometrical cut

The distributions of simulated events, after the reconstruction, are submitted to the same cuts made to the experimental data. The diagonal cut is an exception, because this Monte-Carlo does not allow the simulation of the transverse energy released in the collisions.

Regarding the $P * Dtarget$ cut, some considerations are necessary. The Monte-Carlo cannot precisely simulate the experimental conditions. In the backwards extrapolation of the reconstructed tracks into the vertex zone, the dispersion of the $Dtarget$ distances is systematically smaller for the simulated tracks than for the experimental ones. The set of $P * Dtarget$ coefficients adjusted to the data, as explained in Chapter 3 and Appendix C, when applied to the MC events, do not produce uniform distributions for the probability of χ^2 of $P * Dtarget$. It is thought that this problem of the Monte-Carlo is due to an insufficient simulation of the multiple scattering and of the energy losses in the absorbers.

Using the Monte-Carlo low mass generation, a tuning of the $P * Dtarget$ coefficients shows that the σ coefficients have a dependency on the muon momentum identical to

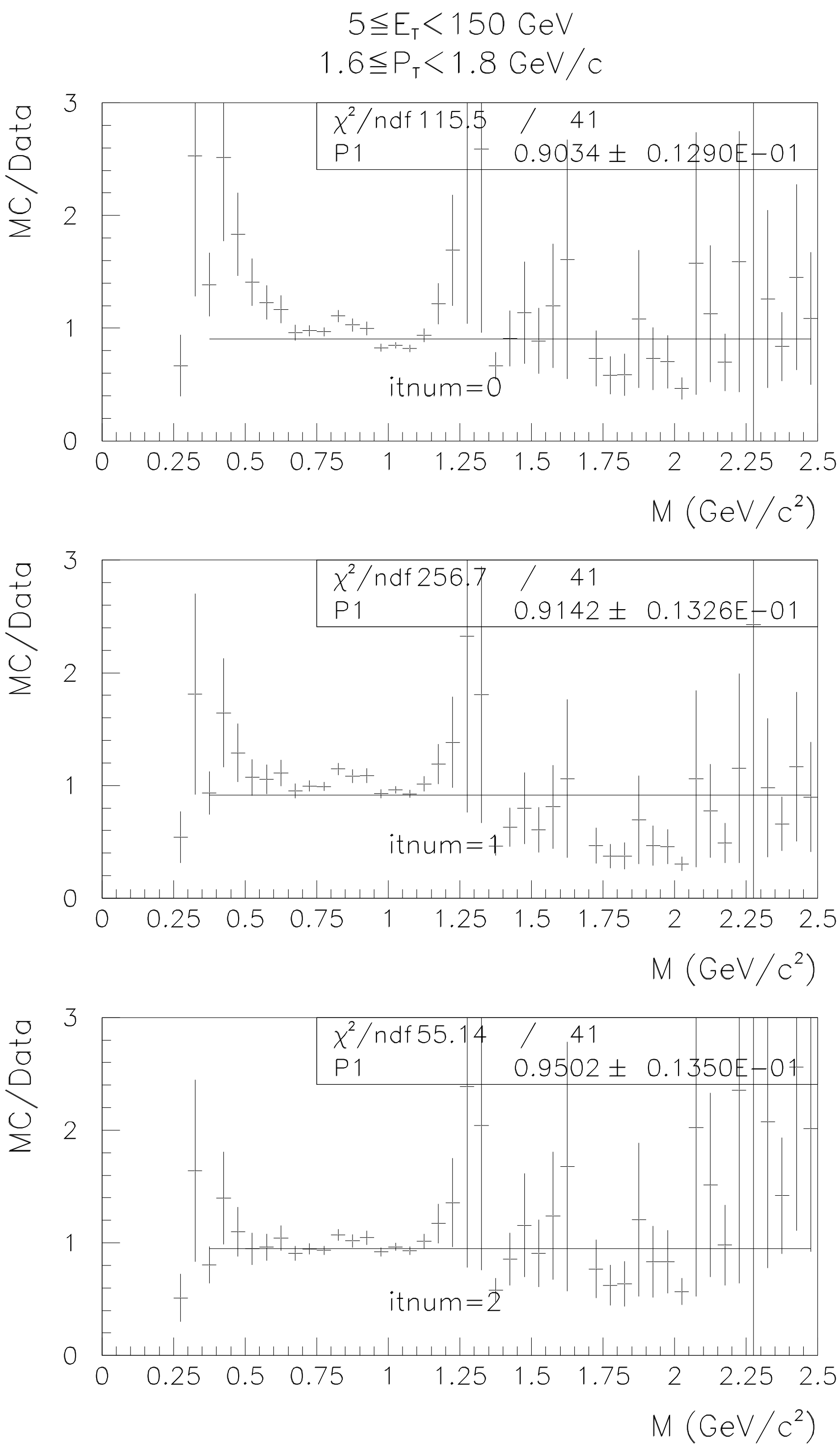

Figure 4.5: Comparison between the mass distributions of reconstructed Monte-Carlo events and the experimental mass spectra. Ratio MC/Data without correction, and after one or two iterations.

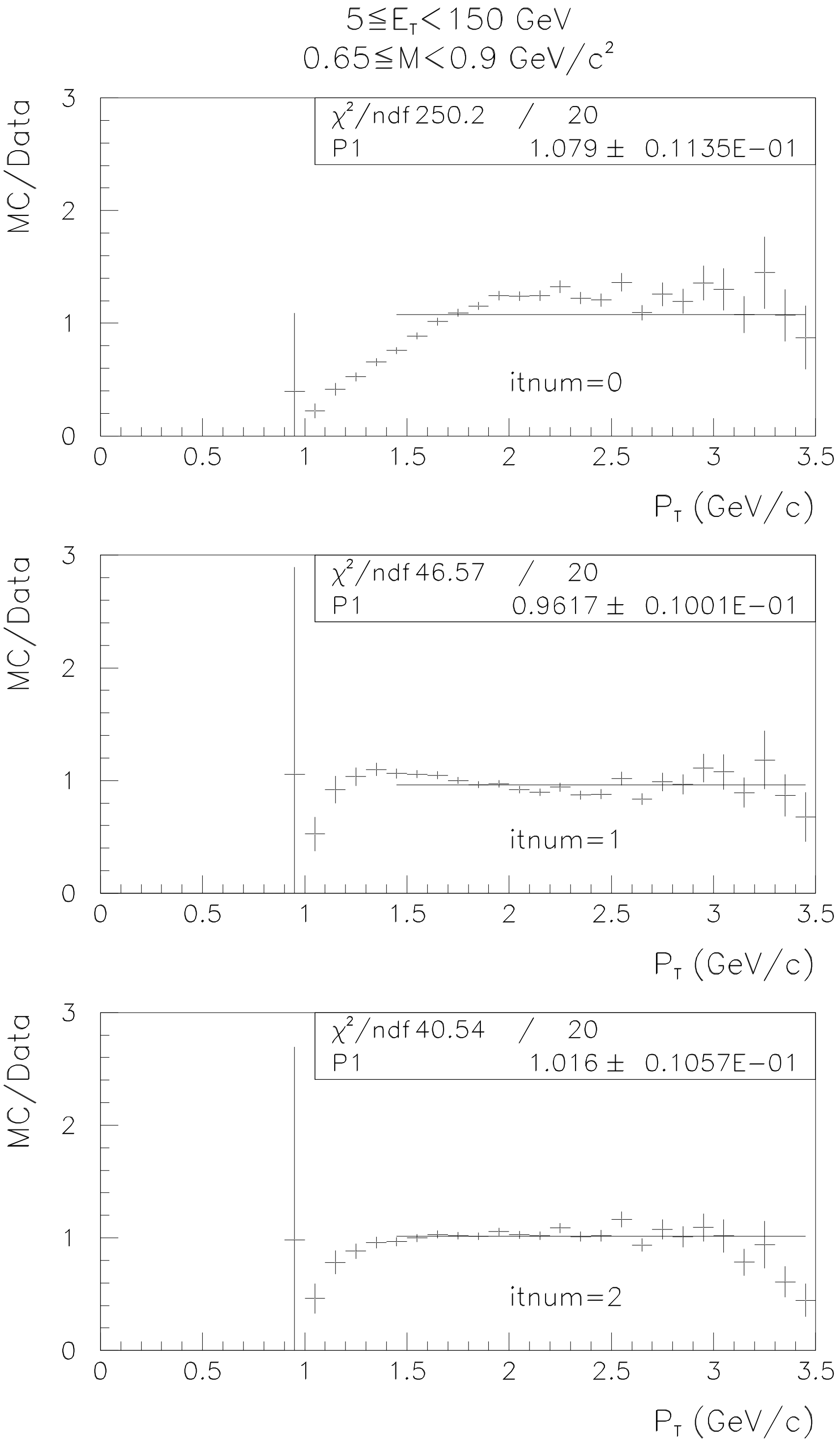

Figure 4.6: Comparison between the P_T distributions of reconstructed Monte-Carlo events and the experimental P_T spectra. Ratio MC/Data without correction, and after one or two iterations.

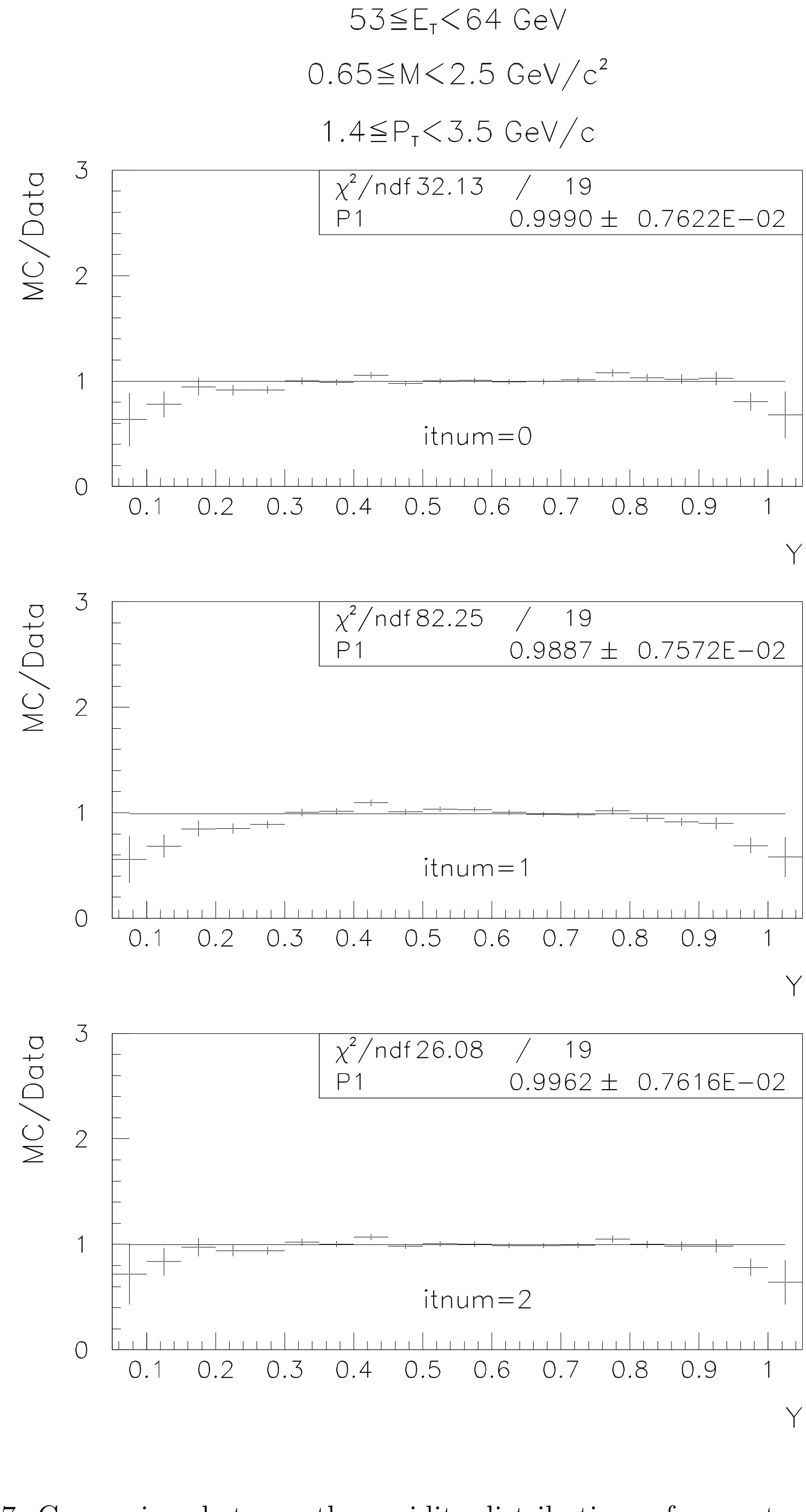

Figure 4.7: Comparison between the rapidity distributions of reconstructed Monte-Carlo events and the experimental rapidity spectra. Ratio MC/Data without correction, and after one or two iterations.

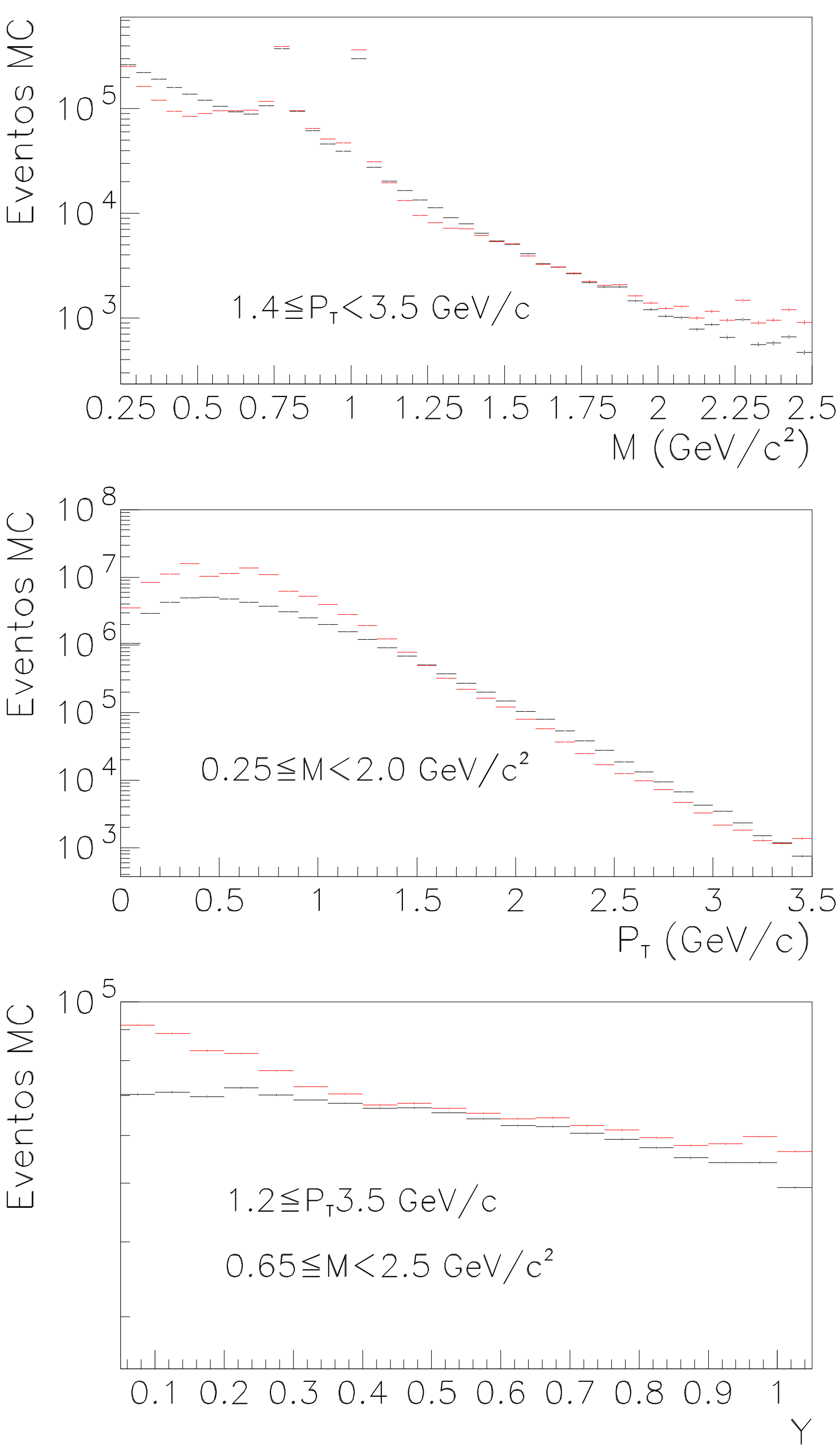

Figure 4.8: Generated Monte-Carlo distributions as functions of the dimuons mass, transverse momentum and rapidity, before (black) and after (red) applying the weights to adjust MC to data.

the one observed for the data muons, except for a multiplicative factor. As is shown in figure 4.9, this factor is 1.10, both for convergent and divergent tracks.

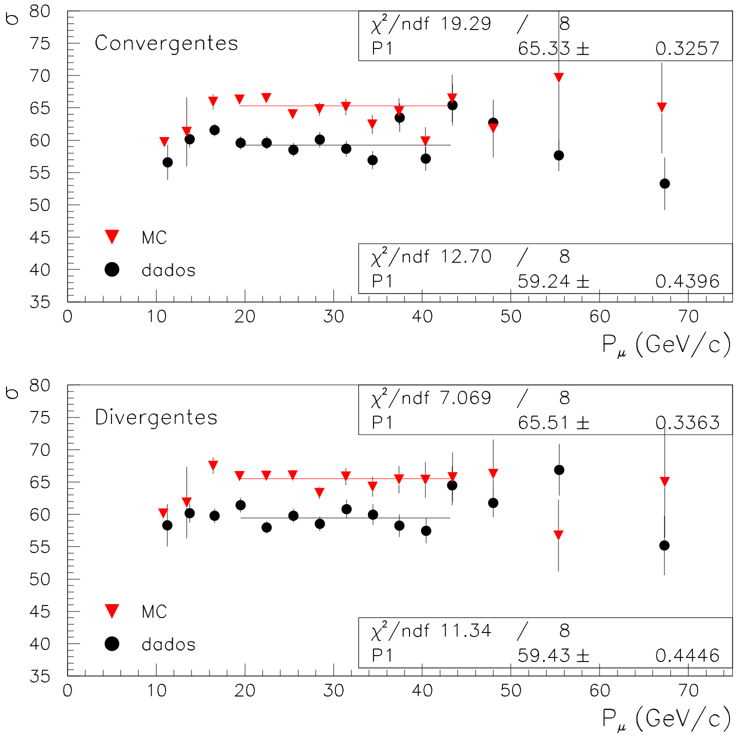

Figure 4.9: Comparison between the σ coefficients tuned on the Monte-Carlo $P * Dtarget$ distributions and those tuned on data, for convergent and divergent tracks.

All the Monte-Carlo events are "good", in the sense that they are all simulated originating from the target, and that they are all signal events. Therefore, the aim of the $P * Dtarget$ cut is here only to eliminate a percentage of statistics identical to the one of the data, with the same criterium used in the data (to eliminate the events whose tracks deviate more from the centre of the target in its backwards extrapolation), and not to eliminate background.

The cut on the χ^2 probability of $P * Dtarget$ of the convergent (divergent) tracks at 4% represents a cut on statistics of Y%. Admitting that the "bad" events (events produced out of the target) are all in the peak of the χ^2 probability distribution, that cut corresponds to eliminating 4% of "good" tracks and (Y-4)% of background tracks. Thus, the cut $P * Dtarget$ applied to the MC simulated tracks is of 4% in statistics of the total convergent (divergent) tracks, after applying all the other cuts. Since the χ^2 probability distributions of $P * Dtarget$ are different for convergent and divergent tracks, the correspondent cut in probability of $P * Dtarget$ is also different: 6.3% for convergent tracks and 4.5% for divergent tracks.

4.4 Acceptances and smearing

The differential acceptances as functions of mass, transverse momentum and rapidity of the dimuon are calculated with the equation (4.2), from the Monte-Carlo generated distributions (and adapted according to the data, as described in section 4.2), and from the distributions of reconstructed simulated events (to which the same cuts of the data were applied).

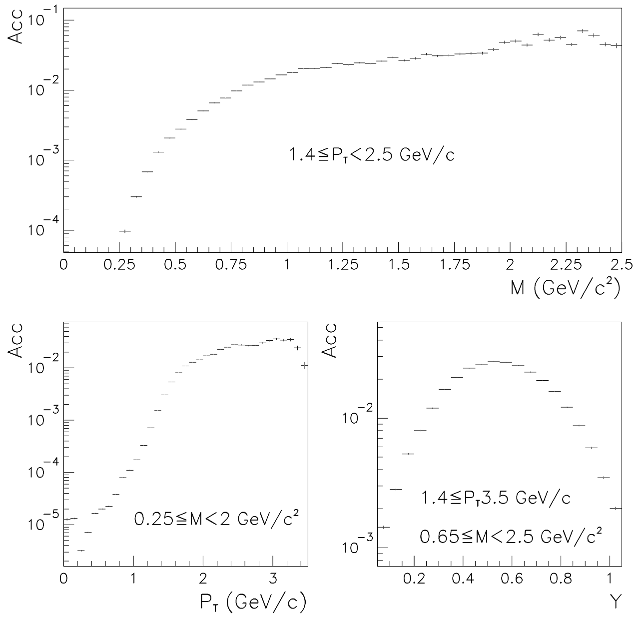

Figure 4.10: Acceptance as a function of the dimuons mass, P_T and rapidity.

In this study, instead of using the acceptances and smearing calculated independently (figures 4.10 and 4.11), the acceptances convoluted with smearing, calculated using the equation (4.4) by dividing the MC distributions reconstructed on the measured variable by the correspondent distributions generated on the generated variable, are used. These differential acceptances (Acc*) are obtained in each region of P_T and of E_T, from a MC that is adjusted to the data also in each of those regions.

In figures 4.12 and 4.13 the acceptances convoluted with smearing per P_T and mass bins, respectively, are presented, for the integrated transverse energy window $5 \leq E_T <$ 150 GeV.

From figure 4.12 one can conclude that the acceptance in the low mass region, for dimuons with $P_T < 1.4$ GeV/c, is lower than 1%. Therefore, as a way to avoid the extreme uncertainty that a correction of the data with such low acceptances would imply, the analysis of the data is only made in the four regions of P_T in which the acceptances

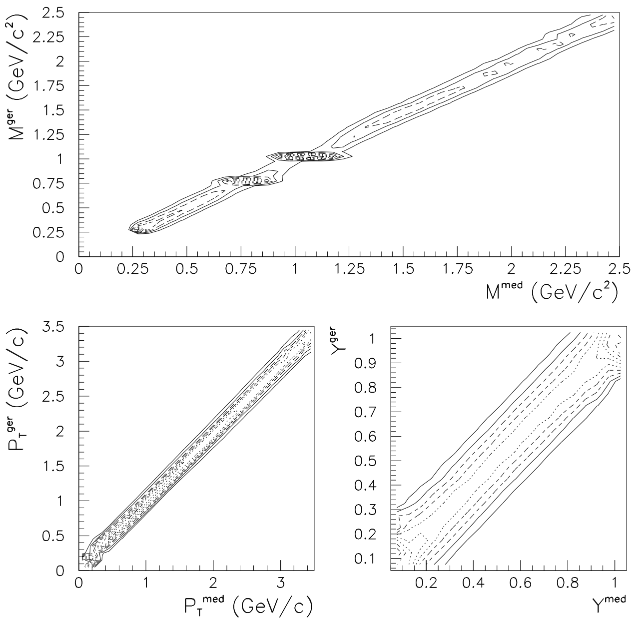

Figure 4.11: Inverse smearing matrices, as functions of the dimuons mass, P_T and rapidity (integrations on the same regions as in figure 4.10).)

are higher than 1%; that is, a cut at $P_T \geq 1.4$ GeV/c is applied. The acceptances per P_T bins to apply to the 9 regions of transverse energy of the analysis do not differ much, from region to region of E_T (those differences come only from the adjustment of the same set of MC events to the experimental distributions in each bin of E_T).

The low acceptance of the NA50 experiment in the low mass region is due fundamentally to the strong magnetic field, since the current in the magnet is 7000 A, sweeping the lighter particles out off the spectrometer's acceptance. The NA38 experiment, predecessor of NA50, used a current in the magnet of 4000 A, obtaining acceptances in the mass region of the "ϕ" from 3 to 4 times greater than the ones in this analysis, but worsening the mass resolution for J/ψ and ψ' resonances.

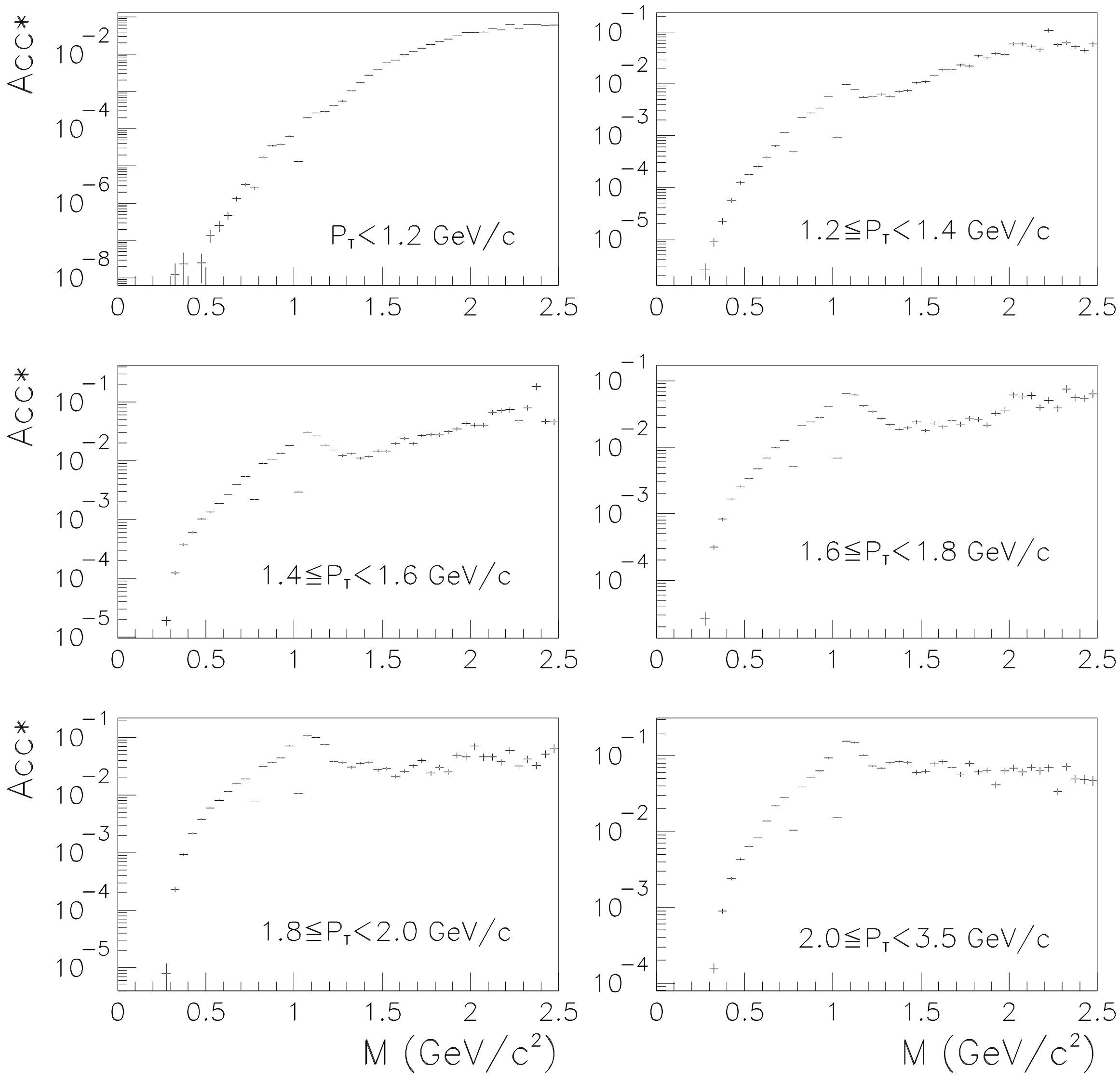

Figure 4.12: Differential acceptance convoluted with smearing as a function of the dimuons transverse momentum, per P_T regions, for $5 \leq E_T < 150$ GeV.

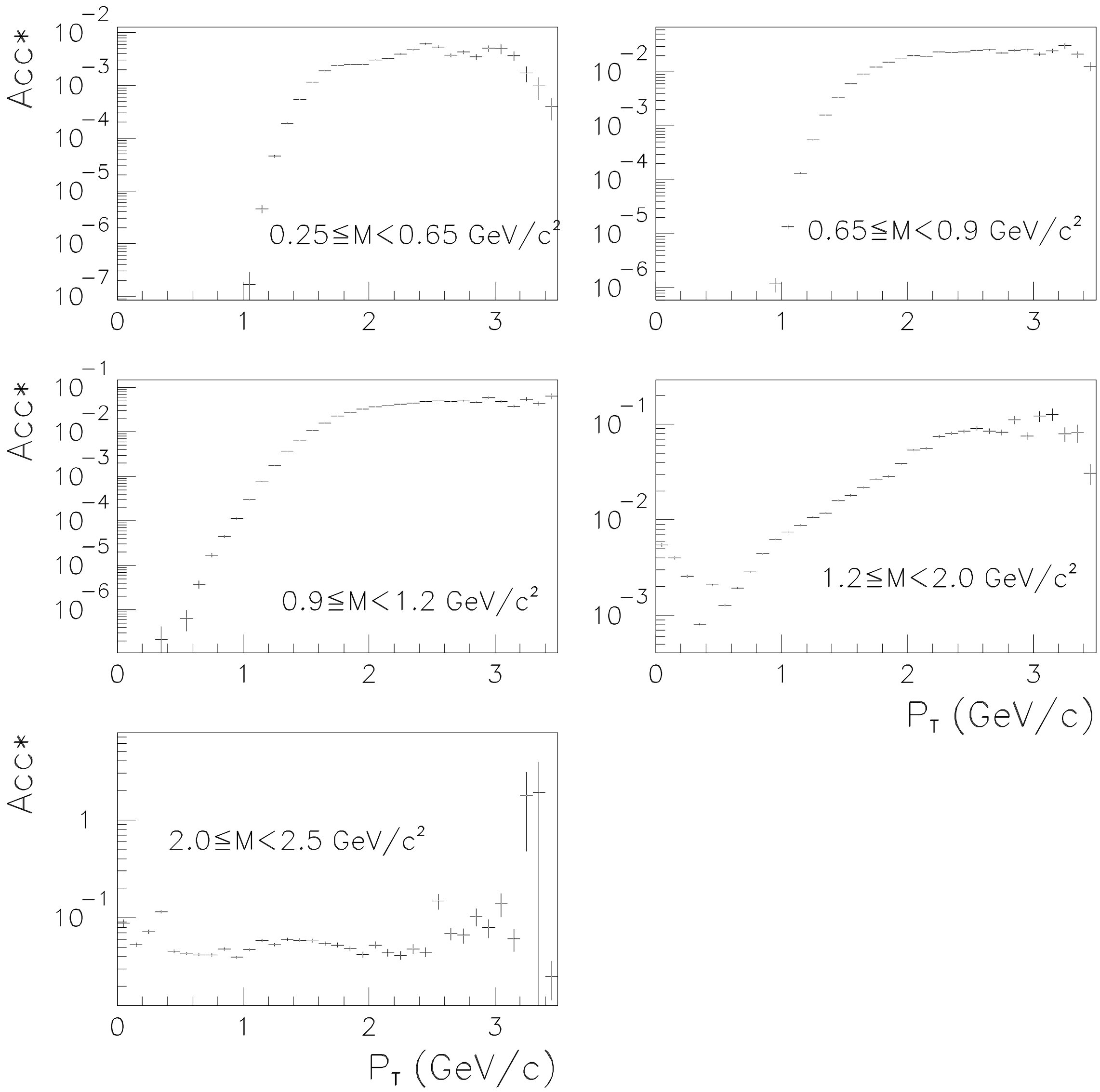

Figure 4.13: Differential acceptance convoluted with smearing as function of the dimuon's transverse momentum, by regions of mass, for $5 \leq E_T < 150$ GeV.

Chapter 5

Experimental results

The dimuon signal distributions are corrected for acceptance and smearing effects, per transverse momentum and transverse energy regions. Once corrected, these are fitted by a function including all the expected physics contributions: direct decays of ρ, ω and ϕ resonances, and a dimuons' continuum. In this way, it is possible to extract the ratios $BR_{\mu\mu}\sigma_\phi/(BR_{\mu\mu}\sigma_\rho + BR_{\mu\mu}\sigma_\omega)$ (from now on referred to as $\phi/(\rho+\omega)$) as functions of the transverse momentum and the transverse energy. All the results presented here refer to the decay channel into dimuons, being implicit the branching ratio $BR_{\mu\mu}$ of each process into dimuons.

The two resonances ρ and ω, with mass poles differing by only 13 MeV, cannot be distinguished, since the NA50 spectrometer's mass resolution is about 70 MeV/c^2 in the ϕ mass and slightly worse for ω and ρ masses. Thus, the obtained results are always expressed in terms of the joint contribution of these two resonances, $\rho+\omega$. Only the sum of the two has physics meaning, due to the experimental constraints.

The differential cross-section for the resonances $\rho+\omega$ and ϕ shows a universal dependency on the dimuons transverse mass ($M_T = \sqrt{P_T + M}$), as explained in Chapter 1. Thus these vector-mesons have a characteristic T parameter, the inverse slope of the M_T distribution, extracted from the fit to the differential cross-sections as a function of the dimuons transverse mass.

5.1 Relative production of the vector-mesons ϕ and $\rho+\omega$

The fit function to the dimuon mass spectra describes the resonances ρ, ω and ϕ as classical Breit-Wigner functions:

$$BW_v = \frac{\Gamma/4}{(M - m_v)^2 + \Gamma/4} \tag{5.1}$$

where $v \equiv \rho, \omega, \phi$; and fixing the resonance's mass pole m_v and total width Γ to the values from table 1.1 [9]. While this is an obvious choice for the resonances ω and ϕ, since their widths are small, for the ρ maybe this is not the best description (see Appendix A). In this analysis the classical Breit-Wigner function is used and the influence of this choice in the final results is studied ahead, in Chapter 6.

The three Breit-Wigner functions are normalised to their area in the mass region of interest (0.35 to 2.5 GeV/c^2), so that the free parameter associated with each of them gives directly the number of ρs, ωs and ϕs, in each integrated P_T and/or E_T region. The normalisation factors are $\int BW_\rho = 4.39$, $\int BW_\omega = 0.26$, $\int BW_\phi = 0.14$.

The dimuon continuum extending from 0.35 to 2.5 GeV/c^2 (this analysis' mass limits), including under the resonances, is the sum of several processes: Dalitz decays of η and $\eta\prime$ into a pair of muons and a photon, and of ω into a pair of muons and a neutral pion; the Drell-Yan mechanism; and the semi-leptonic decays of $D\bar{D}$ pairs. As explained in the previous chapter, the shape of some of these contributions is not well-known in the low mass region (namely the Drell-Yan process). Also because of the possibility of interference between some processes (for example the ω-ρ interference) makes it very hard to calculate analytically the shape of the dimuon continuum. As done for the simulation of the dimuon mass spectrum, the physics continuum (the sum of all non-resonant processes) is parametrised by a decreasing exponential function, whose normalisation and slope are free parameters of the fit. The influence of this parametrisation in the final results is also discussed in Chapter 6.

A five free parameters function is used to fit the experimental data:

$$\mathcal{F} = P_1 BW_\rho + P_1 P_2 BW_\omega + P_1 P_3 (1 + P_2) BW_\phi + P_4\ exp(-P_5 M) \tag{5.2}$$

where P_1 is the ρ normalisation, P_2 the ratio ω/ρ and P_3 the ratio $\phi/(\rho + \omega)$. This parameters' definition has the advantage that the statistical error associated with $\phi/(\rho+\omega)$ is directly the error of the P_3 parameter from the fit.

5.1.1 $\frac{\phi}{\rho+\omega}$ as a function of P_T and E_T

The fit to the data using function (5.2) is done in 4 transverse momentum regions and 9 transverse energy regions. The fit method used is the χ^2 method[1]. Figure 5.1 exemplifies the fit to a mass spectrum.

[1]The data analyses in experimental particle physics also use very often the maximum likelihood fit method, that cannot be applied in this case, since the spectra are deconvoluted. The maximum likelihood

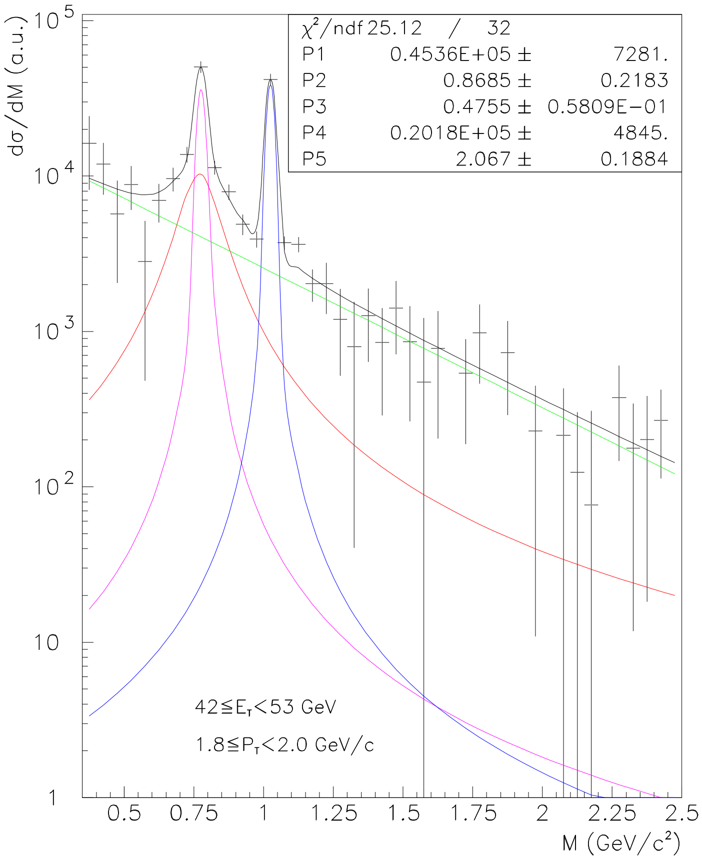

Figure 5.1: Fit to the dimuons mass spectrum in the region $1.8 \leq P_T < 2.0$ GeV/c and $42 \leq E_T < 150$ GeV.

The ratio $\phi/(\rho+\omega)$ is presented in table 5.1, per transverse momentum and transverse energy regions, the quoted errors being only statistical. In some bins the error is very large, and also the χ^2 per degree of freedom is sometimes less than 1, indicating that the statistics per region is not enough. Later on, this study will be presented in broader transverse energy regions (5 instead of 9 regions), which allows to verify the stability of the results.

The obtained results show that the ratio $\phi/(\rho+\omega)$ increases with the centrality of the collisions (figure 5.3), and it is independent of the dimuon transverse momentum (figure 5.2).

method always considers $\sqrt{N}$ as the error associated to each data point having N countings. In this analysis, the background subtraction and the acceptance and smearing correction, done prior to the fit, imply an error propagation. Therefore, for the errors to be correctly taken into account in the mass spectra fit, one has to use the χ^2 method.

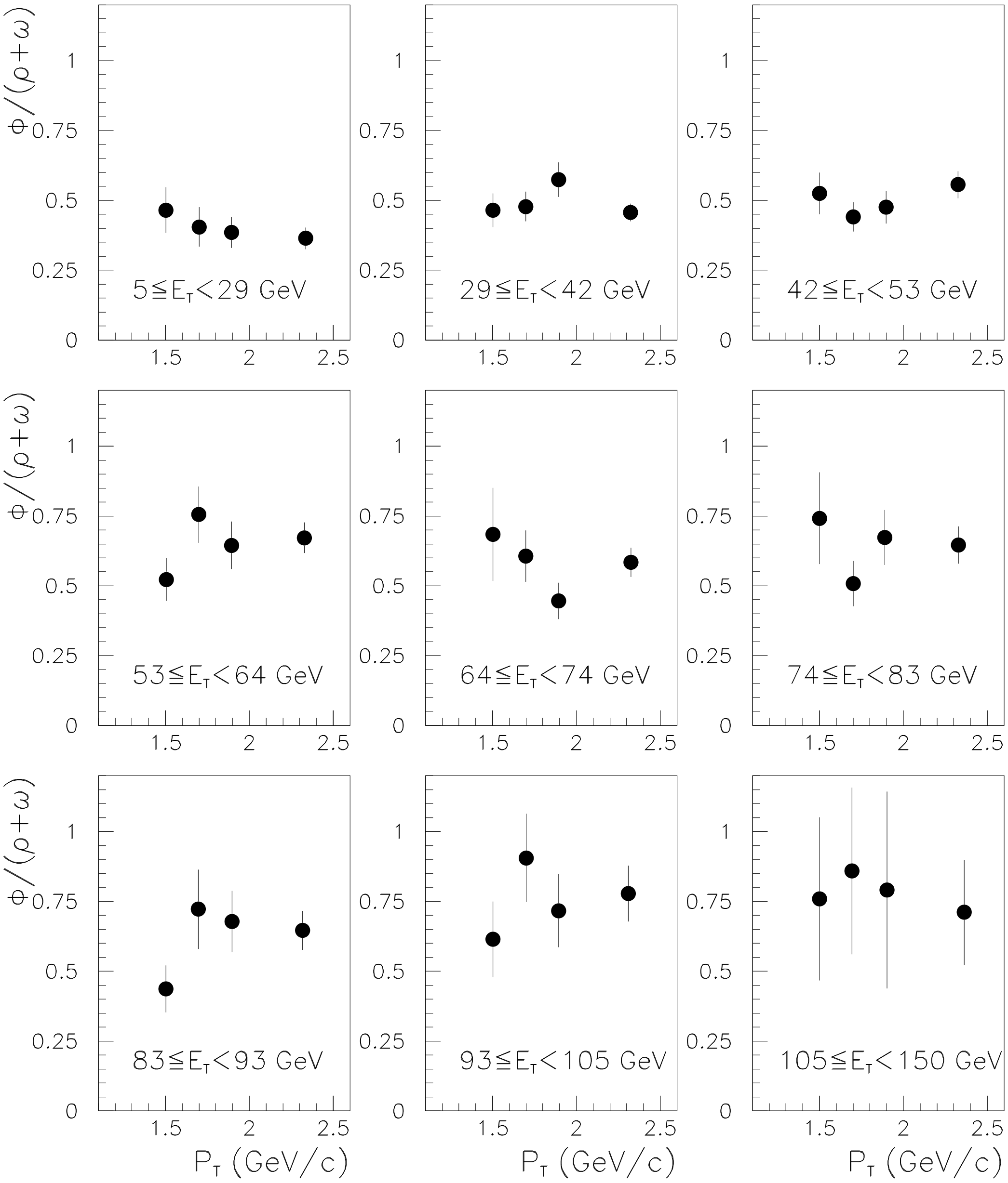

Figure 5.2: Ratios $\phi/(\rho+\omega)$ as a function of P_T, per 9 E_T regions.

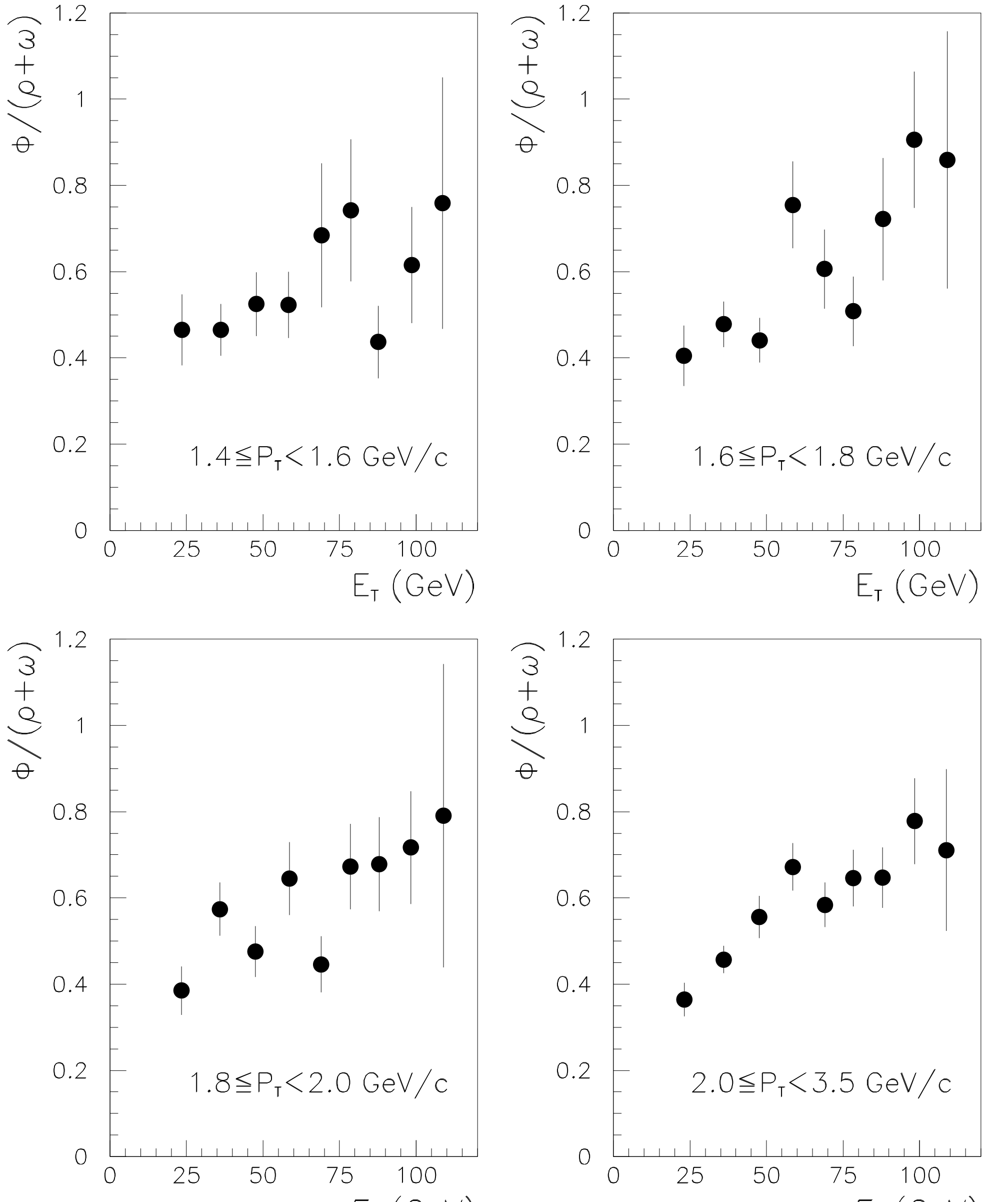

Figure 5.3: Ratios $\phi/(\rho+\omega)$ as a function of E_T, per 4 P_T regions.

$\phi/(\rho+\omega)$ (χ^2/ndf)	$1.4 \leq P_T < 1.6$ GeV/c	$1.6 \leq P_T < 1.8$ GeV/c	$1.8 \leq P_T < 2.0$ GeV/c	$2.0 \leq P_T < 3.5$ GeV/c
$5 \leq E_T < 29$ GeV	0.465 ± 0.082 (0.7)	0.405 ± 0.070 (2.0)	0.385 ± 0.056 (1.6)	0.364 ± 0.039 (1.4)
$29 \leq E_T < 42$ GeV	0.465 ± 0.060 (1.4)	0.478 ± 0.053 (0.8)	0.574 ± 0.062 (0.9)	0.457 ± 0.032 (2.9)
$42 \leq E_T < 53$ GeV	0.525 ± 0.074 (1.5)	0.441 ± 0.052 (1.3)	0.476 ± 0.059 (0.8)	0.556 ± 0.049 (2.7)
$53 \leq E_T < 64$ GeV	0.523 ± 0.077 (1.1)	0.755 ± 0.101 (1.1)	0.645 ± 0.085 (0.9)	0.672 ± 0.055 (2.8)
$64 \leq E_T < 74$ GeV	0.684 ± 0.167 (1.5)	0.606 ± 0.092 (2.2)	0.446 ± 0.065 (1.5)	0.584 ± 0.052 (2.1)
$74 \leq E_T < 83$ GeV	0.742 ± 0.165 (1.2)	0.508 ± 0.081 (1.4)	0.673 ± 0.099 (1.4)	0.646 ± 0.066 (2.8)
$83 \leq E_T < 93$ GeV	0.437 ± 0.084 (1.2)	0.722 ± 0.142 (1.2)	0.678 ± 0.109 (1.2)	0.647 ± 0.070 (2.3)
$93 \leq E_T < 105$ GeV	0.615 ± 0.135 (0.7)	0.906 ± 0.158 (1.8)	0.717 ± 0.131 (0.9)	0.778 ± 0.100 (1.8)
$105 \leq E_T < 150$ GeV	0.759 ± 0.292 (0.7)	0.859 ± 0.298 (0.7)	0.791 ± 0.352 (0.6)	0.711 ± 0.188 (1.2)

Table 5.1: Ratio $\phi/(\rho+\omega)$, per transverse momentum and transverse energy regions. In brackets the χ^2 per degree of freedom of the fit to the mass spectrum

5.1.2 $\frac{\phi}{\rho+\omega}$ as a function of P_T

The study of $\phi/(\rho+\omega)$ as a function of the transverse momentum is done fitting the mass spectra integrated in the transverse energy region $5 \leq E_T < 150$ GeV. But, because the contribution from lead-air originated events concentrates in the region of small transverse energies (a contribution that is very difficult to subtract) one studies also the mass spectra integrated in the region $42 \leq E_T < 150$ GeV.

Figure 5.4 shows the fits to the dimuon mass spectra, in 4 P_T regions, with integration in $5 \leq E_T < 150$ GeV. The corresponding fits in the integrated region $42 \leq E_T < 150$ GeV are presented in figure 5.5 .

The χ^2 per degree of freedom is much worse than the ones obtained from fits to the mass spectra per P_T and E_T regions (previous sub-section). The problem with these fits is the integration in a same mass spectrum of data from very different centrality regions, where there are different physics phenomena taking place. The fit function has not enough flexibility to adjust to this integration.

As can be seen in table 5.2 and figure 5.6, the ratio $\phi/(\rho+\omega)$ is approximately constant with the dimuon transverse momentum, taking into account the statistical errors.

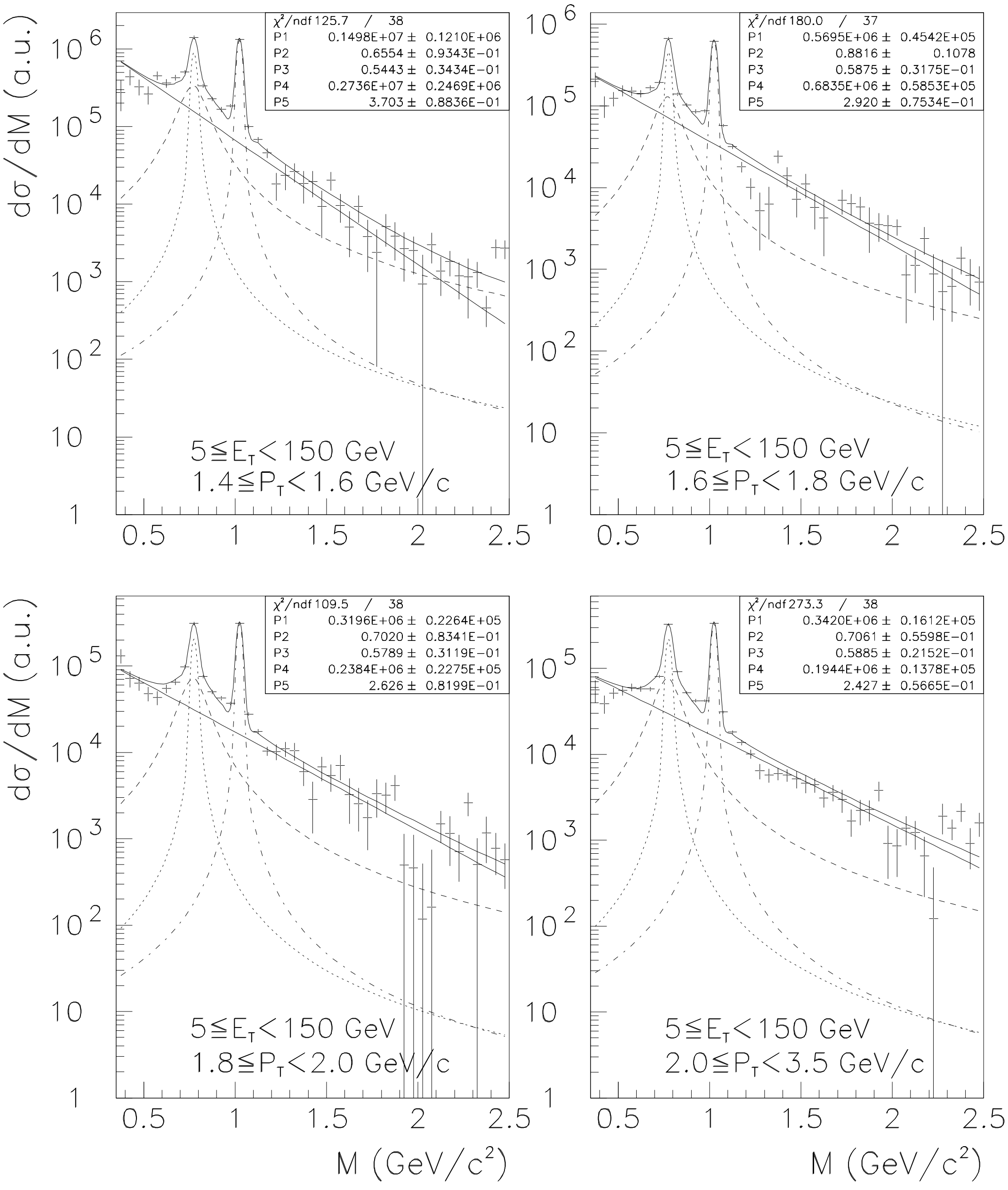

Figure 5.4: Fits to the dimuon mass spectra, in 4 P_T regions, integrated in $5 \leq E_T < 150$ GeV.

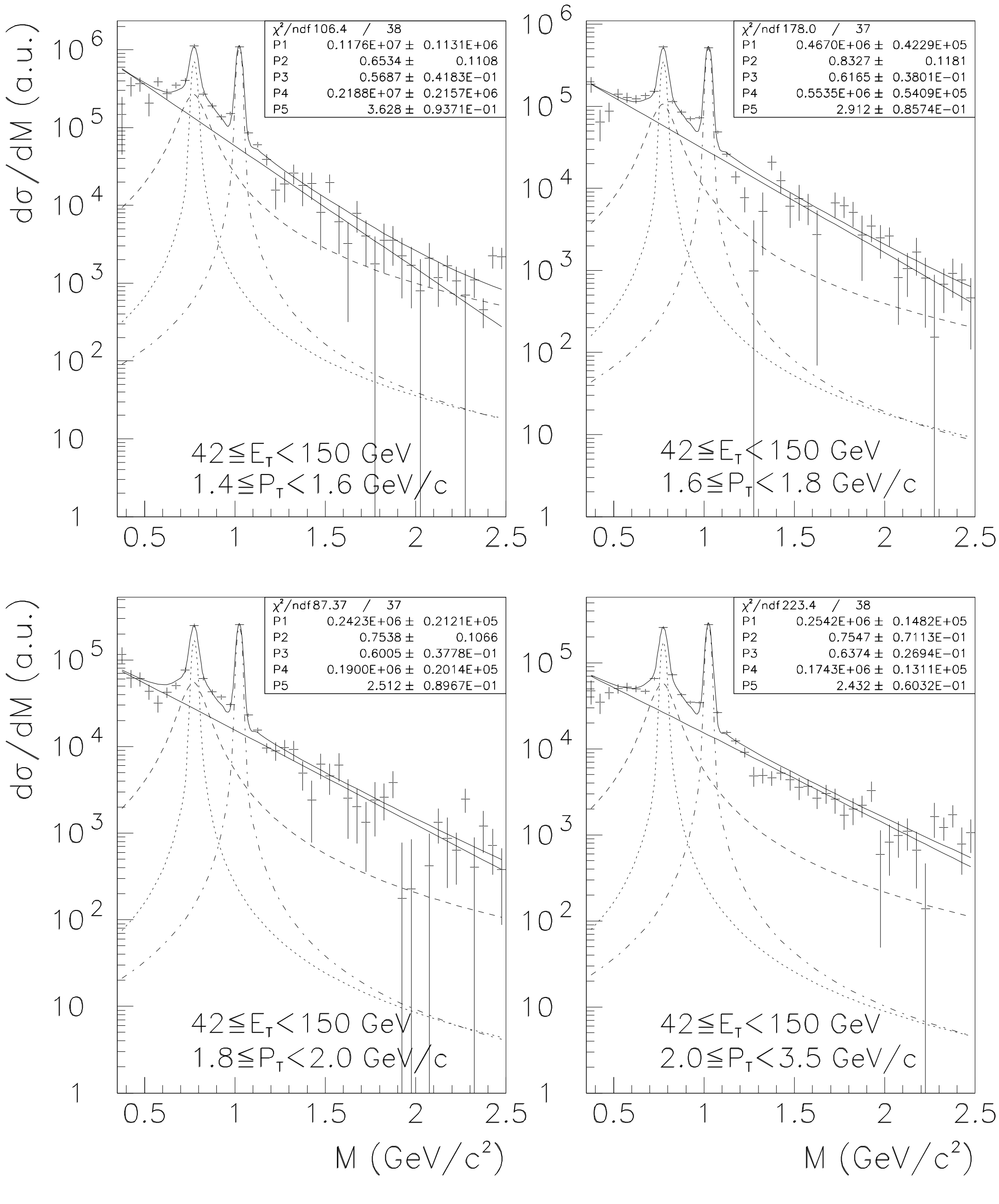

Figure 5.5: Fits to the dimuon mass spectra, in 4 P_T regions, integrated in $42 \leq E_T < 150$ GeV.

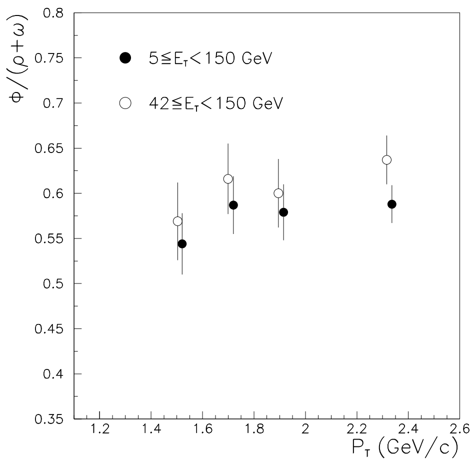

Figure 5.6: Ratios $\phi/(\rho+\omega)$ as a function of P_T, in the integrated regions $5 \leq E_T < 150$ GeV and $42 \leq E_T < 150$ GeV.

$\phi/(\rho+\omega)$ (χ^2/ndf)	$5 \leq E_T < 150$ GeV	$42 \leq E_T < 150$ GeV
$1.4 \leq P_T < 1.6$ GeV/c	0.544 ± 0.034 (3.3)	0.569 ± 0.043 (2.8)
$1.6 \leq P_T < 1.8$ GeV/c	0.587 ± 0.032 (4.9)	0.616 ± 0.039 (4.8)
$1.8 \leq P_T < 2.0$ GeV/c	0.579 ± 0.031 (2.9)	0.600 ± 0.038 (2.4)
$2.0 \leq P_T < 3.5$ GeV/c	0.588 ± 0.021 (7.2)	0.637 ± 0.027 (5.9)

Table 5.2: $\phi/(\rho+\omega)$ in 4 P_T regions, with the mass spectra integrated in 2 E_T regions.

5.1.3 $\frac{\phi}{\rho+\omega}$ as a function of E_T

The fits to the dimuon mass spectra in 9 transverse energy regions, and integrated in the transverse momentum region $1.4 \leq P_T < 3.5$ GeV/c, are presented in figure 5.7. The ratios $\phi/(\rho+\omega)$ obtained (table 5.3 and figure 5.7) increase with the transverse energy of the collisions, and saturate in the more central bins.

5.2 Temperatures of $\rho+\omega$ and ϕ

For every particle, the differential cross-section as a function of the transverse mass presents an universal scaling with M_T (or with P_T), as explained in Chapter 1. Thus,

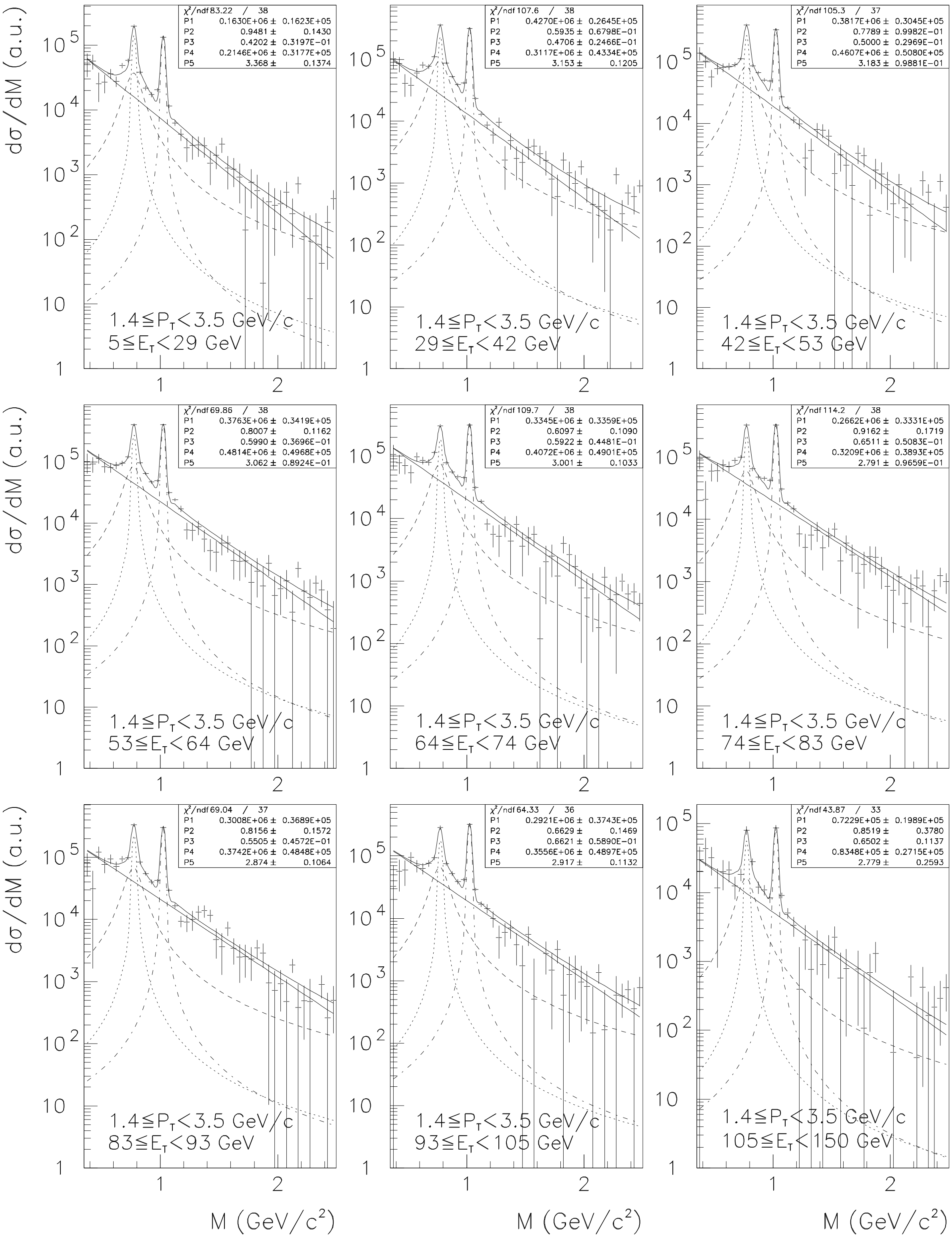

Figure 5.7: Fits to the dimuon mass spectra, in 9 E_T regions, and for the integrated region $1.4 \leq P_T < 3.5$ GeV/c.

$\phi/(\rho+\omega)$ (χ^2/ndf)	$1.4 \leq P_T < 3.5$ GeV/c
$5 \leq E_T < 29$ GeV	0.420 ± 0.032 (2.2)
$29 \leq E_T < 42$ GeV	0.471 ± 0.024 (2.8)
$42 \leq E_T < 53$ GeV	0.500 ± 0.030 (2.8)
$53 \leq E_T < 64$ GeV	0.599 ± 0.037 (1.8)
$64 \leq E_T < 74$ GeV	0.592 ± 0.045 (2.9)
$74 \leq E_T < 83$ GeV	0.651 ± 0.050 (3.0)
$83 \leq E_T < 93$ GeV	0.550 ± 0.046 (1.9)
$93 \leq E_T < 105$ GeV	0.662 ± 0.059 (1.8)
$105 \leq E_T < 150$ GeV	0.650 ± 0.109 (1.3)

Table 5.3: $\phi/(\rho+\omega)$ in 9 E_T regions, for the mass spectra integrated in $1.4 \leq P_T < 3.5$ GeV/c.

the inverse slope of the transverse mass distribution, also called effective temperature, characterises each particle.

The signal event distributions as a function of the dimuon mass, corrected for acceptance and smearing, are fitted with a five free parameters function describing all the expected physics contributions:

$$\mathcal{F} = P_1 BW_\rho + P_2 BW_\omega + P_3 BW_\phi + P_4 \; exp(-P_5 M) \tag{5.3}$$

where P_1, P_2 and P_3 are the number of vector-mesons ρ, ω and ϕ, respectively (the free parameters give directly the number of particles produced, since the classical Breit-Wigner fitting functions are already normalised to unity). Using function (5.3) instead of (5.2) has the advantage that the error of each parameter P_1, P_2 and P_3 is already the statistical error on the number of resonant events (thus avoiding calculations using the correlation between parameters).

5.2.1 The inverse slope from the M_T distribution

The 4 P_T regions considered in this analysis correspond to different dimuon transverse mass regions for the resonances $\rho + \omega$ or ϕ. This is a direct consequence of the M_T definition $M_T = \sqrt{M^2 + P_T^2}$. Table 5.4 shows each region limits, translated into M_T intervals.

ΔM_T (GeV/c^2)	$\rho + \omega$	ϕ
$1.4 \leq P_T < 1.6$ GeV/c	$1.60 \leq M_T < 1.78$	$1.73 \leq M_T < 1.90$
$1.6 \leq P_T < 1.8$ GeV/c	$1.78 \leq M_T < 1.96$	$1.90 \leq M_T < 2.07$
$1.8 \leq P_T < 2.0$ GeV/c	$1.96 \leq M_T < 2.14$	$2.07 \leq M_T < 2.24$
$2.0 \leq P_T < 3.5$ GeV/c	$2.14 \leq M_T < 3.58$	$2.24 \leq M_T < 3.64$

Table 5.4: Dimuon transverse mass regions for the resonances $\rho + \omega$ and ϕ.

From the fit to the mass spectra integrated in transverse energy ($5 \leq E_T < 150$ GeV), one obtains the number of resonant events $\rho+\omega$ and ϕ, produced in the acceptance window given in section 3.6, in each one of the 4 transverse momentum regions.The event numbers are normalised to the width of the transverse mass interval where they were fitted (table 5.5, the errors being only statistical).

Events/M_T	$\int \frac{d\sigma(\rho+\omega)}{dM_T} dM_T/\Delta M_T$	$\int \frac{d\sigma(\phi)}{dM_T} dM_T/\Delta M_T$
$1.4 \leq P_T < 1.6$ GeV/c	$(139.620 \pm 8.390) \times 10^5$	$(81.626 \pm 3.518) \times 10^5$
$1.6 \leq P_T < 1.8$ GeV/c	$(58.904 \pm 3.000) \times 10^5$	$(36.711 \pm 1.329) \times 10^5$
$1.8 \leq P_T < 2.0$ GeV/c	$(29.385 \pm 1.503) \times 10^5$	$(17.873 \pm 0.670) \times 10^5$
$2.0 \leq P_T < 3.5$ GeV/c	$(4.053 \pm 0.135) \times 10^5$	$(2.452 \pm 0.062) \times 10^5$

Table 5.5: Number of events $\rho+\omega$ e ϕ produced in the acceptance window given in section 3.6, in each P_T region, and normalised to the width of the corresponding region in M_T. Spectra integrated in $5 \leq E_T < 150$ GeV.

The universal scaling of the differential resonance's production cross-sections with the transverse mass is described by a modified Bessel function, according to equation (1.7) from Chapter 1.

For particles with mass not too large and momentum not too low, as is the case here, equation (1.7) can be approximated by:

$$\frac{d\sigma}{dM_T} \propto M_T^{3/2}\ exp(-M_T/T) \quad . \tag{5.4}$$

This expression allows to fit the transverse mass distributions for $\rho + \omega$ and ϕ (table 5.5) and obtain the parameter T. In figure 5.8 the fits to cross-sections [2] of the resonances as a function of the transverse mass are shown. The fits use the method of the areas' difference minimisation. The integral of events in each region is compared to the integral defined by the fit function in the same transverse mass limits. The abscissa

[2] Apart from normalisation factors, these are in fact differential cross-sections, given in arbitrary units.

from figure 5.8 is not an ingredient in the fit, but is calculated a posteriori, from the fit function obtained. These abscissas correspond to the k points verifying:

$$\frac{d\sigma}{dM_T}(k) = \frac{\int \frac{d\sigma}{dM_T} dM_T}{\Delta M_T} \quad . \tag{5.5}$$

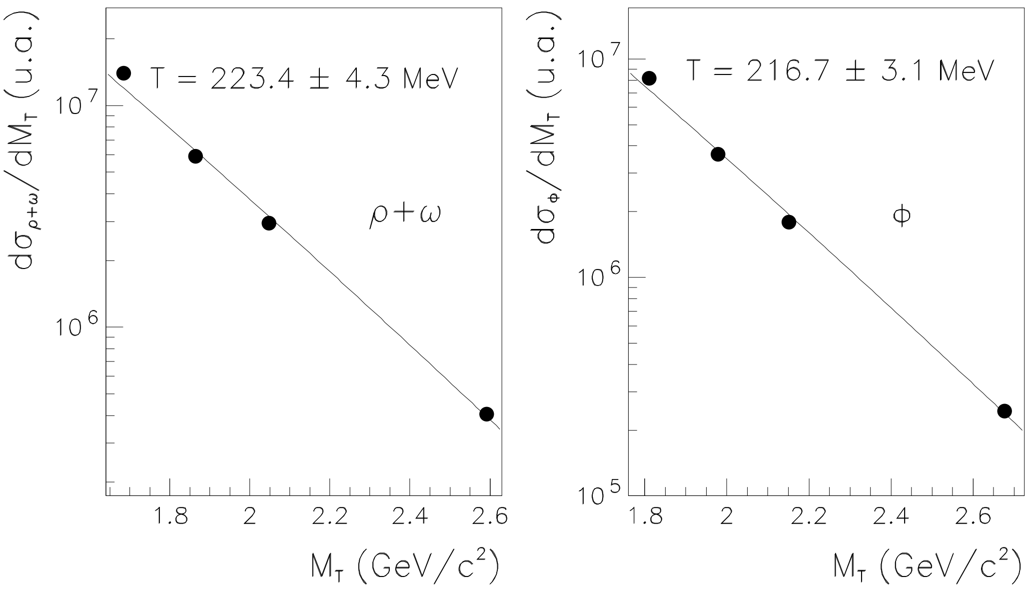

Figure 5.8: Fit to the $\rho + \omega$ and ϕ cross-sections, as a function of the dimuons transverse mass. Data integrated in $5 \leq E_T < 150$ GeV.

In this way one obtains the effective temperatures $T(\rho + \omega) = 223.0 \pm 4.5$ MeV and $T(\phi) = 217 \pm 3.5$ MeV. But, as can be easily seen in figure 5.8, the quality of these fits is not good. The experimental errors included are too small, reason why the χ^2 of the fits are very large. This is due to the fact that only statistical errors were included, and these are very small since the number of resonant events is large. The correct evaluation of the temperatures requires an estimate of the systematic errors, namely those that depend on the transverse momentum (or transverse mass). This study will be presented ahead in this chapter.

5.2.2 Temperatures as a function of centrality

The event distributions as a function of the dimuon mass, per transverse momentum and transverse energy regions allow the study of the temperature as a function of the centrality (figures 5.9, 5.10, 5.11 and 5.12).

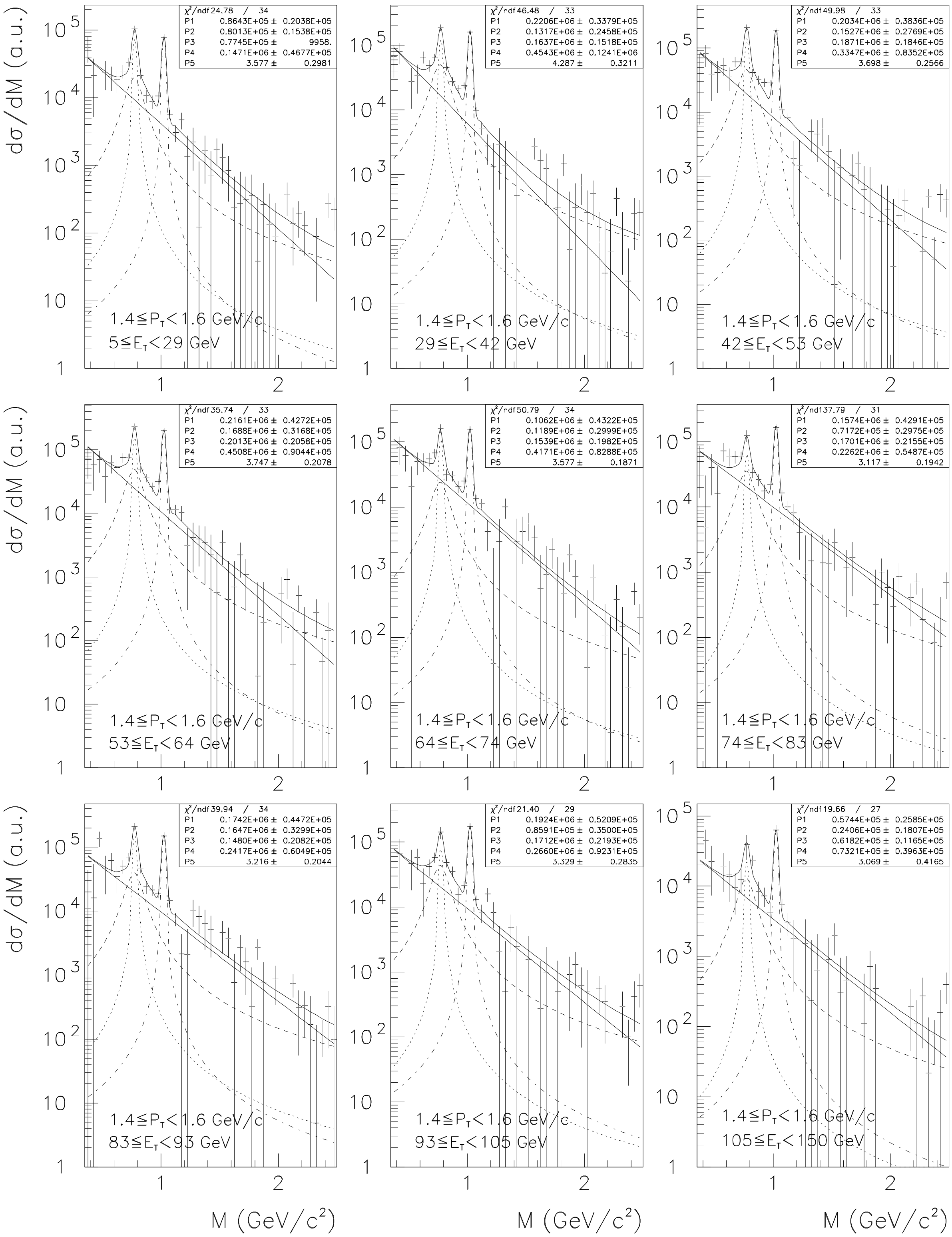

Figure 5.9: Fit to the mass spectra, for temperature studies, per E_T bins in the region $1.4 \leq P_T < 1.6$ GeV/c.

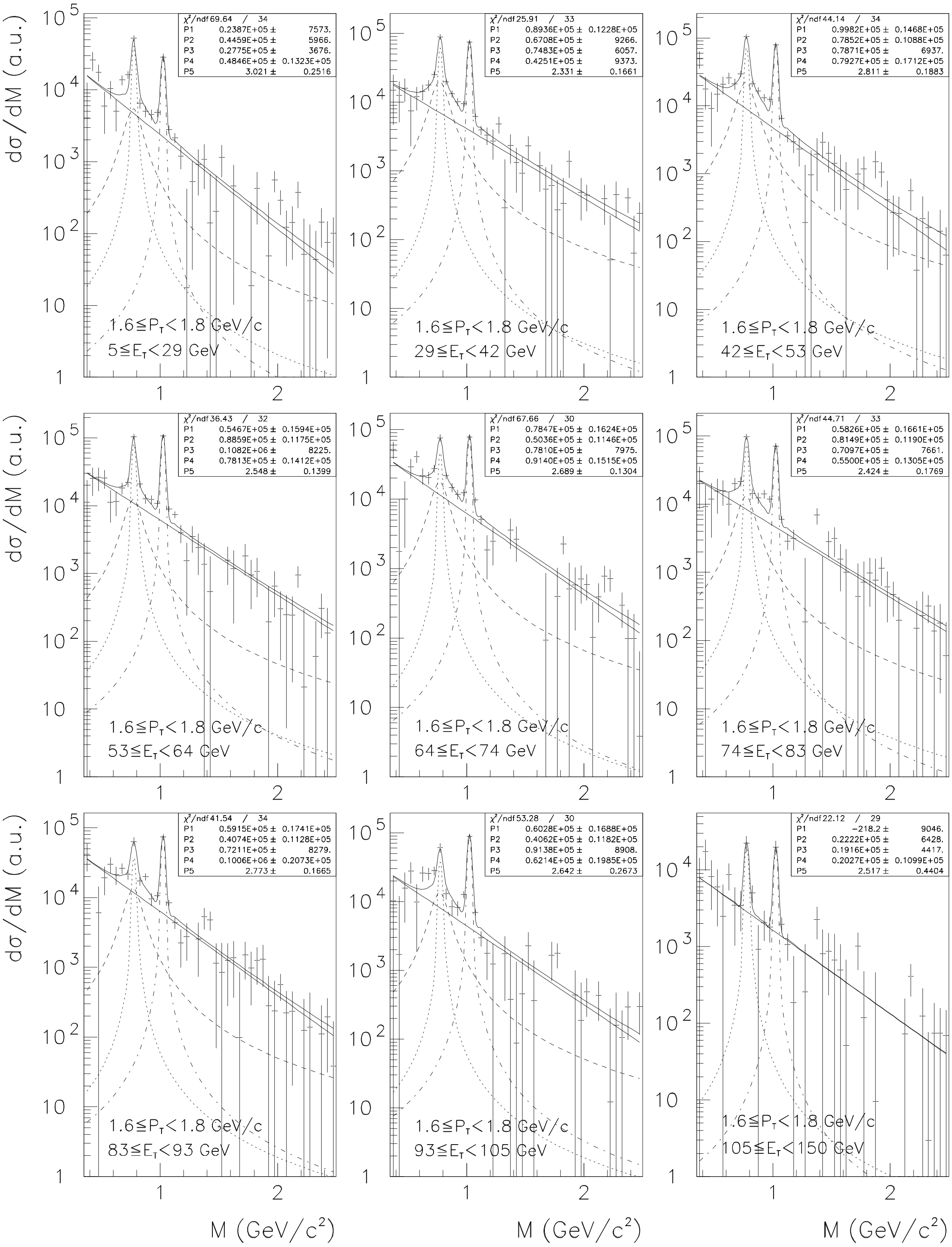

Figure 5.10: Fit to the mass spectra, for temperature studies, per E_T bins in the region $1.6 \leq P_T < 1.8$ GeV/c.

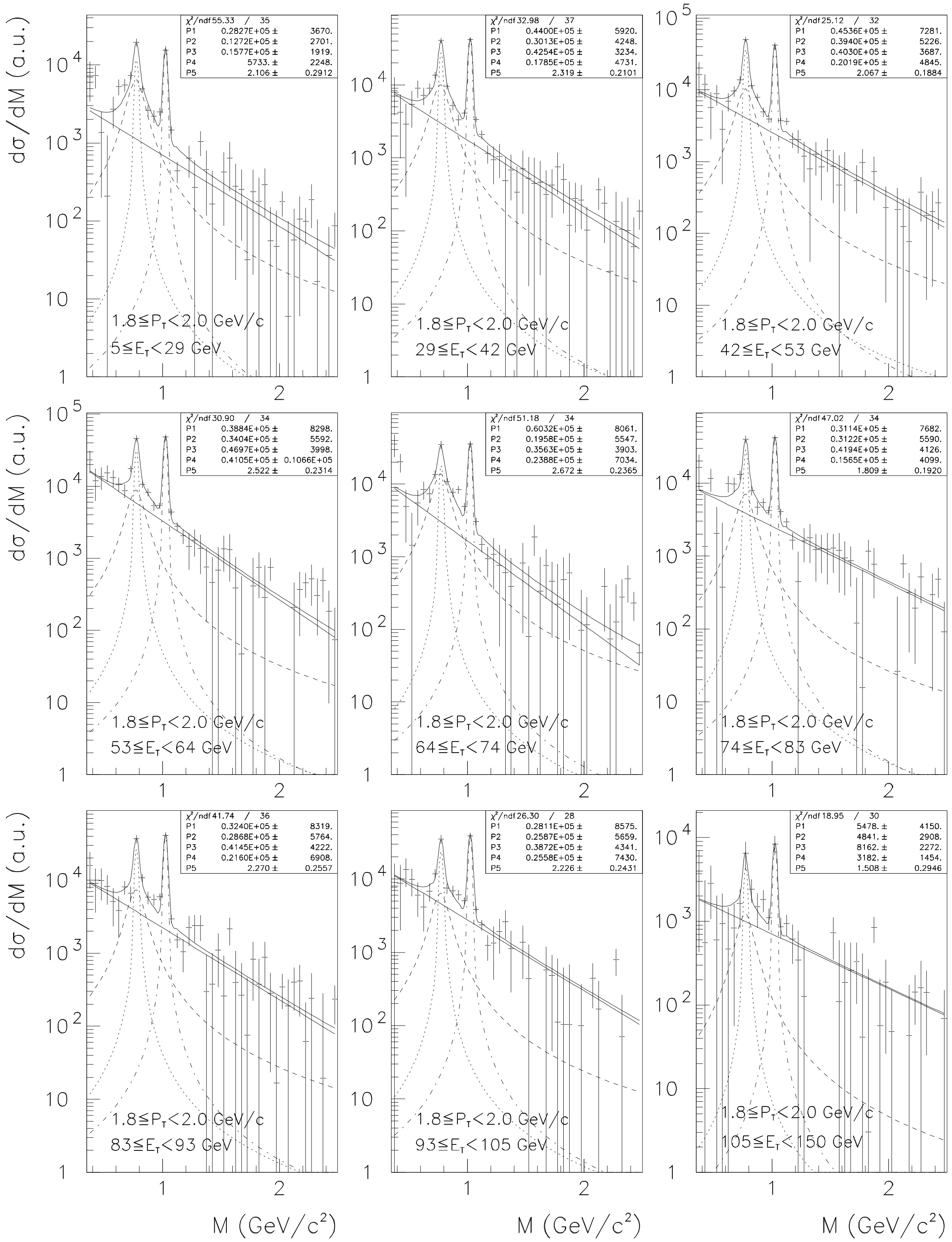

Figure 5.11: Fit to the mass spectra, for temperature studies, per E_T bins in the region $1.8 \leq P_T < 2.0$ GeV/c.

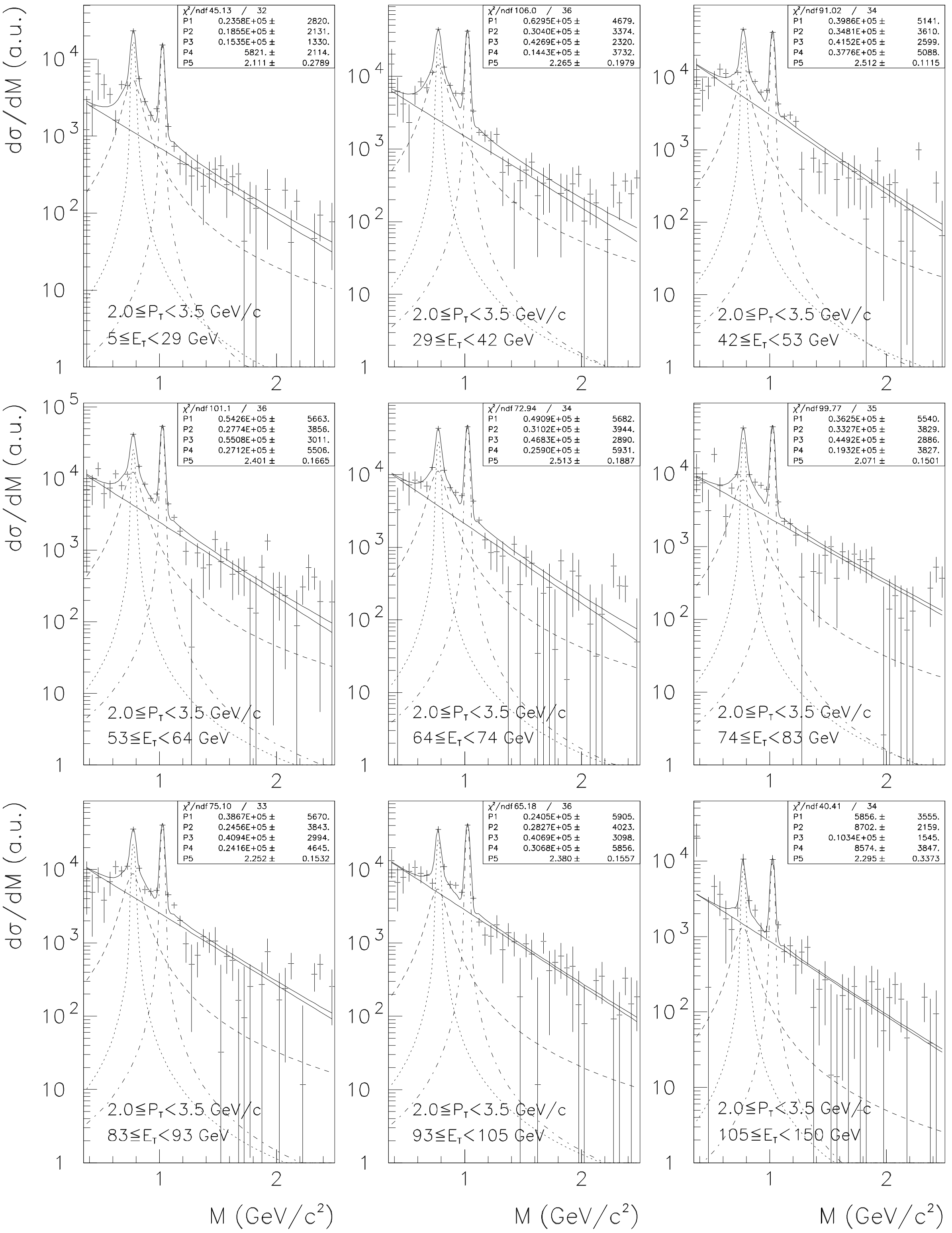

Figure 5.12: Fit to the mass spectra, for temperature studies, per E_T bins in the region $2.0 \leq P_T < 3.5$ GeV/c.

T (MeV)	$\rho + \omega$	ϕ
$5 \leq E_T < 29$ GeV	230.3 ± 11.0	206.6 ± 9.9
$29 \leq E_T < 42$ GeV	235.2 ± 9.4	218.4 ± 6.7
$42 \leq E_T < 53$ GeV	207.7 ± 8.6	209.8 ± 7.2
$53 \leq E_T < 64$ GeV	222.5 ± 11.1	217.7 ± 7.1
$64 \leq E_T < 74$ GeV	241.9 ± 13.3	231.0 ± 9.7
$74 \leq E_T < 83$ GeV	229.6 ± 13.5	225.2 ± 9.2
$83 \leq E_T < 93$ GeV	219.8 ± 14.2	220.3 ± 9.4
$93 \leq E_T < 105$ GeV	213.9 ± 15.6	206.3 ± 8.4
$105 \leq E_T < 150$ GeV	223.8 ± 39.0	198.5 ± 17.7

Table 5.6: Effective temperatures for $\rho + \omega$ and ϕ, per E_T regions.

From the number of $\rho + \omega$ and ϕ events in each transverse mass interval, normalised to the width of the interval, and calculated in each transverse energy region, one obtains the temperatures, using the method already explained. Table 5.6 presents temperatures for $\rho + \omega$ and ϕ, as a function of centrality. In sub-section 5.5.4 the systematic errors are evaluated and figure 5.31 presents the temperatures of $\rho + \omega$ and ϕ as a function of the centrality, with systematics included.

From these results one concludes that $T_{\rho+\omega}$ and T_ϕ are the same, within statistical errors, although there seems to be a tendency for the $\rho + \omega$ temperature to be slightly higher than the ϕ one. The temperatures do not depend on the centrality.

Once more, the fact that the differential cross-sections in transverse mass were used with only statistical errors included means that these temperatures have to be taken with caution. The systematic errors study is crucial to obtain meaningful temperatures.

5.3 $\rho + \omega$ and ϕ multiplicities

In section 5.1 it is shown that $\phi/(\rho + \omega)$ increases with the collisions' centrality. In order to clarify if this increase correspond to an enhanced production of the ϕ or to a reduced production of the $\rho + \omega$, the study of these resonances' multiplicities in lead collisions is now presented.

The $\rho + \omega$ and the ϕ multiplicity, defined as the number of resonant events per collision, is obtained by comparing the total number of resonant events with the total number of produced hadrons, in the same transverse energy region. This last quantity is evaluated from the minimum bias spectrum[3].

[3]The events obtained with trigger minimum bias are those where only a minimum amount of energy deposited in the ZDC is required. Thus, events corresponding to a certain hadronic cross-section, where at least a pion is produced (i.e. of the generic form $AB \to \pi X$).

5.3.1 The minimum bias events distribution

Theoretically, the distribution of minimum bias events (MB) as a function of the transverse energy is given by the expression:

$$\frac{dN^{MB}}{dE_T} \propto \int 2\pi b(1 - P(0,b)) \cdot P(E_T, b)db \tag{5.6}$$

where the factor $(1 - P(0,b))$ corresponds to ask for at least one nucleon-nucleon collision to occur with impact parameter b; and $P(E_T, b)$ is the probability of measuring the transverse energy E_T when having a collision with impact parameter b (as can be seen equivalently in equation (B.19) from Appendix B). This probability has a Gaussian distribution like in equation (B.20), with a mean value $\langle E_T \rangle$ proportional to the number of participant nucleons in the collision:

$$\langle E_T(b) \rangle = qN_{part}(b) \quad , \tag{5.7}$$

and with a width D:

$$D = wq^2 N_{part}(b) \quad . \tag{5.8}$$

The parameters w and q are obtained fitting the experimental MB distribution as a function of the transverse energy. N_{part} is calculated for each impact parameter b, with the Glauber model [86], as explained in Appendix B. For the Glauber calculations one uses the inelastic cross-section for nucleon-nucleon collisions $\sigma_o = 30$ mb [9], and the Woods-Saxon nuclear density profiles, with nuclear density $\rho_o = 0.16$ fm^{-3}. Using an integration step of 0.2 fm, one obtains the correlation between N_{part} and b shown in figure 5.13.

In this study, only the MB events originated in the target region are considered (NOCIBI=4 selection), so that we can compare the dimuons with the produced hadrons. The diagonal cut is also applied to the MB, so that the acceptance in the correlation E_T *vs* E_{ZDC} is the same as for dimuons. Due to the huge beam intensity of this data taking, 5.5×10^7 ions/burst, the MB trigger rate was too high. Thus, a pre-scaling factor was used when recording these events — only 10% of the total amount of data recorded correspond to MB triggers [76]. The pre-scaling factor used in this analysis was calculated from the ratio between the number of dimuon events identified with MB trigger and those identified with dimuon trigger. This way, one obtains $f_{pres} = (1.285 \pm 0.077) \times 10^{-5}$. This pre-scaling factor corresponds to a mean value, the pre-scaling value itself was changed several times during the data taking. The systematic error of this mean value cannot be estimated, due to the lack of enough information to calculate absolute cross-sections.

Figure 5.14 shows the MB data accepted and used in this analysis (corresponding to the same runs used in the $\rho + \omega$ and ϕ study).

The fit to the MB spectrum is done using equations (5.7) and (5.8). Although the number of participant nucleons has been calculated with a step of 50 fm in the impact

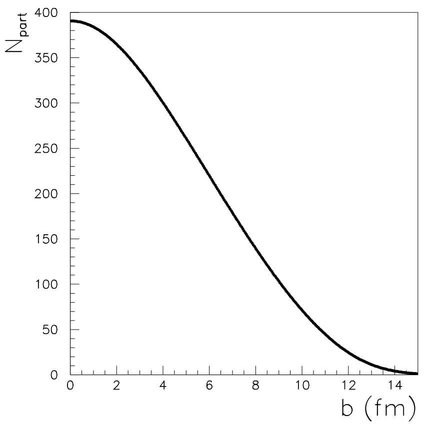

Figure 5.13: Correlation N_{part} versus b for Pb+Pb collisions at 158 GeV/nucleon, using the Glauber model with Woods-Saxon nuclear density profiles (given in [7]).

parameter evaluation, the E_T spectrum fitted has a bin width of 5 GeV, in order to be in agreement with the experimental resolution in energy. The fitted region is $80 \leq E_T < 130$ GeV, allowing at the same time a good covering of the "knee" region (very important for the q parameter evaluation); and to avoid the known distortions in the MB energy spectrum. These distortions are due to inefficiencies in the target recognition algorithm; to that fact that no "empty-target" subtraction was done; and also, for the data taken in 1996 and 1998, to a synchronisation problem between the MB trigger and the dimuon trigger [87]. The fit is presented in figure 5.15, the values q e w being obtained:

$$q = 0.2820 \pm 0.0002 \; GeV \qquad w = 1.28 \pm 0.02 \; GeV^{-1} \quad . \tag{5.9}$$

This q parameter is similar to the one obtained with another data selection ($q = 0.2809 \pm 0.0002$, [87]); while the parameter w is smaller (in that analysis the value obtained was $w = 1.45 \pm 0.03$ GeV^{-1}), due to the different diagonal cuts used: the one used in this analysis is much more restrictive, rejecting on the transverse energy distribution the Gaussian tails at 2σ (see section 3.4).

The problem identified in the synchronisation of the MB trigger with the dimuon trigger distorts the transverse energy scale measured. This problem was studied in [87], and evaluated to be:

$$E_T(2\mu \; 98) = 0.968 \; E_T(MB \; 98) \tag{5.10}$$

The difference between the two E_T scales is taken into account when applying the diagonal cut to the MB events. The diagonal bands used for the selection of dimuon events are translated into the MB $E_T(MB)$ vs E_{ZDC} scale.

Finally, the number of participant nucleons is calculated according to equation (5.7 and taking into account the trigger synchronisation problem and according to equation

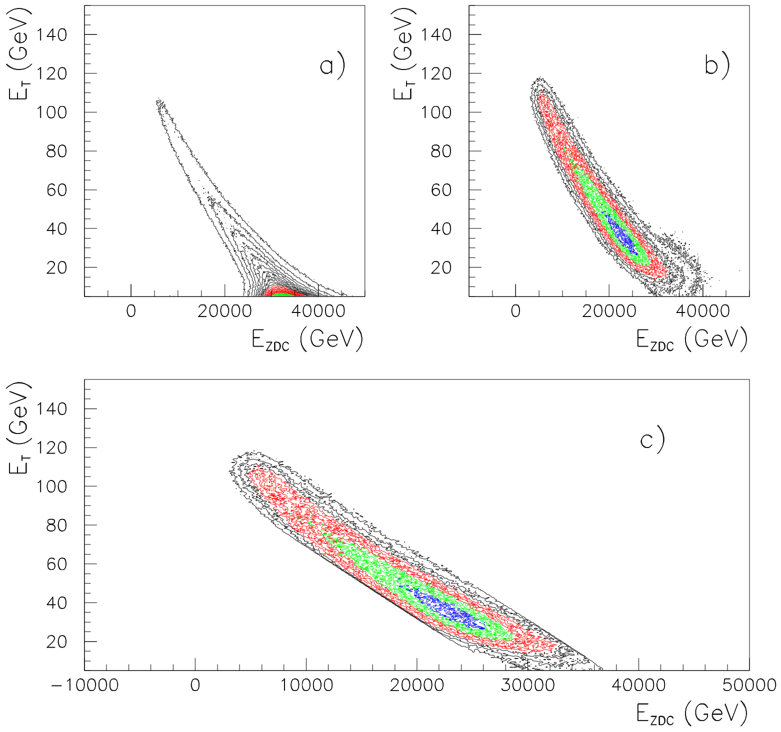

Figure 5.14: Correlation E_T *vs* E_{ZDC} for MB events (a); with NOCIBI=4 selection (b); and after diagonal cut (c).

(5.7):

$$E_T = 0.273\ N_{part} \quad . \tag{5.11}$$

5.3.2 Multiplicities measurement

The ϕ multiplicity per event is the ratio between the produced ϕs and the total number of produced particles, in the same transverse energy of the collisions interval; and the same way for $\rho+\omega$:

$$Mult^R = \frac{\frac{1}{BR_{\mu\mu}\ \epsilon^{\mu\mu}_{trig}\ \epsilon^{\mu\mu}_{2\mu}} \int \frac{d^2N^R}{dM_T dE_T}\ dM_T\ dE_T}{\frac{1}{\epsilon^{MB}_{trig}\ f_{pres}} \int \frac{dN^{MB}}{dE_T}\ dE_T} \tag{5.12}$$

The total number of events produced is calculated from the MB events, corrected with the pre-scaling factor $f_{pres} = (1.285 \pm 0.077) \times 10^{-5}$ and the MB trigger efficiency

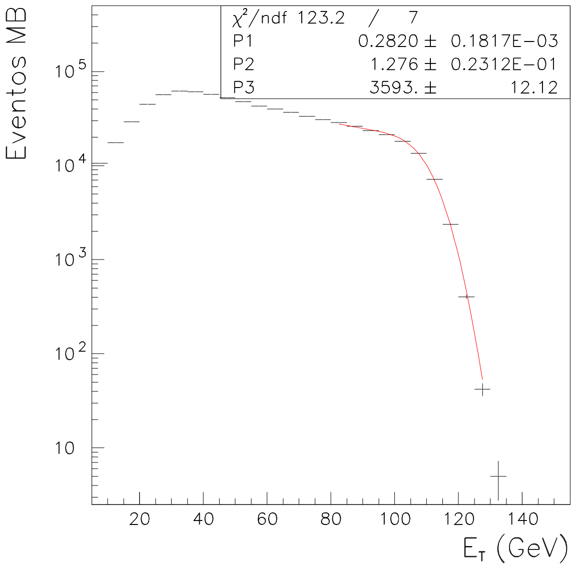

Figure 5.15: Distribution of MB events as a function of the transverse energy, with NOCIBI=4 selection and after diagonal cut.

ϵ_{trig}^{MB}. The number of ϕs is also evaluated including its branching ratio into dimuons, the reconstruction efficiency for dimuons $\epsilon_{2\mu}^{\mu\mu}$, and the dimuon trigger efficiency $\epsilon_{trig}^{\mu\mu}$.

The dimuon trigger efficiency information is obtained from special runs, using the coincident signals from the trigger hodoscopes P1 and P2 (see Chapter 2). In 1998 this efficiency was $\epsilon_{trig}^{\mu\mu} = 88.4 \pm 0.4\%$ [88]. The reconstruction efficiency is $\epsilon_{2\mu}^{\mu\mu} = 98.0 \pm 0.4\%$ [89]. The MB trigger efficiency is considered to be 100%.

The branching ratio of the ϕ into dimuons is presented in table 1.1. Since the branching ratio of the ω into dimuons has not been directly measured yet, its value is obtained indirectly, by assuming that $\frac{BR_{\mu\mu}^{\omega}}{BR_{mu\mu}^{\rho}} = \frac{BR_{ee}^{\omega}}{BR_{ee}^{\rho}} = 1.575 \pm 0.088$, and thus $BR_{\mu\mu}^{\rho+\omega} = (5.92 \pm 0.30) \times 10^{-5}$. Figure 5.16 presents the $\rho + \omega$ and ϕ multiplicities in the regions $3 \leq Y < 4$ and $1.4 \leq P_T < 3.5$ GeV/c, using the target selection given by NOCIBI.

The trend of the resonances' multiplicity per participant allows to check which of the resonances is responsible for the increase in the ratio $\phi/(\rho + \omega)$. This trend shows an excess production, as compared to the simple superposition of nucleon-nucleon collisions.

The multiplicity per participant as a function of the number of participant nucleons is shown in figure 5.17. From the fit with a straight line one can observe that the $\rho + \omega$ slope is compatible with zero, while for the ϕ there is an increase with N_{part} [4]. So we

[4]For the ϕ, the horizontal fit has χ^2/ndf=1.74, considerably worse than the value obtained when the slope is also let free (in that case χ^2/ndf= 1.07).

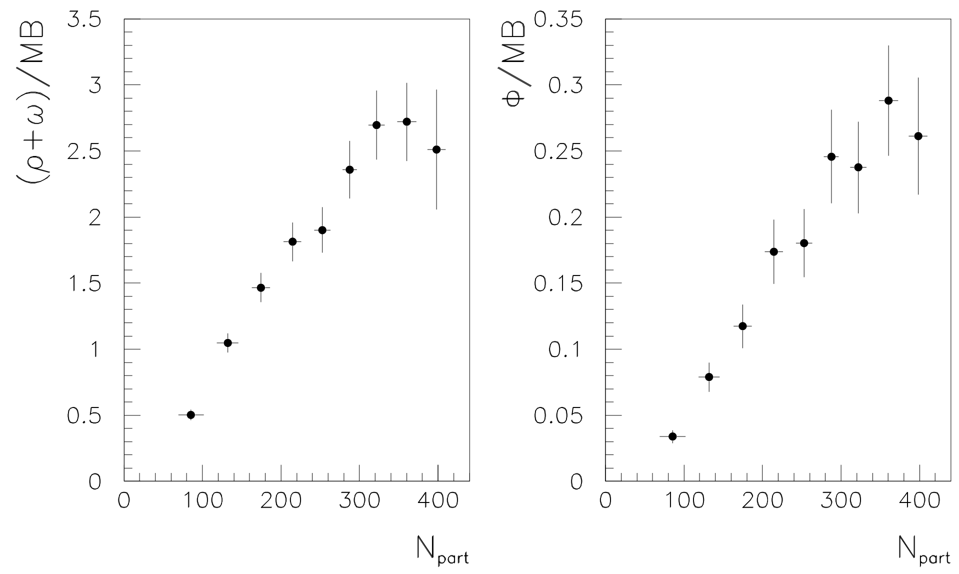

Figure 5.16: Multiplicities of $\rho + \omega$ and ϕ, evaluated in the regions $3 \leq Y < 4$ and $1.4 \leq P_T < 3.5$ GeV/c.

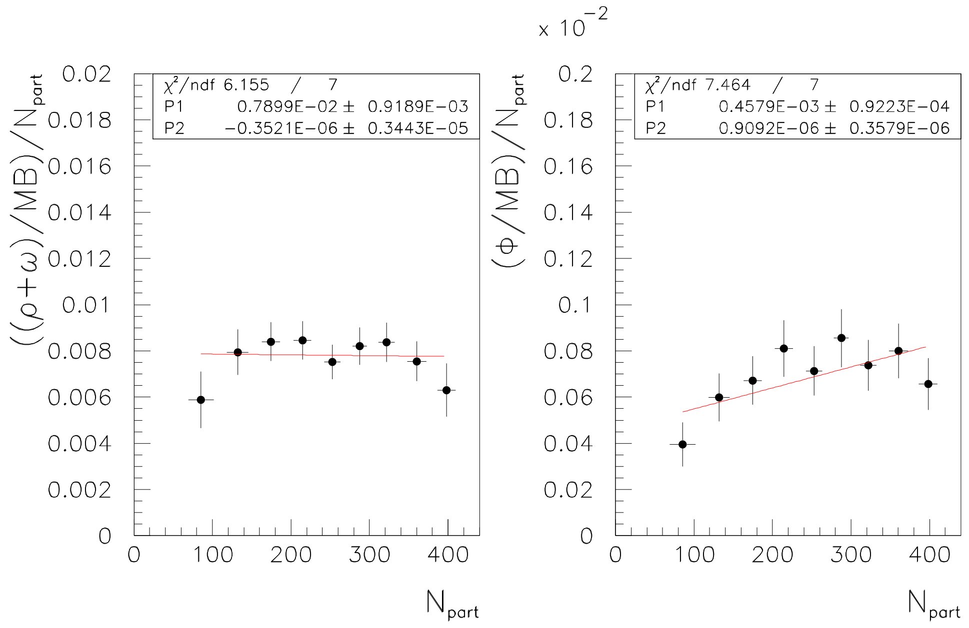

Figure 5.17: Multiplicities per participant of $\rho + \omega$ and ϕ, as a function of the number of participants. Fit with a straight line $y = P_1 + P_2 x$.

Events	Selection NOCIMD
Dimuon Triggers	16.2×10^6
After NOHALO cut	15.2×10^6
After pile-up cut	10.8×10^6
After image cut	4.88×10^6
NOCIMD=4 selection	3.12×10^6
After kinematical cuts	3.03×10^6
After diagonal cut	2.37×10^6
After $P * Dtarget$ cut	2.18×10^6

Table 5.7: Pb+Pb 1998 data statistics, with NOCIMD selection. Sum of the dimuons $+-$,$++$ and $--$.

conclude that there is an enhanced production of the ϕ in central lead-lead collisions, higher than expected from the simple superposition of nucleon-nucleon collisions.

5.4 Other data selections and respective analysis

In the experiment NA50 there is a certain degree of redundancy and/or complementarity in the information given by the several sub-detectors. For example in the case of the two calorimeters, the electromagnetic and the ZDC, these complement each other, making it possible to check the events quality through the correlation between the energy deposited by the spectator particles in the ZDC and the neutral transverse energy of the produced particles deposited in the electromagnetic calorimeter. In the same sense, there is also the possibility to confirm the information given by the target recognition algorithm using the active target system (NOCIBI selection) by comparing it with the information from the multiplicity detector, placed near the target (selection NOCIMD).

5.4.1 Selection NOCIMD

An event selection based in the interaction target identification given by the multiplicity detector is also studied and presented here. This identification method is globally less efficient than the active target system, but it has a better efficiency than NOCIBI to identify peripheral interactions. Asking for NOCIMD=4 means that the "interaction vertex" found by the MD must point to the sub-target position 4.

Table 5.7 presents the statistics used for the analysis with NOCIMD selection. In this case, only 297 runs are analysed[5], to be compared with the NOCIBI selection statistics, given previously in table 3.1 .

[5]The MD detector information is not available for the runs **7041** to **7130**, since there were optimisation tests of the MD being done during these runs. Also runs **7180** to **7230** cannot be analysed due to problems

θ (mrad)	σ	x_o	χ^2/ndf
3.69	8.64	121.10	20.05
3.59	8.63	119.76	20.02
3.49	**8.60**	**118.37**	**12.94**
3.39	8.71	117.01	13.92
3.29	8.89	115.62	12.49

Table 5.8: Minimisation of the Gaussian width σ fitted in the transverse projection of the E_T *vs* E_{ZDC} correlation, for the NOCIMD selection.

The kinematical cuts applied are the same as for the NOCIBI selection. On the contrary, the diagonal and $P * Dtarget$ cuts have to be tuned for this new data set.

The rotation method explained in Chapter 3 is used to obtain the diagonal bands containing the E_T *vs* E_{ZDC} correlation at 2σ. Table 5.8 shows the results from the optimisation procedure on the rotation angle to find the longitudinal axis of the correlation. The transversal projection is then shown in figure 5.18, together with the cut diagonals. Thus, the diagonal cut in the correlation between the neutral transverse energy of the produced particles and the energy deposited by the spectator particles, with the NOCIMD event selection, is:

$$(101.17 - 3.49 \times 10^{-3} E_{ZDC}) < E_T < (135.58 - 3.49 \times 10^{-3} E_{ZDC}) \quad . \tag{5.13}$$

The $P * Dtarget$ cut is tuned with the procedure already explained in Chapter 3. The selection Prob$(\chi^2_{pdtgt}) \geq 3\%$ proves to be enough to ensure an horizontal distribution. Figure 5.19 shows the probability distributions Prob(χ^2_{pdtgt}), for convergent and divergent tracks, from opposite sign dimuons with $M \geq 3$ GeV/c^2, used to decide the percentage of cut to apply.

The events identified by the MD detector with origin in-target are shown in figure 5.20 as a function of the reconstructed vertex, before and after $P * Dtarget$ cut at 3%. The distribution is narrowed by this cut, and the mean value is shifted towards the real position of the sub-target (placed at ZVertex≈ -45 cm). After background subtraction this shift is even more obvious, since the background events are not produced in-target, but come mostly from pions and kaons produced in the target that decay later into muons.

Table 5.9 presented the statistics for signal events with selection NOCIMD, per P_T and E_T regions. As can be seen in figure 5.21, this analysis has less 38% statistics than the one with selection NOCIBI. although, it has the advantage that it identifies more peripheral events. In the transverse energy region $5 \leq E_T < 29$ GeV the NOCIMD selection identifies 42% more events than the active target system selection (in the integrated region $1.4 \leq P_T < 3.5$ GeV/c).

As explained in section 5.1, fitting the dimuon mass spectra corrected from acceptance and smearing, the ratios $\phi/(\rho + \omega)$ are obtained in each transverse momentum and

in the MD performance.

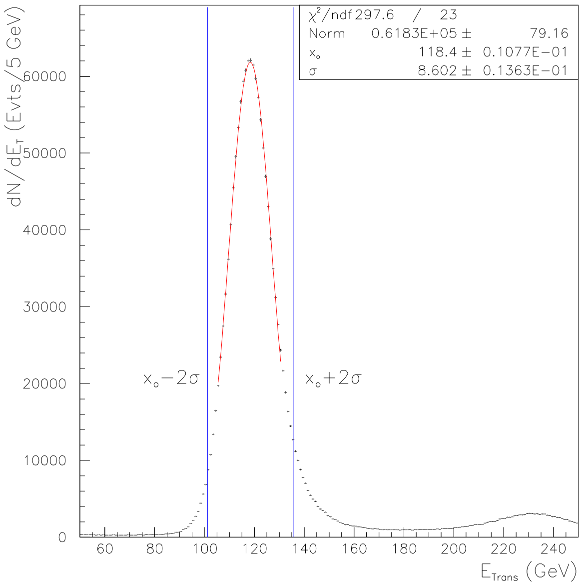

Figure 5.18: Gaussian fit to the transverse projection of the E$_T$ *vs* E$_{ZDC}$ correlation, for the NOCIMD selection.

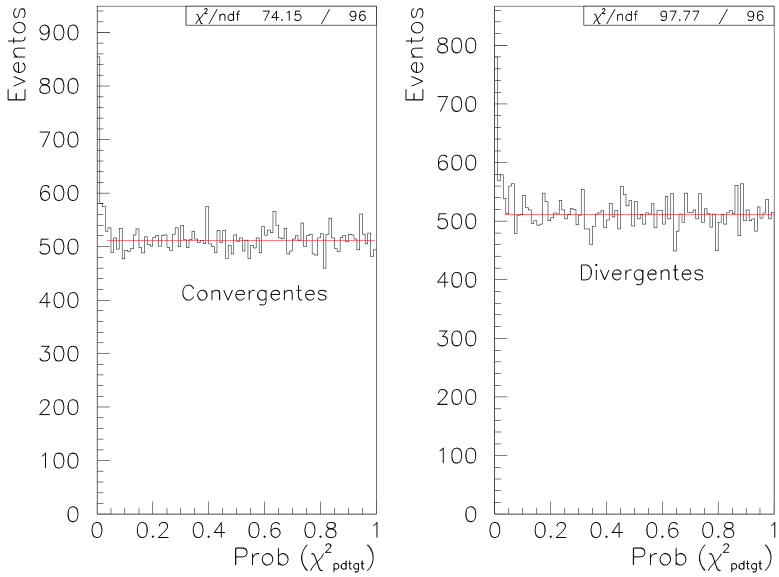

Figure 5.19: χ^2 probability of $(P * Dtarget)^2$, for convergent and divergent tracks. Event selection including $\mu^+\mu^-$ with $M \geq 3$ GeV/c^2 and NOCIMD=4.

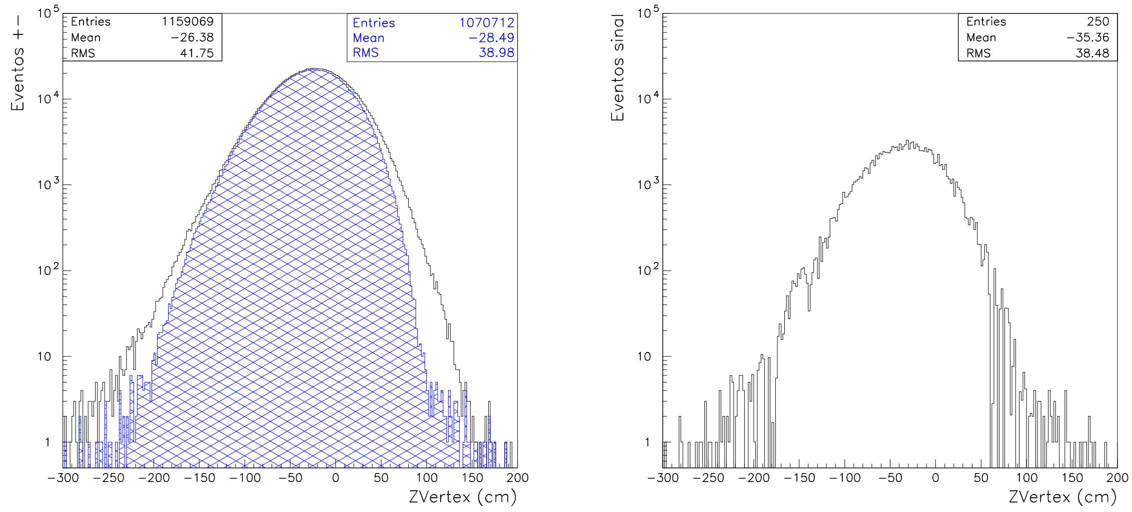

(a) (b)

Figure 5.20: Reconstructed vertex distribution, for $\mu^+\mu^-$ events with $M < 2.5$ GeV/c^2, and selected with NOCIMD (a). Superimposed are the distributions before and after $P * Dtarget$ cut at 3%. Reconstructed vertex distribution for the corresponding signal events after cuts.

transverse energy region. Table 5.10 shows the ratios $\phi/(\rho+\omega)$ for the data integration in the region $5 \leq E_T < 150$ GeV.

From these results one can conclude that the ratio does not depend on the dimuon transverse momentum. The values obtained are very similar to the ones from the analysis with NOCIBI selection, as can be seen in figure 5.22 . The errors quoted in table 5.10 are only statistical errors. They are bigger than the ones from the NOCIBI selection analysis since in this case the statistics is smaller.

The ratios $\phi/(\rho+\omega)$ in 9 transverse energy regions, for the data integrated in $1.4 \leq P_T < 3.5$ GeV/c with NOCIMD selection are shown in table 5.11 and figure 5.23. The ratio increases smoothly with the centrality of the collisions and then saturates, as was already seen in the previous analysis from section 5.1 .

The multidimensional study of the ratio $\phi/(\rho+\omega)$ in 9 E_T regions and 4 P_T regions, using NOCIMD selection, is limited by the lack of statistics. This is more obvious in the very central regions, where the fits to the mass spectra become meaningless, since there are too many cells without any events (thus less points to be fitted) and huge error bars in those existing. Still, the result are in perfect agreement, within errors, with the ones from the previous (standard) analysis, as can be seen in table 5.12 .

Events	$1.4 \leq P_T < 1.6$ GeV/c	$1.6 \leq P_T < 1.8$ GeV/c	$1.8 \leq P_T < 2.0$ GeV/c	$2.0 \leq P_T < 3.5$ GeV/c
$5 \leq E_T < 29$ GeV	3033	3010	2294	3153
$29 \leq E_T < 42$ GeV	3006	3315	2668	3737
$42 \leq E_T < 53$ GeV	3285	3385	2693	3859
$53 \leq E_T < 64$ GeV	3442	3478	3054	4229
$64 \leq E_T < 74$ GeV	3082	3695	2621	3787
$74 \leq E_T < 83$ GeV	2969	3063	2590	3510
$83 \leq E_T < 93$ GeV	3180	3318	2660	3589
$93 \leq E_T < 105$ GeV	2920	2611	2461	3125
$105 \leq E_T < 150$ GeV	770	615	414	822

Table 5.9: Signal events statistics with NOCIMD selection and after cuts from table 5.7 are applied.

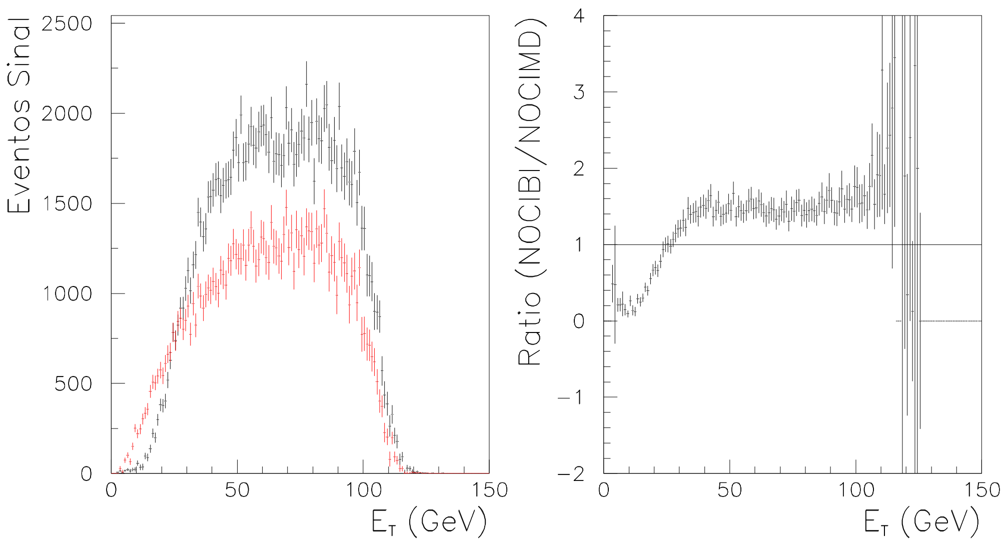

Figure 5.21: Signal events distribution as a function of E_T, with NOCIBI selection (in black) and NOCIMD selection (in red).

$\phi/(\rho+\omega)$ (χ^2/ndf)	$5 \leq E_T < 150$ GeV
$1.4 \leq P_T < 1.6$ GeV/c	0.499 ± 0.036 (3.6)
$1.6 \leq P_T < 1.8$ GeV/c	0.628 ± 0.041 (3.7)
$1.8 \leq P_T < 2.0$ GeV/c	0.588 ± 0.036 (2.3)
$2.0 \leq P_T < 3.5$ GeV/c	0.582 ± 0.023 (5.0)

Table 5.10: Ratios $\phi/(\rho+\omega)$ in 4 P_T regions, for data integration in the region $5 \leq E_T < 150$ GeV, and with NOCIMD selection.

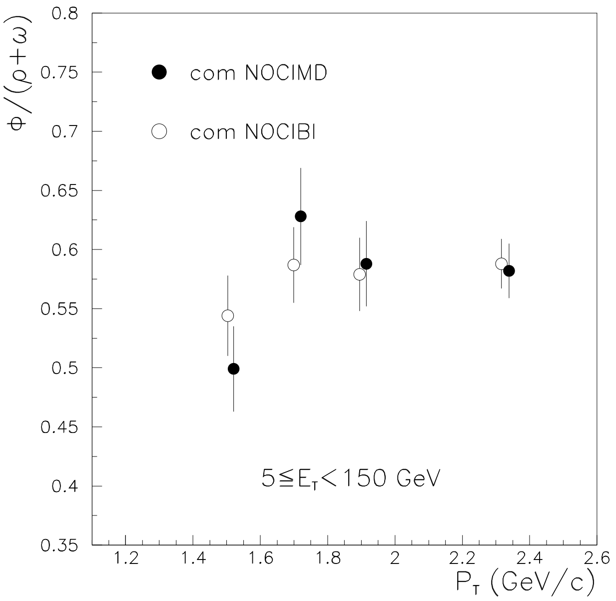

Figure 5.22: Ratios $\phi/(\rho+\omega)$ as a function of P_T, for the integrated region $5 \leq E_T < 150$ GeV. Comparison of results using NOCIMD or NOCIBI selection.

$\phi/(\rho+\omega)$ (χ^2/ndf)	$1.4 \leq P_T < 3.5$ GeV/c
$5 \leq E_T < 29$ GeV	0.366 ± 0.022 (3.0)
$29 \leq E_T < 42$ GeV	0.506 ± 0.030 (2.7)
$42 \leq E_T < 53$ GeV	0.509 ± 0.036 (2.8)
$53 \leq E_T < 64$ GeV	0.643 ± 0.052 (2.2)
$64 \leq E_T < 74$ GeV	0.718 ± 0.062 (2.4)
$74 \leq E_T < 83$ GeV	0.575 ± 0.056 (2.2)
$83 \leq E_T < 93$ GeV	0.616 ± 0.074 (1.2)
$93 \leq E_T < 105$ GeV	0.553 ± 0.062 (1.9)
$105 \leq E_T < 150$ GeV	0.771 ± 0.168 (0.6)

Table 5.11: Ratios $\phi/(\rho+\omega)$ in 9 E_T regions, for data integrated in $1.4 \leq P_T < 3.5$ GeV/c, and with selection NOCIMD.

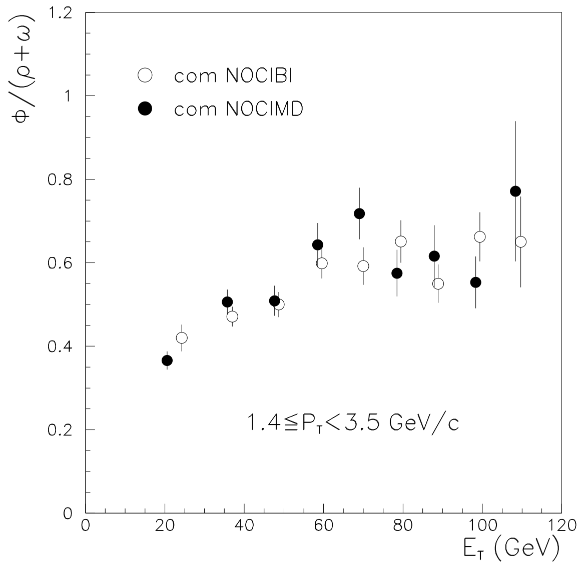

Figure 5.23: Ratios $\phi/(\rho+\omega)$ as a function of E_T, in the integrated region $1.4 \leq P_T < 3.5$ GeV/c. Comparison of results obtained with NOCIMD and NOCIBI selections.

$\phi/(\rho+\omega)$ (χ^2/ndf)	$1.4 \leq P_T < 1.6$ GeV/c	$1.6 \leq P_T < 1.8$ GeV/c	$1.8 \leq P_T < 2.0$ GeV/c	$2.0 \leq P_T < 3.5$ GeV/c
$5 \leq E_T < 29$ GeV	0.376 ± 0.053 (1.2)	0.403 ± 0.057 (1.9)	0.400 ± 0.046 (1.9)	0.346 ± 0.030 (1.9)
$29 \leq E_T < 42$ GeV	0.484 ± 0.075 (1.8)	0.566 ± 0.073 (0.9)	0.593 ± 0.074 (1.2)	0.474 ± 0.040 (2.3)
$42 \leq E_T < 53$ GeV	0.509 ± 0.078 (1.6)	0.528 ± 0.081 (1.1)	0.447 ± 0.065 (0.8)	0.616 ± 0.068 (1.9)
$53 \leq E_T < 64$ GeV	0.509 ± 0.099 (0.9)	0.858 ± 0.132 (1.5)	0.600 ± 0.097 (0.7)	0.660 ± 0.065 (1.7)
$64 \leq E_T < 74$ GeV	0.940 ± 0.258 (1.1)	0.773 ± 0.140 (1.7)	0.453 ± 0.080 (1.3)	0.563 ± 0.057 (1.4)
$74 \leq E_T < 83$ GeV	0.624 ± 0.187 (0.9)	0.450 ± 0.095 (1.8)	1.075 ± 0.242 (0.8)	0.699 ± 0.082 (2.0)
$83 \leq E_T < 93$ GeV	0.513 ± 0.178 (1.0)	0.596 ± 0.123 (1.5)	0.631 ± 0.115 (1.4)	0.664 ± 0.083 (1.8)
$93 \leq E_T < 105$ GeV	0.450 ± 0.111 (0.9)	0.880 ± 0.218 (1.6)	0.774 ± 0.208 (1.1)	0.704 ± 0.100 (1.7)
$105 \leq E_T < 150$ GeV	0.723 ± 1.157 (0.6)	1.552 ± 0.912 (0.7)	0.461 ± 0.363 (0.8)	0.734 ± 0.185 (1.7)

Table 5.12: Ratios $\phi/(\rho+\omega)$, per P_T and E_T regions. Between brackets the χ^2 per degree of freedom of the fit is shown.

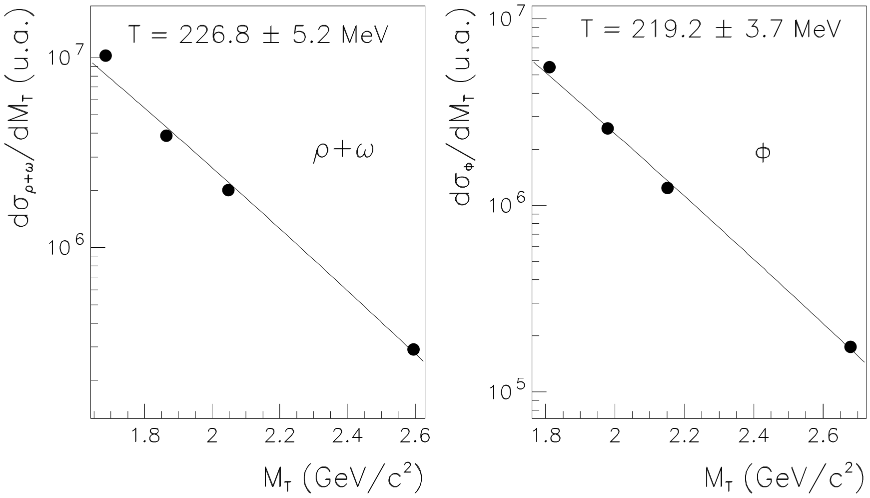

Figure 5.24: Fit to the cross-sections of $\rho+\omega$ and ϕ as a function of the transverse mass, to obtain effective temperatures. NOCIMD selection.

The method of analysis to obtain the temperatures for $\rho+\omega$ and ϕ with NOCIMD selection is the same as for the NOCIBI selection. Figure 5.24 shows the fit to the differential cross-sections in transverse mass for the $\rho+\omega$ and for the ϕ, to obtain the corresponding inverse slopes. In this case there is integration in the whole E_T region of analysis.

This study as a function of the transverse energy confirms the results obtained with NOCIBI selection (table 5.13 and figure 5.25). Temperatures for $\rho+\omega$ and for ϕ are identical and do not present any dependency with the collisions' centrality. Once more, these temperatures have an incertitude not fully evaluated, since systematic errors were not included in the cross-sections. These systematic errors can depend on the transverse momentum, influencing the fitted values for the temperatures.

5.4.2 Analysis with beam pile-up rejection

There is beam pile-up when, having a dimuon trigger, the beam hodoscope BH sees two ions passing in the trigger time window. This does not mean that both ions interact in the target, but there is a probability (although small, since the lead target is only 3 mm thick) for two interactions to occur and be seen as a single one.

The probability of having an event without beam pile-up (i.e. an event that is triggered, giving rise to the opening of the 20 ns gate for the ADC's reading, and without

T (MeV)	$\rho+\omega$	ϕ
$5 \leq E_T < 29$ GeV	232.9 ± 9.2	212.0 ± 8.2
$29 \leq E_T < 42$ GeV	234.3 ± 11.3	214.0 ± 7.5
$42 \leq E_T < 53$ GeV	203.2 ± 10.3	208.7 ± 8.9
$53 \leq E_T < 64$ GeV	228.1 ± 14.6	218.5 ± 8.4
$64 \leq E_T < 74$ GeV	254.1 ± 18.0	215.3 ± 9.8
$74 \leq E_T < 83$ GeV	238.9 ± 21.4	243.6 ± 12.9
$83 \leq E_T < 93$ GeV	240.6 ± 18.6	245.4 ± 13.7
$93 \leq E_T < 105$ GeV	218.8 ± 20.6	216.5 ± 12.0
$105 \leq E_T < 150$ GeV	284.3 ± 68.0	230.0 ± 27.9

Table 5.13: Effective temperatures for $\rho + \omega$ and ϕ, per E_T regions, with NOCIMD selection. Errors quoted are only statistical.

a second ion being observed in this time window) is given by the Poisson distribution:

$$P(0) = exp(-\bar{n}) \tag{5.14}$$

where $\bar{n}$ is the mean number of ions seen in the time window Δt:

$$\bar{n} = \Delta t \frac{I}{T_s} \quad , \tag{5.15}$$

I being the beam intensity (the number of ions per burst) and T_s the spill. Knowing that this data taking had Δt = 20 ns, a mean beam intensity of 5.5×10^7 ions/burst, and a spill $T_s = 4.5$ s, one obtains $P(0) = 78.3\%$. The probability to have more than one ion in the trigger time window is complementer of this, so amounting to 21.7%.

The thin lead target used for this data taking is 3 mm thick, corresponding to 7.2% of interaction length. This value leads to an interaction probability $P_{\mu\mu}$ when having an hadronic interaction, for each ion hitting the target. Thus, one concludes that the probability that, having a dimuon produced in-target, there is a second dimuon produced (interaction pile-up) is given by $P(0) \times P_h \times N_{\mu\mu}/N_h$, i.e., of the order of $(10^{-5}\%$. Since the probability of interaction pile-up is very low, in the standard analysis the events signaled as having beam pile-up are not rejected, in order not to penalise too much the statistics.

In this sub-section a study is presented with data selection using NOCIBI identification and cutting beam pile-up (NIBHAD cut). As can be seen in figure 5.26, events with beam pile-up spread on the whole E_T spectrum but concentrate mostly in the region $E_T < 15$ GeV. The NIBHAD cut reduces the data statistics by 10%.

The method of analysis used is the same already explained previously. Table 5.14 shows the ratios $\phi/(\rho + \omega)$ as a function of the dimuon transverse momentum, once more proving the independence of the ratio with P_T.

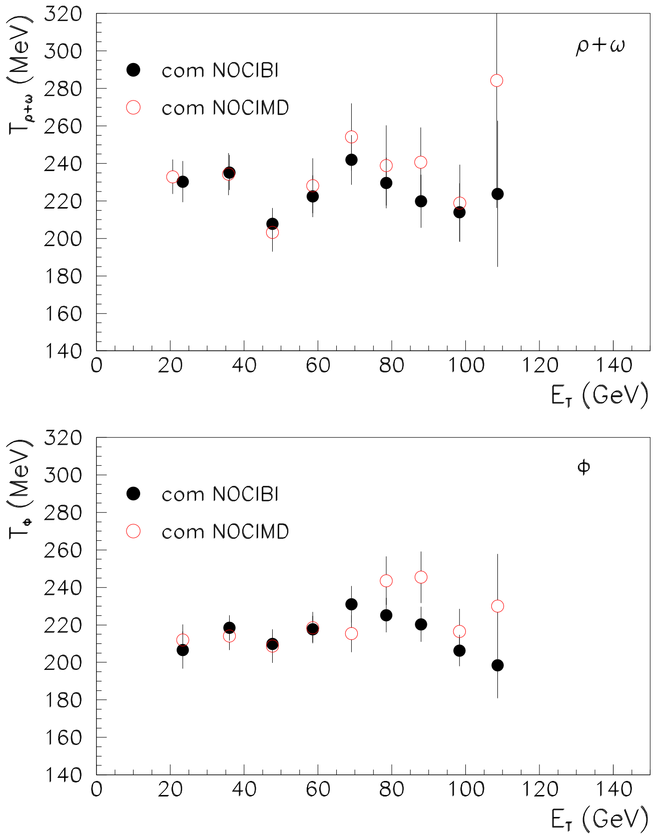

Figure 5.25: $\rho + \omega$ and ϕ effective temperatures, as a function of the transverse energy, obtained with NOCIMD or NOCIBI selections, and only considering statistical errors.

The results obtained cutting beam pile-up are compatible with the ones without this cut (presented in section 5.1), as shown in figure 5.27 .

The results of the analysis in 9 transverse energy regions are presented in table 5.15 and figure 5.28, where one can verify that results are almost the same, with or without beam pile-up.

5.5 Study of the systematic errors

The results obtained in the previous sections are now interpreted in terms of their coherence, by comparing the bi-differential results (as function of P_T and E_T) with their "projections" (as a function of P_T or as a function of E_T). The study of the systematic errors is very important for the evaluation of the effective temperatures, since these errors can depend on the transverse momentum, and therefore affect differently the differential cross section in transverse mass. Most of the systematic errors affect the resonances $\rho+\omega$

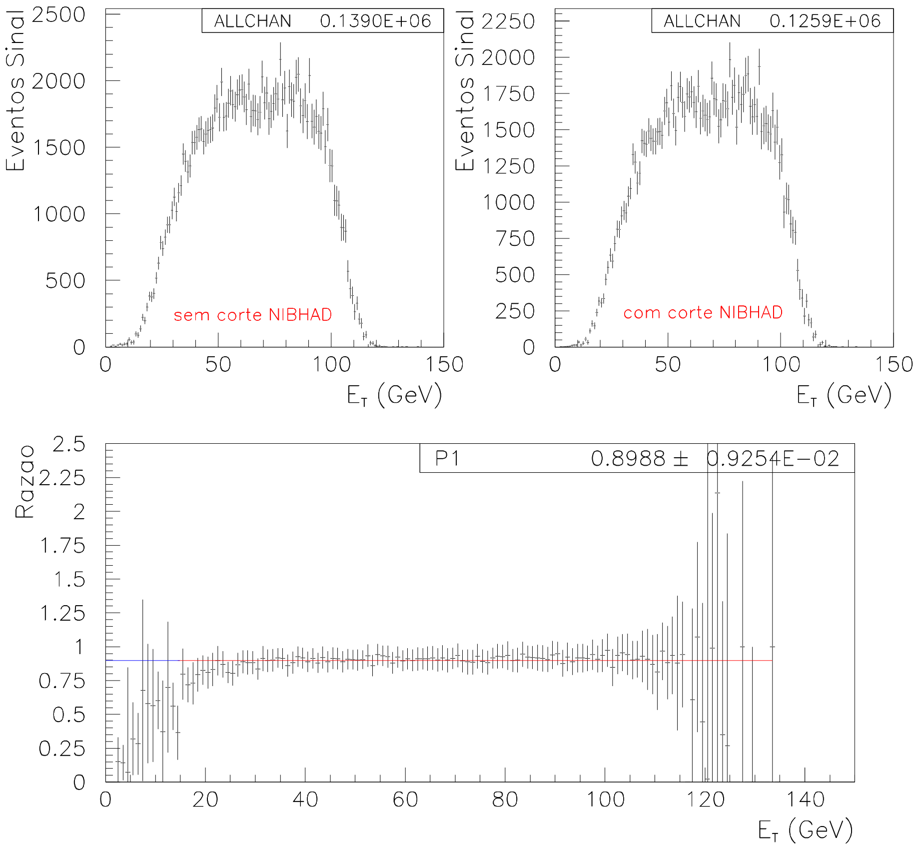

Figure 5.26: Signal events distribution as a function of E_T, with and without NIBHAB cut; and ratio of the two E_T spectra.

$\phi/(\rho+\omega)$ (χ^2/ndf)	$5 \leq E_T < 150$ GeV
$1.4 \leq P_T < 1.6$ GeV/c	0.542 ± 0.036 (3.2)
$1.6 \leq P_T < 1.8$ GeV/c	0.593 ± 0.034 (5.1)
$1.8 \leq P_T < 2.0$ GeV/c	0.612 ± 0.034 (2.7)
$2.0 \leq P_T < 3.5$ GeV/c	0.588 ± 0.023 (6.6)

Table 5.14: Ratios $\phi/(\rho+\omega)$ in 4 P_T regions, for the mass spectra integrated in $5 \leq E_T < 150$ GeV. NOCIBI selection with NIBHAD cut.

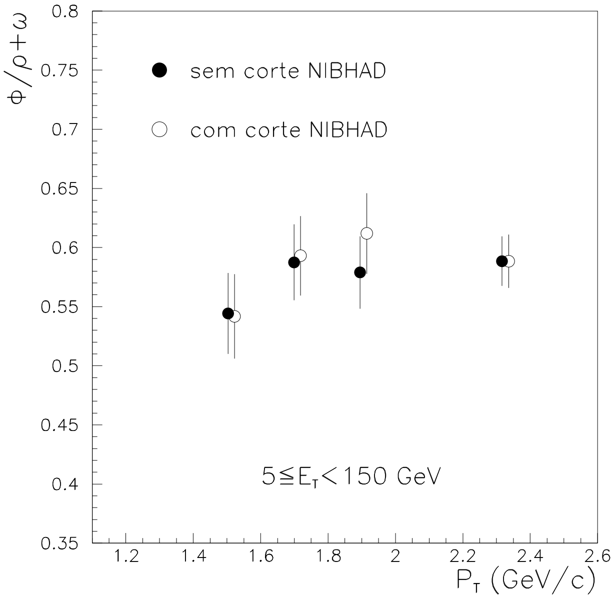

Figure 5.27: Ratios $\phi/(\rho+\omega)$ as a function of P_T, for the integrated region $5 \leq E_T < 150$ GeV. Comparison of analyses with and without NIBHAD cut.

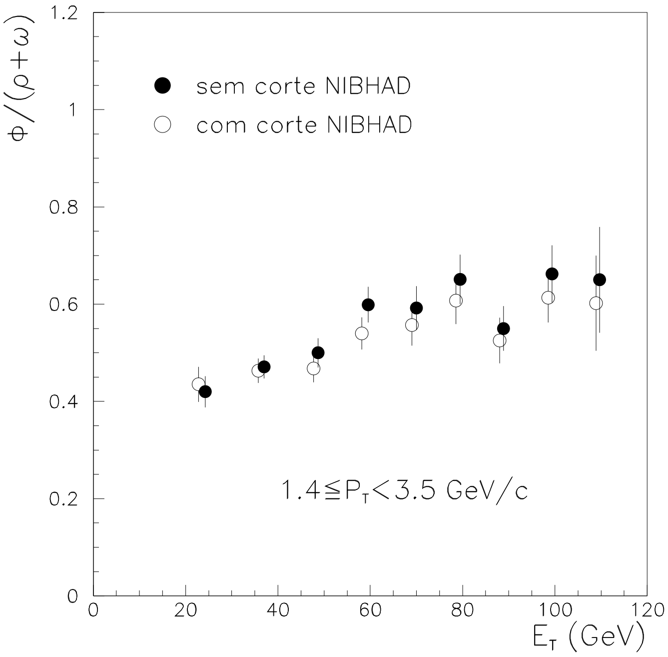

Figure 5.28: Ratios $\phi/(\rho+\omega)$ as a function of E_T, with NOCIBI selection. Comparison of analyses with and without NIBHAD cut.

$\phi/(\rho+\omega)$ (χ^2/ndf)	$1.4 \leq P_T < 3.5$ GeV/c
$5 \leq E_T < 29$ GeV	0.435 ± 0.036 (2.4)
$29 \leq E_T < 42$ GeV	0.463 ± 0.025 (3.0)
$42 \leq E_T < 53$ GeV	0.468 ± 0.029 (3.0)
$53 \leq E_T < 64$ GeV	0.540 ± 0.033 (1.6)
$64 \leq E_T < 74$ GeV	0.557 ± 0.042 (3.0)
$74 \leq E_T < 83$ GeV	0.607 ± 0.048 (2.9)
$83 \leq E_T < 93$ GeV	0.525 ± 0.047 (1.8)
$93 \leq E_T < 105$ GeV	0.613 ± 0.051 (2.5)
$105 \leq E_T < 150$ GeV	0.602 ± 0.098 (1.4)

Table 5.15: Ratios $\phi/(\rho+\omega)$ in 9 E_T regions, for the mass spectra integrated in $1.4 \leq P_T < 3.5$ GeV/c. Selection NOCIBI with NIBHAD cut.

e ϕ the same way, so that they cancel in the ratio $\phi/(\rho+\omega)$.

In this analysis there are several sources of systematic errors. To quantify these errors is very difficult. The errors affecting the luminosity, due to measurement uncertainties in the target's dimension and density, to the error in the calculated efficiencies (for the target recognition algorithm, for the two planes of the beam hodoscope, for the trigger and the tracks reconstruction) cancel in what concerns the ratios $\phi/(\rho+\omega)$. This is not the case for cross-section measurements as a function of the dimuon transverse mass, but since these errors affect the same way all transverse mass bins, they do not influence the temperatures measurement for $\rho+\omega$ and ϕ.

There are two sources of systematic errors that depend on the dimuons' transverse momentum: the systematic error coming from differences between the simulated Monte-Carlo spectra and the experimental distributions; and the error from the background subtraction.

5.5.1 Differences between MC and data

The multidimensional distributions of Monte-Carlo events are adjusted to the experimental ones, using an iterative method as explained in Chapter 4. The method converges after 2 iterations. The remaining differences are a systematic error affecting the acceptances, that reflects in the final measurement of $\phi/(\rho+\omega)$ and the differential cross-sections.

This systematic error is evaluated with a third iteration in the adjustment of the MC to the data, and comparing the final results with the ones obtained in the standard analysis (2 iterations). This difference between the two results is a measurement of the systematic error in the differential acceptance, that propagates to the deconvoluted experimental spectra.

$\phi/(\rho+\omega)$ (χ^2/ndf)	$5 \leq E_T < 150$ GeV
$1.4 \leq P_T < 1.6$ GeV/c	0.544 ± 0.034 (3.5)
$1.6 \leq P_T < 1.8$ GeV/c	0.587 ± 0.032 (5.2)
$1.8 \leq P_T < 2.0$ GeV/c	0.576 ± 0.030 (3.0)
$2.0 \leq P_T < 3.5$ GeV/c	0.588 ± 0.021 (6.9)

Table 5.16: Ratios $\phi/(\rho+\omega)$ in 4 P_T regions, with a MC adjusted to the data in 3 iterations.

Table 5.16 presents the ratio $\phi/(\rho+\omega)$ in 4 dimuon transverse momentum regions,

ΔP_T (GeV/c)	$\Delta(\rho+\omega)$ %	$\Delta(\phi)$ %	$\Delta(\phi/(\rho+\omega))$ %
$1.4 \leq P_T < 1.6$	-3.17 ± 8.81	$+2.05 \pm 6.21$	-0.09 ± 8.83
$1.6 \leq P_T < 1.8$	$+2.01 \pm 7.52$	$+1.87 \pm 5.20$	-0.14 ± 7.65
$1.8 \leq P_T < 2.0$	$+2.01 \pm 7.06$	$+1.44 \pm 5.33$	-0.58 ± 7.45
$2.0 \leq P_T < 3.5$	$+1.25 \pm 4.70$	$+1.24 \pm 3.60$	-0.01 ± 5.08
$\langle - \rangle$	$+2.2$	$+1.6$	-0.2

Table 5.17: Systematic error from the differences between simulated and experimental distributions.

for data integrated in $5 \leq E_T < 150$ GeV, and deconvoluted from an acceptance calculated with a MC adjusted to the data in 3 iterations.

The systematic error in the difference between the simulated and the experimental distributions is calculated in each P_T region, for the ratio $\phi/(\rho+\omega)$, and for the number of resonant events $\rho+\omega$ and ϕ. The differences relative to the standard analysis (section 5.1.2) are presented in table 5.17 . The mean value of these relative differences is calculated by the simple mean in the 4 P_T regions. This error is shown to be very small.

5.5.2 Systematic error from the background subtraction

The statistical subtraction of the combinatorial background, done according to equation (3.5), is valid in the conditions explained in Chapter 3. $R = 1$ can only be used in the equation if the multiplicity of produced particles is high enough (i.e. is Poissonian). This condition is thought to be more or less fulfilled for lead collisions, even for peripheral ones. The systematic error coming from this assumption, different for $\rho+\omega$ and for ϕ (since the background under these resonances is different) has to be evaluated.

With a Monte-Carlo simulation using the event generator VENUS 4.12, it is possible to study the charge correlations occurring for peripheral collisions, when the multiplicity of produced particles is low. Through this kind of simulation it is possible to obtain the dependency of the R factor with the impact parameter, for Pb+Pb collisions at 158 A GeV/c [8] (figure 5.29).

This dependency is parameterised by the function:

$$R(b) = 1. \ + \ 0.092 \ (\frac{b}{13})^{3.05} \tag{5.16}$$

The impact parameter b for a given collision is calculated from the neutral transverse energy measured. With the Glauber model, one can relate the impact parameter with the number of participant nucleons. Besides, the Wounded Nucleon model [90], using the Glauber formalism, allows to correlate N_{part} with the transverse energy (equation(5.7)). Some details of these models are explained shortly in Appendix B.

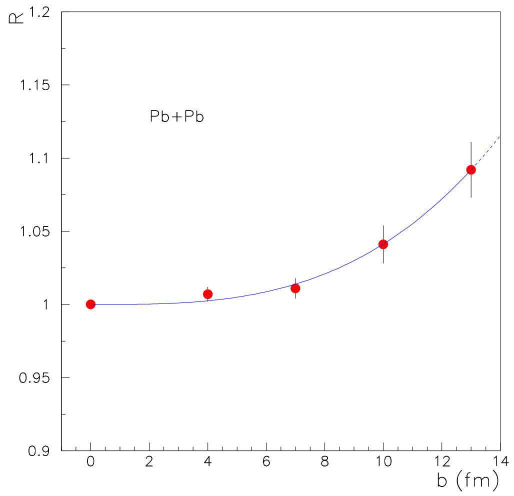

Figure 5.29: Dependency of the background subtraction R parameter with the impact parameter b, according to a MC simulation for Pb+Pb collisions at 158 GeV/nucleon [8].

Table 5.18 presents the mean impact parameters for each transverse energy region of this analysis. The correspondence between E_T and N_{part} is done according to equation (5.11), except for the last transverse energy region. The bin $105 \leq E_T < 150$ GeV locates after the "knee" of the E_T distribution, and so its mean value is only the barycentre from a Gaussian tail. Thus we assume that in this region the number of participants is maximum and the collisions totally central (b=0). Table 5.18 also shows the correspondence between E_T and the R factor, obtained from parameterisation (5.16).

The systematic error due to the use of $R = 1$ is evaluated comparing the results from the standard analysis with the ones obtained using the R values from table 5.18 . This study is done in the 9 E_T regions, with data integrated in $1.4 \leq P_T < 3.5$ GeV/c, using NOCIBI selection and without beam pile-up cut. Table 5.19 presents the results of this study, while the comparison with the standard analysis is shown in figure 5.30 .

The relative difference in the ratio $\phi/(\rho + \omega)$ and in the number of resonant events $\rho + \omega$ and ϕ, obtained with background subtraction using R factor from MC simulation to the ones from the standard analysis presented in section 5.1.3 is shown in table 5.20 . The simple mean of the deviations is also presented for all E_T regions, and it is around 2% for the $\rho + \omega$ and ϕ absolute cross-sections, and $\approx 0.5\%$ for the ratio $\phi/(\rho + \omega)$. The most critical region is for $E_T \leq 40$ GeV (but still not exceeding 5% difference).

The same study was repeated for the integrated region $5 \leq E_T < 150$ GeV, in 4 transverse momentum regions, and the deviations obtained are presented in table 5.21. From both tables, one can conclude that the systematic error due to the use of $R = 1$ for the lead peripheral collisions is very small.

ΔE_T (GeV)	$\langle E_T \rangle$ (GeV)	N_{part}	N_{col}	$\langle b \rangle$ (fm)	R
$5 < E_T < 29$	23.3	85	126	9.6	1.036
$29 < E_T < 42$	36.0	132	225	8.2	1.022
$42 < E_T < 53$	47.7	175	324	7.1	1.014
$53 < E_T < 64$	58.6	214	420	6.2	1.010
$64 < E_T < 74$	69.0	253	522	5.2	1.006
$74 < E_T < 83$	78.5	287	614	4.4	1.003
$83 < E_T < 93$	87.9	322	713	3.4	1.002
$93 < E_T < 105$	98.4	360	820	2.2	1.000
$105 < E_T < 150$	108.7	391	914	0.	1.000

Table 5.18: Number of participants, number of collisions, impact parameter and the correspondence to the R factor, for this analysis' mean E_T values.

5.5.3 Final systematic error

The several sources of systematics contribute to a final systematic error given by their quadratic sum. Table 5.22 presents these final errors, for the integrated region $5 \leq E_T < 150$ GeV, obtained from the simple mean value of the errors in the 4 P_T regions.

5.5.4 Temperature calculation including systematic errors

As explained in section 5.2, the evaluation of the systematic errors is very important for the effective temperatures study.

The $\rho + \omega$ and ϕ effective temperatures are calculated assuming the scaling in the dimuon transverse mass from equation (5.4), as done in section 5.2; but the number of resonant events $\rho + \omega$ and ϕ (divided by the width of the corresponding transverse mass region) is now taken with an error that is the quadratic sum of its statistic and systematic errors. In these calculations the systematic error used is the one evaluated for each transverse momentum region, and not the mean value presented in table 5.22 . The fit to the transverse mass distributions using function (1.7) is presented in figure 5.31 .

The same procedure is followed to obtain the resonances temperature as a function of the centrality, including statistic and systematic errors. Once more, the error values used are not the ones from table 5.22, but those evaluated in the bi-differential regions of P_T and E_T. Table 5.23 and figure 5.32 show the obtained results.

One thus concludes that there is no dependence seen in the $\rho + \omega$ and ϕ effective temperatures with the collisions' centrality.

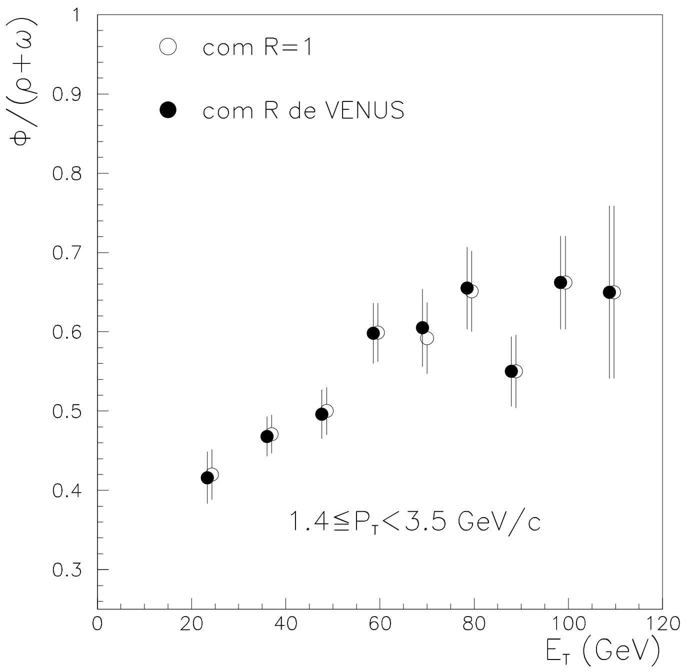

Figure 5.30: Ratios $\phi/(\rho+\omega)$ using $R = 1$ compared to the ones using R from MC (according to figure 5.29).

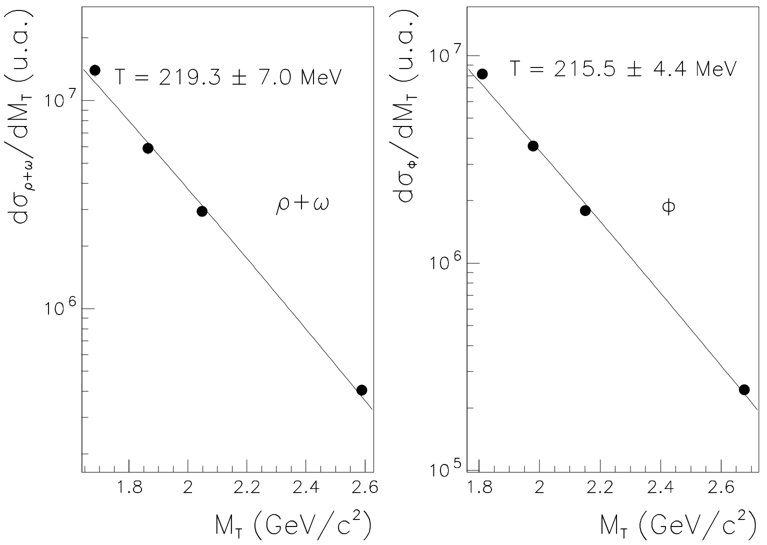

Figure 5.31: Fit to obtain the effective temperatures of $\rho+\omega$ and ϕ, considering statistic and systematic errors.

$\phi/(\rho+\omega)$ (χ^2/ndf)	$1.4 \leq P_T < 3.5$ GeV/c
$5 \leq E_T < 29$ GeV	0.416 ± 0.033 (2.3)
$29 \leq E_T < 42$ GeV	0.468 ± 0.025 (3.1)
$42 \leq E_T < 53$ GeV	0.496 ± 0.031 (2.9)
$53 \leq E_T < 64$ GeV	0.598 ± 0.038 (2.0)
$64 \leq E_T < 74$ GeV	0.605 ± 0.049 (2.5)
$74 \leq E_T < 83$ GeV	0.655 ± 0.052 (2.9)
$83 \leq E_T < 93$ GeV	0.550 ± 0.044 (1.9)
$93 \leq E_T < 105$ GeV	0.662 ± 0.059 (1.8)
$105 \leq E_T < 150$ GeV	0.650 ± 0.109 (1.3)

Table 5.19: Ratios $\phi/(\rho+\omega)$ in 9 E_T regions, with data integrated in $1.4 \leq P_T < 3.5$ GeV/c, using the R factors obtained from MC simulation using VENUS, or using R=1.

ΔE_T (GeV)	$\Delta(\rho+\omega)$ %	$\Delta(\phi)$ %	$\Delta(\phi/(\rho+\omega))$ %
$5 \leq E_T < 29$	-2.0 ± 8.9	-2.5 ± 8.2	-0.5 ± 10.9
$29 \leq E_T < 42$	-0.7 ± 6.7	-1.6 ± 5.3	-0.9 ± 7.5
$42 \leq E_T < 53$	-0.6 ± 7.6	-1.1 ± 5.9	-0.5 ± 8.4
$53 \leq E_T < 64$	-0.2 ± 8.7	-0.4 ± 5.5	-0.2 ± 8.8
$64 \leq E_T < 74$	-4.0 ± 10.6	-1.8 ± 6.9	$+2.4 \pm 11.2$
$74 \leq E_T < 83$	-0.3 ± 11.0	-0.2 ± 6.8	$+0.2 \pm 11.0$
$83 \leq E_T < 93$	$+0.0 \pm 11.3$	-0.1 ± 7.6	-0.1 ± 11.8
$93 \leq E_T < 105$	$+0.0 \pm 12.7$	-0.1 ± 7.2	-0.1 ± 12.6
$105 \leq E_T < 150$	$+0.0 \pm 0.0$	$+0.0 \pm 0.0$	0.0 ± 0.0
$\langle - \rangle$	-1.0	-1.0	$+0.0$

Table 5.20: Relative difference for the number of resonant events $\rho+\omega$ and ϕ and for the ratio $\phi/(\rho+\omega)$, from the analysis with background subtraction using R from MC relative to the standard analysis.

ΔP_T (GeV/c)	$\Delta(\rho+\omega)$ %	$\Delta(\phi)$ %	$\Delta(\phi/(\rho+\omega))$ %
$1.4 \leq P_T < 1.6$	-3.2 ± 8.2	-2.3 ± 5.8	$+0.9 \pm 10.5$
$1.6 \leq P_T < 1.8$	-3.8 ± 7.1	-2.0 ± 4.9	$+1.9 \pm 9.1$
$1.8 \leq P_T < 2.0$	-2.0 ± 6.9	-1.6 ± 5.0	$+0.5 \pm 8.8$
$2.0 \leq P_T < 3.5$	-5.3 ± 4.5	-2.5 ± 3.4	$+3.0 \pm 6.1$
$\langle - \rangle$	-3.60	-2.09	$+1.57$

Table 5.21: Relative difference in the $\rho+\omega$ and ϕ number and in the ratio $\phi/(\rho+\omega)$, between the analysis using background subtraction with R from the MC and the standard analysis, per P_T regions.

Error source	$\Delta(\rho+\omega)$ %	$\Delta(\phi)$ %	$\Delta(\phi/(\rho+\omega))$ %
Differences MC – Data	$+2.2$	$+1.6$	-0.2
Background subtraction	-1.0	-1.0	$+0.0$
Total	2.4	1.9	0.2

Table 5.22: Final mean systematic errors affecting measurements.

T (MeV)	$\rho+\omega$	ϕ
$5 \leq E_T < 29$ GeV	229.2 ± 12.2	193.5 ± 2.3
$29 \leq E_T < 42$ GeV	235.3 ± 9.8	218.5 ± 7.1
$42 \leq E_T < 53$ GeV	207.8 ± 8.7	209.8 ± 7.6
$53 \leq E_T < 64$ GeV	221.3 ± 11.8	217.6 ± 7.5
$64 \leq E_T < 74$ GeV	242.4 ± 13.7	231.5 ± 10.0
$74 \leq E_T < 83$ GeV	229.8 ± 13.9	225.1 ± 9.4
$83 \leq E_T < 93$ GeV	218.4 ± 14.6	220.3 ± 9.5
$93 \leq E_T < 105$ GeV	213.2 ± 16.3	206.3 ± 8.5
$105 \leq E_T < 150$ GeV	222.2 ± 42.2	198.6 ± 18.7

Table 5.23: $\rho+\omega$ and ϕ effective temperatures, per E_T regions. Standard analysis, including statistical and systematic errors.

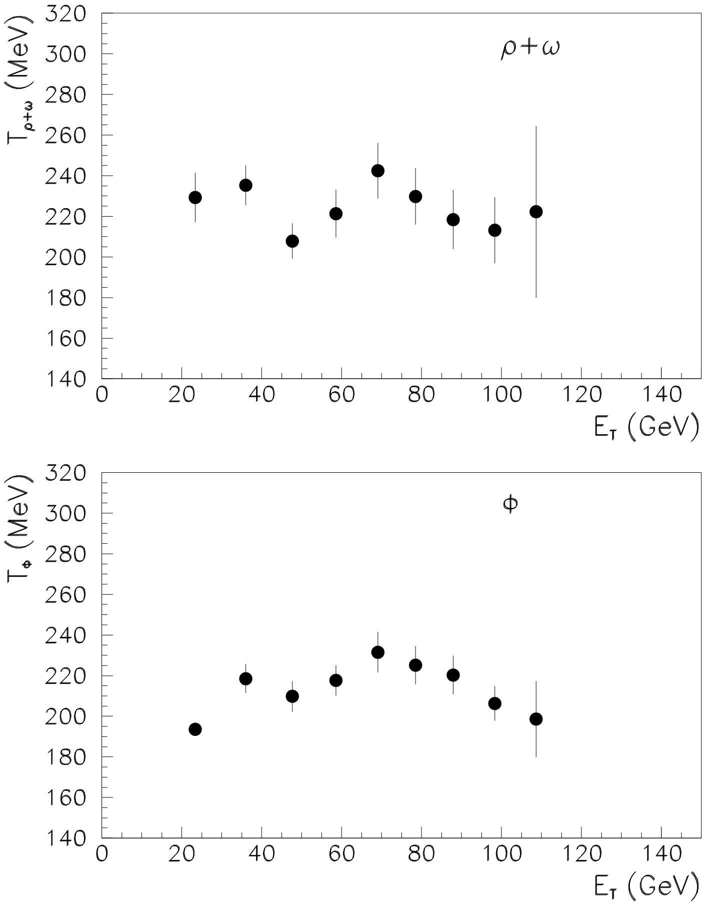

Figure 5.32: $\rho + \omega$ and ϕ effective temperatures, considering statistical and systematic errors on the cross-sections, as a function of E_T.

Chapter 6

Results discussion

The stability of the results is studied by varying different factors. A regrouping of transverse energy bins, in 5 E_T regions instead of the 9 used until now allows the reduction of the fluctuations due to the low statistics available. One tries also to confirm the results obtained with other alternative fit functions to the mass spectrum. Other factors, like the number of free parameters in the fit are also studied.

The interpretation of the results is done here, comparing these with previous analyses and with results from other experiments.

Finally, conclusions are obtained relative to the results from this study.

6.1 Stability of the results

As was seen in the previous chapter, the bi-dimensional study (4 P_T and 9 E_T regions) of the deconvoluted mass spectra shows some evidences of lack of statistics and so some of the results are inconclusive. In this section a study of the stability of these results is presented, for the different analysis stages.

6.1.1 Study in 5 E_T regions

A regrouping of the transverse energy regions considered in the analysis increases the statistics in each region, therefore reducing the statistical fluctuations of the data which, after deconvolution, may introduce biases in the fit to the mass spectra.

Five regions of transverse energy are defined from the regrouping two by two of the previously considered ones, with the exception of the last bin, since its lower limit is already after the “knee” of the E_T distribution:

$$\begin{aligned} 5 \leq E_T &< 42 \\ 42 \leq E_T &< 64 \\ 64 \leq E_T &< 83 \\ 83 \leq E_T &< 105 \\ 105 \leq E_T &< 150 \quad \text{GeV} \quad . \end{aligned}$$

All the procedure for the mass spectra analysis, as a function of E_T and P_T, and as a function of E_T and with P_T integration, is redone using this new definition of the E_T regions. Table 6.1 shows the ratios $\phi/(\rho+\omega)$ obtained, for the bi-dimensional analysis.

$\phi/(\rho+\omega)$ (χ^2/ndf)	$1.4 \leq P_T < 1.6$ GeV/c	$1.6 \leq P_T < 1.8$ GeV/c	$1.8 \leq P_T < 2.0$ GeV/c	$2.0 \leq P_T < 3.5$ GeV/c
$5 \leq E_T < 42$ GeV	0.479 ± 0.051 (1.5)	0.460 ± 0.042 (1.5)	0.492 ± 0.041 (1.7)	0.439 ± 0.026 (2.5)
$42 \leq E_T < 64$ GeV	0.528 ± 0.056 (1.9)	0.586 ± 0.052 (1.3)	0.558 ± 0.050 (1.0)	0.610 ± 0.038 (4.2)
$64 \leq E_T < 83$ GeV	0.700 ± 0.109 (2.0)	0.546 ± 0.059 (2.5)	0.540 ± 0.056 (2.0)	0.624 ± 0.042 (2.9)
$83 \leq E_T < 105$ GeV	0.529 ± 0.074 (0.6)	0.748 ± 0.093 (2.1)	0.709 ± 0.088 (1.5)	0.703 ± 0.059 (2.5)
$105 \leq E_T < 150$ GeV	0.758 ± 0.281 (0.7)	0.858 ± 0.296 (0.8)	0.791 ± 0.427 (0.6)	0.711 ± 0.322 (1.2)

Table 6.1: $\phi/(\rho+\omega)$ ratio, in 4 P_T regions and 5 E_T regions. The χ^2 per degree of freedom of the fit to the mass spectra is inside brackets.

Figure 6.1 shows the ratios $\phi/(\rho+\omega)$ as a function of P_T, in the 5 E_T regions. Thanks to the increased statistics in each region and consequent reduction of the error bars, one observes the constant ratio with P_T, more obvious here than in the analysis with 9 E_T bins (figure 6.2).

The results from these rebinning are in perfect agreement with the ones previously obtained, as can be seen in figure 6.2; i.e. the tendency of the ratio $\phi/(\rho+\omega)$ to increase with the transverse energy is confirmed, in all four P_T bins. The smooth increase behaviour, with apparent saturation from $E_T \approx 80$ GeV on, is more evident in the region of higher P_T.

6.1.2 χ^2 per point study

When fitting the deconvoluted mass spectra one observes that some points are badly fitted by the used function. This is more visible for the points at half-height of the

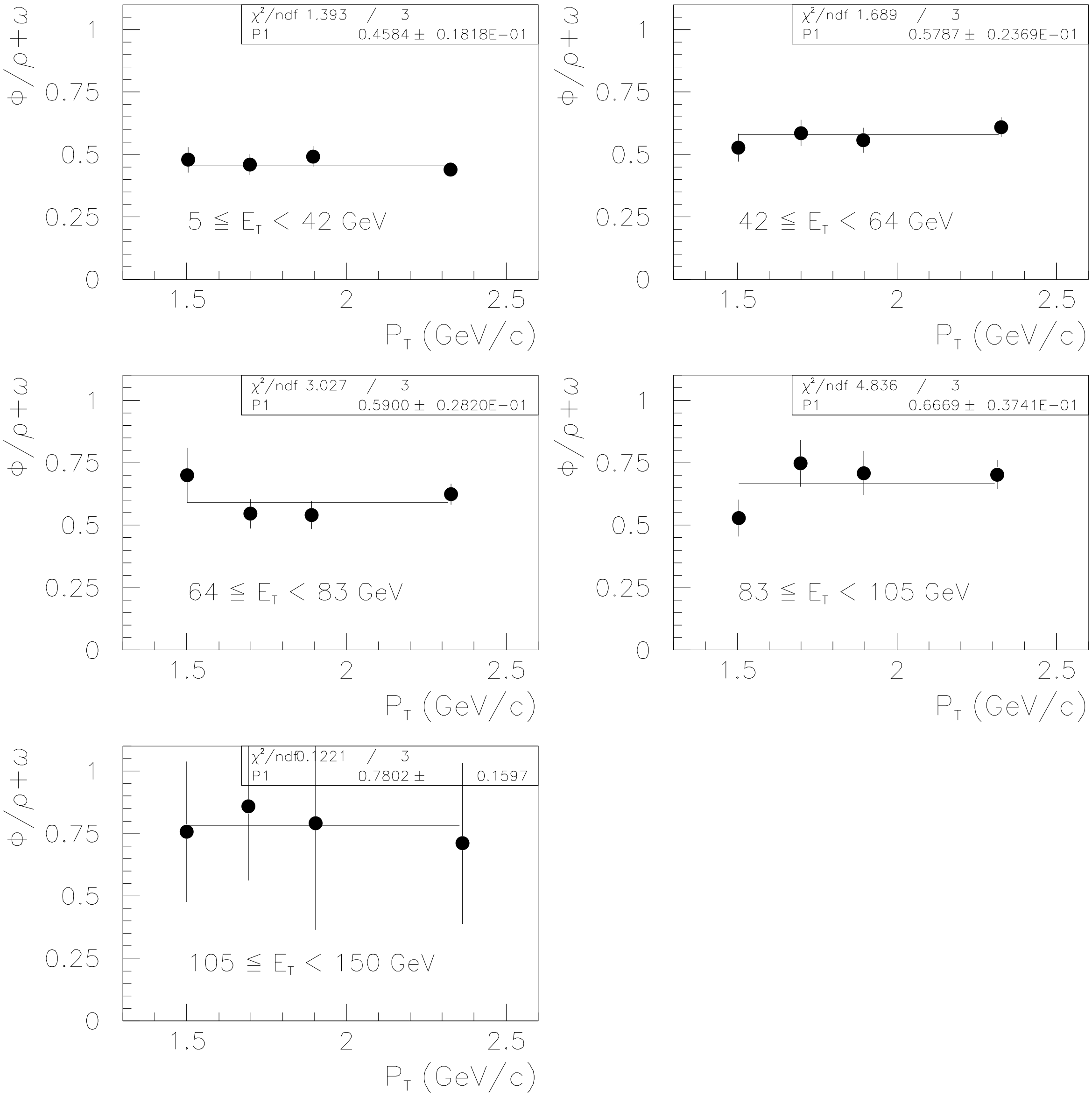

Figure 6.1: Ratios $\phi/(\rho + \omega)$ as a function of P_T, in 5 E_T regions.

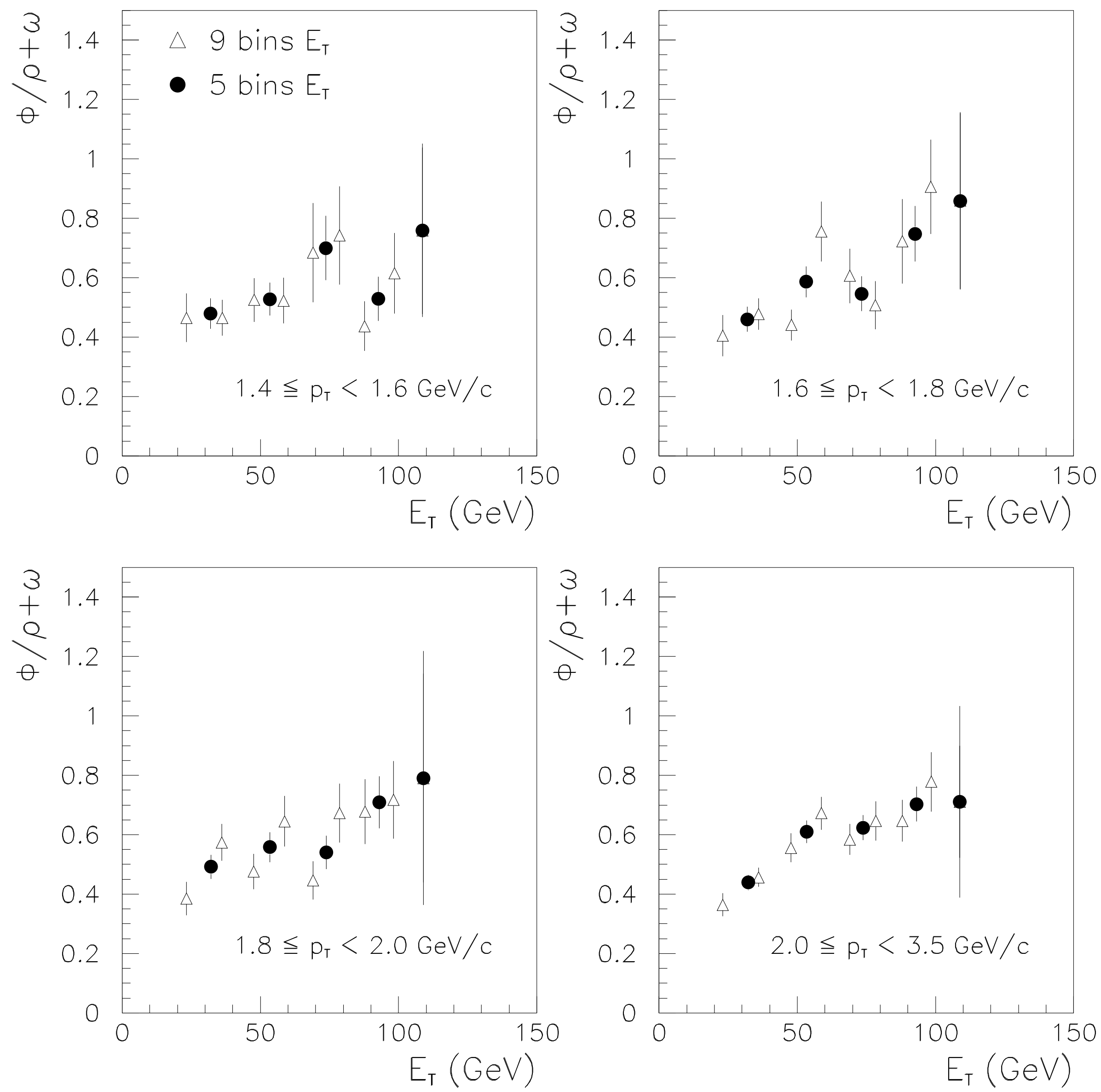

Figure 6.2: Comparison between the ratios $\phi/(\rho+\omega)$ as a function of E_T, per P_T regions, with 5 or 9 points in E_T.

resonances, and in the overlap region. This effect is probably due to the limitations of the deconvolution method in correcting transition regions. In order to know if the fit is forced by these badly described points, a study of the χ^2 per point is done, in the mass distributions fit.

Figure 6.3 shows the χ^2 per point distributions, relative to the fit to the mass spectra integrated in transverse energy, in 4 P_T regions, shown in figure 5.4.

The fit to the mass spectra is redone, rejecting the points for which the χ^2 per point is higher than 5 (figure 6.3), as shown in figure 6.4. Table 6.2 has the values obtained for the ratios $\phi/(\rho+\omega)$, and also the χ^2 of the fit, rejecting the points identified in the standard fit.

$\phi/(\rho+\omega)$ (χ^2/ndf)	Rejecting points	Standard analysis
$1.4 \leq P_T < 1.6$ GeV/c	0.470 ± 0.034 (1.1)	0.544 ± 0.034 (3.3)
$1.6 \leq P_T < 1.8$ GeV/c	0.518 ± 0.033 (1.1)	0.587 ± 0.032 (4.9)
$1.8 \leq P_T < 2.0$ GeV/c	0.565 ± 0.031 (1.1)	0.579 ± 0.031 (2.9)
$2.0 \leq P_T < 3.5$ GeV/c	0.521 ± 0.021 (1.2)	0.588 ± 0.021 (7.2)

Table 6.2: Ratios $\phi/(\rho+\omega)$ in 4 P_T regions, for the mass spectra integrated in $5 \leq E_T < 150$ GeV region, rejecting points with $\chi^2 > 5$, identified in the standard fit. Comparison with the standard analysis.

If the fit presented in figure 5.4 does not include those points with $\chi^2 > 5$ from the standard fit, one obtains a χ^2 of 1.3, 1.2, 1.3 and 1.8, respectively for increasing P_T. In table 6.2 and figure 6.5 these results are compared with the previously obtained ones (section 5.1.2). Even if the quality of the fits increases when we remove "bad" points, there is a systematic decrease of the ratio $\phi/(\rho+\omega)$. The relative deviations, in percentage, are presented in table 6.3 .

ΔP_T (GeV/c)	$\Delta(\rho+\omega)$ %	$\Delta(\phi)$ %	$\Delta(\phi/(\rho+\omega))$ %
$1.4 \leq P_T < 1.6$	$+11.8 \pm 10.5$	-3.5 ± 6.0	-13.7 ± 8.3
$1.6 \leq P_T < 1.8$	$+8.8 \pm 8.8$	-4.0 ± 5.0	-11.8 ± 7.4
$1.8 \leq P_T < 2.0$	-0.2 ± 7.1	-2.6 ± 5.2	-2.4 ± 7.6
$2.0 \leq P_T < 3.5$	$+8.5 \pm 5.4$	-3.8 ± 3.5	-11.4 ± 4.8

Table 6.3: Relative deviations on the resonant event numbers $\rho+\omega$ and ϕ and on the ratio $\phi/(\rho+\omega)$, between the *standard* analysis and the one rejecting points with $\chi^2 > 5$.

Bad χ^2 data points locate mainly at half height on the resonances peak, with the fit function passing under the data points, and this may be a sign of resonance modifications

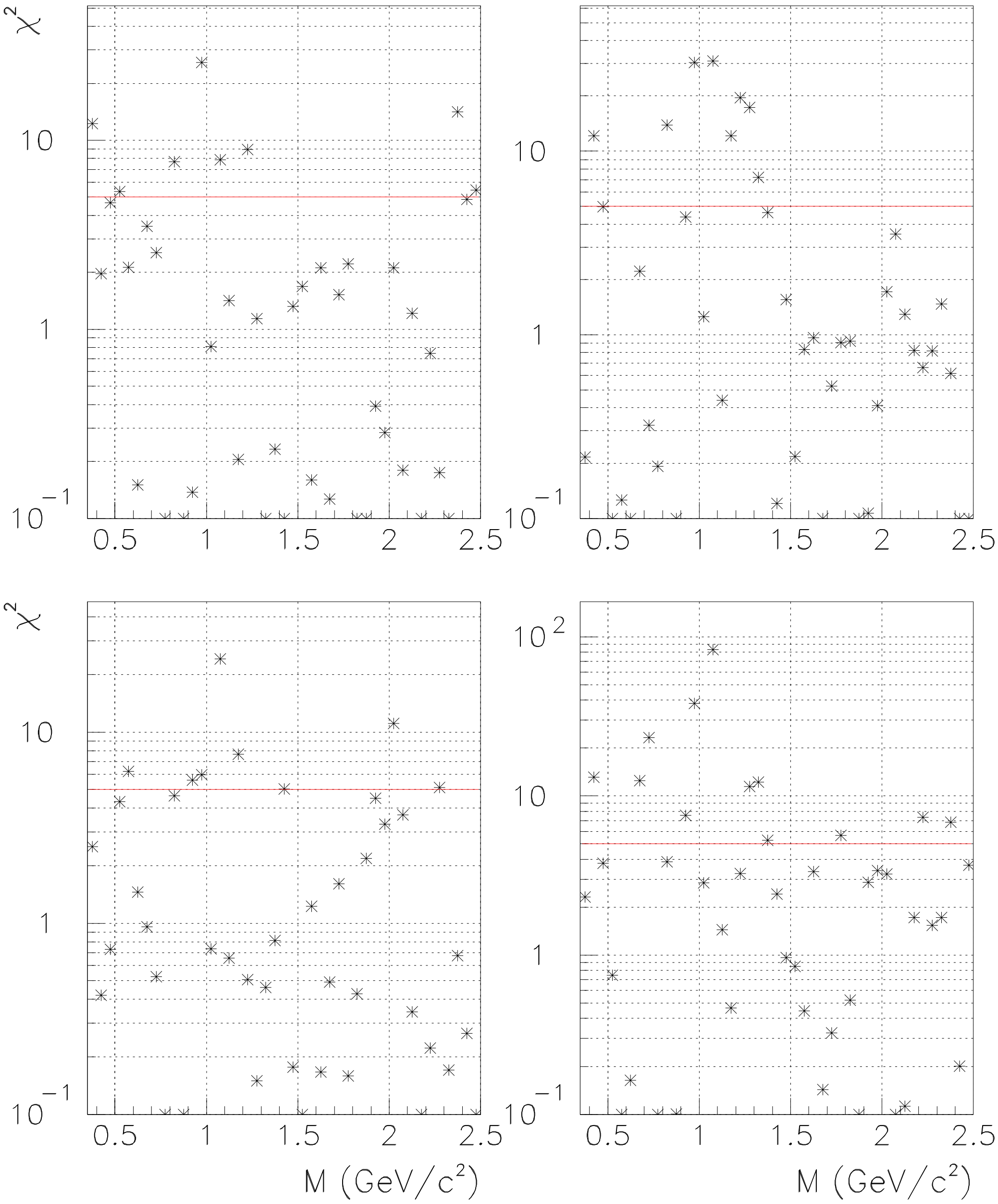

Figure 6.3: χ^2 per point distributions of the fits to the mass spectra shown in figure 5.4. The points with $\chi^2 > 5$ are located above the red line.

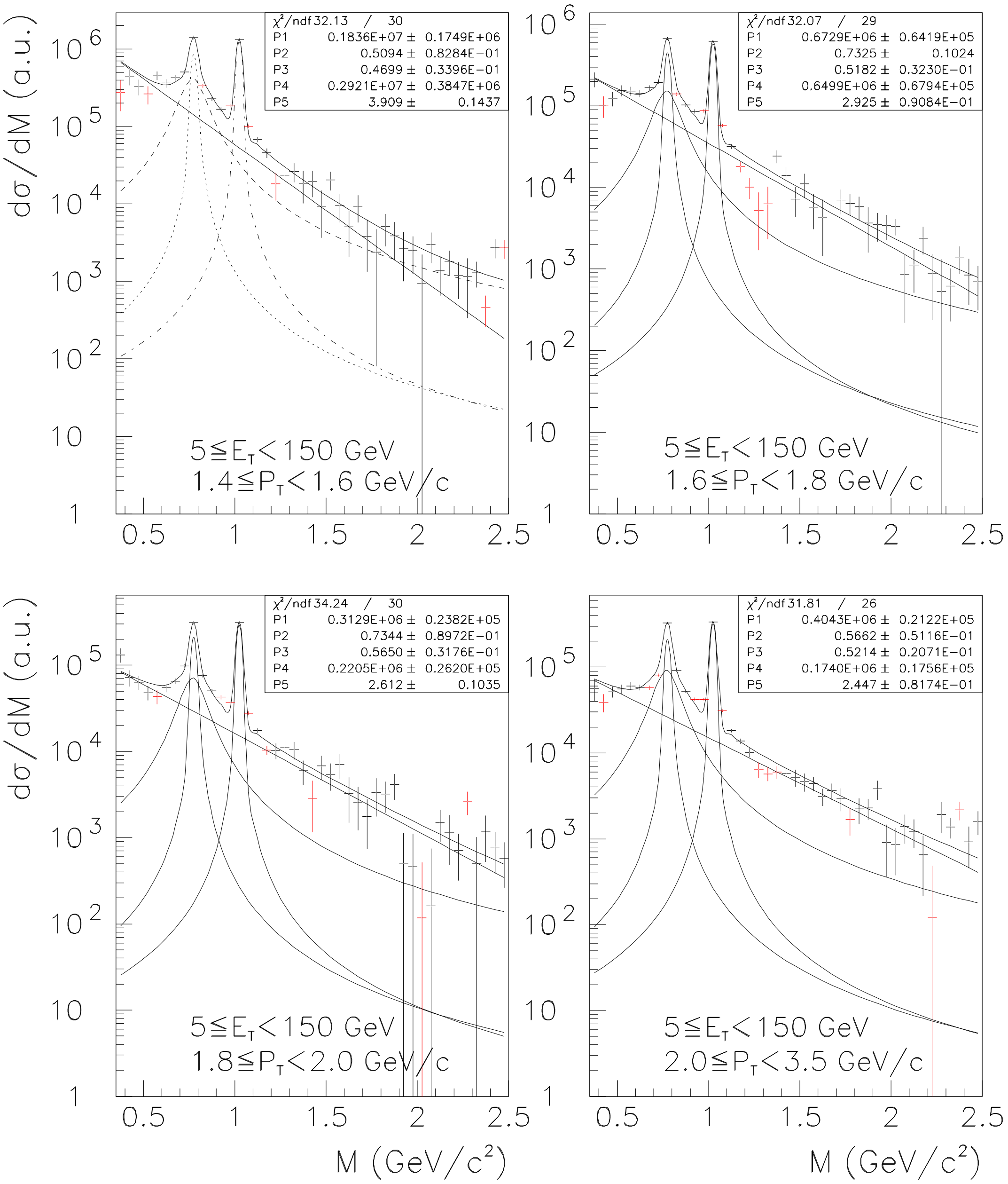

Figure 6.4: Fit to the deconvoluted mass spectra, rejecting the points with $chi^2 > 5$. The rejected points, not taken in account by the fit, are shown in red.

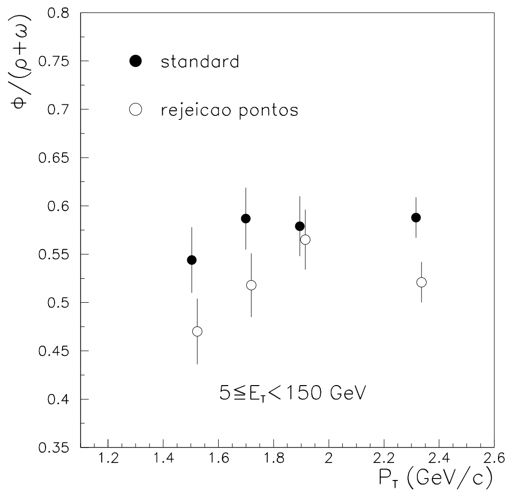

Figure 6.5: Ratios $\phi/(\rho+\omega)$ as a function of P_T, rejecting or not the data points with $\chi^2 > 5$ in the fit to the mass spectra.

in the dense medium. But this "effect" is more visible in the ϕ peak than in the $\rho + \omega$ peak, contrary to the theoretical predictions (see Chapter 1). The mass spectra transverse energy integration is not ideal to study in-medium modifications. The study per centrality regions, though, showed that in this case there are less points with bad χ^2, and the existent ones are in the ϕ peak.

The conclusion of this study is that the bad quality of the fits is mostly due to the half-height data points in the ϕ peak, in what seems to be a problem of the deconvolution method that cannot correct completely the smearing effects in the ϕ region, due to its narrow width. In reference [91] the NA38 experiment discusses in more detail the consequences of a deconvolution method in the mass spectrum that, although not the same used here, is based in similar assumptions.

6.1.3 Sensitivity to the deconvolution method

As explained in Chapter 4, in the deconvolution method used in this analysis the data are differentially corrected for acceptance and smearing, in mass or in transverse momentum, using an acceptance function convoluted with smearing given by equation 4.4.

Equation 4.2 constitutes an alternative to the method used in the standard analysis, and it is used here to evaluate the stability of the results by comparing different deconvolution methods. The signal event distributions are first corrected for smearing, and then for acceptance. Figure 6.6 shows an example using this other deconvolution deconvolution procedure. As can be seen, this method tends to smooth the data points fluctuations, and as a consequence in the fit to the mass spectra the continuum gains an increased relative weight (since for this contribution the statistics is poor and the fluctuations large).

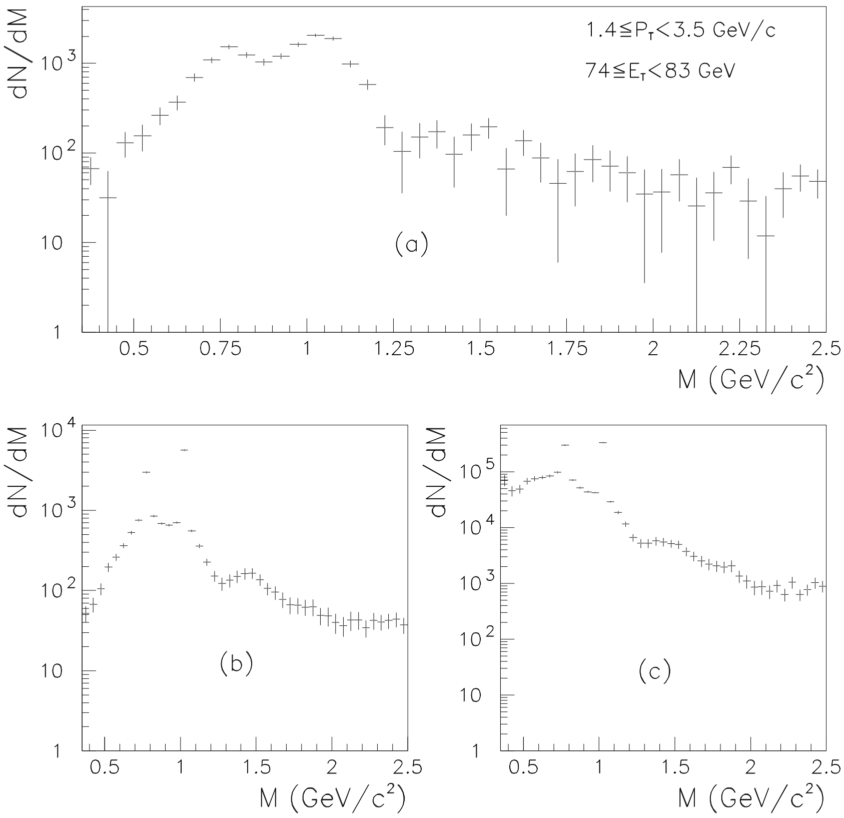

Figure 6.6: Example of the alternative deconvolution procedure. Mass distribution of signal events (a); after smearing correction (b); after smearing and acceptance correction (c).

ΔP_T (GeV/c)	$\Delta(\rho+\omega)$ %	$\Delta(\phi)$ %	$\Delta(\phi/(\rho+\omega))$ %
$1.4 \leq P_T < 1.6$	$+6.4 \pm 7.3$	-4.4 ± 4.8	-10.2 ± 6.6
$1.6 \leq P_T < 1.8$	$+7.1 \pm 6.5$	-1.8 ± 4.2	-8.3 ± 5.9
$1.8 \leq P_T < 2.0$	$+3.8 \pm 6.1$	-1.5 ± 4.4	-5.1 ± 6.0
$2.0 \leq P_T < 3.5$	$+3.5 \pm 4.2$	$+0.5 \pm 3.1$	-2.9 ± 4.3

Table 6.4: Relative differences in the number of $\rho+\omega$s and ϕs and in the ratio, for the standard analysis and for the one in which the data is deconvoluted for acceptance and smearing separately.

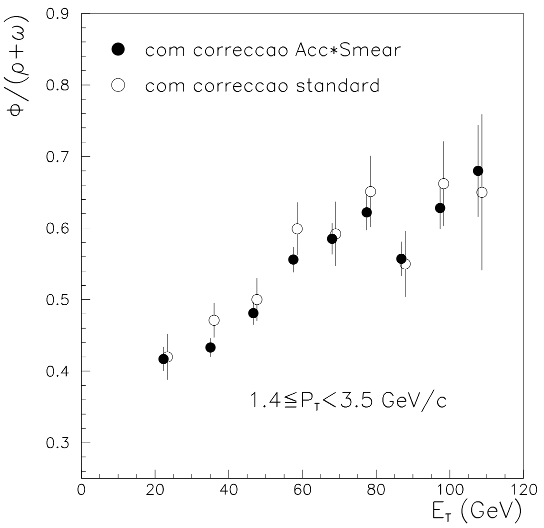

Figure 6.7: Comparison of the ratio $\phi/(\rho+\omega)$ obtained by the method of correcting for acceptance and smearing effects separately, and the standard method.

The ratio $\phi/(\rho+\omega)$ as a function of E_T obtained with this alternative deconvolution method are shown in figure 6.7. The statistical errors of the mass spectra' data points are artificially small, leading to smaller errors in the $\phi/(\rho+\omega)$ fitted, and to much worse χ^2 of the fits, as compared to the standard method. In table 6.4 the relative differences in the number of $\rho+\omega$s and ϕs and in the ratio are calculated. The observed fluctuations are smaller than the statistical error bars (except for one data point), and do not show any tendency.

6.1.4 Sensitivity to the fit function

The choice of the function to fit the mass spectra had as criterium the detailed description of the well known contributions, and the effective parameterisation of all the remaining contributions. Therefore, the ρ, ω and ϕ resonances are described by Breit-

Wigner functions. The physical continuum, resulting from the sum of all the distinct contributions to the dimuon spectrum (some of which are difficult to calculate in the low mass region, since in this region the four-momentum of the particles is typically low, and therefore one cannot use perturbative QCD) is parametrised by a decreasing exponential [1].

This section attempts to evaluate the sensitivity of the results obtained to the chosen fit functions.

The ρ line shape

In the analysis presented in Chapter 5, the three resonances ρ, ω and ϕ are described by classical Breit-Wigner functions. However, due to the fact that the ρ lifetime is extremely small (see table 1.1), there are several theoretical arguments for the non-applicability of the classical Breit-Wigner function to the ρ case. The line shape of this vector-meson is a current discussion issue. More details on this subject can be found on Appendix A.

This study uses a relativistic Breit-Wigner function as an alternative way to describe the ρ, with a mass dependent width.

$$F_{BW}(M) = \frac{M^2\ \Gamma^2_{\mu\mu}(M)}{(M^2 - m_\rho^2)^2\ +\ M^2\ \Gamma^2_{\pi\pi}(M)} \quad , \tag{6.1}$$

where the $\Gamma_{\mu\mu}$ and $\Gamma_{\pi\pi}$ widths are functions of the dimuon mass:

$$\Gamma_{\mu\mu}(M) = \Gamma_\rho\ (\frac{p_\mu}{p_\mu^\rho})\ (\frac{2\ m_\mu^2\ +\ M^2}{2\ m_\mu^2\ +\ m_\rho^2})(\frac{m_\rho}{M})^6 \tag{6.2}$$

$$\Gamma_{\pi\pi}(M) = \Gamma_\rho\ (\frac{p_\pi}{p_\pi^\rho})^3 * (\frac{m_\rho}{M})^2 \quad . \tag{6.3}$$

The p_μ and p_π variables represent the momentum of a muon and a pion, respectively, in the rest frame of the decaying ρ:

$$p_\mu = \frac{1}{2}\sqrt{M^2 - 4m_\mu^2} \tag{6.4}$$

[1]Other NA50 analysis tried to solve these problems by doing a detailed study of the several physics components that contribute to the low mass dimuon spectrum (masses smaller than m_ρ) [92].

$\phi/(\rho+\omega)$ (χ^2/ndf)	ρ as a relativistic BW	Standard analysis
$1.4 \leq P_T < 1.6$ GeV/c	0.490 ± 0.037 (5.6)	0.544 ± 0.034 (3.3)
$1.6 \leq P_T < 1.8$ GeV/c	0.582 ± 0.044 (7.9)	0.587 ± 0.032 (4.9)
$1.8 \leq P_T < 2.0$ GeV/c	0.650 ± 0.046 (7.3)	0.579 ± 0.031 (2.9)
$2.0 \leq P_T < 3.5$ GeV/c	0.785 ± 0.038 (18.4)	0.588 ± 0.021 (7.2)

Table 6.5: Ratios $\phi/(\rho+\omega)$ in 4 P_T regions, for the mass spectra integrated in $5 \leq E_T < 150$ GeV region, with ρ described by a modified relativistic Breit-Wigner function. Comparison with the standard analysis.

ΔP_T (GeV/c)	$\Delta(\rho+\omega)$ %	$\Delta(\phi)$ %	$\Delta(\phi/(\rho+\omega))$ %
$1.4 \leq P_T < 1.6$	$+12.4 \pm 10.9$	$+1.1 \pm 6.1$	-10.0 ± 8.8
$1.6 \leq P_T < 1.8$	$+1.7 \pm 8.4$	$+0.7 \pm 5.1$	-0.9 ± 9.2
$1.8 \leq P_T < 2.0$	-10.6 ± 7.7	$+0.4 \pm 5.3$	$+12.3 \pm 9.9$
$2.0 \leq P_T < 3.5$	-25.1 ± 4.6	-0.2 ± 3.6	$+33.4 \pm 8.0$

Table 6.6: Relative differences in the number of resonant events and in the $\phi/(\rho+\omega)$ ratio, with ρ parametrised by a modified relativistic Breit-Wigner function or by a classical Breit-Wigner.

$$p^{\pi} = \frac{1}{2}\sqrt{M^2 - 4m_{\pi}^2} \tag{6.5}$$

where $p_{\mu} = p_{\mu}^{\rho}$ for $M = m_{\rho}$ and $p_{\pi} = p_{\pi}^{\rho}$ for $M = m_{\rho}$.

This parameterisation of the ρ resonance is identical to the one used by the HELIOS-3 experiment from CERN [45]. The fit to the mass spectra integrated in the $5 \leq E_T < 150$ GeV region, using function 6.1 is shown in figure 6.8. Table 6.5 shows the obtained values for the ratio $\phi/(\rho+\omega)$.

The χ^2 of the fits using this ρ line shape is significantly worse than the ones obtained with the classical ρ description, showing that this is not a good alternative to adjust the experimental data, when taken together with the other contributions to the mass spectra. Still, figure 6.9 shows the comparison of the obtained ratios $\phi/(\rho+\omega)$, using this parametrisation or the classical ρ line shape.

By comparing these results with the ones from the standard analysis, one observes significant relative differences, as shown in table 6.6.

As expected, the modification in the ρ line shape has the consequence of a significant variation in the number of $\rho+\omega$ events, which is propagated to the $\phi/(\rho+\omega)$ ratio. This

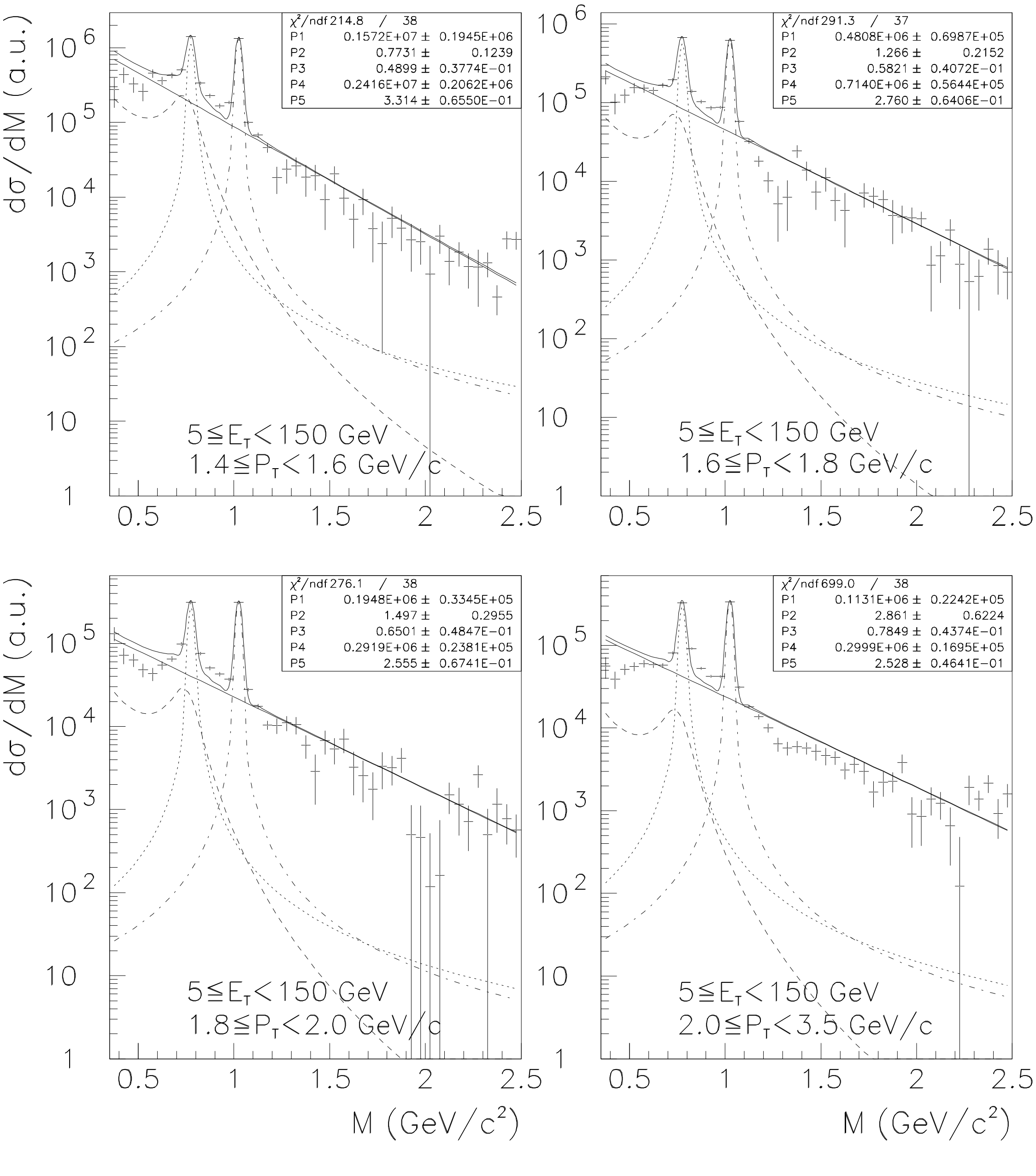

Figure 6.8: Fit to the mass spectra integrated in the region $5 \leq E_T < 150$ GeV, with a modified relativistic Breit-Wigner function for the ρ.

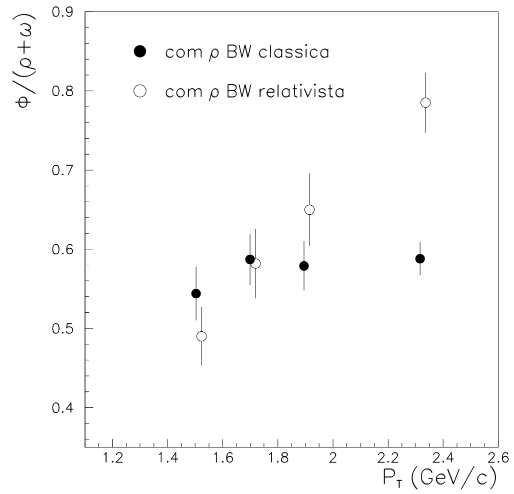

Figure 6.9: Ratios $\phi/(\rho+\omega)$ as a function of P_T, in the region $5 \leq E_T < 150$ GeV, using the relativistic BW ρ line shape, compared with the results using the classical one.

variation is not P_T dependent, and seems to be bigger for higher P_T, but the very high χ^2 per degree of freedom of these fits does not allow any conclusion. The variation on the number of ϕ events is not significant. On the other hand, one observes a strong correlation between the ρ line shape and the ω/ρ ratio (the second parameter on the mass spectra fit).

The ω/ρ ratio

In the standard analysis presented in the previous chapter, the ω/ρ ratio is one of the free parameters in the fit to the mass spectra. The ω branching ratio into dimuons was not measured experimentally, existing only an upper limit for its value [9]. However, from the arguments presented in section 5.3 and from the PDG, assuming the the ratio of the ω and ρ BRs into dimuons and the one into dielectrons is the same, one expects a ratio $\omega/\rho \approx 1.6$.

It is easily seen from the fits shown in this study that the ratios ω/ρ in Pb+Pb collisions tend to be significantly smaller than that value: $\langle\omega/\rho\rangle \approx 0.7$. This fact was also observed in the past, by the NA38 [81] experiment, in sulphur induced collisions. However, the NA50 experimental mass resolution (and also NA38) does not allow to measure this ratio, since it is not possible to distinguish experimentally between the two resonances. It is only possible to have a sensitivity to the values preferred for this ratio by the fit.

In order to study the sensitivity of the results to the ω/ρ ratio, the fit to the mass spectra is done using equation (5.2) with 4 free parameters, fixing the ω/ρ ratio to 1.6 (ta-

$\phi/(\rho+\omega)$ (χ^2/ndf)	with $\omega/\rho = 1.6$	with ω/ρ free
$1.4 \leq P_T < 1.6$ GeV/c	0.622 ± 0.040 (4.1)	0.544 ± 0.034 (3.3)
$1.6 \leq P_T < 1.8$ GeV/c	0.642 ± 0.034 (5.3)	0.587 ± 0.032 (4.9)
$1.8 \leq P_T < 2.0$ GeV/c	0.659 ± 0.036 (3.8)	0.579 ± 0.031 (2.9)
$2.0 \leq P_T < 3.5$ GeV/c	0.667 ± 0.025 (9.3)	0.588 ± 0.021 (7.2)

Table 6.7: Ratios $\phi/(\rho+\omega)$ in 4 P_T regions, for the mass spectra integrated in all the E_T region, fixing $\omega/\rho = 1.6$, compared to the standard analysis.

ΔP_T (GeV/c)	$\Delta(\rho+\omega)$ %	$\Delta(\phi)$ %	$\Delta(\phi/(\rho+\omega))$ %
$1.4 \leq P_T < 1.6$	-13.0 ± 6.6	-0.6 ± 6.1	$+14.2 \pm 10.3$
$1.6 \leq P_T < 1.8$	-8.6 ± 6.0	-0.4 ± 5.0	$+9.1 \pm 8.3$
$1.8 \leq P_T < 2.0$	-12.6 ± 5.5	-0.5 ± 5.2	$+13.8 \pm 8.6$
$2.0 \leq P_T < 3.5$	-12.1 ± 3.7	-0.4 ± 3.6	$+13.3 \pm 5.8$

Table 6.8: Relative differences in the number of $\rho+\omega$ and ϕ resonant events and in the $\phi/(\rho+\omega)$ ratio, between the analysis with fixed $\omega/\rho = 1.6$ and the standard analysis.

ble 6.7).

The relative differences comparing with the standard analysis are shown in table 6.8 and figure 6.10 . Although one observes significant differences, the χ^2 of the fits when the ω/ρ ratio is fixed is much worse, allowing for the conclusion that the fit function does not have sufficient flexibility for an accurate description of the data with that ratio fixed. The ω/ρ value is strongly correlated with the ρ line shape, and also with the shape of the continuum. One can also conclude that by fixing $\omega/\rho = 1.6$ the ratio $\phi/(\rho+\omega)$ increases systematically by about (13±8)%.

6.1.5 Sensitivity to the ρ pole

In order to study the sensitivity of the fitting method to the ρ pole, this was let as an additional free parameter in the fit to the mass spectra. One of the expected signatures for the formation of a very hot and dense interaction medium is a shift in the resonances' poles, in particular for the ρ, as was explained in Chapter 1. One expects that, if these hadronic modifications will be visible at all in the NA50 experiment, it will be in the ρ resonance, according to the theoretical predictions. Although, the experimental mass resolution is higher than 70 MeV/^{2} in the low mass region, so probably the experiment would not be able to observe such modifications.

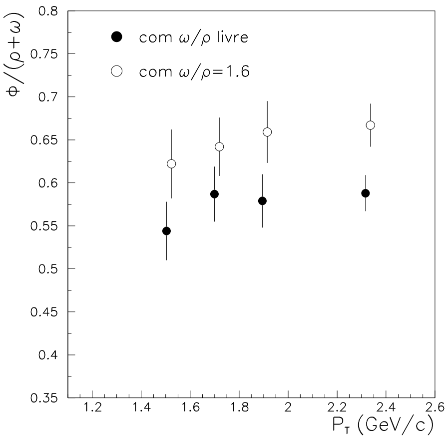

Figure 6.10: Ratios $\phi/(\rho+\omega)$ as a function of P_T, for $5 \leq E_T < 150$ GeV, fixing $\omega/\rho =$ 1.6 . Comparison with the standard analysis.

Figure 6.11 shows the value of the ρ pole as a function of the transverse energy. When this is let as a free parameter of the mass spectra fits one observes that the pole's mean value is compatible with the PDG one ($m_\rho = 769.3 \pm 0.8$ MeV/c^2), taking errors into account.

6.1.6 The continuum line shape

By fitting the continuum in the MC reconstructed mass distributions, using an empirical function of as many free parameters as needed, one can study the influence of the continuum line shape in the final results. This function is used later to adjust the experimental mass spectra, with only the normalisation parameter let free.

The reconstructed Monte-Carlo events (with statistics similar to the experimental data) are treated with the same method applied to the experimental events; i.e., the distributions are deconvoluted using differential acceptances. The resulting MC spectra are fitted with a function:

$$\begin{aligned}\frac{d\sigma}{dM} &= P_1 BW_\rho + P_2 BW_\omega + P_3 BW_\phi + P_4(exp(-P_5 M) + \\ &P_6 exp(-P_7(M-P_8)^2) + P_9 exp(-P_{10}M) + P_{11} exp(-P_{12}M)) \quad .\end{aligned} \tag{6.6}$$

Parameters P_5 to P_{12} from the MC fit are used in the experimental spectra fit as fixed parameters — thus the experimental mass fits have only 4 free parameters, for the normalisations of resonances and the continuum. Figure 6.12 shows these fits to the experimental data. The ratios $\phi/(\rho+\omega)$ obtained are presented in table 6.9 .

The ratio $\phi/(\rho+\omega)$ obtained when the continuum shape is fixed from the Monte-Carlo, is systematically higher than in the standard method, as can be seen in figure 6.13

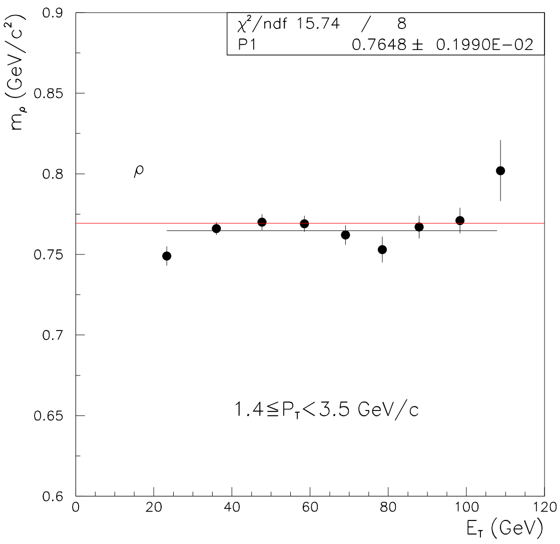

Figure 6.11: Stability of the ρ pole, when it is let as a free parameter of the mass spectra fits. The red line shows the ρ pole given by the PDG, and the black one the mean value obtained here.

and table 6.10 . This is due to the fact that this continuum line shape has a stronger contribution in the $\rho+\omega$ region. Still, the increase of the ratio $\phi/(\rho+\omega)$ with centrality, followed by a saturation continues to be visible, even if the error bars are bigger when using this method.

6.1.7 Study of the M_T distributions' scaling

The scaling of the transverse mass distributions of the $\rho + \omega$ and ϕ, given by a modified Bessel function (1.7 was approximated in this study by the equation (5.4), appropriate for low mass resonances with transverse momentum relatively high. Although, other heavy ion experiment have also been studying these resonances' effective temperatures, namely for the ϕ, using a different scaling in M_T, simpler but theoretically less correct:

$$\frac{d\sigma}{dM_T} \propto M_T\ exp(-M_T/T) \quad . \tag{6.7}$$

In order to compare results with other experiments, and also to study the sensitivity of the effective temperatures to the scaling function used, the analysis presented in section 5.2 is repeated using function (6.7) to fit the M_T differential cross-sections of the resonances (considering both statistical and systematical errors). The effective temperatures obtained are $T_{\rho+\omega}$ = 231.6 ± 7.7 MeV and T_ϕ = 226.6 ± 4.8 MeV. These are 10 MeV

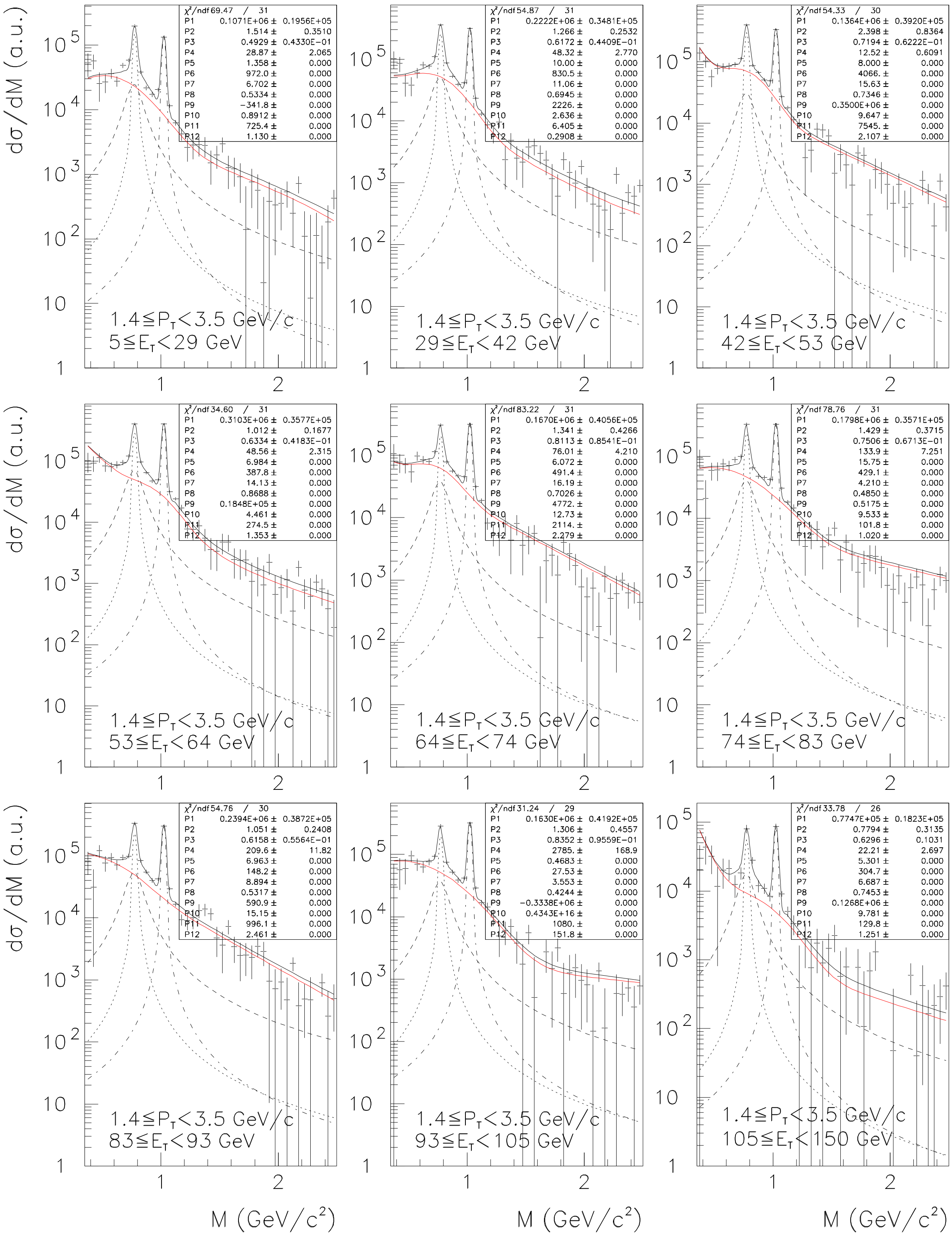

Figure 6.12: Fit to the mass spectra in 9 E_T regions, using the continuum line shape fitted in the reconstructed MC distributions (in red).

$\phi/(\rho+\omega)$ (χ^2/ndf)	with a continuum fitted in the MC	Standard analysis
$5 \leq E_T < 29$ GeV	0.493 ± 0.043 (2.2)	0.420 ± 0.032 (2.2)
$29 \leq E_T < 42$ GeV	0.617 ± 0.042 (1.8)	0.471 ± 0.024 (2.8)
$42 \leq E_T < 53$ GeV	0.719 ± 0.067 (1.8)	0.500 ± 0.030 (2.8)
$53 \leq E_T < 64$ GeV	0.633 ± 0.043 (1.1)	0.599 ± 0.037 (1.8)
$64 \leq E_T < 74$ GeV	0.811 ± 0.078 (2.7)	0.592 ± 0.045 (2.9)
$74 \leq E_T < 83$ GeV	0.751 ± 0.066 (2.5)	0.651 ± 0.050 (3.0)
$83 \leq E_T < 93$ GeV	0.616 ± 0.056 (1.8)	0.550 ± 0.046 (1.9)
$93 \leq E_T < 105$ GeV	0.835 ± 0.107 (1.1)	0.662 ± 0.059 (1.8)
$105 \leq E_T < 150$ GeV	0.630 ± 0.099 (1.3)	0.650 ± 0.109 (1.3)

Table 6.9: Ratios $\phi/(\rho+\omega)$ in 9 transverse energy regions, using a continuum line shape fitted in the MC. Comparison with the results from the standard analysis.

higher than the ones obtained with the scaling from equation (5.4). Figure 6.14 shows these new fits.

6.2 Comparison with other results

The low mass vector-mesons $\rho+\omega$ and ϕ produced in ultra-relativistic heavy ion collisions have been studied since 15 years ago, with the use of heavier and heavier AB systems, and also different beam energies. The comparison with proton induced collisions is also very important to reach any conclusions.

When one wants to compare different experiments, or even the same experiment but with different setups, one should find variables that are independent of the specific conditions of the data acquisition. Therefore, instead of the neutral transverse energy of the collisions, a variable that depends on the system in collision, another estimator of the centrality is used, that is the number of participants N_{part}. This variable is defined in Appendix B and its calculation to use in this analysis is presented in Chapter 5.

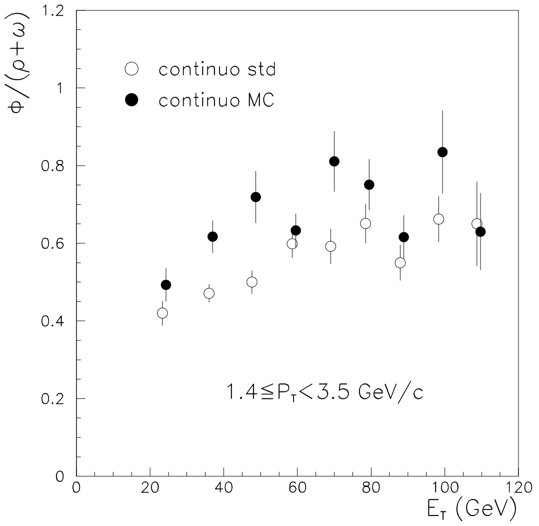

Figure 6.13: Ratios $\phi/(\rho+\omega)$ obtained using a continuum fitted in the reconstructed and modified MC, or using the standard decreasing exponential.

6.2.1 Comparison with other analyses

The Pb+Pb data with a beam of 158 GeV/nucleon, taken by the NA50 experiment in 1996 were object of a study for the low mass resonances region, with an analysis method totally different from the one presented here [93] [2].

In that study the non-deconvoluted mass spectra (that is, the mass spectra in the measured variable) were fitted, by fixing the ratio $\omega/\rho = 1.6$. Figure 6.15 shows the comparison between the results of the these two data periods, analysed with different methods, but imposing on both the ratio $\omega/\rho = 1.6$ [3]. The results are in good agreement, within statistical errors.

The resonances' effective temperatures obtained by that analysis — $T_{\rho+\omega} = 213 \pm 4$ MeV and $T_\phi = 217 \pm 5$ MeV — are also identical to the ones here obtained. Table 6.11 summarises these results.

As was mentioned in Chapter 1, NA49 is another experiment that measured the ϕ effective temperature in Pb+Pb collisions at 158 A GeV/c, but using the decay channel $\phi \to K^+K^-$. This experiment uses equation (6.7) as an approximation to the Bessel

[2]The analysis presented in [93] obtains the ratio $\phi/(\rho+\omega)$ from the fit to measured mass spectra. The acceptance correction is done afterwards, using a global acceptance value for each resonances' mass region.

[3]In the results of the analysis [93] here presented, a correction is included for the N_{part} calculation. This correction is due to the trigger timing problem (unknown by the time the analysis was done). Thus, the expression $E_T^{\mu\mu}(1996) = 1.020 \times 0.294\ N_{part}$ is used.

ΔE_T (GeV)	$\Delta(\rho+\omega)$ %	$\Delta(\phi)$ %	$\Delta(\phi/(\rho+\omega))$ %
$5 \leq E_T < 29$	-15.2 ± 9.0	-0.5 ± 8.2	$+17.3 \pm 13.5$
$29 \leq E_T < 42$	-26.0 ± 6.8	-2.9 ± 5.2	$+31.2 \pm 11.2$
$42 \leq E_T < 53$	-31.7 ± 7.6	-1.8 ± 5.9	$+43.9 \pm 16.0$
$53 \leq E_T < 64$	-7.8 ± 8.5	-2.6 ± 5.4	$+5.7 \pm 9.8$
$64 \leq E_T < 74$	-27.4 ± 10.3	-0.6 ± 6.9	$+37.0 \pm 16.8$
$74 \leq E_T < 83$	-14.4 ± 10.7	-1.3 ± 6.8	$+15.3 \pm 13.4$
$83 \leq E_T < 93$	-10.1 ± 11.1	$+0.6 \pm 7.6$	$+11.8 \pm 13.8$
$93 \leq E_T < 105$	-22.6 ± 12.3	-2.4 ± 7.2	$+26.1 \pm 19.7$
$105 \leq E_T < 150$	$+3.0 \pm 24.5$	-0.3 ± 14.1	-3.2 ± 22.3

Table 6.10: Relative differences in the number of $\rho + \omega$ and ϕ resonant events and in the ratio $\phi/(\rho+\omega)$, between the standard analysis and one using the continuum fitted in the MC.

Effective temperature (MeV)	$\rho+\omega$	ϕ
dN/dM : Deconvolution method dN/dM$_T$: $M_T^{3/2}\ exp(-M_T/T)$	219.3 ± 7.0	215.5 ± 4.4
dN/dM : Deconvolution method dN/dM$_T$: $M_T\ exp(-M_T/T)$	231.6 ± 7.7	226.6 ± 4.8
dN/dM : Method from ref. [93] dN/dM$_T$: $M_T^{3/2}\ exp(-M_T/T)$	213 ± 4	217 ± 5
dN/dM : Method from ref. [93] dN/dM$_T$: $M_T\ exp(-M_T/T)$	224 ± 4	228 ± 5

Table 6.11: $\rho + \omega$ and ϕ effective temperatures, obtained with two different methods of analysis, and different scalings in M_T, from the NA50 experiment.

function to fit the M_T distributions, obtaining $T_\phi = 305 \pm 15$ MeV [49]. The fit using equation (5.4) leads to temperatures about 10 MeV lower than the ones using equation (6.7), as explained above. Still, the difference between temperatures from NA49 and NA50 is much higher. Some theoretical explanations for this discrepancy are based in the hadronic multiple scattering of the kaons in the dense medium, resulting in an increased ϕ effective temperature as measured by NA49 [51] [52][53]. In this sense, T_ϕ measured by NA50 would correspond to a more primordial dense medium.

Also, NA49/SPS as well as STAR/RHIC experiments observe a scaling violation, with effective temperatures that increase proportionally to the mass of the concerned particles — thus supporting for the existence of flow.

Phenomenological calculations based on the microscopic coalescence re-hadronization model for quarks in a thermalized medium (the MICOR model [94]) predict the effective

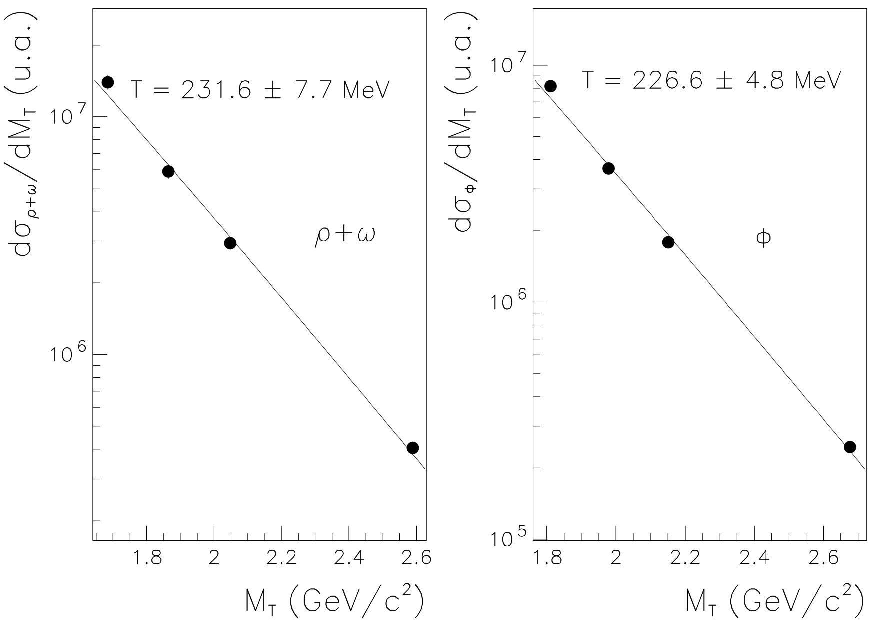

Figure 6.14: Effective temperatures fit for $\rho + \omega$ and for ϕ, including statistic and systematic errors in the cross-sections, and using as M_T scaling $M_T\ exp(-M_T/T)$.

temperature of hadrons produced in Pb+Pb collisions at 158 GeV/nucleon. T_ϕ from this model agrees well with the one measured by NA50 (the prediction for $\rho + \omega$ is also in good agreement, while for the J/ψ the model over-estimates the measured temperature), as shown in figure 6.16 .

The NA49 experiment measures the total multiplicity of ϕs produced in the whole kinematical domain as being $\langle\phi\rangle = 7.6 \pm 1.1$ for central Pb+Pb collisions ($b < 3.5$) [49]. A simple calculation allows to extrapolate this result for the transverse mass and rapidity regions of NA50:

$$\langle\phi\rangle(NA49 \rightarrow NA50) \approx 7.6 \frac{\int_{1.7}^{3.6} M_T\ exp(-M_T/T) dM_T}{\int_{1}^{2.2} M_T\ exp(-M_T/T) dM_T} \frac{\int_3^4 exp(-\frac{(y-2.9)^2}{2\sigma_y^2}) dY}{\int_3^{3.8} exp(-\frac{(y-2.9)^2}{2\sigma_y^2}) dY} \tag{6.8}$$

using $T = 305 \pm 15$ MeV and $\sigma_y = 1.22 \pm 0.16$, measured values from NA49 for Pb+Pb collisions at 158 GeV/nucleon. Expression (6.8), corrected for the branching ratio into K^+K^- (49.2%) gives $\langle\phi\rangle(NA49 \rightarrow NA50) = 0.45$. This multiplicity can be compared with the one from section 5.3.2 (figure 5.16), after the correction to the whole $\cos\theta_{CS}$ domain is done:

$$\langle\phi\rangle(NA50) = 0.26 \times 2/f_{cos\theta} \tag{6.9}$$

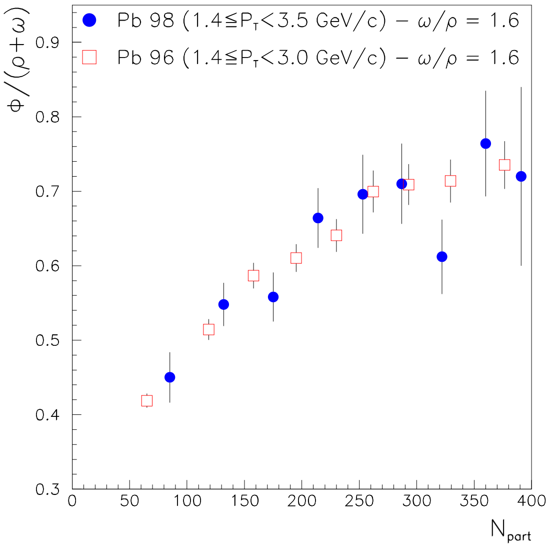

Figure 6.15: Comparison between different analyses of the lead data, this analysis and the non-deconvoluted analysis.

where the factor 2 comes from the extrapolation of the $\cos\theta_{CS}$ uniform distribution from the region [-0.5;0.5[to the total region [-1;1[; and $f_{cos\theta} = 1.025$ is a corrective factor to the $\cos\theta_{CS}$ acceptance, needed because the MC used was generated with a $(1 + \cos^2\theta)$ distribution instead of a uniform one, appropriate for the resonances. Equation (6.9) gives the value $\langle\phi\rangle(NA50) = 0.51$. Although this is only a rough calculation, since the systematical errors in the multiplicity measurement are not fully evaluated, there seems to be a reasonable agreement between the two experiments with respect to the ϕ multiplicity [4].

6.2.2 Comparison with other systems

The NA38 experiment, that preceded NA50, studied the collisions induced by sulphur ions at an energy of 200 GeV/nucleon, with thin targets of sulphur, copper and uranium (the first two represent short data takings, while S+U collisions were done with high statistics). In order to be able to compare the results with a reference, data were also taken using a proton beam with 200 GeV/c on an extended tungsten target [95].

Figure 6.17 presents the ratio $\phi/(\rho+\omega)$ as a function of the transverse momentum for Pb+Pb collisions as compared to S+S, S+Cu, S+U and p+W collisions. These lighter systems were analysed in the past with the same method here presented [81][96] [95]. As

[4] **Note:** After this thesis was presented, further discussion with NA49 collaborators allowed to conclude that the value $\langle\phi\rangle = 7.6 \pm 1.1$ from NA49 is already divided by the width of the rapidity window, and the branching ratio into kaons is already taken into account. Thus, $\langle\phi\rangle(NA49 \to NA50) = 1.35$, not compatible with the value from NA50 $\langle\phi\rangle(NA50) = 0.51$.

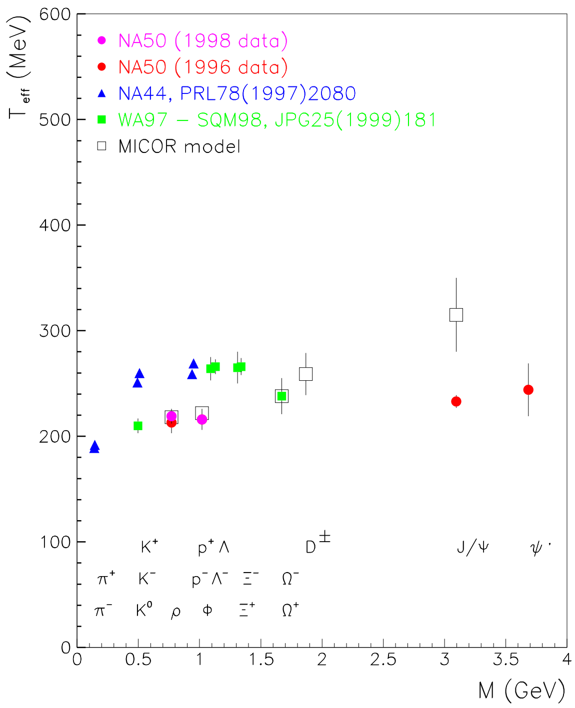

Figure 6.16: Measured hadronic effective temperatures for Pb+Pb collisions at 158 GeV/nucleon, compared to the quarks coalescence model MICOR.

can be seen, the ratio $\phi/(\rho+\omega)$ increases with AB. This was already observed for lighter systems and is confirmed in lead induced collisions, but none of the systems shows a dependence of the ratio with P_T.

The analysis as a function of the number of participant nucleons is compared with the NA38 results in figure 6.18, showing a gradual increase with the centrality of the collisions, and what seems to be a saturation for high centralities. Although the analysed region in Pb+Pb is $1.4 \leq P_T < 3.5$ GeV/c, while for the NA38 data it was $0.6 \leq P_T < 3.0$ GeV/c, since there is no dependence of the ratio with P_T, the difference in the P_T domains is irrelevant. The increase of the ratio $\phi/(\rho+\omega)$ in lead central collisions is shown in figure 6.18 to be a factor of 7 higher than this ratio in p+W collisions.

To check that the increase in the ratio $\phi/(\rho+\omega)$ with centrality comes from an additional production of ϕs, in NA38 the dependence of the $\rho+\omega$ and ϕ cross-sections with AB was studied [44] (while in NA50 this is checked studying the resonances' multiplicities). By comparing p+W and S+U collisions at 200 GeV/nucleon, and assuming that $\sigma \propto (A \cdot B)^{\alpha}$, the NA38 experiment obtained $\alpha_{\rho+\omega} = 1.00 \pm 0.02 \pm 0.07$ and $\alpha_{\phi} = 1.23 \pm 0.03 \pm 0.05$.

As for the effective temperatures analysis, one obtains the same temperatures for the $\rho+\omega$ and for ϕ in Pb+Pb and in lighter systems, namely the S+U system (figure 6.19), and no dependence of the temperature with the centrality is seen.

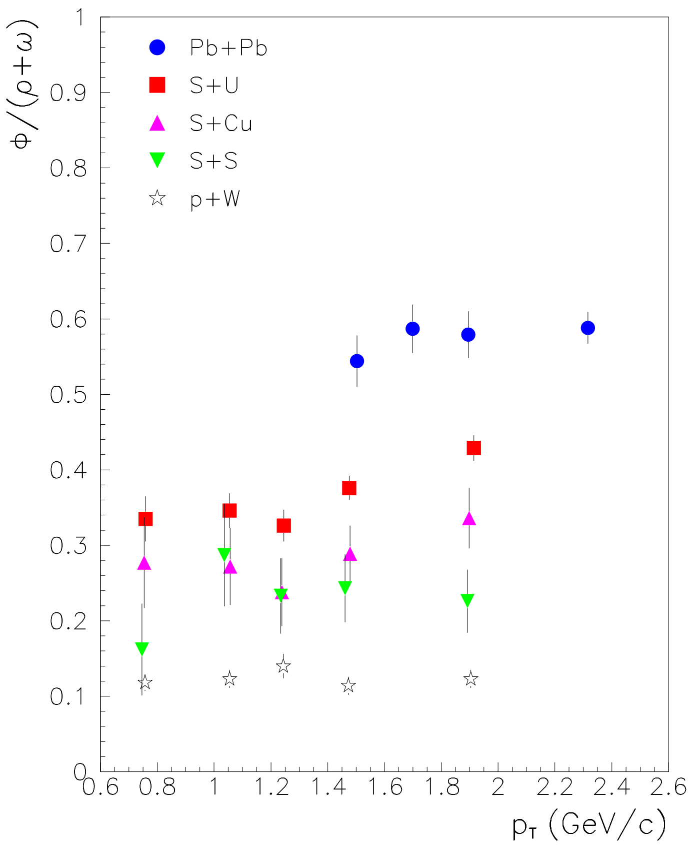

Figure 6.17: Comparison of the ratio $\phi/\rho+\omega)$ as a function of P_T for Pb+Pb collisions at 158 GeV/nucleon with sulphur and proton induced collisions at 200 GeV/nucleon (taken by NA38).

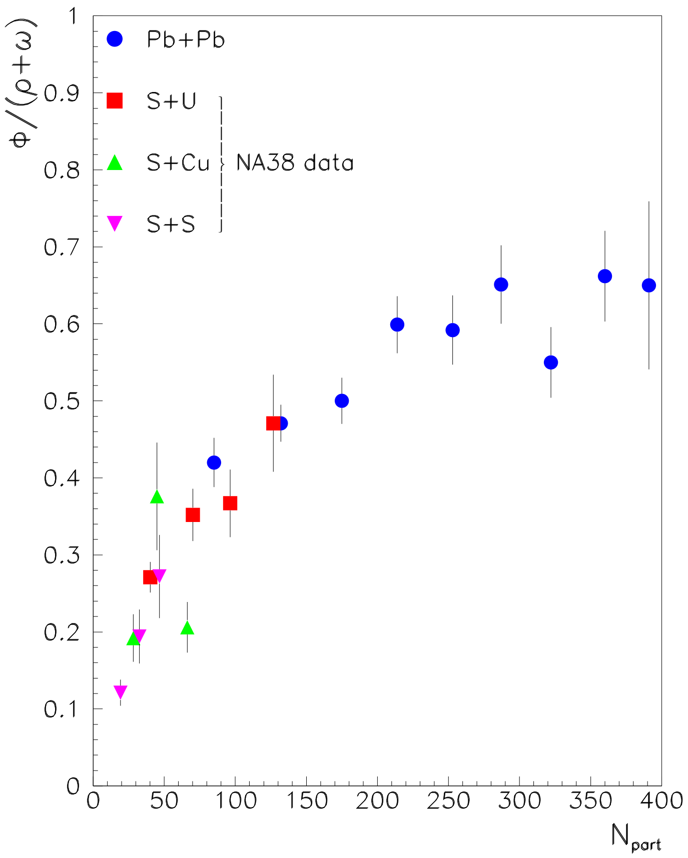

Figure 6.18: Comparison of the ratio $\phi/(\rho+\omega)$ as a function of E_T for Pb+Pb collisions at 158 GeV/nucleon with sulphur induced collisions at 200 GeV/c (NA38).

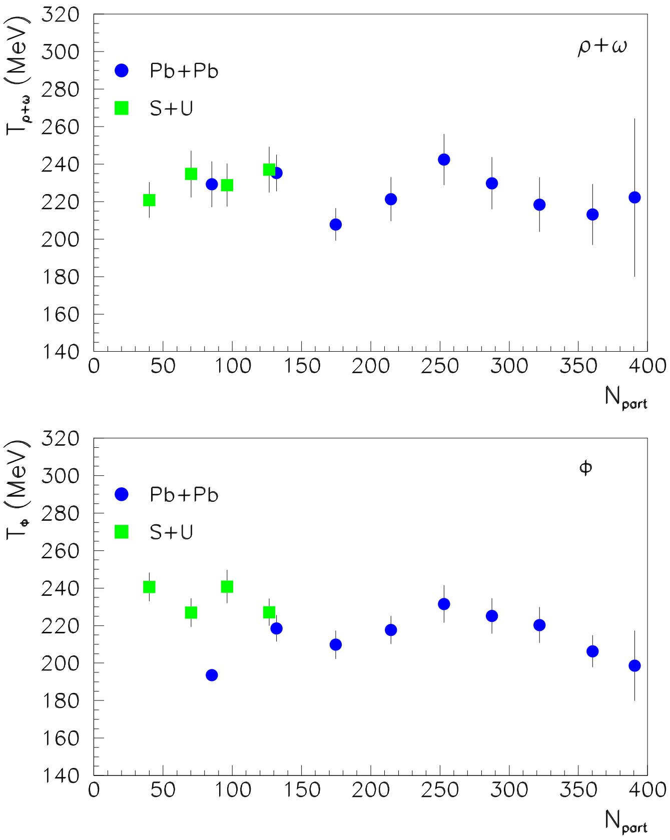

Figure 6.19: Effective temperatures of $\rho+\omega$ and ϕ as a function of E_T obtained in Pb+Pb collisions at 158 GeV/nucleon. Comparison with temperatures obtained in S+U collisions at 200 GeV/nucleon (NA38).

6.3 Conclusions

An increase of the ratio $\phi/(\rho+\omega)$ with the neutral transverse energy, or with the number of participant nucleons, is observed in Pb+Pb collisions at 158 GeV/nucleon. This increase is present up to a transverse energy of $\approx$ 80 GeV (or $N_{part} = 290$), and it is followed by a saturation for the most central collisions. This kind of trend was already observed by the NA38 experiment in sulphur induced collisions at 200 GeV/nucleon. The ratio $\phi/(\rho+\omega)$ for central S+U collisions is compatible with the one for peripheral Pb+Pb collisions.

The $\rho+\omega$ and ϕ multiplicities' study as a function of E_T shows that both increase with the centrality of the collisions. The measured total multiplicity of ϕs in central collisions is in agreement with the one from the NA49 experiment [5]. The NA50 obtained value is only qualitative, since the full estimation of the systematic errors involved in this measurement cannot done.

From the multiplicity of resonant events per participant, as a function of the number of participant nucleons, one can conclude that the increase in the ratio $\phi/(\rho+\omega)$ is due to an additional production of ϕs with centrality. While the multiplicity of $\rho+\omega$ per participant keeps constant with the transverse energy, the number of ϕs per participant increases with E_T.

The ratio $\phi/(\rho+\omega)$ does not depend on the dimuons transverse momentum for Pb+Pb collisions, as was observed by NA38 for sulphur induced collisions.

The ratio ω/ρ cannot be measured by NA50, due to the mass resolution of the experiment, that is not sufficient to distinguish the two resonances. Still, the data seems to favour, for Pb+Pb collisions, a ratio lower than the one expected from the PDG (obtained experimentally mostly from proton induced collisions). In principle, this can be clarified by NA60 experiment in 2003, with In+In collisions. This experiment expect to have a mass resolution in the low masses region of $\approx$ 20 MeV, thanks to a pixels vertex detector, thus being able to separate the ρ and the ω resonances.

Still due to the insufficient mass resolution, NA50 cannot distinguish vector-meson modifications in the dense medium. This leads us to the conclusion that, if such modifications occur, they must be small (smaller than 70 MeV/c^2, the experimental resolution in this mass region).

The effective temperatures of the resonances $\rho+\omega$ and ϕ in the dimuon decay channel are identical, around 216 - 219 MeV. These temperatures do not follow the linear behaviour the the mass, observed for other hadrons. Also the ϕ temperature in the dilepton channel is confirmed to be smaller than the corresponding one in the kaons channel; this seems to be understood from the final state multiple scattering of the kaons.

[5] **Note:** As explained before, after this thesis was presented it was found out that these two measurements are not in agreement.

The $\rho + \omega$ and ϕ effective temperatures is the same, within errors, for Pb+Pb and S+U collisions, and higher than the one for p+W collisions. These effective temperatures are shown to be independent of the centrality of the collisions.

Appendix A

The Breit-Wigner functions

The shape of the cross-section for a resonance decay is in general well described by a classical Breit-Wigner function:

$$F_{BW}(M) = \frac{\Gamma^2/4}{(M - m_R)^2 \ + \ \Gamma^2/4} \tag{A.1}$$

where Γ is the decay width of the resonance R, m_R the resonance mass and M the invariant mass. The corresponding relativistic expression is:

$$F_{BW}(M) = \frac{m_R^2 \ \Gamma^2}{(M^2 - m_R^2)^2 \ + \ m_R^2 \ \Gamma^2} \quad . \tag{A.2}$$

There are, however, many other shapes for the Breit-Wigner function. A more suitable expression to describe the kinematic dependencies can be obtained by substituting $(m_R \ \Gamma)$ by $(M \ \Gamma)$ [9] [97]:

$$F_{BW}(M) = \frac{M^2 \ \Gamma^2}{(M^2 - m_R^2)^2 \ + \ M^2 \ \Gamma^2} \quad . \tag{A.3}$$

Sometimes, there is more than one possible decay channel for the same resonance. In those cases, the shape of the invariant mass spectra in a given channel $(R \to rr)$ will be given by the Breit-Wigner function:

$$F_{BW}(M) = \frac{M^2 \ \Gamma^2_{R \to rr}}{(M^2 - m_R^2)^2 \ + \ M^2 \ \Gamma^2_{total}} \tag{A.4}$$

where

$$\Gamma_{R \to rr} = BR_{R \to rr} \cdot \Gamma_{total} \tag{A.5}$$

The above expressions describe narrow width resonances, as the vector-mesons ω or ϕ. On the other hand, short lived resonances require the introduction of a mass dependent width. Equation (A.3) then becomes [98]:

$$F_{BW}(M) = \frac{M^2\ \Gamma^2(M)}{(M^2 - m_R^2)^2\ +\ M^2\ \Gamma^2(M)} \tag{A.6}$$

with

$$\Gamma(M) = \Gamma_R\ (\frac{p_r}{p_r^o})^{2l+1}\frac{\varrho(M)}{\varrho(m_R)} \quad , \tag{A.7}$$

$\varrho(M)$ being a slowly varying function of M, to be determined for each specific case, either through perturbation theory or empirically. In equation A.7, l is the relative angular momentum of the particles to which R decays; and p_r is the momentum of one of the decay products r in the mother particle's rest frame ($p_r^o = p_r$ for $M = m_R$).

The main decay channel of the neutral vector-meson ρ^o is $\rho^o \rightarrow \pi^+\pi^-$, with a decay branching ratio $BR \approx 100\%$. Since the spin of the vector-meson is $S = 1$, while the pion spin is $s = 0$, the relative angular momentum of the two pion system is $l = 1$ — thus represented by a P-wave. An example of an adequate empirical parametrisation for $\Gamma_{\rho\rightarrow\pi\pi}$ (in terms of spin and parity: $(1^-) \rightarrow (0^-)(0^-)$) is [99]:

$$\varrho(M) = \frac{1}{(p_\pi)^2 + (p_\pi^o)^2} \tag{A.8}$$

p_π is the momentum of one of the pions in the ρ^o rest frame; and so:

$$p_\pi = \frac{1}{2}\sqrt{M^2 - 4m_\pi^2} \tag{A.9}$$

$$p_\pi^o = \frac{1}{2}\sqrt{m_\rho^2 - 4m_\pi^2} \quad . \tag{A.10}$$

However, this was not the parametrisation used in this study; the one used instead is obtained by perturbative field theory and will be presented in what follows.

The ρ^o ($S = 1$) decay into a muon pair has a BR $\approx 4.6 \times 10^{-5}$. Since the muons have spin $s = 1/2$, the relative angular momentum of the $\mu^+\mu^-$ system must be $l = 0$, and thus $\rho \rightarrow \mu^+\mu^-$ is represented by a S-wave.

The ρ^o invariant mass distributions in the $\mu^+\mu^-$ channel must then obey, according to equations (A.4) and (A.6), to a Breit-Wigner function:

$$F_{BW}(M) = \frac{M^2\ \Gamma^2_{\rho\rightarrow\mu\mu}(M)}{(M^2 - m_R^2)^2\ +\ M^2\ \Gamma^2_{\rho\rightarrow\pi\pi}(M)} \tag{A.11}$$

where Γ_{total}, in the denominator, was replaced by $\Gamma_{\rho\rightarrow\pi\pi}$, as a good approximation.

The $\rho \rightarrow rr$ decay width can be written generically as:

$$\Gamma_{\rho\rightarrow rr}(M) = \frac{\sum|\mathcal{M}(\rho\rightarrow rr)|^2}{\sum_{spin}|\mathcal{M}^o(\rho\rightarrow rr)|^2}\ \frac{m_\rho^2}{M^2}\ \frac{|p_r|}{|p_r^o|}\Gamma_{\rho\rightarrow rr} \quad , \tag{A.12}$$

$\mathcal{M}$ being the transition amplitude for the ρ^o decay process, summed over all spin states. The ^{o} symbol (in p_r^o and $\mathcal{M}^o$) stands for the original expression evaluated at $M^2 = m_\rho^2$. The partial widths used in the analysis reported in this study, and referred to as "relativistic Breit-Wigner for ρ^o", are thus obtained as [100]:

$$\Gamma_{\rho\rightarrow\pi\pi}(M) = \frac{|p_\pi|^3}{|p_\pi^o|^3}\ (\frac{m_\rho}{M})^2\ \Gamma_{\rho\rightarrow\pi\pi} \tag{A.13}$$

$$\Gamma_{\rho\rightarrow\mu\mu}(M) = \frac{p_\mu}{p_\mu^o}\ \frac{(2m_\mu^2+M^2)}{(2m_\mu^2+m_\rho^2)}\ \frac{m_\rho^6}{M^6}\ \Gamma_{\rho\rightarrow\mu\mu} \tag{A.14}$$

with

$$p_\mu = \frac{1}{2}\sqrt{M^2-4m_\mu^2} \tag{A.15}$$

$$p_\mu^o = \frac{1}{2}\sqrt{m_\rho^2-4m_\mu^2} \quad . \tag{A.16}$$

The shape of the relativistic Breit-Wigner function used to parametrise the ρ^o peak in the dimuon invariant mass spectra is similar to the one used by the HELIOS-3 experiment [45] for the same decay channel, apart from the fact that HELIOS-3 uses in the numerator of expression (A.11) the expression $\sigma(M)M^2\Gamma^2_{\rho\rightarrow\mu\mu}(M)$. This $\sigma(M)$ factor, the production cross-section for a stable particle of mass M, summed over all spin states, can be interpreted as the non-resonant background under the resonance's peak, due to the interference between the vector-mesons ρ and ω, with poles very close. In the present study, the continuum spectra is described in an effective way, and so the contribution of the ρ-ω interference is also taken into account. This is the reason why the σ(M) factor was not included in the ρ^o shape.

In figure A.1 different possible shapes for the parametrisation of ρ are compared. It can be seen that, as expected, the classical and relativistic Breit-Wigner functions are exactly identical for M near m_ρ. The main difference is introduced by the assumption of a mass dependent width. The peak of the relativistic Breit-Wigner function used in this study (A.11) is shifted to lower masses by 26 MeV with respect to the relativistic function with fixed width (A.3).

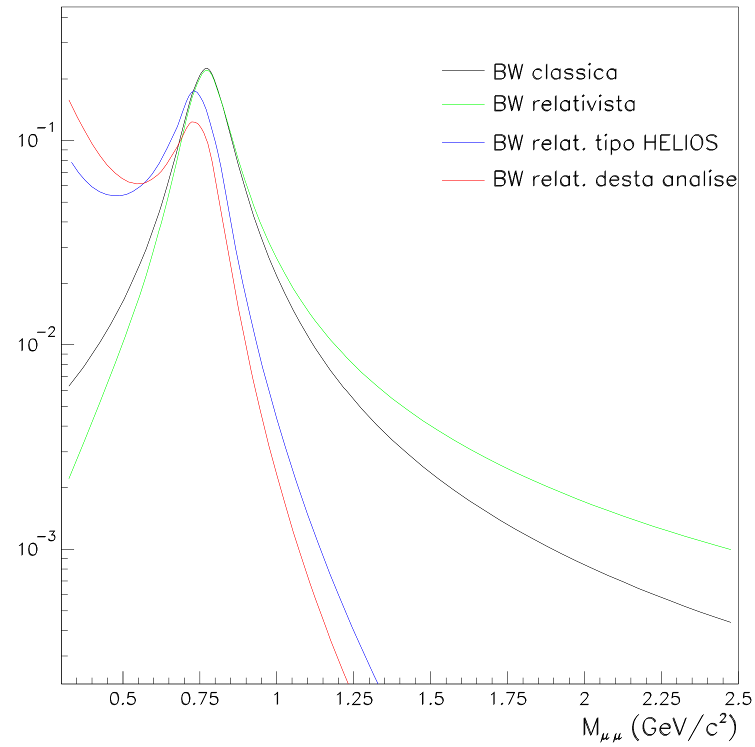

Figure A.1: Comparison of different possible parameterisations of ρ^o, being the classical and relativistic with fixed width; and the ones used by HELIOS and the present study, relativistic and with variable width.

Appendix B

Definition of some interesting variables

B.1 Rapidity and pseudo-rapidity

A particle's rapidity is an adimensional kinematic variable widely used in experimental particle physics. It is defined from the components of the momentum four-vector of the particle, according to:

$$y = \frac{1}{2}\ln(\frac{p_o + p_z}{p_o - p_z}) \quad . \tag{B.1}$$

In the non-relativistic limit, the rapidity of a particle travelling in the longitudinal direction is given by its velocity in units of c. The rapidity y in a Lorentz frame is related to the rapidity y' in another Lorentz frame by the addition of a constant, which makes it a practical variable for the description of relativistic particle dynamics. In Pb+Pb collisions at 158 GeV per nucleon, the relation between the dimuon rapidity in the laboratory frame and in the dimuon centre-of-mass frame is, then, given by:

$$y^{CM} = y^{lab} - y_o \tag{B.2}$$

where y_o is the rapidity of the centre-of-mass in the laboratory frame. Being:

$$y_o = \tanh^{-1}\frac{P_{beam}}{E_{beam}} \tag{B.3}$$

which, for collisions with 158 A GeV/C lead beam, gives $y_o = 5.82$. Being that the rapidity of the projectile is 5.82, and the target rapidity is 0, the central rapidity in the laboratory frame is of 2.91 [101].

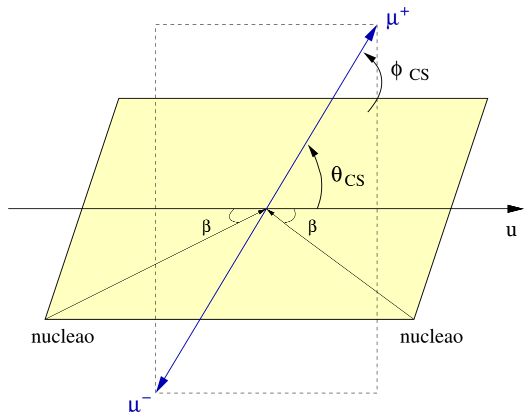

Figure B.1: The Collins-Soper frame and definition of the θ_{CS} and ϕ_{CS} angles.

The fact that, in many experiments, only the emission angle of the particle relative to the beam direction can be measured, lead to the definition of pseudo-rapidity:

$$\eta = -\ln(\tan\frac{\theta}{2}) \tag{B.4}$$

where θ is the angle between the momentum vector of the particle $\vec{p}$ and the beam direction.

The two variables, rapidity and pseudo-rapidity, coincide when the momentum $\vec{p}$ is large: $|\vec{p}| \approx E$.

B.2 The Collins-Soper frame

The Collins-Soper frame [102] is defined at the dimuon centre-of-mass. Being the u axis the bisectrix of the angle formed by the parent-nucleons of target and projectile, θ_{CS} is the angle between the direction of one of the muons and the u axis. The angle ϕ_{CS} is defined between the two nucleon collision plane and one of the muons. Figure B.1 shows the definition of these angles.

B.3 Variables for collision centrality

In ultra-relativistic heavy-ion collisions the estimation of the collision's centrality is crucial. Being the heavy ions extensive and not necessarily spherical objects, all possible collision types must be distinguished, from very peripheral collision (in which the ions interact "superficially") to central collisions (i.e., situations of head-on collisions). There are several possibilities for centrality estimators, ranging from the transverse energy released in the collision (which is a direct measurement of centrality but does not allow for the comparison of results obtained with different systems due to geometrical differences) to more sophisticated estimators, based on theoretical models.

B.3.1 Energy density

The energy density measures centrality while taking into account the collision geometry. It is thus an universal thermodynamical variable which allows the comparison of different experiments and collision systems. It is defined from the transverse energy released in the collision and requires an estimate of the initial volume of the interaction. The energy density can be calculated from theoretical models, the hydrodynamical Bjorken model (already quoted in Chapter 1 [10]) being one of the simplest and most widely used:

$$\epsilon = \frac{1}{\pi R^2 \tau} \left(\frac{dE_T}{dy}\right)_{y=0} \quad , \tag{B.5}$$

in which πR^2 is the transverse area of the projectile-ion, with a radius estimated by $R = 1.12 A^{1/3}$; and τ is the longitudinal dimension of the system in the initial moment (or, equivalently, the plasma formation time), τ=1 fm/c is considered a reasonable value. This expression is equivalent to:

$$\epsilon = \frac{\langle M_T \rangle}{\pi R^2 \tau} \left(\frac{dN}{dy}\right)_{y=0} \quad . \tag{B.6}$$

The analysis of charged particle multiplicity produced in NA50, for the most central events, gives [87]:

$$\left(\frac{dN_{ch}}{dy}\right)_{y=0} = 428 \pm 1(stat) \pm 34(syst) \quad . \tag{B.7}$$

Since most of the secondaries produced are pions, with mean transverse mass $M_T \approx 0.4$ GeV/c^2 [103], the corresponding energy density for lead beams at 158 GeV per nucleon is ≈ 3 GeV/fm^3 – around 20 times higher than that of the usual nuclear matter (ρ_o=0.17 GeV/fm^3). According to theoretical predictions, at these densities matter should behave as a quark-gluon plasma. Although it is known today that the Bjorken model is not adequate to describe lead collisions in the SPS, because it assumes longitudinal expansion of the system alone, neglecting collective expansion, it is believed that the energy density achieved in the SPS is of the order of the critical energy density of the phase transition.

From a theoretical point of view, the energy density gives the system temperature, assuming it behaves as a black body radiator. For low energy densities, and so temperatures below the critical value T_c, the system is basically a pion gas, with the relation:

$$\epsilon = 3 \frac{\pi^2}{30} T^4 \quad . \tag{B.8}$$

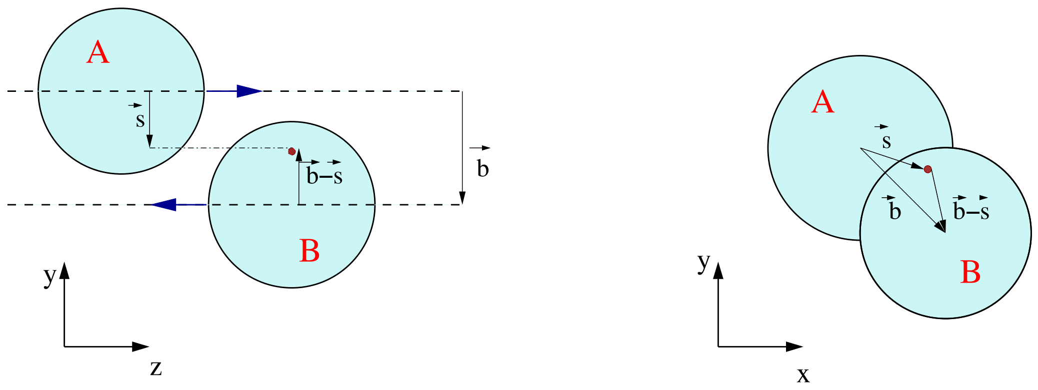

Figure B.2: Nucleon-nucleon collision scheme.

An increase in the system density corresponds to a (much slower) increase of the temperature. At $T = T_c$ a phase transition occurs, with the system becoming a quark-gluon plasma for $T > T_c$, in which:

$$\epsilon = 37\frac{\pi^2}{30}T^4 \tag{B.9}$$

if only gluons and u and d quarks are considered [1].

B.3.2 Impact parameter, N_{col} and N_{part}

Another widely used centrality estimator is the impact parameter b, defined as the minimal distance between the centre of the target and projectile nucleons which take part in the collision. A very central collision corresponds to $b \approx 0$. Although the impact parameter can not be directly measured, it can be deduced from the transverse energy measurement, using a geometrical model.

Figure B.2 gives a schematic representation of a nucleon-nucleon collision. According to the Glauber geometrical model [86] for AB collisions, the nucleus-nucleus collisions can be seen as the superposition of nucleon-nucleon collisions. This model assumes that the projectile nucleus A crosses the target nucleus B in a straight line, with the nucleons undergoing one or multiple inelastic collisions, but all with the same nucleon-nucleon interaction cross-section, σ_o.

The nuclear density of the target nucleus A and the projectile nucleus B, ρ_A and ρ_B, are assumed to be non-homogeneous and to depend on the type of nucleus considered.

[1] Expression B.8 assumes that there are only 3 degrees of freedom in the system, which correspond to the 3 pion types, π^+, π^o e π^-. When $T = T_c$ there is a sudden increase of the energy density, due to the "de-freezing" of the quark and gluon degrees of freedom. The number of degrees of freedom becomes then $n = 8 \times 2 + \frac{7}{8}(2 \times 3 \times 2 \times 2)$, corresponding to $n = color_{gluons} \times spin + \frac{7}{8}((q\ and\ \bar{q}) \times color_{quarks} \times spin \times flavor_{quarks})$. The $\frac{7}{8}$ factor comes from the use of Bose statistics for gluons and Fermi statistics for quarks.

In general, they are described by Woods-Saxon parameterisations with 2 or 3 parameters (2pF or 3pF, depending on the nuclei [7]):

$$\rho(r) = \frac{\rho_o}{1 + \exp{(r - r_o)/C}} \tag{B.10}$$

r being the distance to the centre of the nucleus; and r_o, C and ρ_o obtained from electron-nuclei scattering experiments.

The inelastic interaction cross-section, σ_o, is of 30 mb. The probability that a nucleon in nucleus A collides with a nucleon in nucleus B, separated by a distance $\vec{s}$ in the transverse plane to the collision axis AB, and with an impact parameter $\vec{b}$, is:

$$T_{AB}(\vec{b})\sigma_o = \int d^2s \int \rho_A(\vec{s}, z_A)dz_A \int \rho_B(\vec{b} - \vec{s}, z_B)dz_B\sigma_o \tag{B.11}$$

where $T_{AB}(\vec{b})$ represents the nucleon density per normalised surface units, for an impact parameter $\vec{b}$ (i.e., $T_{AB}(\vec{b})$ is a superposition function of the nuclei A and B in the transverse plane, which verifies $\int T_{AB}(\vec{b})d^2b = 1$).

The probability that n nucleus-nucleus collisions occur, $P_n(\vec{b})$, is described by a binomial function. For a given impact parameter $\vec{b}$:

$$P_n(\vec{b}) = \frac{(AB)!}{n!(AB-n)!}(T_{AB}(\vec{b})\sigma_o)^n(1 - T_{AB}(\vec{b})\sigma_o)^{AB-n} \quad . \tag{B.12}$$

The inelastic cross-section for event production is the probability that there is at least one nucleon-nucleon collision, given by:

$$\frac{d\sigma_{AB}}{d^2b} = \sum_{n=1}^{AB} P_n(\vec{b}) = 1 - (1 - T_{AB}(\vec{b})\sigma_o)^{AB} \approx 1 \quad . \tag{B.13}$$

The mean number of collisions $\langle n(\vec{b})\rangle$ is, according to the binomial distribution assumed:

$$\langle n(\vec{b})\rangle = \sum_{n=1}^{AB} nP_n(\vec{b}) = \sigma_o AB T_{AB}(\vec{b}) \quad . \tag{B.14}$$

Thus, demanding at least one collision, gives a mean number of nucleon-nucleon collisions, $N_{col}(\vec{b})$:

$$N_{col}(\vec{b}) = \frac{\sum_{n=1}^{AB} nP_n(\vec{b})}{\sum_{n=1}^{AB} P_n(\vec{b})} \approx \langle n(\vec{b})\rangle = \sigma_o ABT_{AB}(\vec{b}) \quad . \tag{B.15}$$

The number of nucleons which interacted during the AB collision, N_{part}, can be calculated through the "wounded nucleon model" [90], which also uses the Glauber model formalism. Within this model, N_{part} can be obtained as a function of the impact parameter, but can also be related to directly measured quantities, like the transverse energy released in the collision.

The mean number of nucleons taking part in an AB collision, occurring at impact parameter $\vec{b}$ is given by [104][105]:

$$\begin{aligned} N_{part} = A\int d^2s \int \rho_A(\vec{s}, z_A)dz_A\big(1 - (1-\sigma_o \int \rho_B(\vec{b}-\vec{s}, z_B)dz_B)^B\big) + \\ + B\int d^2s \int \rho_B(\vec{b}-\vec{s}, z_B)dz_B\big(1 - (1-\sigma_o \int \rho_A(\vec{s}, z_A)dz_A)^A\big) \quad . \end{aligned} \tag{B.16}$$

If each of the participant nucleons produces in average N_h secondary hadrons, and each of these hadrons has a mean transverse energy q_h, then each participant nucleon contributes with a quantity $q \equiv q_h N_h$ to the total transverse energy E_T produced in the collision. It is then:

$$E_T(\vec{b}) = qN_{part}(\vec{b}) \quad . \tag{B.17}$$

Both the number of participant nucleons for collisions with a given impact parameter $\vec{b}$ and the transverse energy q produced by each participant nucleon can fluctuate. These are Gaussian fluctuations with variance D_{AB}^2, such that:

$$D_{AB} = wq^2 N_{part}(\vec{b}) \quad . \tag{B.18}$$

Experimentally, the w and q parameters can be obtained from a fit to the transverse energy spectra resulting from all AB collisions (independently of the production of a dimuon – this is what is called the "minimum bias spectra"), $d\sigma^{MB}/dE_T$:

$$\frac{d\sigma^{MB}}{dE_T} \propto \int d^2b P(E_T, \vec{b})\sigma_{AB} \tag{B.19}$$

where $P(E_T, \vec{b})$ is the probability of measuring a transverse energy E_T in a collision with impact parameter $\vec{b}$, described by a Gaussian function:

$$P(E_T, \vec{b}) = \frac{1}{\sqrt{2\pi} wq^2 N_{part}(\vec{b})} \exp\left(-\frac{(E_T - qN_{part}(\vec{b}))^2}{2(wq^2 N_{part}(\vec{b}))^2}\right) \quad . \tag{B.20}$$

B.3.3 The L variable

Historically, the L variable was invented due to the necessity of a good collision centrality estimator for the specific case of the study of the J/ψ resonance suppression in ultra-relativistic heavy ion collisions. This variable measures the mean path of the pre-resonant $c\bar{c}g$ state in the nuclear matter [106][107].

In proton induced collision, the J/ψ suppression factor is defined as:

$$\frac{\sigma_{pA}^{J/\psi}}{\sigma_{pp}^{J/\psi}} \approx A \exp\bigl(-\sigma_{abs}\rho_o L\bigr) \quad , \tag{B.21}$$

while in the nucleus-nucleus collisions this factor is:

$$\frac{\sigma_{AB}^{J/\psi}}{\sigma_{pp}^{J/\psi}} \approx AB \exp\bigl(-\sigma_{abs}\rho_o L\bigr) \quad , \tag{B.22}$$

in which $\rho_o \approx 3/(4\pi r_o^3) = 0.17$ nucleons/fm^3 is the nuclear matter density (and $r_0 = 1.12$ fm the mean radius of a nucleon). For p+A collision, the L variable is then calculated according to:

$$L = \frac{1}{\rho_o} \int d^2 s \biggl(\frac{A-1}{2} \bigl(\int_{-\infty}^{+\infty} \rho_A(\vec{s}, z_A) dz_A \bigr)^2 \biggr) \quad , \tag{B.23}$$

while in nucleus-nucleus collisions it is:

$$\begin{aligned} L = \frac{1}{2\rho_o} \int d^2 b \; d^2 s \int_{-\infty}^{+\infty} \rho_A(\vec{s}, z_A) dz_A \int_{-\infty}^{+\infty} \rho_B(\vec{b} - \vec{s}, z_B) dz_B \\ \biggl((A-1) \int_{-\infty}^{+\infty} \rho_A(\vec{s}, z_A) dz_A + (B-1) \int_{-\infty}^{+\infty} \rho_B(\vec{b} - \vec{s}, z_B) dz_B \biggr) \quad . \end{aligned} \tag{B.24}$$

Appendix C

Fine tuning of the $P * Dtarget$ cut

As was explained in Chapter 3, the $P * Dtarget$ cut allows the elimination of the tracks for which the extrapolation to the target plane is too far from the vertex in the beam line (see figure 3.5). The variable $P * Dtarget$ is approximately independent from the momentum. One defines:

$$Dtarget = \sqrt{(Dx)^2 + (Dy)^2} \tag{C.1}$$

where Dx and Dy are the distances to the axis in the target plane, and involve the constants Δx and Δy. As can be seen in figure 3.6, the momentum of the individual muons varies between 7.5 GeV/c and 75 GeV/c, and the mean value is $\langle p_\mu \rangle \approx 25$ GeV/c. The coefficients Δx and Δy are related with the fact that the beam optics varies slightly with time, and the mean is not always perfectly centred with the target. One defines therefore two sets of 25 coefficients Δx and Δy, one for convergent tracks and the other for divergent, in each momentum bin [1], corresponding to the mean value of the Gaussians which, in the corresponding P_μ bin, describe the distributions of the distances Dx and Dy. Therefore

$$Dx = Dx^o - \Delta x \tag{C.2}$$

$$Dy = Dy^o - \Delta y \quad . \tag{C.3}$$

Figure C.1 shows the distributions of the Dx and Dy shifts as a function of the momentum P_μ of the tracks, in this case for convergent muons.

The distributions of the $P * Di$ variable, with $i = x, y$, in each P_μ bin are fitted with a Gaussian function, and the two sets of 25 σ coefficients are therefore obtained for the

[1] The momentum bins are chosen with a constant width of 3 GeV/c, in the 0< $P_\mu <$ 75 GeV/c region, making a total of 25 bins.

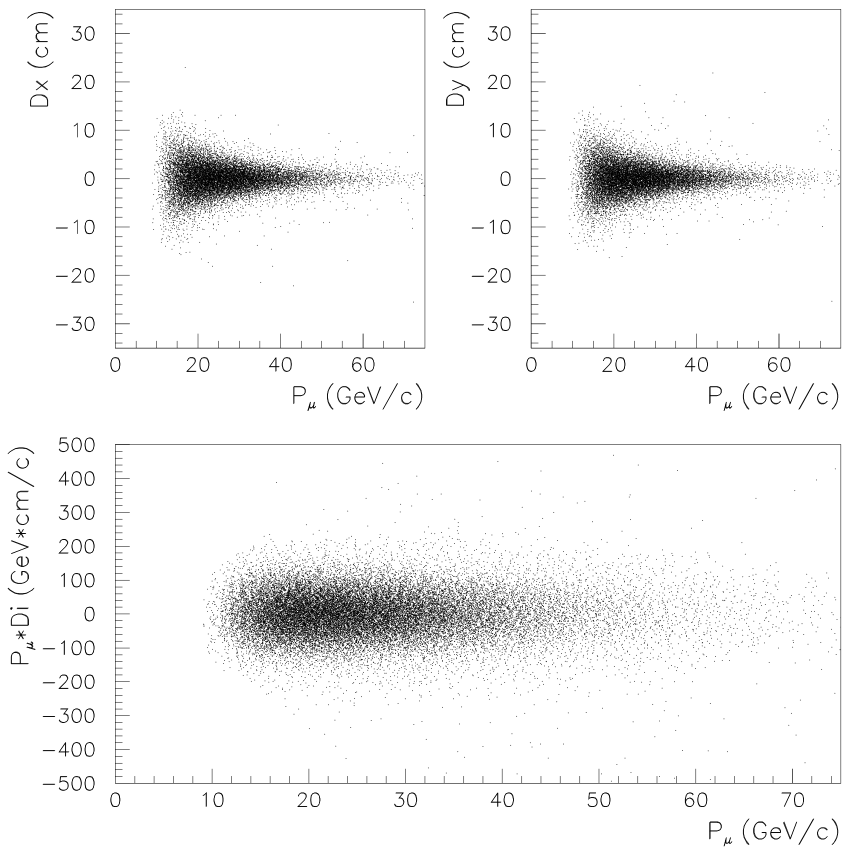

Figure C.1: Distributions of the shifts for convergent muons, Dx and Dy as a function of the momentum of the muons, and corresponding distribution of the $P * Di$ variable, with $i = x$ and y.

typical widths of the distributions. These coefficients are used as a normalisation value of the $P * Dtarget$ variable in each track:

$$pdtgt = \frac{P_\mu \cdot Dtarget}{\sigma} \quad . \tag{C.4}$$

Since the $P * Dtarget$ variable (or equivalently $pdtgt$) has a Gaussian distribution, $(P * Dtarget)^2$ has a χ^2 probability distribution with two degrees of freedom [82]. For this kind of distribution the probability $(P * Dtarget)^2 \geq \chi^2$, with $0 \leq \chi^2 < \infty$, is:

$$Q(\chi^2|N) = \frac{1}{\sqrt{2^N}\,\Gamma(N/2)} \int_{\chi^2}^{\infty} t^{\frac{N}{2}-1} e^{-t/2} dt \tag{C.5}$$

where in this case $N = 2$. With the adjusted coefficients, and for a sample of $\mu^+\mu^-$ events subtracted from combinatorial background, the distribution of tracks in probability should be horizontal. The events for which the tacks are too far from the vertex appear as an excess in the Gaussian tales of $P * Dx$ and $P * Dy$, and give rise to a peak in low χ^2_{pdtgt} probabilities, as one can see from figure 3.7 .

When one uses the coefficients adjusted in the high mass region of events in the $P * Dtarget$ calculation of a set of events with $M < 2.5$ GeV/c^2, one obtains, for low momentum tracks, the probability distributions of figure C.2 .

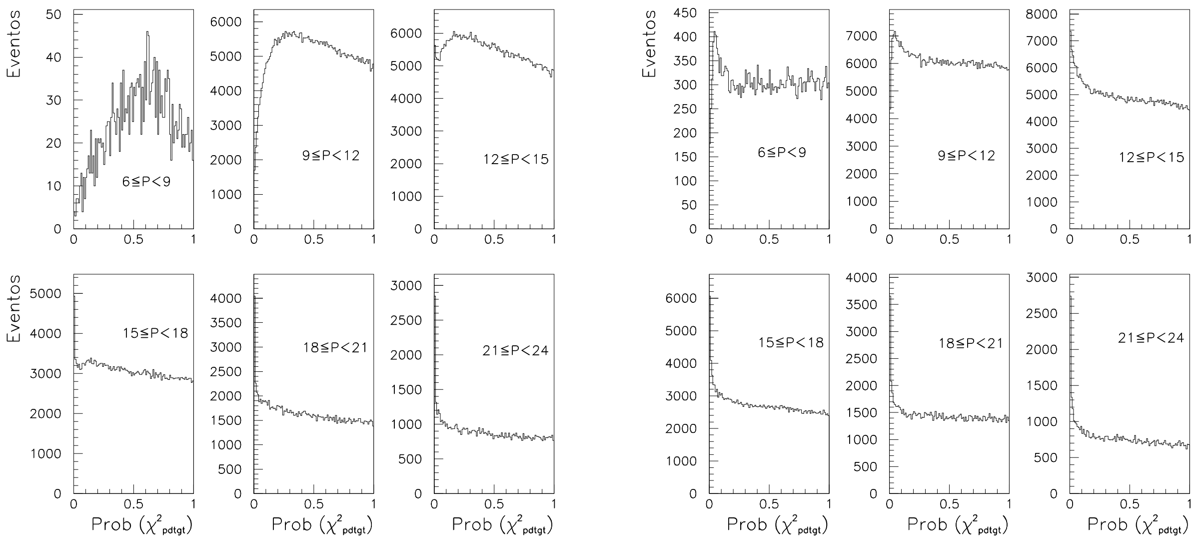

(a) (b)

Figure C.2: χ^2_{pdtgt} probability distributions of convergent (a) and divergent (b) tracks, with a selection of $\mu^+\mu^-$ events with $M < 2.5$ GeV/c^2 and NOCIBI=4 .

For tracks of momentum higher than 24 GeV/c, not shown in figure C.2, the probability distributions are horizontal, except for very low probability, which show a peak, as expected. The tracks with $P_\mu < 18$ GeV/c show an unexpected behaviour, which can in principle be attributed to the contributions of tracks from the combinatorial background [83].

With the purpose of studying this hypothesis, the χ^2_{pdtgt} probabilities for each one of the tracks of each event are represented in a bi-dimensional histogram "First muon probability" *versus* "Second muon probability". Histograms of this kind are defined for both $\mu^+\mu^-$ dimuons, and for the like sign muon pairs. Using the usual formula for the combinatorial background subtraction on these histograms, one obtains a bi-dimensional histogram with the χ^2_{pdtgt} probabilities of both tracks of each event.

Although this method implies loosing information relative to the convergence/divergence of the tracks, it allows to verify that the probability distributions for signal dimuon tracks are approximately horizontal (figure C.3).

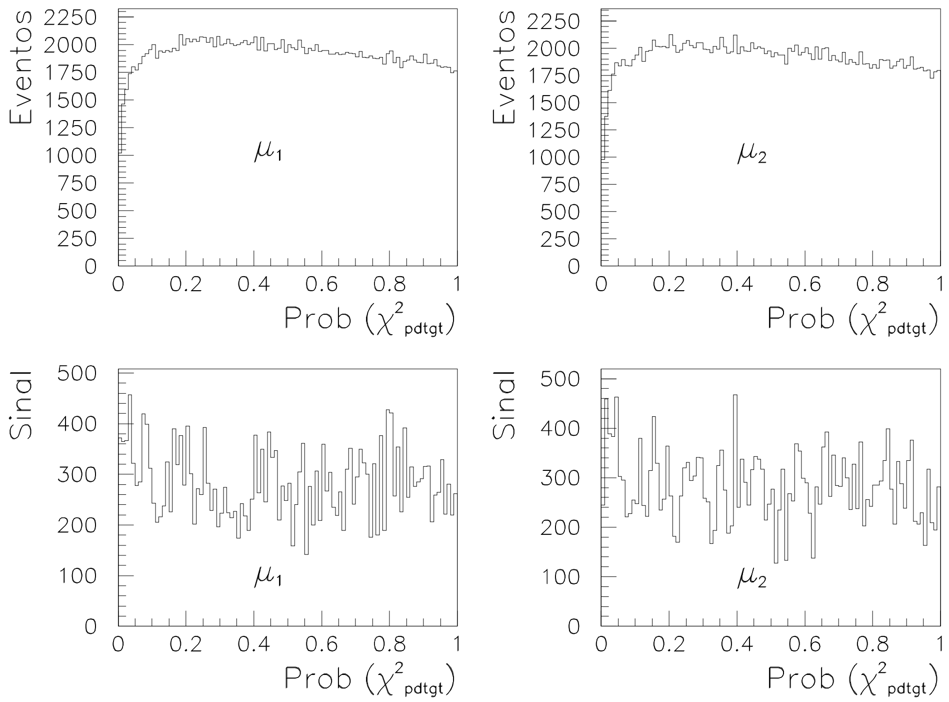

Figure C.3: χ^2_{pdtgt} probability distributions for the first and second muon of signal events, in a set with $M < 2.5$ GeV/c^2, $P_\mu < 12$ GeV/c and with NOCIBI=4 selection.

Bibliography

[1] CERES Col., G. Agakichiev *et al.*, Phys. Rev. Lett. **75** (1995) 1272–1275.

[2] CERES Col., G. Agakichiev *et al.*, Eur. Phys. J. C **4** (1998) 231.

[3] C. Heros, *Low mass dielectron production in S-Au collisions at 200 GeV/n (CERES Col.)*, Tese de Doutoramento, Weizmann Institut of Science, Israel (1996).

[4] K. Gallmeister, B. Kampfer, O. P. Pavlenko e C.Gale, Nucl. Phys. A **688** (2001) 939–955.

[5] NA57 Col., F. Antinori *et al.*, Nucl. Phys. A **698** (2002) 118c–126c.

[6] A. Coc, *Le spectromètre à dimuon de l'expérience NA10 et son système de déclenchement*, Tese de Doutoramento, Université Paris VII (1980).

[7] C. W. Jager, H. Vries e C. Vries, Atomic Data and Nuclear Data Tables **14** (1974) 479.

[8] NA38 e NA50 Col., M. C. Abreu *et al.*, Eur. Phys. J. C **14** (2000) 443.

[9] Particle Data Group, D. Groom *et al.*, Eur. Phys. J. C **15** (2000) 1.

[10] J. D. Bjorken, Phys. Rev. D **27** (1983) 140–151.

[11] U. Heinz e K. S. Lee, Phys. Lett. B **259** (1991) 162–168.

[12] G. E. Brown e M. Rho, Phys. Rev. Lett. **66** (1991) 2720–2723.

[13] T. Hatsuda e S. Lee, Phys. Rev. C **46** (1992) R34–R38.

[14] C. M. Shakin e W.-D.Sun, Phys. Rev. C **49** (1994) 1185–1189.

[15] E. L. Bratkovskaya e C. M. Ko, Phys. Lett. B **445** (1999) 265–270.

[16] K. Haglin, Nucl. Phys. A **584** (1995) 719–736.

[17] R. Rapp, G.Chanfray e J.Wambach, Phys. Rev. Lett. **76** (1996) 368–371.

[18] M. Lutz, S. Klimt e W. Weise, Nucl. Phys. A **542** (1992) 521.

[19] M. Asakawa, C. Ko, P. Levai e X. Qiu, Phys. Rev. C **46** (1992) R1159–R1162.

[20] M. Asakawa e C. M. Ko, Phys. Rev. C **48** (1993) R526–R529.

[21] F. Klingl, N. Kaiser e W. Weise, Nucl. Phys. A **624** (1997) 527–563.

[22] Y. Golubeva, L. Kondratyuk e W. Cassing, Nucl. Phys. A **625** (1997) 832–854.

[23] J. Gasser, H. Leutwyler e M. E. Sainio, Phys. Lett. B **253** (1991) 252–260.

[24] U. Meissner, in *7th International Symposium on Meson-nucleon Physics and the Structure of the Nucleon - MENU '97*, 1997 7–15, 7–15.

[25] W. S. Chung, C. M. Ko e G. Q. Li, Nucl. Phys. A **641** (1998) 357–378.

[26] DLS Col., G. Roche *et al.*, Phys. Rev. Lett. **61** (1988) 1069–1072.

[27] DLS Col., C. Naudet *et al.*, Phys. Rev. Lett. **62** (1989) 2652–2655.

[28] DLS Col., R. J. Porter *et al.*, Phys. Rev. Lett. **79** (1997) 1229–1232.

[29] G. Wolf *et al.*, Nucl. Pys. A **552** (1993) 549.

[30] G. Q. Li, C. M. Ko e G. E. Brown, Phys. Rev. Lett. **75** (1995) 4007–4010.

[31] W. Cassing, W. Ehehalt e C. M. Ko, Phys. Lett. B **363** (1995) 35–40.

[32] CERES Col., G. Agakichiev *et al.*, Phys. Lett. B **422** (1998) 405.

[33] A. Drees, Nucl. Phys. A **610** (1996) 536c–551c.

[34] W. Cassing, W. Ehehalt e I. Kralik, Phys.Lett. B **377** (1996) 5–10.

[35] NA38 e NA50 Col., M. C. Abreu *et al.*, Eur. Phys. J. C **13** (2000) 69.

[36] J. Rafelski e B. Muller, Phys. Rev. Lett. **48** (1982) 1066.

[37] C. Wong, ORNL-CTP-95-14 (1995).

[38] B. Svetitski, T. Matsui e L. McLerran, Phys. Rev. D **34** (1986) 2047–2060.

[39] G. Odyniec, Nucl. Phys. A **681** (2001) 197c–204c.

[40] A. Shor, Phys. Rev. Lett. **54** (1985) 1122–1125.

[41] NA45 Col. e C. P. Heros, CERN-PPE/96-111 (1996) 1–6.

[42] U. Heinz, CERN-TH/99-045 (1999).

[43] G. Odyniec, Nucl. Phys. A **638** (1998) 135c.

[44] NA38 Col., M. C. Abreu *et al.*, Phys. Lett. B **368** (1996) 239.

[45] HELIOS-3 Col., A. Angelis *et al.*, Eur. Phys. J. C **5** (1998) 63–75.

[46] NA50 Col., P. Bordalo *et al.*, Nucl. Phys. A **698** (2002) 127c–134c.

[47] NA50 Col., N. Willis *et al.*, Nucl. Phys. A **661** (1999) 534c–537c.

[48] NA50 Col., M. C. Abreu *et al.*, Phys. Lett. B **499** (2001) 85.

[49] NA49 Col., S. V. Afanasiev *et al.*, Phys. Lett. B **491** (2000) 59–66.

[50] NA50 Col., L. Villatte *et al.*, Ric. Sci. Educ. Perm. Suppl. **116** (2000) 241–248.

[51] S. C. Johnson, B. V. Jacak e A. Drees, Eur. Phys. J. C **18** (2001) 645–649.

[52] S. Soff *et al.*, J. Phys. G **27** (2001) 449–457.

[53] N. Xu, hep-ph/0112122 (2001).

[54] J. Ollitrault, Phys. Rev. D **46** (1992) 229–245.

[55] STAR Col., P.Kolb *et al.*, Nucl. Phys. A **696** (2001) 175–193.

[56] U. Heinz, in *CERN Heavy Ion Physics School - CHIPS 99*, 1999 .

[57] NA49 Col., H. Appelshauser *et al.*, Eur. Phys. J. C **2** (1998) 661–670.

[58] C. Wong, Nucl. Phys. A **681** (2001) 22c–33c.

[59] H. Satz, Nucl. Phys. B, Proc. Suppl. **94** (2001) 204–218.

[60] WA98 Col., A. Lebedev *et al.*, Nucl. Phys. A **698** (2002) 135c–142c.

[61] NA38 Col., C. Lourenço *et al.*, Nucl. Phys. A **566** (1994) 77.

[62] NA50 Col., L. Capelli *et al.*, Nucl. Phys. A **681** (2002) 539c–542c.

[63] R. Rapp e Shuryak, Phys. Lett. B **473** (2000) 13.

[64] C. Y. Wong e Z. Q. Wang, Phys. Lett. B **367** (1996) 50.

[65] T. Matsui e H. Satz, Phys. Lett. B **178** (1986) 416.

[66] NA50 Col., M. C. Abreu *et al.*, Phys. Lett. B **410** (1997) 337–343.

[67] NA50 Col., M. C. Abreu *et al.*, Phys. Lett. B **477** (2000) 28–36.

[68] NA50 Col., C. Quintans *et al.*, a publicar - proceedings de ICHEP'2002 (2002).

[69] NA60 Col., R. Arnaldi *et al.*, Study of Prompt Dimuon and Charm Production with Proton and Heavy Ion Beams at the CERN SPS, Proposal SPSC/P316 (2000).

[70] P. Senger, J. Phys. G **28** (2002) 1869–1875.

[71] X. Altuna *et al.*, CERN-SL/96-023-OP (1996).

[72] J. Astruc, *Production de mésons ϕ, ρ et ω dans les collisions d-C, d-U, S-U à 200 GeV/nucléon et Pb-Pb à 158 GeV/nucléon*, Tese de Doutoramento, Université Paris VI, IPN - Orsay (1997).

[73] B. Alessandro *et al.*, Nucl. Instr. Meth. A **360** (1995) 189.

[74] B. Alessandro *et al.*, Nucl. Phys. B **44** (1995) 303.

[75] E. Chiavassa *et al.*, Proceedings of the 6th Int. Conf. in Calorimetry in High Energy Physics, Frascati (1996) 289.

[76] R. Arnaldi, *Étude de la suppression du J/ψ dans les collisions Pb-Pb au SPS du CERN en fonction de la centralité mesurée avec le calorimètre à zero degré (NA50)*, Tese de Doutoramento, Université Blaise Pascal, Clermont-Ferrand (2000).

[77] R. Arnaldi *et al.*, Nucl. Instr. and Meth. A **411** (1998) 1–16.

[78] NA10 Col., L. Anderson *et al.*, Nucl. Instr. and Meth. A **223** (1984) 26.

[79] NA50 Col., M. C. Abreu *et al.*, Phys. Lett. B **410** (1997) 327–336.

[80] S. Silva, *Software engineering methodologies for the DAS in the NA38/NA50 experiments at CERN*, Tese de Doutoramento, Universidade Técnica de Lisboa, IST (1997).

[81] R. Ferreira, *Produção de dimuões de baixa massa em colisões protão-Núcleo e Núcle-Núcleo à energia de 200 GeV/nucleão*, Tese de Doutoramento, Universidade Técnica de Lisboa, IST (1992).

[82] M. Abramowitz e I. Stegun (eds.), *Handbook of Mathematical Functions with Formulas, Graphs and Mathematical Tables*, Dover, 1972.

[83] C.Quintans *et al.*, *Conclusions from the 21 Nov 2000 video-conference on the $P*Dtarget$ studies*, Rel. téc., NA50 internal note (2000).

[84] M. *et al.*. (NA38 Col.), Nucl.Phys. .

[85] NA49 Col., C. Hohne *et al.*, Nucl. Phys. A **661** (1999) 485c–488c.

[86] R. J. Glauber, in *Lectures in Theoretical Physics*, eds. W. E. Brittin *et al.*, volume I, Interscience Publishers, 1959 315–414, 315–414.

[87] F. Prino, *Study of the phase transition to QGP at the CERN SPS with the NA50 multiplicity detector*, Tese de Doutoramento, Universitá degli Studi di Torino (2001).

[88] NA50 Col., G. Puddu *et al.*, Internal Note NA50 meeting 00/04 (2000).

[89] NA50 Col., R. Shahoyan *et al.*, Internal Note NA50 meeting 00/03 (2000).

[90] A. Bialas *et al.*, Nucl. Phys. B **111** (1976) 461–476.

[91] NA38 Col., M. C. Abreu *et al.*, Nucl. Instr. and Meth. A **405** (1998) 139.

[92] NA38 e NA50 Col., M. C. Abreu *et al.*, Eur. Phys. J. C **13** (2000) 69.

[93] L. Villatte, *Étude de la production des mésons ϕ, ρ et ω dans les collisions d'ions lourds ultra-relativistes au SPS du CERN (dans l'experience NA50)*, Tese de Doutoramento, Université Paris Sud, IPN - Orsay (2001).

[94] P. Csizmadia e P. Lévai, Phys. Rev. C **61** (2000) 031903.

[95] NA50 Col., C. Quintans *et al.*, J. Phys. G **27** (2001) 405–412.

[96] J. Guimarães, *Estudo da produção relativa de mesões-vector $\pi/(\rho+\omega)$ em colisões enxofre-urânio a 200 GeV/nucleão*, Tese de Mestrado, Universidade Técnica de Lisboa, IST (1996).

[97] G. J. Gounaris e J. J. Sakurai, Phys. Rev. Lett. **21** (1968) 244–247.

[98] J. D. Jackson, Il Nuovo Cimento **34** (1964) 1644–1666.

[99] F. Selleri, Phys. Lett. **3** (1962) 76.

[100] Z. Y. Fang, G. L. Castro e J. Pestieau, Il Nuovo Cimento A **100** (1988) 155–165.

[101] C. Wong, *Introduction to High-Energy Heavy-Ion Collisions*, World Scientific, 1994.

[102] J. Collins e D. Soper, Phys. Rev. D **16** (1977) 2219.

[103] C. Vale, *Estudo da produção de mesões π e K em colisões Pb-Pb a 158 GeV/nucleão*, Tese de Mestrado, Universidade Técnica de Lisboa, IST (1997).

[104] D. Kharzeev *et al.*, CERN-TH/96-328 (1996).

[105] F. Fleuret, *Recherche du plasma de quarks et de gluons par l'etude des mésons J/ψ et $\psi\prime$ dans les collisions d'ions Pb et de protons ultrarelativistes sur divers noyaux*, Tese de Doutoramento, École Polytechnique (1997).

[106] C. Gerschel e J. Hufner, Phys. Lett. B **207** (1988) 253–256.

[107] C. Gerschel e J. Hufner, Z. Phys. C **56** (1992) 171–174.